Searching for time-reversal symmetry violation with molecular ions: Quantum state control and photofragment imaging

by

William B. Cairncross

B.Sc., Queen's University, 2013

M.S., University of Colorado Boulder, 2016

A thesis submitted to the

Faculty of the Graduate School of the

University of Colorado in partial fulfillment

of the requirements for the degree of

Doctor of Philosophy

Department of Physics

2019

This thesis entitled:
Searching for time-reversal symmetry violation with molecular ions:
Quantum state control and photofragment imaging
written by William B. Cairncross
has been approved for the Department of Physics

_____

Prof. Eric A. Cornell

_____

Prof. Jun Ye

Date _____

The final copy of this thesis has been examined by the signatories, and we find that both the content and the form meet acceptable presentation standards of scholarly work in the above mentioned discipline.

Cairncross, William B. (Ph.D., Physics)

Searching for time-reversal symmetry violation with molecular ions:

Quantum state control and photofragment imaging

Thesis directed by Prof. Eric A. Cornell

The relative abundance of matter over antimatter in the observable universe cannot be accounted for by the Standard Model of particle physics (SM), and requires additional sources of time-reversal symmetry violation to be explained. Theories seeking to explain this imbalance generically predict electric dipole moments of fundamental particles such as the electron. We search for the electron's electric dipole moment (eEDM) using HfF^+ molecular ions confined in a radiofrequency trap, polarized by a rotating electric bias field. We have produced a first result with this system that is consistent with zero, setting an upper bound $|d_e| < 1.3 \times 10^{-28}$ e cm (90% confidence) – equivalent to setting a lower bound on the mass of beyond SM particles of several TeV. In this thesis, we describe the first generation measurement and progress towards a second-generation measurement with more than an order of magnitude improved sensitivity. In particular, we discuss quantum state preparation of molecular ions by optical pumping, and a new technique for simultaneous differential measurement of molecules with opposite orientations, which allows us to attain the shot-noise limit with hundreds of detected ions and multi-second coherence.

Dedication

To Mum, Dad, John, and Zoe.

Acknowledgements

I have been immensely lucky in my PhD to be advised by Eric Cornell and Jun Ye, two brilliant scientists who bring a wealth of knowledge to every problem we encounter in the lab. They have been patient teachers, enthusiastic supporters, and wise sages, guiding the experiment on our sometimes slow (but hopefully always forward) progress.

On the laboratory side, I would like to thank Matt Grau, Kevin Cossel, and Dan Gresh for guiding my education in the ways of eEDM from Fall 2013. Since then, we have been joined in the lab by Yan Zhou, Kia Boon Ng, Tanya Roussy, Yuval Shagam, Tanner Grogan, Maddie Pettine, and Antonio Vigil. I have learned something from each and every one of these talented people, and I am happy to be leaving the lab in their capable hands. Thanks as well to Krista Beck, Amy Allison, the greater Cornell and Ye groups, and the JILA community as a whole, who have made this a wonderful place to work and learn.

I have received invaluable help from JILA staff Hans Green, James Uhrich, Kim Hagen, Todd Asnicar, Carl Sauer, Terry Brown, James Fung-A-Fat, and Felix Vietmayer. Their knowledge of all things mechanical and electrical has been instrumental in bringing the eEDM experiment to where it is today.

Finally, I would like to thank my friends: Gabby Subia Smith, Kurt Hill, Maggie Jacoby, Sade Odumuye, Andrea Egan, Peter Madigan, Abhinav Prem, Pattilynn McLaughlin, Allison Duh, Will and Annie Jay, Dan Hackett, Joseph Samaniego, Mike Stefferson, Molly May, Matt Norcia, Martha Hawkinson, Maddie Schlick, Stephen Hibbs, and others. Thank you for reminding me that there is a world outside the lab. I hope to see each of you before too long.

Contents

Chapter

Tables

Table

Figures

Figure

Chapter 1

Introduction

1.1 Motivation

This section is reproduced from Ref. [17]

The discovery of the Higgs boson in 2012 [23, 24] marked the completion of the Standard Model of particle physics (SM), in the sense that all of its fundamental particles have now been observed. Predictions of the SM have been confirmed with unparalleled precision [54], making it the best-tested fundamental theory yet developed. Along with general relativity, the SM could in principle model an evolving universe from times as early as nanoseconds after the Big Bang to the present. However, such a universe would look very different from our own: it would be nearly devoid of matter, and – even if that issue were resolved – it would lack the cold dark matter (CDM) whose gravitation is thought to help create the large-scale structure of matter in our universe. In addition, the mass of the SM Higgs boson is small compared to expectations – one incarnation of an issue referred to as the hierarchy problem [38]. These discrepancies and others have for several decades motivated searches for physics beyond the SM (BSM).

The near-absence of matter in a SM universe would result from the near-perfect annihilation of matter particles with their corresponding antiparticles, which are produced in nearly equal quantities. In order to leave behind the matter we observe in our universe, particles and antiparticles must have been produced in unequal amounts. A fundamental theory that can model this process must fulfill the Sakharov conditions: charge conjugation (C) and time reversal (T) symmetries must

be violated [1] , and the universe's evolution must take place out of thermal equilibrium – for example, a first-order phase transition could occur, "freezing in" a matter-antimatter imbalance [33, 106]. While T-violation within the SM has been observed in the decays of K and B mesons governed by the Cabbibo-Kobayashi-Maskawa model of quark flavor mixing [70], it is highly suppressed in the SM, and is believed to be insufficient to explain the observed imbalance of matter over antimatter in the universe [33].

BSM theories seeking to explain the Baryon asymmetry of the universe (BAU) and other phenomena generally include additional sources of CP-violation (Fig. 1.1b), which generate T-violating low-energy phenomena: electric dipole moments (EDMs) of nucleons, nuclei, atoms, and molecules (Fig. 1.1a, [37, 70, 105]). EDMs thus provide a set of observables that are complementary to direct searches for BSM particles in collider experiments. Using only tabletop-scale apparatus, the present generation of atomic and molecular EDM experiments provides constraints on the masses of BSM particles that are comparable to, or even exceed, the reach of the LHC [2, 31].

BSM particles at the TeV scale have long been anticipated [33], as they have the potential to solve several outstanding problems: (i) a stable, weakly interacting massive particle (WIMP) is a natural dark-matter candidate [31, 105]; (ii) SUSY partners at TeV energies could resolve the hierarchy problem and stabilize the Higgs mass [33]; (iii) new CP violating particles at TeV scale could solve the baryogenesis problem, and give rise to EDMs in existing, stable particles [37]. However, so far the LHC has discovered no BSM particles, WIMP dark matter has not been detected, and no electric dipole moments have been discovered. These null results point to the critical importance of enhancing EDM sensitivities, and of expanding the search for new physics in form of very weakly-coupled, lower-mass particles.

Recent progress in atomic, molecular, and optical physics (AMO) techniques such as cooling, trapping, and quantum state control combined with advances in laser technology have led to enormous improvements in precision experiments. In the latest generation of optical atomic clocks, for

[1] According to the CPT Theorem, a quantum field theory conforming with the requirements of locality and Lorentz invariance (special relativity) must be symmetric under combined C, P and T symmetry operations. We assume that all fundamental theories obey this property, and therefore CP-violation is equivalent to T-violation.

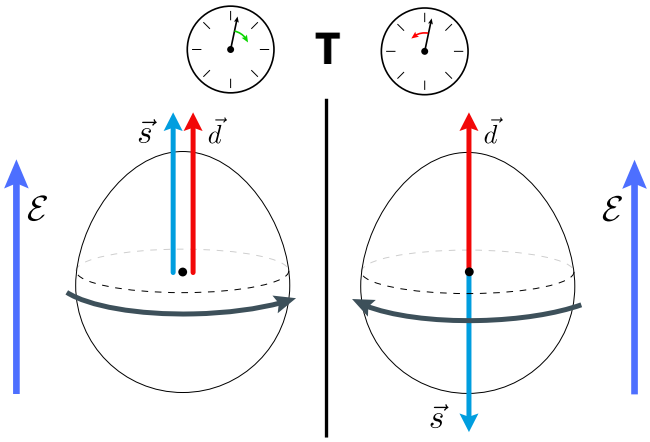

(a)

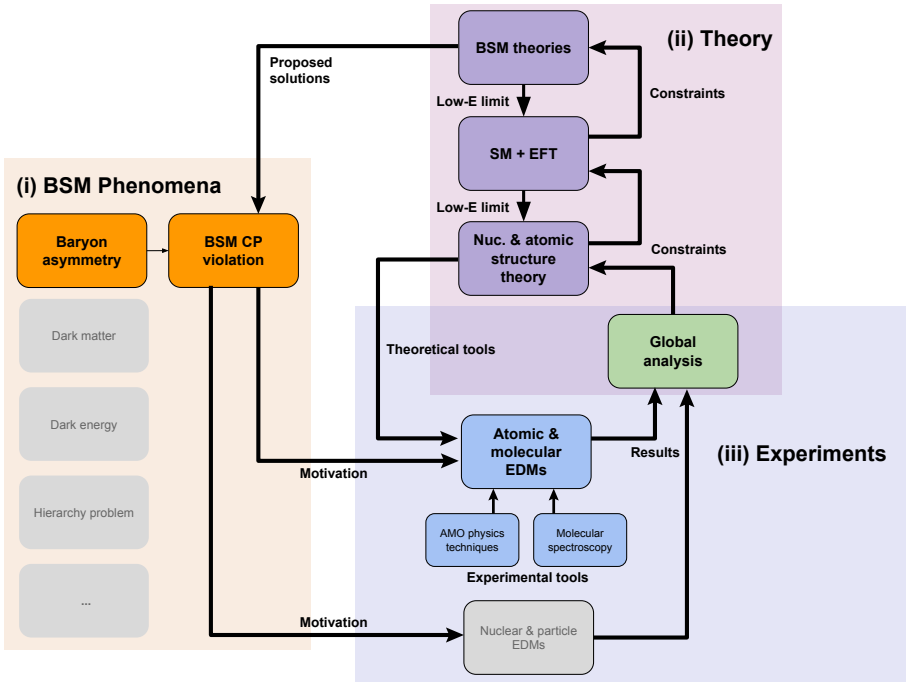

(b)

Figure 1.1: Basic concepts and context of EDM experiments. (a) An electric dipole moment of a particle with spin violates time-reversal symmetry, and assuming CPT symmetry holds, violates CP symmetry. (b) Context for EDM experiments: (i) the Baryon asymetry of the Universe, one of several phenomena not explained within the Standard Model, requires additional sources of CP violation. (ii) BSM theories supply sources of additional CP violation, and an effective field theory approach parameterizes the sensitivity of low-energy composite systems to BSM physics. (iii) Low energy precision measurements of EDMs can be interpreted in a global analysis to constrain BSM theories. Nuclear and particle EDMs contribute on equal footing with results from atoms and molecules in a global analysis.

example, confinement of ultracold alkaline earth-like atoms a three-dimensional optical lattice and probing with light from ultra-stable lasers has enabled fractional frequency stability on the order of one part in 10^{18} and better [18]. The precision attainable in AMO experiments have led to their application to a wide variety of investigations such as searches for dark matter, tests of general relativity, and precision measurements of atomic parity violation [105].

Amongst precision measurements, searches for fundamental symmetry violations via EDM measurements have an exceptionally long history, and have been reviewed extensively (see Ref. [22] and references therein). Recent theoretical insights and experimental innovations have contributed to substantial advancement in EDM experiments, but challenges and opportunities remain in bringing the full toolset of experimental AMO physics to bear on the particular atomic and molecular species that are sensitive to BSM T-violation through EDMs.

1.2 EDM measurements in atoms and molecules

This section is reproduced from Ref. [17]

While polar molecules such as H_2O and NH_3 are often described as possessing electric dipole moments, in non-relativistic quantum mechanics and in the absence of an applied electric field, the eigenstates of all molecules – and indeed all atoms and their constituent particles – are symmetric (up to a factor ± 1) under an inversion of spatial coordinates (parity, P). The application of an external electric field mixes these opposite-parity states, causing the system to acquire a nonzero expectation value of the electric dipole moment operator – i.e., an electric dipole moment is induced. For polar molecules, the very small spacing of opposite parity states of $\leq 10^{-5}$ eV means that the electric field required to fully polarize the molecule can be very small – on the order of only a few V/cm for some molecules. In atoms, by contrast, opposite-parity eigenstates are typically separated by eV energy scales, meaning they can only be partially polarized by laboratory electric fields (Fig. 1.2, upper panel).

Fundamental CP-violating interactions generate a mixing of opposite-parity states even in the absence of an applied electric field, leading to a T-violating permanent EDM of an atom or

molecule [22, 105]. This atomic or molecular EDM can arise from an EDM of a constituent electron or nucleon, or from other T-violating interactions between constituent particles. A permanent electric dipole moment causes a linear shift in the energies of angular momentum eigenstates that is linear in an applied electric field, which for small applied fields can be described by an effective interaction Hamiltonian [70]

$$H_{\text{eff}} = -\left(\mu\,\mathcal{B} + d\,\mathcal{E}\right)\boldsymbol{F}/F \tag{1.1}$$

where μ is the magnetic moment of the atom or molecule within a particular state of total angular momentum F, d is the T-violating permanent electric dipole moment of the atom or molecule, $\mathcal{B}$ is an applied magnetic field, and $\mathcal{E}$ is an applied electric field. The signature of d can be detected as a change in the Zeeman splitting of total angular momentum eigenstates upon reversal of an applied electric field with respect to a simultaneously applied magnetic field (Fig. 1.2, lower panels).

The fact that $\delta_T \neq 0$ for atoms and molecules in general requires the evasion of Schiff's Theorem [110], which states that the total EDM of a composite system is completely shielded, even if one of the constituent particles possesses an EDM. Schiff pointed out several possible ways to avoid complete shielding, one of which is a difference between the charge and electric dipole moment distributions – commonly called the Schiff moment, and is responsible for a large contribution to diamagnetic atoms' nonzero value of δ_T. Intuitively, the Schiff moment is analogous to an offset between the center of mass and the center of charge of an atomic nucleus, caused by T-violating nuclear forces such as those generated by a nucleon EDM. A further evasion of Schiff's theorem was pointed out by Sandars [108], and leads to an orders of magnitude enhancement in sensitivity to an electron EDM in paramagnetic atoms and molecules. This effect arises from the length contraction of a molecule in the frame of a relativistically moving electron (or equivalently, the length contraction of an electron EDM in the lab frame). A more detailed description of the evasion of Schiff's theorem is given in Refs. [27, 62, 105].

The size of a T-violating permanent atomic or molecular EDM is approximately $d \approx 2D\delta_T/\Delta E$, where D is the ordinary electric dipole matrix element between opposite-parity states, ΔE is the

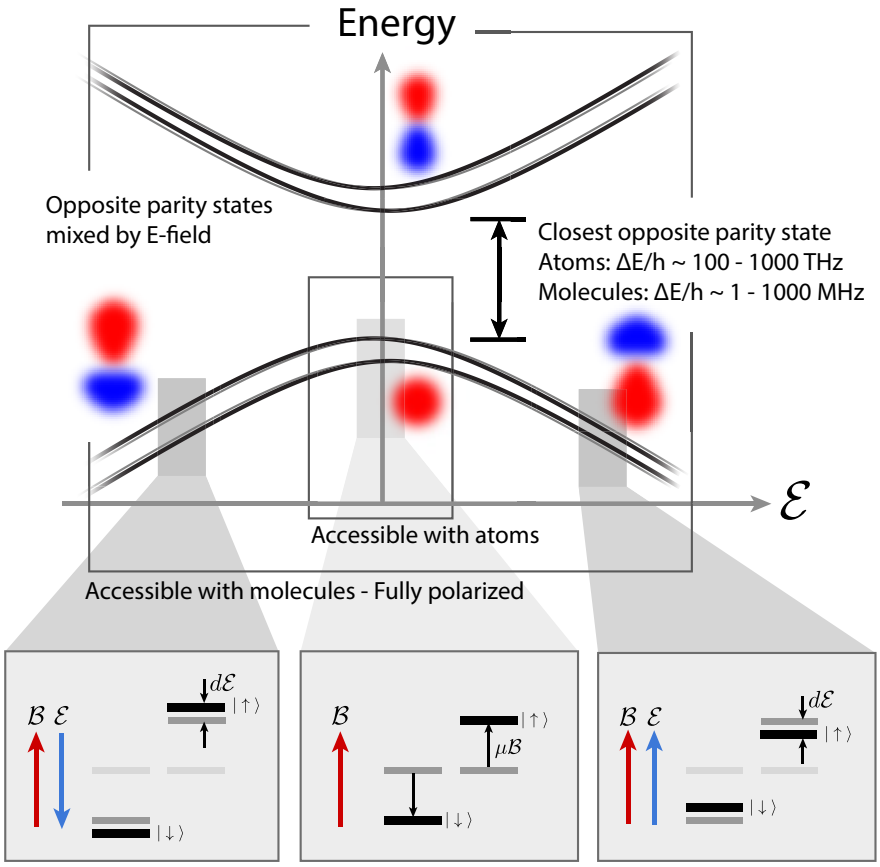

Figure 1.2: Energy levels of an atom or molecule in the presence of an EDM. States of opposite parity are mixed by an applied electric field, while a magnetic bias field orients the magnetic moment. Upper panel: In atoms, only a region of partial polarization can be accessed with typical laboratory electric fields, and excited opposite-parity states decay on the nanosecond scale. In molecules, by contrast, opposite parity states are closely spaced, and regions of complete polarization are accessible. Lower panels: The signature of an EDM is detectable as an electric field-dependent shift in magnetic sublevels $|\uparrow\rangle$ and $|\downarrow\rangle$.

zero-field energy splitting of those states, and δ_T (with units of energy) is the matrix element between opposite parity states induced by T-violating interactions, resulting from the evasion of Schiff's theorem [39, 121]. The large value of D and small spacing ΔE between opposite-parity levels in polar molecules that is a manifestation of their intrinsic deformation also leads to an enhancement of a permanent EDM for a given value of δ_T [121]. An analogous effect leads to enhancement of the Schiff moment in intrinsically deformed nuclei [57, 122].

Essentially all AMO EDM experiments search for a T-violating energy shift in the same way: An atom or molecule is subjected to parallel electric and magnetic fields, and the energy difference between states of opposite magnetic quantum number M is obtained by a measurement of the spin precession angular frequency, $\Delta E = E_\uparrow - E_\downarrow = \hbar\omega$, where up and down arrows represent opposite electronic or nuclear spin states. The usual procedure for such a measurement is Ramsey's method of separated oscillatory fields, illustrated in Fig. 1.3. A pure spin state is prepared by selective population or depletion, and a pair of sequential radiofrequency or laser pulses spaced by a time t maps the relative accumulated quantum phase ωt onto a final relative population between the states being interrogated. A final measurement of populations $N_\uparrow$, $N_\downarrow$ is used to form the asymmetry $\mathcal{A} = (N_\uparrow - N_\downarrow)/(N_\uparrow + N_\downarrow) \approx -\mathcal{C}\cos(\omega t + \phi) + \mathcal{O}$. The contrast $\mathcal{C}$ and offset $\mathcal{O}$ characterize imperfections in state preparation and readout, while γ characterizes decoherence, for example due to instability in the bias magnetic field $\mathcal{B}$.

In one form or another, most EDM experiments are accomplished by counting the number of particles resulting in each spin state. The precision of such a counting experiment (excluding spin squeezing techniques) is limited by quantum projection noise: Projecting the quantum state of a particle in an equal superposition $\sim (|\uparrow\rangle + |\downarrow\rangle)/\sqrt{2}$ onto $|\uparrow\rangle$ and $|\downarrow\rangle$ is analogous to a coin flip, and obeys the same binomial distribution. Identical repetitions of the same projection measurement (or coin toss) will result in scattered values of the asymmetry A with a variance $\sigma^2_{\mathcal{A}} = NP(1-P)$, where N is the total number of particles measured (or coin flips) and $P = 0.5$ is the probability of finding $|\uparrow\rangle$ (or heads). This variance results in an uncertainty in the extracted value of ω, and the

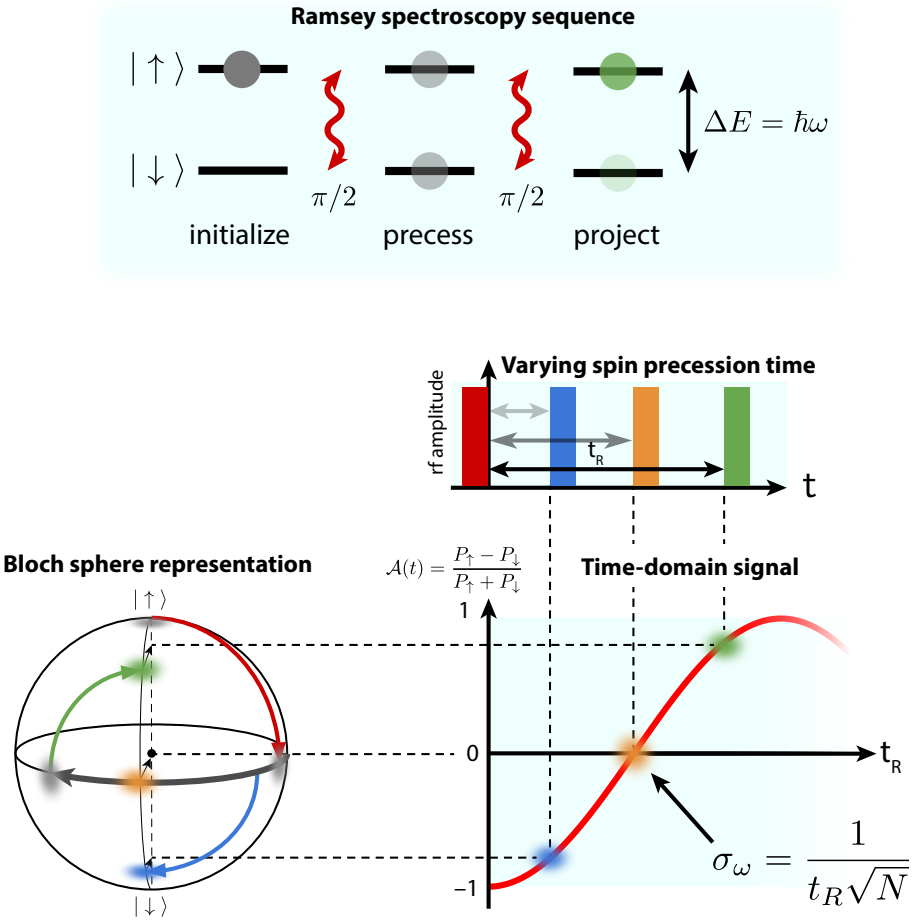

Figure 1.3: A standard method for precision spectroscopy in AMO systems: Ramsey's method of separated oscillatory fields. A pair of RF or laser pulses separated in time by t probes the spin precession phase. The highest attainable precision is given by the shot noise limit, which scales as $1/t\sqrt{N}$.

resulting standard error on a quantum projection noise limited EDM measurement is

$$\sigma_d = \frac{\hbar}{2\mathcal{E}\mathcal{C}_t t\sqrt{N_t f_{\rm rep} T_{\rm tot}}}, \tag{1.2}$$

where $N_t = N_0 e^{-\Gamma t}$ is the number of particles counted in a single experimental cycle including a loss rate Γ, $f_{\rm rep}$ is the repetition rate of the experiment, $\mathcal{C}_t = \mathcal{C}e^{-\gamma t}$ is the measurement contrast including decoherence rate γ, and $T_{\rm tot}$ is the total measurement time.

While quantum projection noise represents the limit of precision for EDM measurements (again neglecting spin squeezing techniques), even attaining this limit is not guaranteed. In most instances, experimental inefficiencies lead to measurements that do not achieve the quantum projection noise limit. This fact makes several features of precision experiments invaluable: The first is high sensitivity to the underlying physics through enhancement factors, which reduces the requisite measurement precision. The second is to make a differential and normalized measurement wherever possible. Finally, sources of technical noise frequently have a "flicker" or $1/f$ spectral character; thus they can often be suppressed by increased measurement frequency. Each of these requirements has played a major role in motivating the present and next generation of EDM experiments.

1.3 Status of the field

This section is reproduced from Ref. [17]

1.3.1 Diamagnetic systems

Diamagnetic atoms and molecules are sensitive to up to 11 of the 13 BSM CPV effective operators that are expected to give dominant contributions to EDMs of low-energy systems [22, 37]. This wide net of possible parameter sensitivities – particularly those connected to strongly-interacting nuclear physics – makes the theoretical interpretation of diamagnetic EDMs challenging [22, 37]. It also makes the benefits of complementary experiments and global analysis highly applicable to diamagnetic EDM measurements [21]. Experiments are underway using a variety of systems, including ^{199}Hg [48], ^{225}Ra [11], ^{129}Xe [74], Rn [124], and TlF [94].

The ^{199}Hg EDM experiment at the University of Washington has set the most stringent constraints on BSM parameters derived from diamagnetic systems, with their most recent limit $|d_{\mathrm{Hg}}| \leq 7.4 \times 10^{-30}$ e cm (95% confidence) in 2016 [48]. To set this limit, the group implemented a Ramsey-like laser spectroscopy scheme conducted on vapor cells of isotopically enriched ^{199}Hg, where they optically pumped and detected the spin orientation of the 1S0 ground state of the atom using near-resonant laser light at 254 nm. The ^{199}Hg experiment attains nuclear spin coherence times on the order of 500 s in their room-temperature, paraffin-coated cells, owing to the shielding of nuclear spin by the closed shells of bound electrons. Less chemically reactive species such as ^{129}Xe attain even longer coherence times [74].

For species such as ^{129}Xe and ^{199}Hg, which have high vapor pressures and long spin coherence times at room temperature, vapor cell experiments are highly advantageous in attaining large signal sizes. However, the large volume occupied by the atomic sample in vapor cell experiments makes them susceptible to systematic errors arising from magnetic and electric field gradients. In addition, the requirement of multiple experimental constraints and the challenges of nuclear theory for ^{199}Hg and ^{129}Xe [37] have led experimenters to consider species such as ^{225}Ra, which has an enhanced Schiff moment through its octupole-deformed nucleus (Fig. 1.4, [5]). This deformation not only leads to an orders-of-magnitude enhancement of BSM physics sensitivity in ^{225}Ra, it also makes this enhancement more readily calculable [4, 35, 41].

An ongoing experiment at Argonne National Laboratory uses AMO techniques of laser slowing, cooling and trapping to perform nuclear spin resonance spectroscopy in the ground state of ^{225}Ra [11, 96]. This isotope is not naturally occurring, but has a long enough half-life of 14.9 days so that it can be produced, transported from Oak Ridge National Laboratory to Argonne National Laboratory, and studied in the EDM experiment. An AMO style experiment allows efficient use of the extremely small available samples by reducing their temperature to the range of 10^{-6} K. The laser-cooled sample can have high optical density and excellent overlap with a probe laser beam, in contrast to the situation in vapor cells.

Despite the challenges of collecting, laser slowing and trapping ^{225}Ra, the Argonne group

has produced two successive limits on d_{Ra}, with the most stringent result $|d_{\mathrm{Ra}}| < 1.4 \times 10^{-23}$ e cm (95% confidence). Since the 2016 result, the group has been working to improve the statistical sensitivity of their experiment: A top priority is the use of electron shelving detection [89], where the population of one nuclear spin projection will be transferred to the $^3\mathrm{D}_1$ state, while the other population is measured using an optical cycling transition. This technique should allow quantum projection noise limited detection of the atoms' spin precession phase, representing an order of magnitude increase in sensitivity.

With improvements to their electric field and spin readout, the Argonne group anticipates attaining EDM precision at the 10^{-25} e cm level, where ^{225}Ra will attain similar sensitivity to BSM physics as ^{199}Hg, and the two experiments' combined constraints on BSM parameters will be more stringent than ^{199}Hg alone. The ultimate precision goal of the experiment is 10^{-28} e cm, which will require improved laser slowing and cooling, as well as a larger source of ^{225}Ra from the Facility for Rare Isotope Beams at Michigan State University [13].

1.3.2 Paramagnetic systems

Until 2011, the most precise measurement of the EDM of a paramagnetic system was set by experiments in the Commins group at UC Berkeley [104]. Since then, a significant advancement has resulted from several key innovations, illustrated in Figure 1.4: the use of diatomic molecules, the cryogenic buffer gas beam, and Ω-doublet electronic states. All EDM results since 2011 in paramagnetic systems have been obtained using diatomic molecules: YbF at Imperial College London in 2011 [64], ThO by the ACME Collaboration (Harvard/Yale) in 2013 and 2018 [2, 6], and HfF^+ at JILA in 2017 [16].

The most recent paramagnetic EDM limit $|d_e| < 1.1 \times 10^{-29}$ e cm or $C_S < 7.3 \times 10^{-10}$ (90% confidence, using a sole-source interpretation) was set by the ACME Collaboration in 2018 [2], representing approximately an order of magnitude improvement over their 2013 limit [6]. Based on generic expressions for how an eEDM could arise in Feynman diagrams including BSM particles, and assuming a near-unity CP-violating phase [105], they estimate that their newest limit constrains

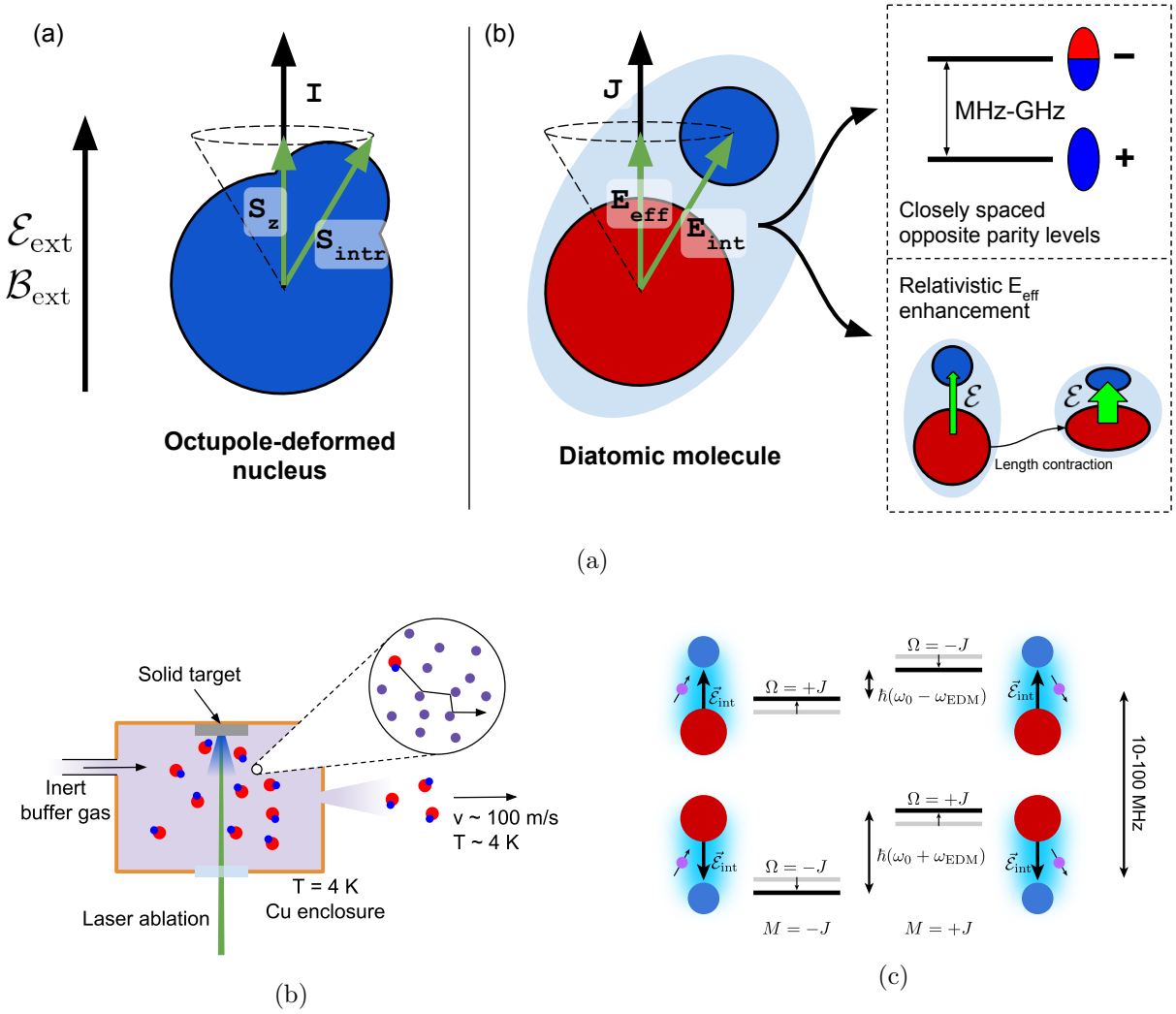

Figure 1.4: Experimental approaches leading to recent results in EDM experiments on diamagnetic and paramagnetic atoms and molecules. (a) Octupole-deformed nuclei have closely spaced nuclear states of opposite parity, enhancing the parity-mixing effect of T-violating matrix elements. These nuclei are orders of magnitude more sensitive to PT-violation than undeformed nuclei. (b) Diatomic molecules for both diamagnetic and paramagnetic EDM searches. Relativistic effects and the distortion of atomic wavefunctions by bonding in heavy polar molecules makes them maximally sensitive to T-violating effects. Molecules also have closely-spaced levels of opposite parity, allowing them to be more easily polarized in the laboratory than atoms – this is analogous to collective Schiff enhancement in octupole-deformed nuclei. (c) Cryogenic buffer gas beams are a highly versatile source of cold, slow, bright beams of almost any small molecule that can be introduced to the inert buffer gas environment. (d) Omega-doublet levels in paramagnetic molecules allow a differential EDM measurement without reversal of a laboratory electric field, greatly suppressing systematics. They are also very closely spaced levels of opposite parity, allowing complete polarization of the molecules in electric fields of tens of V/cm.

the mass scale of new physics to lie above 30 TeV if the contributions are to arise at next-to-leading-order in perturbation theory. This mass range is far beyond the direct reach of the LHC, where the center of mass energy of proton-proton collisions is ~ 14 TeV.

The unprecedented precision achieved by the ACME Collaboration's experiments owes in large part to their extremely high count rate, obtained through the use of a cryogenic buffer gas beam (CBGB, Fig. 1.4b, [67]). In this highly versatile technique, molecules are introduced in the vapor phase into a flow of inert gas inside an enclosure that is cooled to a few Kelvin. The molecules are cooled by collisions with the buffer gas, and escape the enclosure through an aperture to form a cold, bright beam. The versatility of cryogenic buffer gas beams allows molecules to be introduced by a variety of methods: In the first two generations of ACME experiments, ThO molecules have been introduced by ablation of a ThO_2 target. For their third generation experiment, the group have developed a thermochemical source based on the reaction $Th + ThO_2 \rightarrow 2ThO$, which they project will provide an order of magnitude signal increase [97].

The statistical sensitivity of the first-generation ACME experiment was limited by photon shot noise. Sources of technical noise were highly suppressed by their ability to form a differential quantum phase measurement with high bandwidth through polarization switching. The spin readout laser is rapidly alternated between perpendicular linear polarizations, allowing rapid sequential measurements of the projections S_X and S_Y of the quantum state onto perpendicular axes X and Y, respectively, to measure the spin precession angle ϕ. They then form the asymmetry $\mathcal{A} = (S_X - S_Y)/(S_X + S_Y) \propto \cos\phi$ for fluorescence pulses separated by only a few microseconds – a much shorter timescale than variations in the density of molecules in their cryogenic beam. The asymmetry is thus essentially immune to technical noise arising from variations in molecule density, which occur most severely from one pulse of the molecular beam to the next – a timescale of tens of milliseconds.

The ACME II dataset was limited by technical noise, but with a statistical sensitivity approximately 20 times higher than ACME I [6, 7]. While the exact source of excess noise was not definitively established during the data collection, its characteristic timescale was approximately

that of sequential molecular beam pulses, ~ 10 ms. The excess noise enters their EDM measurement because the measured precession phase in two Stark doublets is subtracted to isolate the contribution due to an EDM. Elimination of the noise could be achieved by conducting simultaneous phase measurements in both Stark doublets within a single molecular beam pulse (at the cost of possible systematic effects).

In 2017, our group obtained a limit $|d_e| < 1.3 \times 10^{-28}$ e cm using HfF^+ molecules in an ion trap [16]. While the measurement did not set a new limit on d_e and C_S in a sole-source interpretation, a joint analysis along with the 2014 ACME limit improved the global constraints on d_e and C_S [43]. The first generation molecular ion result was limited by statistics: in a single experimental cycle, only of order $N \approx 10$ signal molecules were detected, out of about 103 trapped molecules. This small fraction of ions contributing to the usable signal resulted from low efficiencies of state preparation and detection. Much like the ^{225}Ra hadronic EDM result, systematic errors and technical noise did not play a dominant role at the present sensitivity – a fact that will certainly change in subsequent measurements as the statistical precision continues to improve.

Towards the second generation eEDM search with HfF^+, our group has implemented an ion trap with a larger trapping volume, allowing the molecular cloud to be cooled by adiabatic expansion. The strong scaling $\gamma_{\text{coll}} \sim T^{13/2}$ of the collisional decoherence rate with temperature [78] has already allowed coherence times of over 2 seconds with 10^4 trapped molecules. The group is also implementing state preparation by optical pumping, which has the potential to improve the usable fraction of trapped molecules from the few-percent level to over 50%, with no change in cycle time or coherence time.

Shot-to-shot variations in ion creation, state preparation and detection efficiency will present a significant challenge for subsequent generations of molecular ion EDM experiments. It is possible to normalize against many of these fluctuations by conducting simultaneous measurements of laser powers and frequencies, however fluctuations in molecular beam properties such as density, velocity, and temperature are significantly more difficult to monitor in situ. A much more robust defense against technical noise is to conduct differential phase measurements within a single experimental

cycle, analogous to the ACME experiment's polarization switching technique. However, such a measurement is difficult to conduct with our group's present detection technique.

The present landscape of EDM searches in paramagnetic systems is one where advancements are being made on several fronts: very large numbers of molecules are produced in a quantum state with high efficiency by the ACME Collaboration through the use of a CBGB and STIRAP [95]; and very long coherence times are being pursued at the JILA trapped molecular ion experiments Future experiments on paramagnetic systems aim to bring together these developments into EDM searches that will constrain BSM physics up to the PeV scale.

1.4 Theoretical interpretation of EDM measurements

This section is reproduced from Ref. [17]

Historically, the possibility of particle EDMs was first pointed out in 1950 by Purcell and Ramsey [103] as a possible counterexample to the common assumption that P is a symmetry of nature – since EDMs violate both P and T symmetries. Their motivation at the time was that lacking a fundamental theory of nuclear structure, P conservation should not be assumed. At the time, a significant nonzero value for the neutron EDM (nEDM) would likely have guided the development of the theory of the strong and weak interactions. Lacking a theoretical interpretation of their null result, however, they did not publish until after PV was proposed and subsequently discovered in 1957 [80, 118, 131]. In a modern context featuring the tools of quantum field theory and the renormalization group, it is possible to interpret the results of EDM experiments as constraints on the mass of BSM particles, and to guide experimental approaches toward systems with optimal sensitivity to BSM physics [21]. Today, EDM searches are more strongly motivated by BSM T-violation and its connection to the BAU.

The theoretical review in Ref. [37] describes in detail the connection of BSM physics to low-energy EDM searches. The authors begin with an effective field theory extension of the SM (SM-EFT, [3, 37, 53]), which supplements the SM with particle interactions of the form $C_i\mathcal{O}_i/\Lambda^2$. Operators $\mathcal{O}_i$ couple SM fields such as electrons and quarks, while the mass scale of BSM physics Λ

suppresses its magnitude, and a dimensionless Wilson coefficient C_i encapsulates the effects of BSM particles that are not directly observed. They identify thirteen effective operators at the SM scale that are expected to give dominant contributions to EDMs, and further apply effective field theory techniques to identify these operators with T-violating observables at the atomic scale (Fig. 1.5).

At low energies, searches for EDMs can be categorized according to the physical system being experimented on: paramagnetic atoms or molecules, diamagnetic atoms or molecules, or particles and nucleons. Permanent EDMs of paramagnetic atoms and molecules arise primarily from the electron EDM d_e and the scalar electron-nucleon coupling C_S [22]. Diamagnetic atom or molecule EDMs arise from the nuclear Schiff moment S, which obtains dominant contributions from nucleon EDMs d_n and d_p and from isoscalar and isovector nucleon-pion interactions $g_\pi^{(0)}$ and $g_\pi^{(1)}$. Independently, diamagnetic EDMs can also arise from scalar and tensor electron-nucleon interactions C_S (at sub-leading order) and C_T (at leading order) respectively [22].

No EDM of an atom, molecule, nucleus, or nucleon has yet been observed. Measurements that are consistent with zero are used to set constraints on CP-violating parameters: typically, it is assumed that the Wilson coefficient C is of order unity, and an upper bound on an EDM is used to set a lower bound on the mass scale Λ of BSM particles. Within a particular BSM theory, limits can be set on the masses of specific particles [38]. Because different experimental searches are sensitive to multiple BSM effects at different levels, and since multiple CPV terms generally arise in the low-energy limit of a BSM theory, the most robust constraints are obtained by a global analysis of experimental results [22, 43]. In the method of Ref. [22], the EDM of a system is parameterized as a sum of contributions $d_i = \sum_j \alpha_{ij} C_j$, where $\alpha_{ij} = \partial d_i / \partial C_j$ is a theoretically obtained sensitivity of the EDM of system i to source C_j. The function $\chi^2(C_j) = \sum_i (d_i^{\rm exp} - d_i)^2 / \sigma^2_{d_i^{\rm exp}}$ then expresses the deviation of the observed value from what might arise from a superposition of multiple sources. Reasonable ranges for BSM physics parameters are then ellipsoids with boundaries of constant χ^2. This model-independent analysis provides an agnostic interpretation of multiple EDM measurements with varying sensitivities to a large number of BSM parameters, and allows predictions of which future measurements may most effectively improve

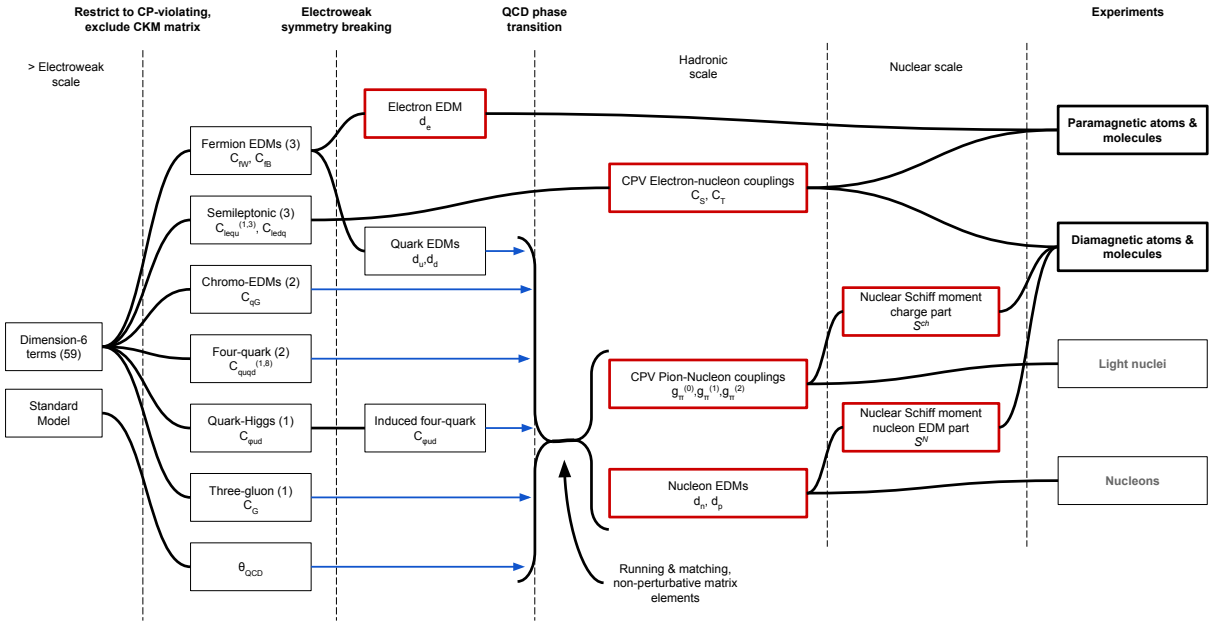

Figure 1.5: Interpretation of EDM experiments. (a) SM-EFT sources of EDMs, interpreted from the text of Ref. [37]. Dimension-six effective operators couple Standard Model degrees of freedom, encapsulating the effects of BSM theories at the electroweak scale. Engel *et al.* [37] trace the effects of a subset of 12 CP-violating effective operators through the hadronic and nuclear scales to their effects on EDMs of paramagnetic and diamagnetic atoms and molecules, nucleons, and nuclei.

upon existing constraints (Fig. 1.6, [22, 43]).

It is also possible to extract constraints on the masses of specific BSM particles from EDM measurements within a particular SM extension [37, 38, 105]. In this case, the contributions of BSM particle interactions to EDMs can be evaluated explicitly, and experimental EDM limits result in constraints on particle masses and mixing angles. In the case of supersymmetric models, the electron EDM constraints on the electron superpartner mass exceeds the reach of the LHC [2, 38].

1.5 About this thesis

This thesis is the seventh to come out of the Cornell/Ye eEDM project, where we have been measuring the electron's electric dipole moment (eEDM) with trapped molecular ions, presently with HfF^+ and in the third-generation experiment with ThF^+. At the inception of this project, HfF^+ and ThF^+ were not molecules whose state assignments and spectroscopic constants could be looked up on the NIST Webbook database [2] , nor anywhere else in the literature. As a matter of fact, it was not even decided which molecular ion the experiment would use until around 2011. An enormous amount of work carried out by the previous PhD students on the project made our first measurement possible in 2017.

Survey spectroscopy of HfF^+ and ThF^+ was carried out by Laura Sinclair, Kevin Cossel, and Dan Gresh in the comb velocity modulation spectroscopy lab, with survey work on ThF^+ being completed in early 2016 [28, 51, 112]. Russell Stutz, Huanqian Loh, and Matt Grau developed techniques for producing neutral HfF in a supersonic beam [120] and conducted studies that enable us to produce large amounts of HfF^+ in their rovibronic ground state: they performed laser-induced fluorescence (LIF) spectroscopy of HfF in the neutral beam to determine suitable intermediate states for ionization [50], they studied the Rydberg states of HfF that autoionize to form HfF^+ and studied their propensities for producing different rotational states [83], and they used LIF of the trapped HfF^+ ions to characterize their resulting internal states [84]. Finally, after having experienced

[2] `https://webbook.nist.gov/`

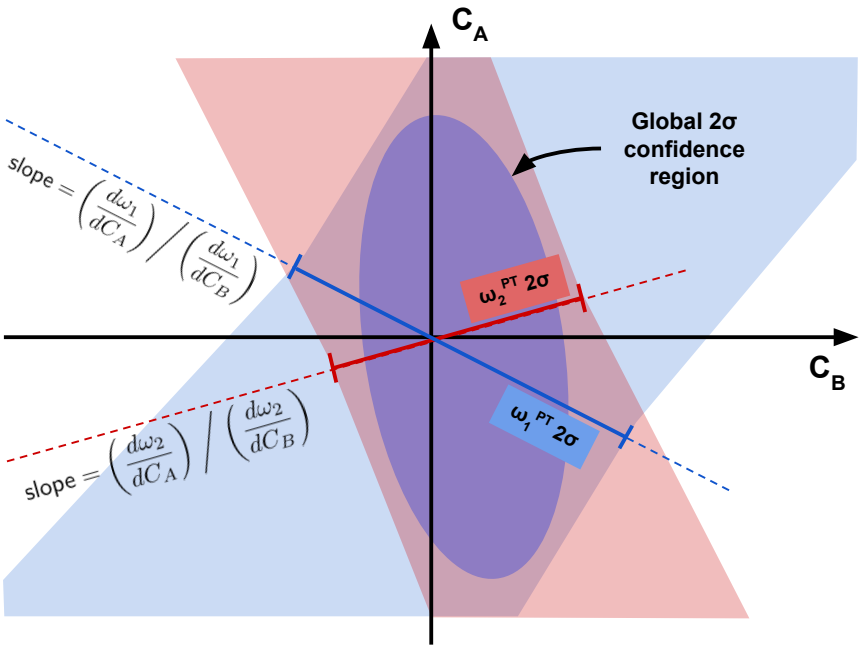

Figure 1.6: Conceptual picture of global analysis of EDM results: Two experiments labeled 1 and 2 have different sensitivities to CPV coefficients C_A and C_B, parameterized by the slopes $\left(\frac{d\omega_{1,2}}{dC_A}\right) / \left(\frac{d\omega_{1,2}}{dC_B}\right)$. A global analysis can be used to obtain simultaneous constraints on C_A and C_B from experiments 1 and 2.

the challenging (to put it mildly) signal-to-noise ratios that come with performing LIF detection of molecular ions without optical cycling transitions, Kang-Kuen Ni, Kevin, Matt, and Huanqian developed our rotational state-selective resonance-enhanced multiphoton dissociation (REMPD) in 2013 [91].

This thesis covers the period from Fall 2013 to Summer 2019 in the HfF^+ eEDM lab. In Fall 2013, Huanqian *et al.* had just demonstrated our first eEDM-sensitive Ramsey fringes in the $^3\Delta_1$ state of HfF^+. In 2014, we worked to understand our statistical sensitivity, in particular working to improve the efficiency of population transfer from $^1\Sigma^+(v=0, J=0)$ to $^3\Delta_1(v=0, J=1)$, and understanding the effects limiting our coherence time. This work is described in detail in Kevin Cossel's thesis [28].

In 2015, we studied systematic errors. The sources of systematic frequency shifts in our experiment are in many cases not particularly comparable to those of previous eEDM experiments, or to trapped-ion atomic clocks, and so this investigation was a significant learning experience wherein we learned the best ways to look for and understand systematics in our unique apparatus. A large number of effects are described in Matt Grau's thesis [49], and others are described in the supplemental information of Ref. [16], which I have reproduced in Section 3.5 of this thesis. Throughout the process of our systematic error investigations, I performed a large number of theoretical calculations regarding the structure of HfF^+ in external electric and magnetic fields, which may be useful in the future. These are described in Chapter 2.

In 2016 and early 2017, with the addition of Dan Gresh (who moved over from ThF^+ spectroscopy) and Tanya Roussy to the HfF^+ ion trap lab, we collected eEDM data and produced our first measurement, which is described in Dan Gresh's thesis [52], and in Ref. [16] which is reproduced in Chapter 3 of this thesis.

The majority of the original content of this thesis covers our progress towards a Generation 2 experiment with at least an order of magnitude improved sensitivity, which covers the period Spring 2017 to Summer 2019. We designed, constructed, and commissioned our Generation 2 ion trap beginning in Fall 2016 and concluding in Fall 2017, described in Chapter 4. We then

completely altered our state preparation scheme to a much lower-tech approach, the motivation and implementation of which is described in Chapter 5.

Next, inspired by a serendipitous combination of Yuval Shagam's experience in velocity map imaging (VMI), very nice photodissociation results from the Zelevinsky group at Columbia [85, 86], and advice from Tanya Zelevinsky herself during a visit in 2018, we developed a scheme by which we can use molecular orientation-resolved REMPD to conduct an eEDM-sensitive differential phase measurement in a single experimental cycle. I feel that this last development breathes new life into the potential precision of this and future precision measurement experiments with trapped molecular ions. The oriented REMPD scheme is described in Chapter 6.

Finally, in Chapter 7, I explore the implications of our improved count rate, coherence time, and new REMPD signal for a Generation 2 eEDM measurement. It is my hope that this will provide a jumping off point for our group to produce a second generation measurement in relatively short order.

1.5.1 Experiment overview

The HfF^+ eEDM experiment is unusually complex, even for a modern AMO physics experiment. Altogether, we have about 13 lasers (listed in Appendix C), and each step of the experiment might have been an atomic physics experiment in its own right a few decades ago. This thesis is primarily about improving several of these steps, rather than inventing each of them – therefore I provide a brief description of the entire experiment here. An overview of the HfF^+ eEDM experiment is shown in Fig. 1.7. One cycle of the experiment consists of the following steps:

(1) **Supersonic beam**

We produce neutral HfF through the reaction of Hafnium with Sulfur Hexafluoride, SF_6, in a supersonic beam of Argon. The SF_6 is seeded with 1% concentration in Ar, and the mixture is allowed into the chamber one 50 microsecond puff at a time through a piezoelectric valve in the source chamber. While the piezo valve is open, we ablate a rod of

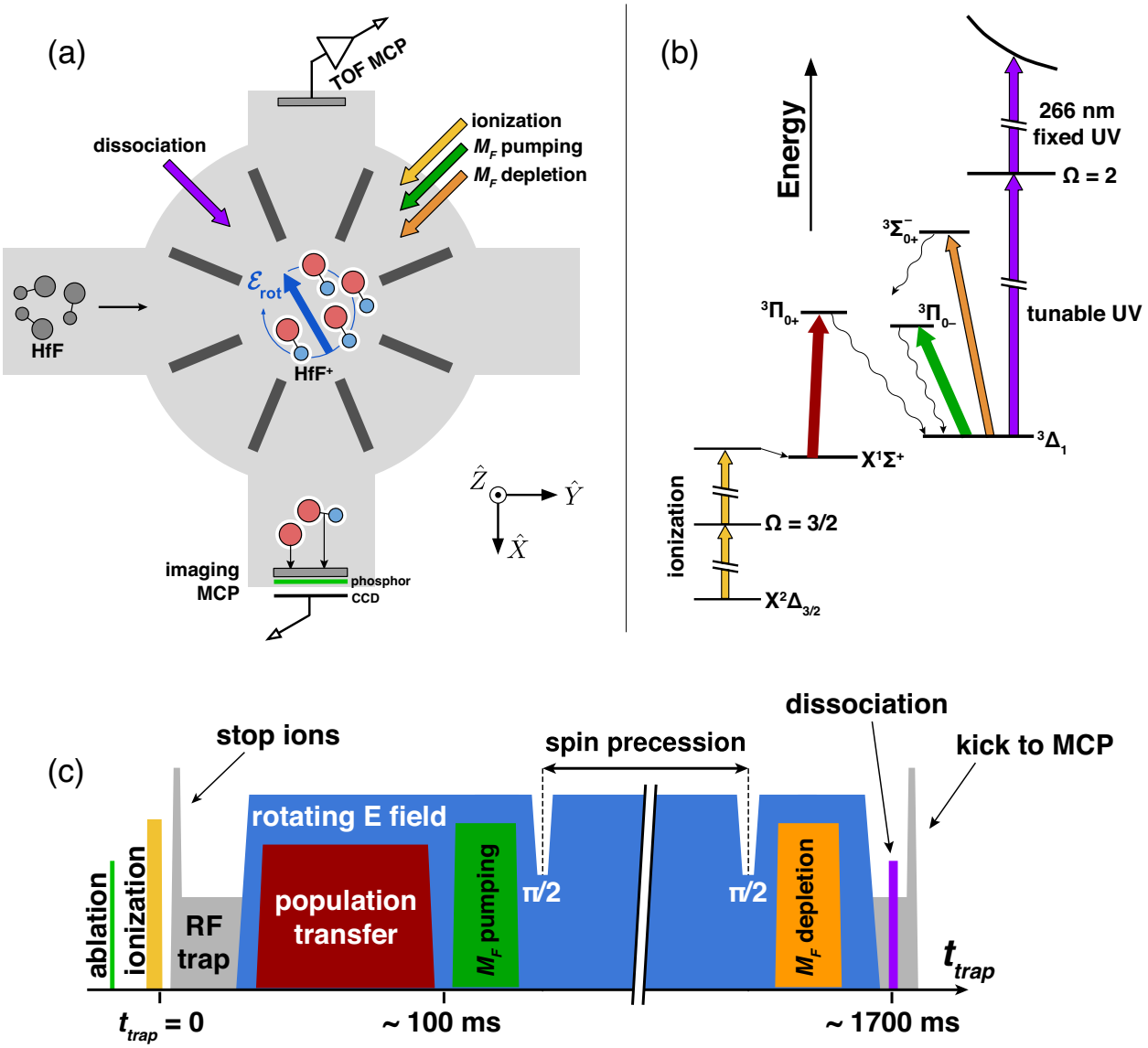

Figure 1.7: Overview of the HfF$^+$ eEDM experiment. (a) Top-down view of the main vacuum chamber containing the RF ion trap. (b) Relevant energy levels of HfF and HfF$^+$, with lasers showing main transitions. (c) Timing diagram showing the major teps of the experiment sequence: (1) Neutral HfF production, (2) ionization, (3) ion trapping, (4) state preparation, (5) Ramsey sequence, (6) dissociation, and (7) detection. These steps are described in detail in Section 1.5.1 of the text.

Hafnium that is mounted next to the valve opening, causing vaporized Hf and Hf^+ to be injected into the supersonic expansion of Ar + SF_6. The HfF (along with whatever other reaction products may be present) are rotationally and vibrationally cooled by collisions with Argon, and accelerated to speeds of about 600 m/s. The beam passes through a pair of skimmers, which for our purposes leaves behind a cold "slug" of HfF traveling through our vacuum chamber towards the ion trap at 600 m/s. Molecular beam production for the HfF^+ experiment was primarily developed by Russell Stutz and Aaron Leanhardt, and is described in Russ' thesis [120].

(2) **Ionization**

Just as the slug of HfF passes through the center of the ion trap, the pulses of UV light from our two ionization lasers ("Harambe," 309 nm and "Bertha," 367 nm) arrive, resonantly ionizing HfF to form HfF^+ in its vibronic ground state $^1\Sigma^+ (v = 0)$, with ions populating the lowest few rotational states N = 0-3. This fairly exact timing is surprisingly easy to achieve, via knowledge of the velocity of an Argon supersonic beam from the literature, measuring the distance from the pulsed valve to the trap center (a measuring tape will do just fine), and using fast photodiodes and an oscilloscope to compare the pulsed valve timing with the arrival time of the laser pulses at the ion trap. The details of HfF^+ resonance-enhanced multiphoton ionization (REMPI) were worked out by Huanqian Loh and others, and are described in Huanqian's thesis [82].

(3) **Ion trapping**

Following their creation, we confine the HfF^+ ions in our RF trap and apply a rotating electric bias field $\mathcal{E}_{\mathrm{rot}}$ to polarize the molecules. While the control, signal generation, and amplification electronics have changed completely since the beginning of the second generation HfF^+ experiment, the mechanics of trapping remain very much the same, and a useful introduction is given in Ref. [82]. The Generation 2 ion trap and electronics are described in Chapter 4 of this thesis.

(4) **State preparation**

While the HfF^+ ions are created in their $^1\Sigma^+$ ground state, we need to prepare them in a single M_F magnetic sublevel of the $^3\Delta_1$ $(v = 0, J = 1)$ state. In Generation 1, this was done by a stimulated Raman process that equilibrated population between $^1\Sigma^+$ $(v = 0, J = 0)$ and $^3\Delta_1$ $(v = 0, J = 1)$, followed by selective depletion of M_F levels. For Generation 2, we have moved to an incoherent state preparation scheme, which is described in Chapter 5.

(5) **Ramsey sequence**

The Ramsey interferometer sequence that extracts the eEDM-induced energy shift between $M_F = \pm 3/2$ levels in $^3\Delta_1$ $(v = 0, J = 1)$ is carried out simply by modulating the magnitude of $\mathcal{E}_{\rm rot}$, which is performed by the same digital synthesis boards that control the trap electronics as a whole. These boards were designed, constructed, and tested by Felix Vietmayer, Dan Gresh, Carl Sauer, and Terry Brown. Following the second $\pi/2$ pulse (i.e., modulation of $\mathcal{E}_{\rm rot}$), we use a circularly polarized laser to deplete one of the M_F levels, thus projecting the population onto the M_F basis. This step is described in Chapter 5.

(6) **Dissociation**

At the end of the Ramsey sequence and following M_F depletion, the ion trap still contains HfF^+ ions in a mixture of internal states, only a small subset of which we would like to know about – namely, those remaining in $^3\Delta_1$ $(v = 0, J = 1)$. We detect those ions by selectively photodissociating them into $Hf^+ + F$, as described in Chapter 6.

(7) **Ion detection**

We detect both Hf^+ and HfF^+ ions using microchannel plate (MCP) ion detectors, which are common tools in physical chemistry and see some use in atomic physics. While many physical chemistry experiments use complex systems of electrostatic lenses to achieve high quality ion imaging, we are less picky, and simply use the arbitrary waveform capabilities of our ion trapping electronics to kick the entire bunch of both HfF^+ and Hf^+ ions simul-

taneously onto an MCP. Thanks to recent lessons from our postdoc Yuval Shagam, we now use our imaging MCP detector to its fullest potential: we apply a gated voltage to the phosphor, allowing us to selectively image the Hf^+ ions, which arrive first in time of flight due to their lower mass than HfF^+. We simultaneously collect a time trace by AC coupling to the middle of the pair of MCPs, giving us access to information about the number of HfF^+ ions in the same experiment cycle.

Chapter 2

Theoretical calculations in HfF^+

2.1 Molecular structure

For both numerical and analytic calculations of frequency shifts and population dynamics in HfF^+, it is essential to have an effective Hamiltonian model of molecular structure. In the Generation 1 eEDM experiment, we primarily used an effective Hamiltonian for the $^3\Delta_1$ state only, along with numerical simulations of ion motion, to predict the values of frequency channels f^0, f^D, f^{BR} and so on. Over the years, I have also found this model useful for simulations of coherent transfer, depletion, optical pumping, and microwave spectroscopy, with varying degrees of success at reproducing experimental observations. In this section, I will describe the various components of the effective Hamiltonian, attempt to motivate their structure, and detail their implementation in Matlab. Along the way, I will give an operational introduction to molecular structure and spherical tensor operators.

2.1.1 Qualitative features of HfF^+

While the details of molecular structure are complex, and our analysis is often fairly mathematical, there are certain general features of HfF^+ that can be understood through freshman undergraduate chemistry methods such as molecular orbital theory. HfF^+ is an ionically bonded molecule, meaning that in the ground and low-lying electronic states, Hf^+ essentially donates an electron to F. The fluoride anion F^- has a $^1S_0$ configuration, so the low-lying states of HfF^+ with nonzero total angular momentum arise from the 5d and 6s orbitals of Hf^{2+}, as shown in Fig. 2.1. As

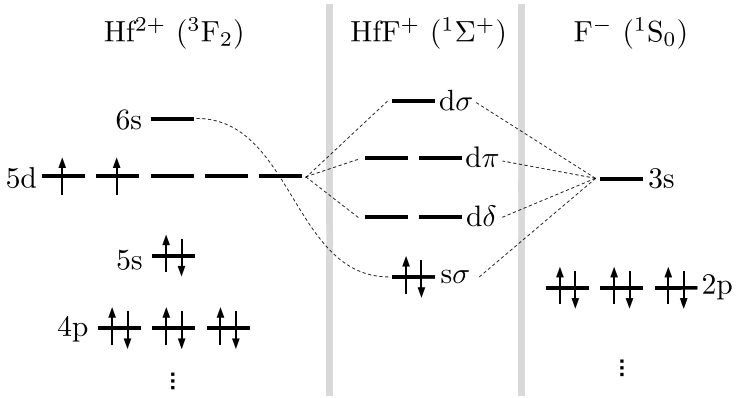

Figure 2.1: Molecular orbital diagram for HfF^+. Since the molecule is ionically bonded, the molecular states correlate with atomic states of Hf^{2+} and F^-. The ground electronic state of Hf^{2+} is $^3F_2$, and correlates with the excited $^3\Phi_2$ state of HfF^+.

discussed in Kevin Cossel's thesis [28], the ground $^1\Sigma^+$ state arises from the sσ molecular orbital, while the low-lying $^3\Delta$, $^1\Delta$, $^3\Pi$, and $^1\Pi$ states (and others) arise from single excitations of the valence electrons from sσ to dδ and dπ. The fact that these molecular states primarily arise from the states of Hf^{2+} allows an estimate of their spin-orbit and Λ-doubling parameters [28]. Interestingly, the ground electronic state of Hf^{2+} is $^3F_2$, like the isoelectronic ion La^+. While the $^3\Phi_2$ state in HfF^+ arises from this state, it is an excited state of HfF^+ by nearly 15000 cm^{-1}. The reasons for the ordering of the states of HfF^+ can be justified using Ligand-field theory, as discussed for the isoelectronic neutral molecule LaF in [109].

Though HfF^+ is ionically bonded, a positive net energy is required to remove an electron from Hf^+ and donate it to F: In other words, the ionization energy of Hf^+ is greater than the electron affinity of F. Therefore, if the HfF^+ molecule were adiabatically dissociated from its ground state, the resulting atomic species would be Hf^+ + F. As a result, the ionic and covalent states cross in the region of internuclear distance where the ionic bond is broken, as illustrated in Figure 2.2. This situation results in a high probability of quasi-bound ("predissociating") states, which presented challenges for our photodissociation-based detection scheme, discussed in Section 6. A further consequence of the ionic nature of the HfF^+ bond is the very large dissociation energy of $D_e \approx$ 52000 cm^{-1} [91], which requires us to use multiple UV photons for photodissociation, as described

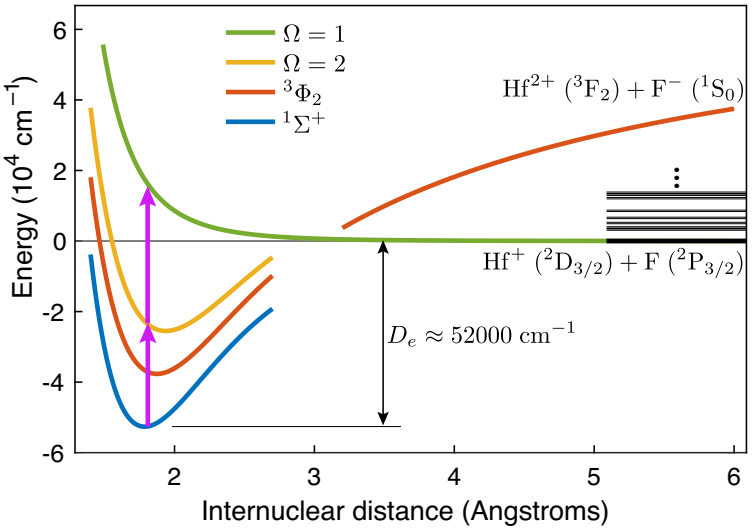

Figure 2.2: Schematic potential energy curves for HfF^+, including a few electronic states of the molecule and free atoms. The low-lying bound states of the molecule are ionically bonded, so they correlate to electronic states of Hf^{2+} and F^-. Shown in black at the right are the energies of low-lying electronic states of free Hf^+ and F below 14000 cm^{-1}. Potential curves are drawn as Morse potentials.

in Section 6.

2.1.2 The molecular wavefunction

The complete wavefunction of a molecule in the nonrelativistic approximation is a solution to the time-independent Schrödinger equation with the total molecular Hamiltonian

$$H = H_{\text{nuc}} + H_{\text{elec}} + H_{\text{spin}}, \tag{2.1a}$$

$$H_{\text{nuc}} = \sum_{\alpha} \frac{P_\alpha^2}{2M_\alpha} + \sum_{\alpha<\beta} \frac{kZ_\alpha Z_\beta}{R_{\alpha\beta}}, \tag{2.1b}$$

$$H_{\text{elec}} = \sum_{i} \frac{p_i^2}{2m_e} + \sum_{i<j} \frac{k}{|\boldsymbol{r}_i - \boldsymbol{r}_j|} - \sum_{\alpha,i} \frac{kZ_\alpha}{|\boldsymbol{r}_i - \boldsymbol{R}_\alpha|}, \tag{2.1c}$$

where Latin indices enumerate electrons, Greek indices enumerate nuclei, m_e is the electron mass, M_α is the mass and Z_α is the charge of nucleus α, and $k = e^2/(4\pi\epsilon_0)$. For the complete system of HfF^+, with $A_{\text{Hf}} + A_F - 1 = 80$ electrons and 2 nuclei, solution of the Schrödinger equation is extremely difficult. To make matters worse, the Hf nucleus with $Z = 72$ causes electrons to experience significant relativistic effects. Thus, strictly speaking, the already intractable Schrödinger equation is not even the correct equation to solve to obtain the complete structure and character of the states of HfF^+!

Despite this complexity, all is not lost for this precision measurement experiment. We seek to measure the eEDM – a quantity that violates T symmetry – and to measure the eEDM precisely does not rely on our knowing the energies or characters of the enormous number of highly coupled states of HfF^+ to a high degree of precision. We endeavor to know the structure of HfF^+ not to further our understanding of molecular structure, but to develop tools for preparing HfF^+ in just a few very well-understood states, for performing a Ramsey spectroscopy sequence, and for detecting the populations of those states with high fidelity. Thus, we primarily turn to the well-developed tools of molecular spectroscopy to allow us to qualitatively characterize the states of our molecule.

To qualitatively understand the states of HfF^+ and small molecules in general, we rely on the separation of energy and time scales of electronic and nuclear motions: the electrons have typical velocities many thousands of times faster than the nuclei, and from their point of view the Coulomb potential imposed by the nuclei can be thought of as classical and quasistatic. Conversely, when considering the motion of the nuclei, we can average over the electronic motion and treat the nuclei as moving in a potential $V(R)$ comprising the nuclear Coulomb repulsion and the attractive force of the average electron density. Finally, the rotational and vibrational degrees of freedom of the nuclei can be approximately separated. Mathematically, these physical ideas are manifested in the Born-Oppenheimer approximation and the Born adiabatic approximation (Chapter 2 of Ref. [15]), where we expand the total wavefunction as a product of electronic and nuclear components. Schematically,

$$\Psi \simeq \psi_{\text{elec}}(\boldsymbol{r}_i; R|\boldsymbol{s}_i)\ \chi_{\text{vib}}(R)\ \psi_{\text{rot}}(\omega), \tag{2.2}$$

where ω is a shorthand for the Euler angles ϕ, θ, χ, $\boldsymbol{s}_i$ represents electron spin, and I have neglected nuclear spin for now.

To obtain a version of the Schrödinger equation where the electronic and nuclear degrees of freedom are separable, we must transform the Hamiltonian from the laboratory-fixed frame [Eq. (2.1)] to the molecule-fixed frame. This requires a translation into the center of mass of the nuclei, followed by a rotation by Euler angles (θ, ϕ, χ) into a frame where the internuclear axis is oriented along $\hat{z}$. The derivation is lengthy, spanning Sections 2.1-2.7 of Ref. [15]! Neglecting the center of mass kinetic energy, the result is

$$H_{\text{nuc}} = \underbrace{-\frac{\hbar^2}{2\mu R^2}\frac{\partial}{\partial R}\left(R^2\frac{\partial}{\partial R}\right) + V(R)}_{H_{\text{vib}}} + \underbrace{\frac{\hbar^2}{2\mu R^2}\left(\boldsymbol{J}-\boldsymbol{J}_a\right)^2}_{H_{\text{tum}}}, \tag{2.3a}$$

$$H_{\text{elec}} = \sum_{i,j}\ \frac{p_i^2}{2m} + \frac{\boldsymbol{p}_i\cdot\boldsymbol{p}_j}{2M_N} + \frac{k}{|\boldsymbol{r}_i-\boldsymbol{r}_j|} - \frac{kZ_1}{|\boldsymbol{r}_i-(\mu/M_1)R\hat{z}|} - \frac{kZ_2}{|\boldsymbol{r}_i+(\mu/M_2)R\hat{z}|} + H_{\text{spin}}, \tag{2.3b}$$

where R is the internuclear distance, M_N is the total nuclear mass, $\mu = M_1M_2/(M_1+M_2)$ is the reduced nuclear mass, $\boldsymbol{J} = \boldsymbol{L}+\boldsymbol{S}+\boldsymbol{R}$ is the total angular momentum including electronic spin and

orbital ($\boldsymbol{L}$ and $\boldsymbol{S}$) along with nuclear rotation $\boldsymbol{R}$, and $\boldsymbol{J}_a = \boldsymbol{L} + \boldsymbol{S}$ is the total electronic angular momentum. In this form, the electronic part of the Hamiltonian depends on the nuclear coordinates only through their relative positions on the body-fixed z axis (coincident with the internuclear axis $\boldsymbol{n}$). This form is simple enough to be attacked by numerical methods. The nuclear part is further separable into components governing end-over-end "tumbling" H_{tum} and vibration H_{vib}. We will discuss the electronic, rotational, and vibrational parts of the wavefunction in the following sections.

2.1.3 Electronic structure

The electronic structure of a diatomic molecule in the Born-Oppenheimer and adiabatic approximations is governed by the Hamiltonian in Eq. (2.3b). Due to the nonsymmetric nature of the Coulomb potential imposed by the two nuclei, the electronic orbital angular momentum $\boldsymbol{L}$ is generally not conserved, in contrast to the situation in the spherically symmetric potential of atoms. Though I have written the electronic and spin parts of the wavefunction separately in Eq. (2.2), spin-orbit coupling couples $\boldsymbol{L}$ and $\boldsymbol{S}$ to form the total electronic angular momentum $\boldsymbol{J}_a$, particularly in heavy molecules such as HfF^+. Depending on the strength of the spin-orbit energy $E_{\text{s-o}}$, it may be useful to express the electronic wavefunction in Hund's case (a) or (c):

$$\psi_{\text{elec}}(\boldsymbol{r}_i; R|\boldsymbol{s}_i) = \begin{cases} \langle \boldsymbol{r}_i; R|\Lambda, S, \Sigma\rangle & \text{case (a): } E_{\text{s-o}} \ll E_{\text{tum}}, \\ \langle \boldsymbol{r}_i; R|J_a, \Omega\rangle & \text{case (c): } E_{\text{s-o}} \gg E_{\text{tum}}, \end{cases} \tag{2.4}$$

where $E_{\text{tum}} \simeq \hbar^2/(2\mu R_e^2)$ is the energy scale of the end-over-end tumbling (rotation) of the molecule.

While numerical calculations of electronic structure are beyond the scope of this thesis, they have been undertaken for HfF^+ by several groups, and are detailed in Refs. [28, 29, 44, 99, 100, 114, 115, 117]. In these works, the electronic Hamiltonian is augmented with relativistic corrections which we have not discussed here. For the purposes of an experimentalist, the results of their calculations are electronic wavefunctions that can be characterized either by case (a) or case (c) in Eq. (2.4). These wavefunctions can then be used to calculate the eEDM sensitivity parameter $\mathcal{E}_{\text{eff}}$, as well as expectation values of the dipole moment operator in order to estimate transition

strengths and radiative decay lifetimes [99]. The low-lying $^1\Sigma$, $^3\Delta$, and $^1\Delta$ states of HfF^+ are well-described by case (a), as indicated by our use of term symbols $^{2S+1}|\Lambda|^{(P)}_{|\Omega|}$ to denote them, where P is the overall parity. Higher lying states such as the nominal $^3\Pi_{0^+}$ are in fact better described in the case (c) notation $|\Omega|^{(P)} = 0^+$, as evidenced by the fact that this state couples to both $^1\Sigma^+$ and $^3\Delta_1$, which would be forbidden for a state with good quantum number S.

Figure 2.3 shows the low-lying electronic states of HfF^+, many of which can be populated by conveniently located near-infrared wavelength lasers. Only two of the electronic states below 15000 cm^{-1} have not been observed; a testament to the effectiveness of the frequency comb velocity modulation spectroscopy technique developed by the Ye & Cornell groups [28, 29, 52, 112].

2.1.4 Rotational structure

The rotational structure of HfF^+ is present throughout the broadband spectroscopy performed in this thesis and earlier eEDM theses, in particular those of Kevin Cossel, Dan Gresh, Laura Sinclair, and Huanqian Loh [82]. In this thesis in particular, we use our understanding of rotational structure to find an $\Omega = 2$ excited electronic state to act as an intermediate in our oriented photodissociation in Section 6.

As discussed in Section 2.1.2, the rotational part of the molecular wavefunction is governed by the "tumbling" part of the Hamiltonian

$$H_{\text{tum}} = \frac{\hbar^2}{2\mu R^2} (\boldsymbol{J} - \boldsymbol{J}_a)^2 . \tag{2.5}$$

The operator $\boldsymbol{R} \equiv (\boldsymbol{J} - \boldsymbol{J}_a)^2$, which represents the purely end-over-end tumbling of the nuclei, can be separated into parts which are diagonal and off-diagonal with respect to the electronic wavefunction,

$$(\boldsymbol{J} - \boldsymbol{J}_a)^2 = (\boldsymbol{J}^2 - 2J_z J_{a,z} + J_{a,z}^2) + (J_{a,x}^2 + J_{a,y}^2 - 2J_x J_{a,x} - 2J_y J_{a,y}),$$

and we can use the fact that both J_z and $J_{a,z}$ have eigenvalue Ω; the total electronic angular momentum projection on the internuclear axis (Ref. [15], Section 2.6). Neglecting off-diagonal

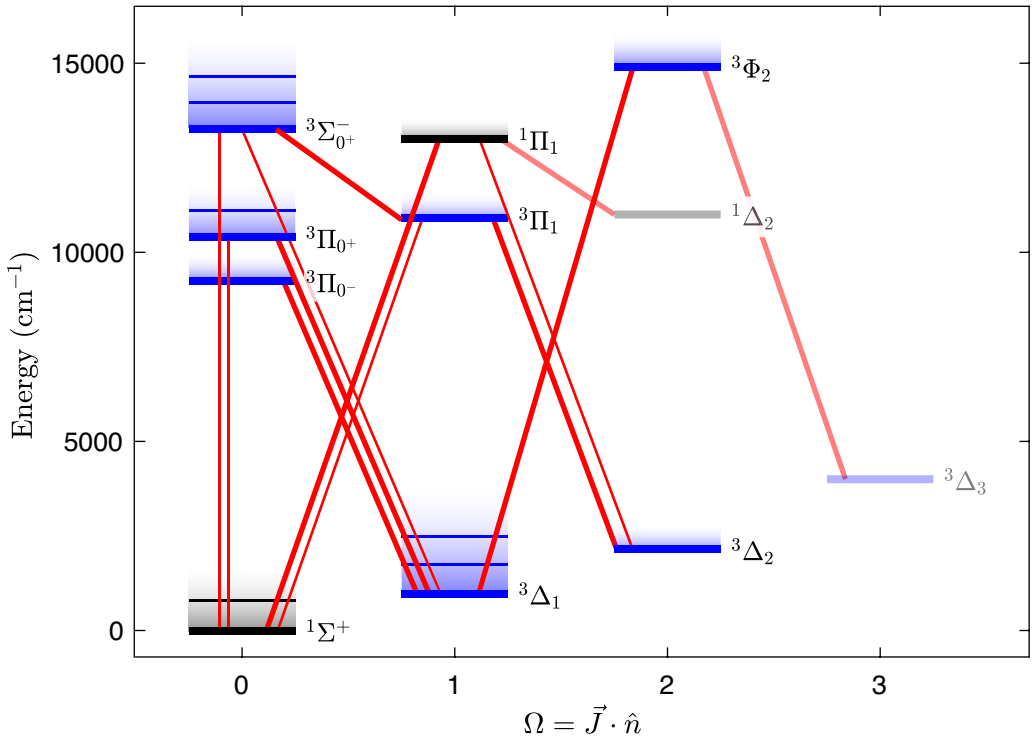

Figure 2.3: Electronic states of HfF^+ up to about 15000 cm^{-1}, with singlet states in black and triplet states in blue. The $^3\Delta_3$ and $^1\Delta_2$ states have not been observed. Red lines indicate known transitions between electronic states, with thick lines indicating dipole allowed transitions and thin lines indicating dipole forbidden (but weakly allowed) transitions. Equally spaced states connected by a shaded region are vibrational levels belonging to the labeled electronic state. Only the excited vibrational levels used in the experiment are shown. Rotational levels exist on a much smaller energy scale of $\lesssim 1$ cm^{-1}.

electronic terms [1] , an approximate effective Hamiltonian for the end-over-end rotation is then

$$H_{\text{tum}} = B(R)(\boldsymbol{J}^2 - \Omega^2)$$

where the rotational constant $B(R) = \hbar^2/(2\mu R^2)$ depends parametrically on the internuclear distance. The constant part $-B(R)\Omega^2$ is often absorbed into the electronic energy. The eigenfunctions of this Hamiltonian are (proportional to) the Wigner rotation matrices,

$$\begin{aligned} \psi_{\text{rot}}(\omega) &= \sqrt{\frac{2J+1}{8\pi^2}}\, \mathcal{D}^{(J)}_{M\Omega}(\omega)^* \\ &\equiv \langle \omega | J\Omega M \rangle \end{aligned} \tag{2.6}$$

with eigenvalues $E_{\text{tum}} = B(R)[J(J+1) - \Omega^2]$. These eigenfunctions are discussed extensively in Chapter 5 of Ref. [15], and have many nice identities.

2.1.5 Vibrational structure

I will not go into great detail on the vibrational structure of HfF^+, as it is addressed in essentially every textbook on molecular structure. The vibrational eigenfunctions $|\psi_{\text{vib}}\rangle \equiv |v\rangle$ are solutions to a time-independent Schrödinger equation with the nuclear Hamiltonian given in Eq. (2.3a), but with the replacement of the rotation operator $(\boldsymbol{J} - \boldsymbol{J}_a)^2 \to J(J+1) - \Omega^2$ due to our separation of the vibrational and rotational degrees of freedom. The internuclear potential $V(R)$ is computationally expensive to calculate numerically, since this involves solution of the electronic Schrödinger equation for each value of the internuclear distance R. A common approximation is the *Morse potential*, which I have used to schematically illustrate internuclear potentials in Fig. 2.2 (See e.g. Ref. [15], Section 2.9). Because the internuclear potential is approximately harmonic near its minimum, the vibrational wavefunctions closely resemble harmonic oscillator states, and their energies are well approximated by

$$E_v = \langle v | H_{\text{vib}} | v \rangle \approx \hbar\omega_e(v + 1/2) - \hbar\omega_e x_e (v + 1/2)^2. \tag{2.7}$$

[1] Neglecting coupling between electronic states caused by nuclear motion is called the adiabatic approximation.

In Section 2.2.4, we will use these energies in evaluating the Einstein coefficients for spontaneous decay and blackbody excitation of vibrational degrees of freedom in the $^3\Delta_1$ electronic state of HfF^+.

2.1.6 Nuclear spin & the total wavefunction revisited

To summarize the results of the previous sections, we have established that the total molecular wavefunction in the Born-Oppenheimer and adiabatic approximations, and in a Hund's case (a) basis, can be represented by a product state ket with the quantum numbers

$$|\Lambda S\Sigma\rangle\,|v\rangle\,|J\Omega M\rangle\,,$$

with electronic, vibrational, and rotational components, respectively. In HfF^+, we must account for one final source of angular momentum: the nuclear spin $\boldsymbol{I}$ of ^{19}F. The coupling of $\boldsymbol{I}$ to the electronic plus rotational angular momentum $\boldsymbol{J} = \boldsymbol{J}_a + \boldsymbol{R}$ can be done in the lab frame to form the total molecular angular momentum $\boldsymbol{F} = \boldsymbol{J} + \boldsymbol{I}$ with projection M_F onto the laboratory-frame z axis. The transformation from one basis to the other can be straightforwardly accomplished using Clebsch-Gordan coefficients:

$$|JIFM_F\rangle = \sum_{M_J,M_I} |JM_JIM_I\rangle\,\langle JM_JIM_I|FM_F\rangle\,. \tag{2.8}$$

The only further complication is that when evaluating matrix elements of vector operators in the lab frame (as we will do in Section 2.2), there will be some spherical tensor algebra involved to decouple $\boldsymbol{I}$ from $\boldsymbol{F}$ to evaluate matrix elements only involving $\boldsymbol{J}$. Happily, all of the expressions we need are handily summarized in Ref. [15], Appendix 5.1. So finally, the total wavefunction of the HfF^+ molecule can be expressed as

$$|\Psi\rangle = |\psi_{\text{elec}}\rangle\,|\psi_{\text{vib}}\rangle\,|\psi_{\text{rot}}\rangle = |\Lambda S\Sigma\rangle\,|v\rangle\,|IJ\Omega FM_F\rangle\,, \tag{2.9}$$

and we can set about evaluating important matrix elements for the JILA eEDM experiment.

2.2 Energy shifts and decay rates in HfF^+

2.2.1 Electric fields

In the HfF^+ eEDM experiment, we use electric fields extensively for the manipulation of both the internal and external degrees of freedom of HfF^+ molecules. The characteristic frequencies of our applied electric fields in our experiment range from the tens of kHz for the RF ion trap, to tens of GHz for rotational spectroscopy with microwave fields, to over 1 PHz (10^{15} Hz!) for photodissociation with 266 nm laser light. The interaction of all of these electric fields with the internal state of the molecules can be described by the Stark Hamiltonian

$$H_{\text{Stark}} = -\boldsymbol{D}\cdot\boldsymbol{\mathcal{E}} = -\sum_{p=-1}^{+1}(-1)^p\, T_p^{(1)}(\boldsymbol{D})\, T_{-p}^{(1)}(\boldsymbol{\mathcal{E}}), \tag{2.10}$$

where $\boldsymbol{D}$ is the electric dipole operator and $\boldsymbol{\mathcal{E}}$ is an applied electric field. On the second line, I have expressed the same Hamiltonian in the language of spherical tensor operators (See Ref. [15], Chapter 5.5) [2] . Spherical tensor operators are a useful way to formalize the algebra of operators acting on angular momenta, and though the notation can be highly intimidating, essentially every important result has been worked out in detail in Refs. [15, 136].

Unlike in atoms, the electric dipole operator acts not only on the electrons, but also on the relative positions of the nuclei:

$$\boldsymbol{D} = \boldsymbol{D}_N + \boldsymbol{D}_e = \left(\frac{Z_1\mu}{M_1} - \frac{Z_2\mu}{M_2}\right) eR\,\boldsymbol{n} - \sum_i e\boldsymbol{r}_i \tag{2.11}$$

In Eq. (2.11), I have expressed the dipole moment operator in the body-fixed frame, in the same way that we did for the molecular Hamiltonian without external fields in Section 2.1.3 in order to simplify the separation of rotational, vibrational, and electronic degrees of freedom. However, the components of the electric field $\boldsymbol{\mathcal{E}}$ are most easily expressed in the laboratory frame. To correctly

[2] The spherical components of a rank-1 vector operator $T_p^{(1)}(\boldsymbol{V})$ in terms of the cartesian components of $\boldsymbol{V}$ are

$$T_{\pm1}^{(1)}(\boldsymbol{V}) = \mp\frac{V_x \pm iV_y}{\sqrt{2}},$$
$$T_0^{(1)}(\boldsymbol{V}) = V_z.$$

Substitution of these components into the second line of Eq. (2.10) straightforwardly returns the first line.

evaluate the matrix elements of H_{Stark}, we must transform the components of $\boldsymbol{D}$ into the laboratory frame. This transformation is most easily done with Wigner rotation matrices, using the expression (Eq. 5.143 of Ref. [15])

$$T_p^{(k)}(\boldsymbol{A}) = \sum_{q=-k}^{k} \mathcal{D}_{pq}^{(k)}(\omega)^* \, T_q^{(k)}(\boldsymbol{A}), \tag{2.12}$$

where $\boldsymbol{A}$ can be any tensor operator. Equation (2.12) can be deceiving: while seemingly this expression represents a simple matrix multiplying a vector, the variable ω is just a shorthand for the three Euler angles ϕ, θ, χ, and the rotational wavefunction of Eq. (2.6) is a function of these variables! To evaluate a matrix element of any molecule-frame operator transformed into the lab frame in this way, these variables must be integrated over. In this sense, we must treat $\mathcal{D}_{pq}^{(k)}(\omega)^*$ as an operator on the rotational part of the wavefunction. Fortunately, the rotational part of the wavefunction always takes the form of Eq. (2.6), so we need only evaluate this expression once. The results are given in Eq. 5.146 of Ref. [15].

In the laboratory frame, the components of $T_p^{(1)}(\boldsymbol{\mathcal{E}})$ are c-numbers, not operators. Thus, the task of evaluating the matrix elements of H_{Stark} reduces to finding the matrix elements of $\mathcal{D}_{pq}^{(1)}(\omega)^* \, T_q^{(1)}(\boldsymbol{D})$. Further, the matrix elements of $\mathcal{D}_{pq}^{(1)}(\omega)^*$ involve only the rotational wavefunction (and therefore only Wigner D matrix identities), so we need only consider the matrix elements of $\boldsymbol{D}$ in the electronic and vibrational parts of the wavefunction, $\langle \Lambda' S' \Sigma', v' | \, \boldsymbol{D} \, | \Lambda S \Sigma, v \rangle$. In the next few sections, we will consider the matrix elements of H_{Stark} within and between electronic states, and do some example calculations that are useful for the HfF^+ eEDM experiment.

2.2.2 Stark effect

In the JILA eEDM experiment and atomic physics experiments in general, the scale of laboratory DC electric fields that can be applied is $\lesssim$ 500 kV/cm in record-setting circumstances, and $\lesssim$ 20 kV/cm in more typical experiments. In these situations, we can usually neglect mixing between electronic states, so that

$$\left\langle \Lambda S \Sigma, v' \right| \boldsymbol{D} \left| \Lambda S \Sigma, v \right\rangle \equiv \left\langle v' \right| D_{\parallel}(R) \left| v \right\rangle \boldsymbol{n}, \tag{2.13}$$

where $\boldsymbol{n}$ is a unit vector pointing between the nuclei, which lie along the z axis in the body-fixed frame. The nuclear contribution to the molecule-frame dipole moment is explicitly a function of R [Eq. (2.11)], while the electronic contribution depends parametrically on R through the nuclear Coulomb potential [Eq. (2.3b)]. The total molecule-frame dipole moment $D_\parallel(R)$ can thus be expanded in a power series in the internuclear distance,

$$\left\langle v' \right| D_\parallel(R) \left| v \right\rangle = D_\parallel \left\langle v' | v \right\rangle + \left(\frac{dD_\parallel}{dQ} \right)_0 \left\langle v' \right| Q \left| v \right\rangle + \left(\frac{d^2 D_\parallel}{dQ^2} \right)_0 \left\langle v' \right| Q^2 \left| v \right\rangle + \ldots . \tag{2.14}$$

where $Q \equiv R - R_e$ is the displacement of the nuclei from their equilibrium positions in the electronic state under consideration. For feasible laboratory electric fields, we can also neglect the mixing of vibrational states and take $v' = v$. The first term in the expansion typically dominates, so for the DC Stark effect we can simply take the electronic and vibrational matrix element to be $D_\parallel \boldsymbol{n}$.

We can now put our molecule-frame dipole matrix element together with some spherical tensor algebra from Ref. [15] to evaluate the energy shifts in HfF^+ states due to an applied DC or quasi-DC electric field $\boldsymbol{\mathcal{E}}$ whose components are known in the lab frame – an exceedingly common and important situation in the JILA eEDM experiment! The results we need from Ref. [15] are Eqs. 5.172, 5.174, and 5.186. Substituting these expressions, we obtain

$$\begin{aligned}
&\left\langle \Lambda S\Sigma, v, I'J'\Omega'F'M_F' \right| H_{\text{Stark}} \left| \Lambda S\Sigma, v, IJ\Omega F M_F \right\rangle \\
&\quad = -\sum_{p,q} (-1)^p \, T^{(1)}_{-p}(\boldsymbol{\mathcal{E}}) \, \left\langle I'J'\Omega'F'M_F' \right| \mathcal{D}^{(1)}_{pq}(\omega)^* \left| IJ\Omega F M_F \right\rangle \left\langle \Lambda S\Sigma, v \right| T^{(1)}_q(\boldsymbol{D}) \left| \Lambda S\Sigma, v \right\rangle \\
&\quad = -\sum_{p=-1}^{+1} (-1)^p \, T^{(1)}_{-p}(\boldsymbol{\mathcal{E}}) \, (-1)^{F'-M_F'} \begin{pmatrix} F' & 1 & F \\ -M_F' & p & M_F \end{pmatrix} \\
&\qquad \times \delta_{I,I'} \, (-1)^{F+J'+1+I'} \sqrt{(2F'+1)(2F+1)} \begin{Bmatrix} J & F & I' \\ F' & J' & 1 \end{Bmatrix} \\
&\qquad \times \sum_{q=-1}^{+1} (-1)^{J'-\Omega'} \begin{pmatrix} J' & 1 & J \\ -\Omega' & q & \Omega \end{pmatrix} \sqrt{(2J'+1)(2J+1)} \, T^{(1)}_q(\boldsymbol{D}).
\end{aligned} \tag{2.15}$$

While this expression may look a little bit intimidating, it simply evaluates to a sum of three numbers multiplying the components of $T^{(1)}_{-p}(\boldsymbol{\mathcal{E}})$. This expression is applicable to the scalar product

	$\lvert F, M_F\rangle$					
$\langle F', M'_F\rvert$	$\lvert\frac{1}{2},-\frac{1}{2}\rangle$	$\lvert\frac{1}{2},\frac{1}{2}\rangle$	$\lvert\frac{3}{2},-\frac{3}{2}\rangle$	$\lvert\frac{3}{2},-\frac{1}{2}\rangle$	$\lvert\frac{3}{2},\frac{1}{2}\rangle$	$\lvert\frac{3}{2},\frac{3}{2}\rangle$
$\langle\frac{1}{2},-\frac{1}{2}\rvert$	$-\frac{\mathcal{E}_z}{3}$	$\frac{\mathcal{E}_\perp}{3}$	$\frac{\mathcal{E}_\perp}{2\sqrt{6}}$	$\frac{\mathcal{E}_z}{3\sqrt{2}}$	$-\frac{\mathcal{E}_\perp}{6\sqrt{2}}$	0
$\langle\frac{1}{2},\frac{1}{2}\rvert$	$\frac{\mathcal{E}_\perp}{3}$	$\frac{\mathcal{E}_z}{3}$	0	$\frac{\mathcal{E}_\perp}{6\sqrt{2}}$	$\frac{\mathcal{E}_z}{3\sqrt{2}}$	$-\frac{\mathcal{E}_\perp}{2\sqrt{6}}$
$\langle\frac{3}{2},-\frac{3}{2}\rvert$	$\frac{\mathcal{E}_\perp}{2\sqrt{6}}$	0	$-\frac{\mathcal{E}_z}{2}$	$\frac{\mathcal{E}_\perp}{2\sqrt{3}}$	0	0
$\langle\frac{3}{2},-\frac{1}{2}\rvert$	$\frac{\mathcal{E}_z}{3\sqrt{2}}$	$\frac{\mathcal{E}_\perp}{6\sqrt{2}}$	$\frac{\mathcal{E}_\perp}{2\sqrt{3}}$	$-\frac{\mathcal{E}_z}{6}$	$\frac{\mathcal{E}_\perp}{3}$	0
$\langle\frac{3}{2},\frac{1}{2}\rvert$	$-\frac{\mathcal{E}_\perp}{6\sqrt{2}}$	$\frac{\mathcal{E}_z}{3\sqrt{2}}$	0	$\frac{\mathcal{E}_\perp}{3}$	$\frac{\mathcal{E}_z}{6}$	$\frac{\mathcal{E}_\perp}{2\sqrt{3}}$
$\langle\frac{3}{2},\frac{3}{2}\rvert$	0	$-\frac{\mathcal{E}_\perp}{2\sqrt{6}}$	0	0	$\frac{\mathcal{E}_\perp}{2\sqrt{3}}$	$\frac{\mathcal{E}_z}{2}$

Table 2.1: Matrix elements $\langle F'M'_F|\, H_{\rm Stark}\, |FM_F\rangle$ for $^3\Delta_1$, $J = 1$, showing only the $\Omega = +1$ components. Matrix elements for $\Omega = -1$ are $(-1)\times$ the matrix elements shown, and matrix elements off-diagonal in Ω are zero. Here $\mathcal{E}_\perp = \mathcal{E}_x - i\mathcal{E}_y$, and entries left blank are zero.

of any pair of vector operators, when the components of one of them is best expressed in the body-fixed frame. It will be useful in Section 2.2.5 in evaluating the Zeeman Hamiltonian, which has a very similar form. Having found just above that $T^{(1)}_q(\boldsymbol{D}) = D_\parallel\ \delta_{q,0}$ at the present level of approximation, and using the fact that $I = I' = 1/2$ in HfF^+, Eq. (2.15) simplifies slightly. After choosing a basis of states with quantum numbers $|IJ\Omega FM_F\rangle$, these matrix elements can be tabulated using Mathematica, Matlab, or tables of Wigner 3j and 6j symbols, which can be found online and in many textbooks.

The most important example of the DC Stark effect for the purposes of the HfF^+ eEDM experiment is the energy shifts of the $^3\Delta_1$, $J = 1$ states under the influence of the rotating electric bias field $\mathcal{E}_{\rm rot}$. The matrix elements of $H_{\rm Stark}$ in the basis of these levels are tabulated in Table 2.1. The calculated energy shifts due to the Stark effect are shown in Fig. 2.4.

2.2.3 Electronic transitions & the Franck-Condon principle

In the electric dipole approximation, the Stark Hamiltonian also governs radiative transitions between states of HfF^+, due to stimulated absorption or emission, or spontaneous emission. In an electronic transition that may also change rotational and vibrational quantum numbers, we must

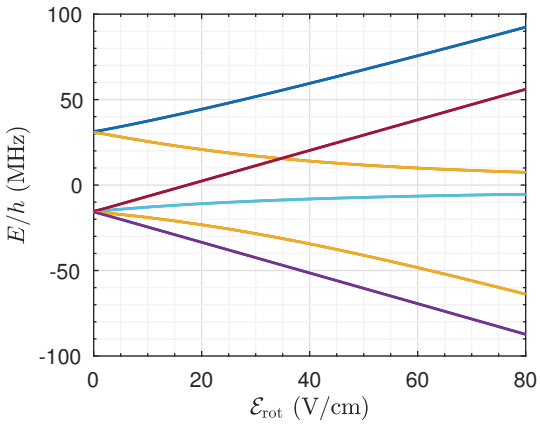

Figure 2.4: Calculated Stark shifts in $^3\Delta_1$, $J = 1$, using experimentally measured parameters for the hyperfine splitting and the molecule-frame dipole moment. While in this figure it appears that the stretched states (red and purple) have linear shifts all the way to $\mathcal{E}_{\mathrm{rot}} = 0$ indicating a permanent electric dipole moment, their shifts are in fact quadratic at very low $\mathcal{E}_{\mathrm{rot}}$ due to Ω doubling, which is discussed in Section 2.2.7

consider matrix elements of the Stark Hamiltonian between any two states of the molecule:

$$\left\langle \Psi' \right| H_{\text{Stark}} \left| \Psi \right\rangle = \sum_{p,q} (-1)^{p+1} \, \boldsymbol{\mathcal{E}}_{-p} \, \left\langle \psi'_{\text{rot}} \right| \mathcal{D}^{(1)*}_{pq} \left| \psi_{\text{rot}} \right\rangle \left\langle \psi'_{\text{elec}} \, \psi'_{\text{vib}} \right| \boldsymbol{D}_q \left| \psi_{\text{elec}} \, \psi_{\text{vib}} \right\rangle \tag{2.16}$$

The electric dipole selection rules for J, Ω, F, and M_F are contained in the matrix element of the rotation matrix, $\langle \psi'_{\text{rot}} | \, \mathcal{D}^{(1)*}_{pq} \, | \psi_{\text{rot}} \rangle$, which encodes angular momentum conservation. At this point, a standard approximation to apply is the *Franck-Condon principle* for the dipole matrix element. Splitting $\boldsymbol{D}$ into its electronic and nuclear parts [Eq. (2.11)] and using the fact that the nuclear dipole moment does not act on the electronic state, we have

$$\left\langle \psi'_{\text{elec}} \, \psi'_{\text{vib}} \right| \boldsymbol{D}_q \left| \psi_{\text{elec}} \, \psi_{\text{vib}} \right\rangle = \left\langle v' \right| \boldsymbol{D}^{\eta'\eta}_{e,q}(R) \left| v \right\rangle + \left\langle \psi'_{\text{elec}} \middle| \psi_{\text{elec}} \right\rangle \left\langle v' \right| \boldsymbol{D}_N \left| v \right\rangle . \tag{2.17}$$

The orthonormality of electronic wavefunctions makes the second term zero for electronic transitions. We have evaluated the electronic part of the dipole operator between electronic wavefunctions to give a function of R that can be expanded as a power series, similarly to the total molecule-frame dipole moment in Eq. (2.14), but this time between electronic states and without the nuclear contribution. The Franck-Condon principle consists of keeping only the first term in this series, which is independent of R,

$$\left\langle \psi'_{\text{elec}} \, \psi'_{\text{vib}} \right| \boldsymbol{D}_q \left| \psi_{\text{elec}} \, \psi_{\text{vib}} \right\rangle \approx \boldsymbol{D}^{\eta'\eta}_{e,q} \left\langle \eta' v' \middle| \eta v \right\rangle . \tag{2.18}$$

The first factor is the transition electric dipole moment between electronic states, while the second factor squared is defined as the *Franck-Condon factor* (FCF), representing the relative strength of transitions that change the degree of vibrational excitation along with the electronic state. Because of the different shape of the internuclear potential in different electronic states of a molecule, the vibrational wavefunctions of different electronic states are not orthonormal, and have no strict selection rules. However, due to the normalization of individual vibrational wavefunctions, the FCFs are normalized with respect to summation over v' or v. After applying the Franck-Condon principle for electronic transitions, we have for the total Stark matrix element

$$\left\langle \Psi' \right| H_{\text{Stark}} \left| \Psi \right\rangle = \sum_{p,q} (-1)^{p+1} \, \boldsymbol{\mathcal{E}}_{-p} \, \left\langle \psi'_{\text{rot}} \right| \mathcal{D}^{(1)*}_{pq} \left| \psi_{\text{rot}} \right\rangle \left\langle \eta' v' \middle| \eta v \right\rangle D^{\eta'\eta}_{e,q}. \tag{2.19}$$

Despite the large number of electric dipole transitions driven by lasers in the HfF^+ eEDM experiment, we rarely have occasion to use Eq. (2.19). However, Kevin Cossel's thesis [28] goes over the important examples: (a) the Raman spectrum of $^3\Delta_1(v = 0, J = 1)$ and (b) evaluating the molecule-frame transition dipole moment $D_{e,q}^{\eta'\eta}$ for the $^3\Pi_{0^+} \leftarrow {}^1\Sigma^+$ and $^3\Pi_{0^+} \leftarrow {}^3\Delta_1$ transitions.

2.2.4 Vibrational decay & blackbody excitation

A particularly relevant type of radiative transition for the Generation 2 JILA eEDM experiment is the spontaneous decay of vibrational levels within a particular electronic state. In this case, we should take $v' \neq v$ in Eq. (2.13), and again consider the Taylor series expansion for $D_\parallel$ from Eq. (2.14),

$$\langle v' | D_\parallel(R) | v \rangle = D_\parallel \langle v' | v \rangle + \left(\frac{dD_\parallel}{dQ}\right)_0 \langle v' | Q | v \rangle + \left(\frac{d^2 D_\parallel}{dQ^2}\right)_0 \langle v' | Q^2 | v \rangle + \dots .$$

Within a particular electronic state, the $|v\rangle$ are orthogonal, so the first term is zero for vibrational transitions. In the approximation that the vibrational levels are harmonic oscillator eigenstates, we can see that the term proportional to the relative internuclear coordinate $Q = R - R_e$ induces transitions between states $v' = v \pm 1$, while Q^2 induces transitions between states $v' = v \pm 2$, and so on. The vibrational states of diatomic molecules are harmonic to a first approximation, and transitions $v' = v \pm 1$ are typically strongest.

In the JILA eEDM experiment, we are typically concerned with excitation of vibrational degrees of freedom by blackbody radiation, and contamination of the $^3\Delta_1$, $v = 0$, $J = 1$ state via decay of $^3\Delta_1$, $v > 0$ states. As an example, we can estimate the rates of these two processes in HfF^+ under typical experimental conditions. To calculate these rates, we need the standard relationships of Einstein A and B coefficients:

$$\begin{aligned} A_{ij} &= \frac{\omega_{ij}^3 |\boldsymbol{D}_{ij}|^2}{3\pi\epsilon_0 \hbar c^3}, \\ B_{ij} &= \frac{\pi^2 c^3}{\hbar \omega_{ij}^3} A_{ij}, \end{aligned} \tag{2.20}$$

where i and j denote any two states in question, and $\omega_{ij} = (E_j - E_i)/\hbar$. First, let's evaluate the Einstein A coefficient for decay of excited $^3\Delta_1$ vibrational states. To do so, we need the modulus

squared of the dipole moment operator,

$$|\boldsymbol{D}|^2 = \sum_p \left| \sum_q \left\langle \psi'_{\rm rot} \right| \mathcal{D}^{(1)}_{pq}(\omega) \left| \psi_{\rm rot} \right\rangle \left\langle \psi_{\rm elec}\, \psi'_{\rm vib} \right| T^{(1)}_q(\boldsymbol{D}) \left| \psi_{\rm elec}\, \psi_{\rm vib} \right\rangle \right|^2 . \tag{2.21}$$

We use Eq. 5.184 of Ref. [15], along with the fact that for rovibrational transitions, $q = 0$. We are also not interested in the details of magnetic sublevel populations, so we should sum over the final state magnetic sublevels M'. Doing all this, we obtain

$$|\boldsymbol{D}|^2 = (2J+1)(2J'+1) \begin{pmatrix} J' & 1 & J \\ -\Omega & 0 & \Omega \end{pmatrix}^2 \left\langle v' \right| D_\parallel \left| v \right\rangle^2 \sum_{p,M'} \begin{pmatrix} J' & 1 & J \\ -M' & p & M \end{pmatrix}^2 . \tag{2.22}$$

We can use Eq. (12) of Ref. [55] to simplify the sum over p and M', which turns out to equal simply $1/(2J+1)$. The Einstein A coefficient for purely vibrational decay from a state $|vJ\rangle$ to state $|v'J'\rangle$ comes out to be

$$A_{v'J'vJ} \approx \frac{\omega^3_{v'v}}{3\pi\epsilon_0 \hbar c^3} \left\langle J, \Omega; 1, 0 \middle| J', \Omega \right\rangle^2 \left\langle v' \right| D_\parallel \left| v \right\rangle^2 , \tag{2.23}$$

where the second factor is a Clebsch-Gordan coefficient that has absorbed the 3j symbol involving Ω and the factor $(2J'+1)$. Happily, and not surprisingly, if we also sum over final rotational states J', all rotational and Ω dependence drops out, and we are left only with $\langle v' | D_\parallel(R) | v \rangle^2$ for the dipole matrix element. Then using the Planck formula for the spectral energy density of blackbody radiation [3] $\rho(\omega_{ij})$, we can evaluate the rate of excitation $R_{ij} = B_{ij}\rho(\omega_{ij})$,

$$R_{v'v} \approx \frac{\omega^3_{v'v}}{3\pi\epsilon_0 \hbar c^3} \left\langle v' \right| D_\parallel \left| v \right\rangle^2 \exp\left(-\frac{\hbar\, \omega_{v'v}}{k_B T} \right) . \tag{2.24}$$

For HfF$^+$ in the $^3\Delta_1$ state, the molecule-frame dipole moment has been evaluated as a function of R by Petrov and coworkers in Ref. [99], and their results are shown in Fig. 2.5. By performing a polynomial fit to their calculation, we can extract the first-order coefficient $\left(\frac{dD_\parallel}{dQ}\right)_0 \approx -1.2\, e$, where in their convention, the internuclear axis is directed from Hf$^+$ to F. With my calculated value of $\langle 1 | Q | 0 \rangle = 0.068\, a_0$ using Morse wavefunctions and $^3\Delta_1$ spectroscopic parameters from Ref. [28], I obtain an estimated $^3\Delta_1$, $v = 1$ lifetime of $\tau \approx 173$ ms, which compares reasonably well to Petrov *et al.*'s estimate of $\tau \approx 184$ ms. From the squared Clebsch-Gordan coefficient in Eq. 2.23, we can

[3] with units of energy per unit volume per unit frequency

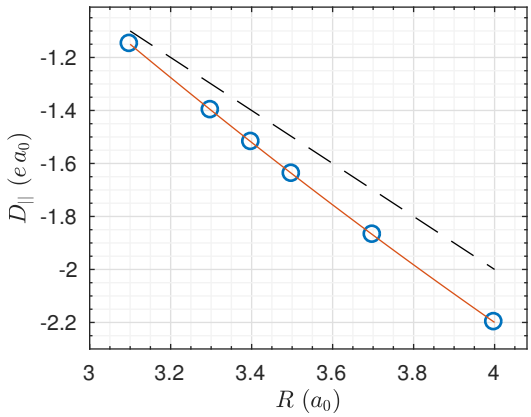

Figure 2.5: Petrov *et al.*'s theoretically calculated molecule-frame dipole moment of HfF^+ in the $^3\Delta_1$ electronic state (points), as a function of internuclear distance. Adapted from Ref. [99]. The red line is a quadratic fit to Petrov *et al.*'s calculation, while the black dashed line is the approximation $D_{||} = -eR$, offset vertically by $2ea_0$. For estimating vibrational lifetimes, this approximation gives 20% error, which is not too bad!

also estimate the rotational branching ratios for vibrational decay. Figure 2.6 shows an example of the rotational branching of decay from $^3\Delta_1$, $v = 3$, $J = 1$. Using Eq. (2.24), and $T = 300$ K, we can estimate a blackbody excitation timescale of $\tau_{\mathrm{BB}} \approx 6.4$ seconds for $^3\Delta_1$, $v = 0$, accounting only for the $v = 0 \to v = 1$ transition.

2.2.5 Zeeman effect

The Zeeman effect describes the interaction of an applied magnetic field with a magnetic dipole moment, and is governed by the Hamiltonian

$$\begin{aligned} H_{\mathrm{Zeeman}} &= -\boldsymbol{\mu} \cdot \boldsymbol{\mathcal{B}} \\ &= -\sum_p (-1)^p \, T^{(1)}_p(\boldsymbol{\mu}) \, T^{(1)}_{-p}(\boldsymbol{\mathcal{B}}) \end{aligned} \tag{2.25}$$

In HfF^+ and in molecules in general, there are multiple contributions to the total magnetic moment of the molecule, and it is easiest to treat each of them separately. These contributions are, in order of their typical size, electronic (spin and orbital), nuclear spin, and rotational magnetic moments:

$$\boldsymbol{\mu} = \boldsymbol{\mu}_e + \boldsymbol{\mu}_{\mathrm{n}} + \boldsymbol{\mu}_r.$$

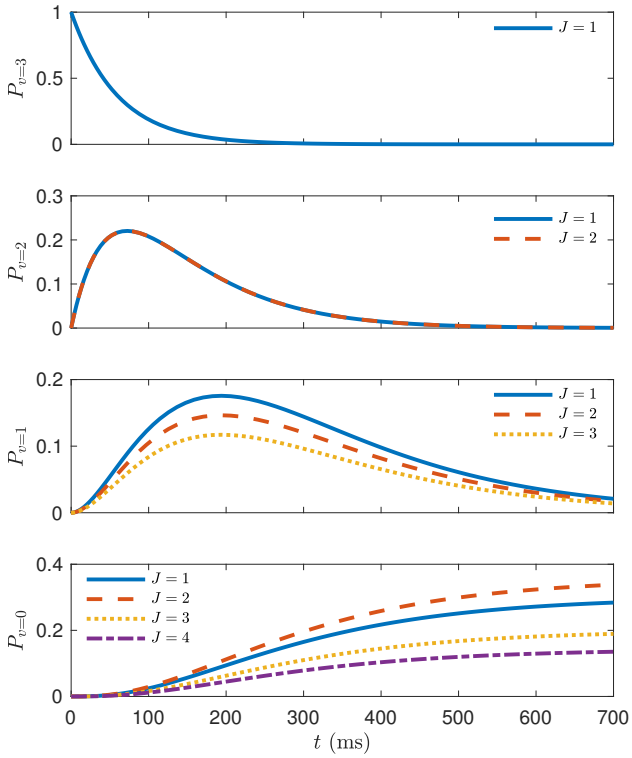

Figure 2.6: Theoretically calculated vibrational decay of $^3\Delta_1$, $v = 3$, $J = 1$, leading to population of rotational levels up to $J = 4$ in $v = 0$. This phenomenon leads to an undesirable background signal in $^3\Delta_1$, $v = 0$, $J = 1$ that hurts our eEDM sensitivity, as discussed in Chapter 5. Populations P_i are expressed as a fraction of the total molecular population.

Due to the strong coupling of the total electronic angular momentum to the internuclear axis – motivating our use of Hund's case (a) basis functions – the total electronic magnetic moment $\boldsymbol{\mu}_e$ is most easily evaluated in the body-fixed frame, similarly to the electronic contribution to the electric dipole moment in Section 2.2.1. The evaluation of the laboratory frame components of $\boldsymbol{\mu}_e$ follows precisely the same form as Eq. (2.15), but with the molecule-frame electronic matrix element

$$\langle \Lambda S \Sigma | \, \boldsymbol{\mu}_e \, | \Lambda S \Sigma \rangle = G_{\parallel} \, \mu_B \, \Omega \, \boldsymbol{n}, \tag{2.26}$$

or equivalently $T^{(1)}_q(\boldsymbol{\mu}_e) = G_{\parallel} \, \mu_B \, \Omega \, \delta_{q,0}$. In principle, $G_{\parallel}$ might also be calculated as a function of internuclear distance and expanded in a power series, as we did for $D_{\parallel}$ in Eq. (2.14). It seems likely that $G_{\parallel}$ would have a much weaker dependence on internuclear distance than $D_{\parallel}$, and to my knowledge this is not typically done. Thus the matrix elements of the electronic part of the Zeeman Hamiltonian can be obtained from Eq. (2.15) with the replacements $\boldsymbol{D} \to \boldsymbol{\mu}_e$ and $\boldsymbol{\mathcal{E}} \to \boldsymbol{\mathcal{B}}$. For the $^3\Delta_1(J = 1)$ state, in the same basis as Table 2.1, the electronic Zeeman Hamiltonian is given by Eq. (2.27).

$$H_{\mathrm{Z},e} = -G_{\parallel} \, \mu_B \begin{pmatrix} -\frac{\mathcal{B}_z}{3} & \frac{\mathcal{B}_\perp}{3} & \frac{\mathcal{B}_\perp}{2\sqrt{6}} & \frac{\mathcal{B}_z}{3\sqrt{2}} & -\frac{\mathcal{B}_\perp}{6\sqrt{2}} & 0 \\ \frac{\mathcal{B}_\perp}{3} & \frac{\mathcal{B}_z}{3} & 0 & \frac{\mathcal{B}_\perp}{6\sqrt{2}} & \frac{\mathcal{B}_z}{3\sqrt{2}} & -\frac{\mathcal{B}_\perp}{2\sqrt{6}} \\ \frac{\mathcal{B}_\perp}{2\sqrt{6}} & 0 & -\frac{\mathcal{B}_z}{2} & \frac{\mathcal{B}_\perp}{2\sqrt{3}} & 0 & 0 \\ \frac{\mathcal{B}_z}{3\sqrt{2}} & \frac{\mathcal{B}_\perp}{6\sqrt{2}} & \frac{\mathcal{B}_\perp}{2\sqrt{3}} & -\frac{\mathcal{B}_z}{6} & \frac{\mathcal{B}_\perp}{3} & 0 \\ -\frac{\mathcal{B}_\perp}{6\sqrt{2}} & \frac{\mathcal{B}_z}{3\sqrt{2}} & 0 & \frac{\mathcal{B}_\perp}{3} & \frac{\mathcal{B}_z}{6} & \frac{\mathcal{B}_\perp}{2\sqrt{3}} \\ 0 & -\frac{\mathcal{B}_\perp}{2\sqrt{6}} & 0 & 0 & \frac{\mathcal{B}_\perp}{2\sqrt{3}} & \frac{\mathcal{B}_z}{2} \end{pmatrix} \tag{2.27}$$

The nuclear part of the magnetic moment $\boldsymbol{\mu}_{\mathrm{n}} \equiv g_N \, \mu_N \, \boldsymbol{I}$ (where $\mu_N \approx 762$ Hz/G is the nuclear magneton) arises from the ^{19}F nuclear spin $\boldsymbol{I}$, which we have chosen to couple to the total electronic plus rotational angular momentum $\boldsymbol{J}$ in the laboratory frame to form $\boldsymbol{F}$. [4] The matrix elements of $\boldsymbol{I}$ are easy to work out by application of the Wigner-Eckart theorem (B&C Eq. 5.172), the formula for "matrix elements of a single operator in a coupled scheme" (B&C Eq. 5.175), and

[4] I have not considered how $\boldsymbol{I}$ might be coupled to $\boldsymbol{J}$ in the molecule frame, but I imagine it is possible. I believe that in either case, all observables should come out the same, since angular momentum coupling is just a choice of basis.

the reduced matrix element of a first-rank tensor between its own eigenstates (B&C Eq. 5.179). The result is

$$\begin{aligned}\left\langle \eta' \right| T_p^{(1)}(\boldsymbol{\mu}_{\mathrm{n}}) \left| \eta \right\rangle = (-1)^{F'-M'_F} & \begin{pmatrix} F' & 1 & F \\ -M'_F & p & M_F \end{pmatrix} \\ & \times \delta_{J'J} \, (-1)^{F'+J'+1+I} \sqrt{(2F'+1)(2F+1)} \begin{Bmatrix} I & F & J' \\ F' & I & 1 \end{Bmatrix} \\ & \times \sqrt{I(I+1)(2I+1)} \, g_N \, \mu_N .\end{aligned} \tag{2.28}$$

Note that here we have made no use of Wigner D matrices, but only identities related to decoupling of angular momenta in the language of spherical tensors. For the $^3\Delta_1(J=1)$ state, the nuclear contribution to the Zeeman Hamiltonian is given by Eq. (2.29) below.

$$H_{\mathrm{Z,n}} = g_N \, \mu_N \begin{pmatrix} -\frac{\mathcal{B}_z}{6} & \frac{\mathcal{B}_\perp}{6} & \frac{\mathcal{B}_\perp}{\sqrt{6}} & \frac{\sqrt{2}\mathcal{B}_z}{3} & -\frac{\mathcal{B}_\perp}{3\sqrt{2}} & 0 \\ \frac{\mathcal{B}_\perp}{6} & \frac{\mathcal{B}_z}{6} & 0 & \frac{\mathcal{B}_\perp}{3\sqrt{2}} & \frac{\sqrt{2}\mathcal{B}_z}{3} & -\frac{\mathcal{B}_\perp}{\sqrt{6}} \\ \frac{\mathcal{B}_\perp}{\sqrt{6}} & 0 & \frac{\mathcal{B}_z}{2} & -\frac{\mathcal{B}_\perp}{2\sqrt{3}} & 0 & 0 \\ \frac{\sqrt{2}\mathcal{B}_z}{3} & \frac{\mathcal{B}_\perp}{3\sqrt{2}} & -\frac{\mathcal{B}_\perp}{2\sqrt{3}} & \frac{\mathcal{B}_z}{6} & -\frac{\mathcal{B}_\perp}{3} & 0 \\ -\frac{\mathcal{B}_\perp}{3\sqrt{2}} & \frac{\sqrt{2}\mathcal{B}_z}{3} & 0 & -\frac{\mathcal{B}_\perp}{3} & -\frac{\mathcal{B}_z}{6} & -\frac{\mathcal{B}_\perp}{2\sqrt{3}} \\ 0 & -\frac{\mathcal{B}_\perp}{\sqrt{6}} & 0 & 0 & -\frac{\mathcal{B}_\perp}{2\sqrt{3}} & -\frac{\mathcal{B}_z}{2} \end{pmatrix} \tag{2.29}$$

Within the eight sublevels of the $F = 3/2$ hyperfine manifold, the electronic and nuclear contributions to the Zeeman Hamiltonian have the same form. We can therefore define an effective magnetic g-factor g_F for this manifold of states only, and parameterize the total Zeeman Hamiltonian as

$$H_{\mathrm{Z},F} = -g_F \, \mu_B \, \boldsymbol{\mathcal{B}} \cdot \boldsymbol{F} = -g_F \, \mu_B \begin{pmatrix} -\frac{3\mathcal{B}_z}{2} & \frac{\sqrt{3}\mathcal{B}_\perp}{2} & 0 & 0 \\ \frac{\sqrt{3}\mathcal{B}_\perp^*}{2} & -\frac{\mathcal{B}_z}{2} & \mathcal{B}_\perp & 0 \\ 0 & \mathcal{B}_\perp^* & \frac{\mathcal{B}_z}{2} & \frac{\sqrt{3}\mathcal{B}_\perp}{2} \\ 0 & 0 & \frac{\sqrt{3}\mathcal{B}_\perp^*}{2} & \frac{3\mathcal{B}_z}{2} \end{pmatrix} \tag{2.30}$$

When performing perturbation theory within $F = 3/2$ only, we can use this parameterization of the Zeeman matrix elements.

In HfF^+, we have typically neglected the rotational contribution to the Zeeman effect, because we expect it to be small in the ground rotational state of $^3\Delta_1$. In fact, I have not evaluated the matrix elements of this operator, so I will just sketch a procedure here. A definition of the rotational magnetic moment consistent with our previous definitions, and which will work in Hund's case (a) and (c), is

$$\boldsymbol{\mu}_r = g_r\,\mu_N\,(\boldsymbol{J} - \boldsymbol{J}_a). \tag{2.31}$$

The only conserved quantum number of the total electronic angular momentum operator $\boldsymbol{J}_a$ is its component along the internuclear axis, $\boldsymbol{J}_a \cdot \boldsymbol{n} = \Omega$. The perpendicular components of $\boldsymbol{J}_a$ act to change Ω and therefore the electronic state, so for example they connect $^3\Delta_1 \leftrightarrow {}^3\Pi_{0^\pm}$. Thus to a first approximation, we can replace $\boldsymbol{J}_a \to \Omega\,\boldsymbol{n}$ in Eq. (2.31). Upon doing this, we can redefine the electronic and rotational magnetic moments as

$$\begin{aligned} \boldsymbol{\mu}_e &\equiv (G_\parallel\,\mu_B - g_r\,\mu_N)\,\Omega\,\boldsymbol{n}, \\ \boldsymbol{\mu}_J &\equiv g_r\,\mu_N\,\boldsymbol{J}. \end{aligned} \tag{2.32}$$

We can absorb the contribution $g_r\,\mu_N$ into the definition of $G_\parallel$, and the matrix elements of $\boldsymbol{\mu}_e$ are unchanged. We can then evaluate the matrix elements of our newly defined $\boldsymbol{\mu}_J$,

$$\begin{aligned} \left\langle \eta' \right| T_p^{(1)}(\boldsymbol{\mu}_J) \left| \eta \right\rangle = (-1)^{F'-M'_F} &\begin{pmatrix} F' & 1 & F \\ -M'_F & p & M_F \end{pmatrix} \\ &\times (-1)^{F+J+1+I} \sqrt{(2F'+1)(2F+1)} \begin{Bmatrix} J & F & I \\ F' & J' & 1 \end{Bmatrix} \\ &\times \sqrt{J(J+1)(2J+1)}\; g_r\,\mu_N. \end{aligned} \tag{2.33}$$

This contribution to the Zeeman Hamiltonian was not accounted for in the Generation 1 JILA eEDM experiment. It is my impression that since we typically use very weak magnetic fields in the HfF^+ experiment, its effects can simply be absorbed into a redefinition of g_F. The validity of this assumption has not been tested, however we can be slightly reassured by considering the size of the rotational Zeeman effect: From Eq. 7.226 of Ref. [15], the contribution of the nuclei to g_r is

$$g_r^{\mathrm{n}} = \frac{m(Z_1 M_2^2 + Z_2 M_1^2)}{M_1 M_2 (M_1 + M_2)} \approx 0.00026, \tag{2.34}$$

which is already very small. The nuclear and electronic contributions to the total g-factor should partially cancel due to their opposite charge, so this can be taken as an upper bound on g_r. Even before any cancellations, the rotational Zeeman energy scale is $g_r^{\mathrm{n}}\,\mu_N \approx 0.2$ Hz/Gauss. Since the rotational Zeeman effect will be indistinguishable from the electronic and nuclear spin contributions in our measurement of the energy difference between $M_F = \pm 3/2$ states, and will be divided down by at least the Stark splitting between M_F states when considering perturbative effects, I think it should be completely negligible in considering systematic effects in the JILA eEDM experiment. A possible systematic effect could arise from an erroneous applied doublet-odd correction for a non-reversing magnetic field effect, where I might expect the effect to be of order (0.2 Hz/G) $\times$ $\delta g/g \times$ (0.002 G) $\approx 10^{-7}$ Hz.

2.2.6 Hyperfine structure

Due to the presence of the Fluorine nucleus in HfF^+ with nuclear spin $I = 1/2$, we must account for nuclear magnetic hyperfine structure, which gives rise to the coupling discussed in Section 2.1.6 and causes the good total angular momentum quantum numbers to be F and M_F for small external electric and magnetic fields. Because the valence electrons in HfF^+ are relativistic, their spin and motion are highly coupled, and the positron amplitude of the electrons' Dirac wavefunction cannot be neglected. To obtain accurate theoretical predictions, theorists performing *ab initio* calculations use Dirac wavefunctions for each electron Refs. [45, 46, 116], and evaluate the matrix element

$$A_\parallel = \frac{\mu_N}{\Omega\, I}\left\langle \psi_e \middle| \sum_i \left(\frac{\boldsymbol{\alpha}_i \times \boldsymbol{r}_{iN}}{r_{iN}^3}\right)\cdot \boldsymbol{n} \middle| \psi_e \right\rangle, \tag{2.35}$$

where $\boldsymbol{r}_{iN}$ is the displacement of electron i from the Fluorine nucleus, μ_N is the Fluorine magnetic moment, and $\boldsymbol{\alpha}$ is a vector of 4×4 Dirac matrices [34]. For our purposes, we can simply use this electronic matrix element as a constant in an effective Hamiltonian, in the same way that we do $G_\parallel$ and $D_\parallel$. We use as an effective Hamiltonian

$$H_{\mathrm{hf}} = A_\parallel (\boldsymbol{I}\cdot\boldsymbol{n})(\boldsymbol{J}_a\cdot\boldsymbol{n}), \tag{2.36}$$

where $\boldsymbol{J}_a \cdot \boldsymbol{n} \equiv \Omega$. The projection of $\boldsymbol{I}$ onto the internuclear axis can be evaluated using the *projection theorem* [107], which is a corollary of the Wigner-Eckart theorem. The projection theorem is

$$\left\langle J'M'\Omega' \right| \boldsymbol{V}_q \left| JM\Omega \right\rangle = \frac{\langle \boldsymbol{V} \cdot \boldsymbol{J} \rangle}{J(J+1)} \left\langle J'M'\Omega' \right| \boldsymbol{J}_q \left| JM\Omega \right\rangle, \tag{2.37}$$

where $\boldsymbol{V}$ is any vector operator. We can then set $\boldsymbol{V} \to \boldsymbol{I}$, and use the defining property of the total angular momentum $\boldsymbol{F}$ that $\boldsymbol{I} \cdot \boldsymbol{J} = \frac{1}{2}(\boldsymbol{F}^2 - \boldsymbol{J}^2 - \boldsymbol{I}^2)$. We are looking for $\boldsymbol{I} \cdot \boldsymbol{n} \equiv \boldsymbol{I}_{q=0}$, but we know that $\boldsymbol{J}_{q=0} \equiv \Omega$. So we simply plug these in and find that the matrix elements of our effective hyperfine Hamiltonian are

$$\left\langle \psi' \right| H_{\mathrm{hf}} \left| \psi \right\rangle = \frac{F(F+1) - I(I+1) - J(J+1)}{2J(J+1)} A_{\parallel}\, \Omega^2\, \delta_{\eta,\eta'},$$

which is independent of M_F and of the sign of Ω. Here η represents all quantum numbers; the hyperfine Hamiltonian is diagonal in the F, M_F basis. In the $^3\Delta_1$ state of HfF^+, we find that the $F = 1/2$ states have a hyperfine energy of $-A_{\parallel}/2$, while the $F = 3/2$ states have energy $A_{\parallel}/4$, for a total separation of $E_{\mathrm{hf}} = -3A_{\parallel}/4 \approx 46$ MHz. This energy splitting is visible in Fig. 2.4 at $\mathcal{E}_{\mathrm{rot}} = 0$. Using microwave spectroscopy, we have also confirmed this formula in $^3\Delta_1$, $J = 2$, where the hyperfine splitting is 1/3 as large as in $J = 1$, or ≈ 15.5 MHz.

2.2.7 Omega doubling

In a heteronuclear diatomic molecule with nonzero total angular momentum, there are two possible projections of the total angular momentum along the internuclear axis, given by $\pm\Omega$. Because these states correspond to exactly the same spatial distribution of electronic charge around the nuclei, one might expect the energies of these two configurations to be exactly degenerate – however, this is not the case. Ω doubling results from the coupling of the electronic and rotational angular momentum, and arises primarily from the electronically off-diagonal part of the operator $\boldsymbol{J} \cdot \boldsymbol{J}_a$ that we discussed in the context of rotational states in Section 2.1.4. Kevin Cossel's thesis [28] discusses in detail the perturbations giving rise to Ω doubling, so I will not go into a detailed derivation here.

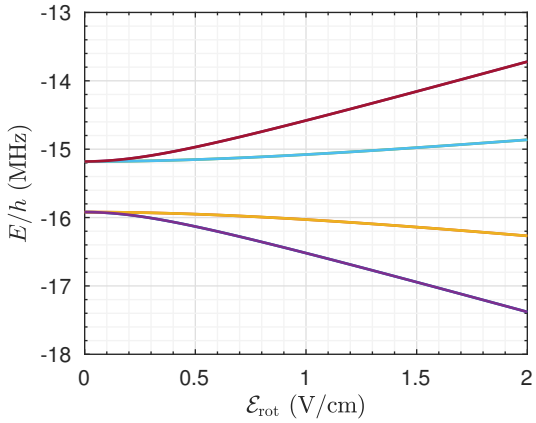

Figure 2.7: Theoretically calculated Stark effect in $^3\Delta_1$, $J = 1$, $F = 3/2$ for small values of the electric bias field, showing Ω doubling – essentially a zoom in of Fig. 2.4 to the region near $\mathcal{E}_{\rm rot} = 0$. As judged by the linearity of the Stark shift as a function of $\mathcal{E}_{\rm rot}$, the $F = 3/2$ states are essentially fully polarized at $\mathcal{E}_{\rm rot} \approx 1$ V/cm. Here the effects of the rotating frame are not included.

For our purposes, we will simply use an effective Hamiltonian description within a single electronic state (See e.g. Ref. [15], Section 7.2). The contribution from Ω doubling in the $^3\Delta_1$ state has the form

$$\left\langle \psi' \right| H_\Omega \left| \psi \right\rangle = \frac{\hbar\omega_{ef}}{4} J(J+1)\, \delta_{\Omega',-\Omega}\, \delta_{\eta',\eta}, \tag{2.38}$$

where η represents all quantum numbers other than Ω. The result of this effective Hamiltonian is that in the absence of an applied electric field, the eigenstates of the molecule are superpositions $\sim |\Omega\rangle \pm |-\Omega\rangle$ separated by an energy splitting $\omega_{ef} \approx 2\pi \times 700$ kHz in $J = 1$. Figure 2.7 shows the Stark effect in $^3\Delta_1$, $J = 1$ for small values of $\mathcal{E}_{\rm rot}$, where the Ω-doubling causes the eigen-energies to be quadratic near $\mathcal{E}_{\rm rot} = 0$.

2.2.8 Effect of $\mathcal{E}_{\rm rot}$ rotation

So far, we have only discussed the energy levels of HfF^+ in static electric and magnetic fields, however in the eEDM experiment, $\mathcal{E}_{\rm rot}$ rotates with a frequency $f_{\rm rot}$ between 150 kHz to 400 kHz. Our eEDM-sensitive Ramsey spectroscopy is performed between the stretched M_F states referred to the rotating electric field. However, the rotating frame in which $\mathcal{E}_{\rm rot}$ lies along the $\hat{z}$ axis is non-inertial, and so we should expect fictitious forces – or more specifically, fictitious torques – to act on

the total angular momentum of a HfF^+ molecule in this frame. The combination of the fictitious torque on $\boldsymbol{F}$ and Ω-doubling in the $^3\Delta_1$ state is a high-order coupling between $M_F = \pm 3/2$ states in the same Stark doublet, which significantly affects the way we perform an eEDM measurement, and is even helpful for performing $\pi/2$ pulses. This effect was discussed generally in Ref. [88], but an explicit calculation in states with nuclear spin was not given. Here I will explicitly calculate this effect with particular application to the HfF^+ eEDM experiment.

Our applied electric and magnetic fields are most easily parameterized in the laboratory frame, where the geometric center of the ion trap defines the origin of coordinates. In this frame, the rotating electric field is

$$\boldsymbol{\mathcal{E}}_{\mathrm{rot}} = \mathcal{E}_{\mathrm{rot}} \left[\hat{X} \cos\left(\omega_{\mathrm{rot}} t\right) + \hat{Y} \sin\left(\omega_{\mathrm{rot}} t\right) \right], \tag{2.39}$$

To transform the Cartesian vector $\boldsymbol{\mathcal{E}}_{\mathrm{rot}}$ into a frame where $\boldsymbol{\mathcal{E}}_{\mathrm{rot}} = \mathcal{E}_{\mathrm{rot}} \hat{z}$, we need to apply a rotation operator

$$R_{\mathrm{cart}}(\theta, \phi) = R_Y(-\theta)\, R_Z(-\phi) = \begin{pmatrix} \cos\theta\, \cos\phi & \cos\theta\, \sin\phi & -\sin\theta \\ -\sin\phi & \cos\phi & 0 \\ \cos\phi\, \sin\theta & \sin\theta\, \sin\phi & \cos\theta \end{pmatrix}, \tag{2.40}$$

where we can then take $\theta = \pi/2$ and $\phi = \omega_{\mathrm{rot}} t$. In much the same way, we need to apply a rotation operator to our Hamiltonian and our quantum states in order to express them in the rotating frame. The rotation operator for an angle α about some vector v in quantum mechanics is $R_v(\alpha) = \exp(-iF_v\alpha)$ where F_v is the total angular momentum operator about v, so by analogy with Eq. (2.40), the appropriate rotation operator is

$$V = \exp\left(iF_Y\theta\right) \exp\left(iF_Z\phi\right). \tag{2.41}$$

If we call the Hamiltonian before the transformation H' (in the lab frame), then the Hamiltonian in the rotating frame is

$$H = V\, H'\, V^\dagger + i\frac{dV}{dt}V^\dagger, \tag{2.42}$$

which can be derived by requiring that the transformed state vector obey the Schrödinger equation with a transformed Hamiltonian. We call the second term on the right hand side H_{rot}; it represents

the fictitious torque experienced by the total angular momentum of HfF^+ molecules in the rotating frame. In terms of angular momentum operators, its value is

$$H_{\text{rot}} = -\boldsymbol{\omega}_{\text{rot}} \cdot \boldsymbol{F} = -\omega_{\text{rot}} F_Z = \omega_{\text{rot}} F_x, \tag{2.43}$$

where I have used the transformation of Cartesian coordinates in Eq. (2.40) to find that $F_Z = -F_x$, where uppercase coordinates are in the lab frame, and lowercase coordinates are in the rotating frame. Combined with Ω-doubling, it is this component of the Hamiltonian that gives rise to the coupling between $M_F = \pm 3/2$ states in the rotating frame. We can derive this coupling by performing perturbation theory to fourth order, with the large and small components of the Hamiltonian

$$\begin{aligned} H_0 &= H_{\text{hf}} + H_{\text{Stark}}, \\ H_1 &= H_{\text{rot}} + H_\Omega. \end{aligned} \tag{2.44}$$

The large component H_0 can be exactly diagonalized, so we can apply fourth order perturbation theory, defining the result as the off-diagonal element of an effective Hamiltonian that couples states $|a\rangle$ and $|b\rangle$ (or $|c\rangle$ and $|d\rangle$, with labels defined in Fig. 2.8). For example, the perturbation theory

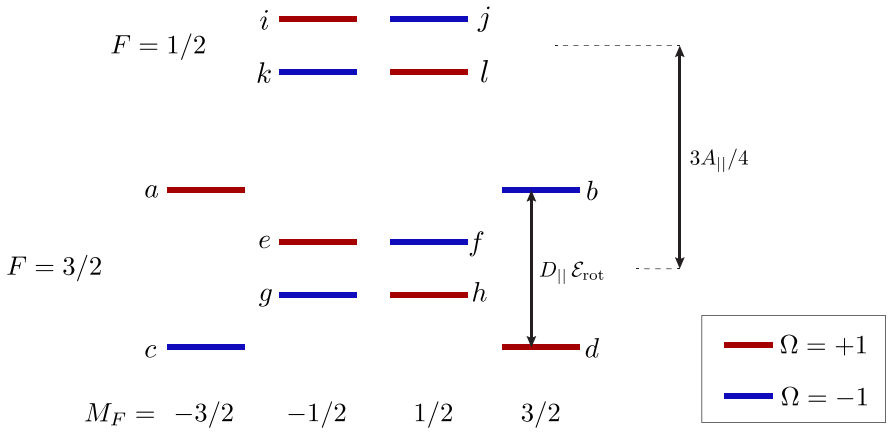

Figure 2.8: Quantum numbers and shorthand alphabetical labels for magnetic and hyperfine sublevels of $^3\Delta_1$, $J = 1$. The quantum number M_F is good for all values of $\mathcal{E}_{\text{rot}}$, but F ceases to be a good quantum number when $D_\parallel \mathcal{E}_{\text{rot}} \approx A_\parallel$.

formula applied to the upper doublet is

$$\frac{\hbar\Delta^u}{2} \equiv \frac{\langle a|\, H_{\rm rot}\, |e\rangle \langle e|\, H_{\rm rot}\, |h\rangle \langle h|\, H_\Omega\, |f\rangle \langle f|\, H_{\rm rot}\, |b\rangle}{(E_a-E_e)(E_a-E_h)(E_a-E_f)} + \frac{\langle a|\, H_{\rm rot}\, |e\rangle \langle e|\, H_\Omega\, |g\rangle \langle g|\, H_{\rm rot}\, |f\rangle \langle f|\, H_{\rm rot}\, |b\rangle}{(E_a-E_e)(E_a-E_g)(E_a-E_f)} + \frac{\langle a|\, H_\Omega\, |c\rangle \langle c|\, H_{\rm rot}\, |g\rangle \langle g|\, H_{\rm rot}\, |f\rangle \langle f|\, H_{\rm rot}\, |b\rangle}{(E_a-E_c)(E_a-E_g)(E_a-E_f)} + \frac{\langle a|\, H_{\rm rot}\, |e\rangle \langle e|\, H_{\rm rot}\, |h\rangle \langle h|\, H_{\rm rot}\, |d\rangle \langle d|\, H_\Omega\, |b\rangle}{(E_a-E_e)(E_a-E_h)(E_a-E_d)} \tag{2.45}$$

We typically express Δ as an average part Δ and a doublet-odd part Δ^D. The result of applying Eq. (2.45) and averaging and differencing the results for the Stark doublets is

$$\Delta = -\frac{3\omega_{ef}}{2}\left(\frac{\hbar\omega_{\rm rot}}{D_\parallel \mathcal{E}_{\rm rot}}\right)^3 \left(\frac{18A_\parallel^2 - 19D_\parallel^2\mathcal{E}_{\rm rot}^2}{A_\parallel^2 - D_\parallel^2\mathcal{E}_{\rm rot}^2}\right) \approx -27\omega_{ef}\left(\frac{\hbar\omega_{\rm rot}}{D_\parallel \mathcal{E}_{\rm rot}}\right)^3, \tag{2.46}$$

$$\Delta^D = \frac{3\omega_{ef}}{2}\left(\frac{\hbar^3\omega_{\rm rot}^3}{D_\parallel^2\mathcal{E}_{\rm rot}^2 A_\parallel}\right)\left(\frac{9A_\parallel^2 - 8D_\parallel^2\mathcal{E}_{\rm rot}^2}{A_\parallel^2 - D_\parallel^2\mathcal{E}_{\rm rot}^2}\right) \approx \Delta \times \frac{D_\parallel \mathcal{E}_{\rm rot}}{2A_\parallel}. \tag{2.47}$$

Note that these results are exact with respect to the size of $D_\parallel\mathcal{E}_{\rm rot}/A_\parallel$, but not exact with respect to $\omega_{ef}/D_\parallel\mathcal{E}_{\rm rot}$. The approximate expressions given are for $D_\parallel\mathcal{E}_{\rm rot} \ll A_\parallel$. In addition, the prefactor given for Δ in Ref. [78] is incorrect by a factor of 2π. Thus we should expect deviation of perturbation theory from exact diagonalization at small values of $\mathcal{E}_{\rm rot}$. Also, note that Δ here has units of rad/s, in contrast to Ref. [16] where it has units of Hz. Figure 2.9 shows the numerical and perturbation theory results for Δ^u and Δ^l as a function of $\mathcal{E}_{\rm rot}$. At the value of $D_\parallel\mathcal{E}_{\rm rot}$ where the $F = 3/2$, $M_F\Omega = -3/2$ and $F = 1/2$, $M_F\Omega = 1/2$ hyperfine states cross, the value of Δ^u diverges. While there is deviation between the perturbation theory and numerical results at low $\mathcal{E}_{\rm rot}$, it is not visible on the scale of the figure. Note that due to the logarithmic scale of the plot, the apparent divergence near $\mathcal{E}_{\rm rot} \approx 31$ V/cm is only a zero crossing and is not real, but the divergence at ~ 35 V/cm is genuine.

2.2.9 eEDM shift

The effect of a P,T-violating electron EDM in the $^3\Delta_1$ state of HfF^+ is to mix states of opposite parity but the same M_F with a constant matrix element $H_d = -d_e\,(\boldsymbol{S}\cdot\boldsymbol{\mathcal{E}}_{\rm int})/S$. In the basis of Hund's case (a) states and in the presence of $\mathcal{E}_{\rm rot} \gg \hbar\omega_{ef}$, we can essentially treat this Hamiltonian at lowest order in perturbation theory by taking $\boldsymbol{S}\cdot\boldsymbol{\mathcal{E}}_{\rm int} \approx (\boldsymbol{S}\cdot\boldsymbol{n})(\boldsymbol{\mathcal{E}}_{\rm int}\cdot\boldsymbol{n}) \equiv \Sigma\,\mathcal{E}_{\rm eff} = -\Omega\,\mathcal{E}_{\rm eff}$,

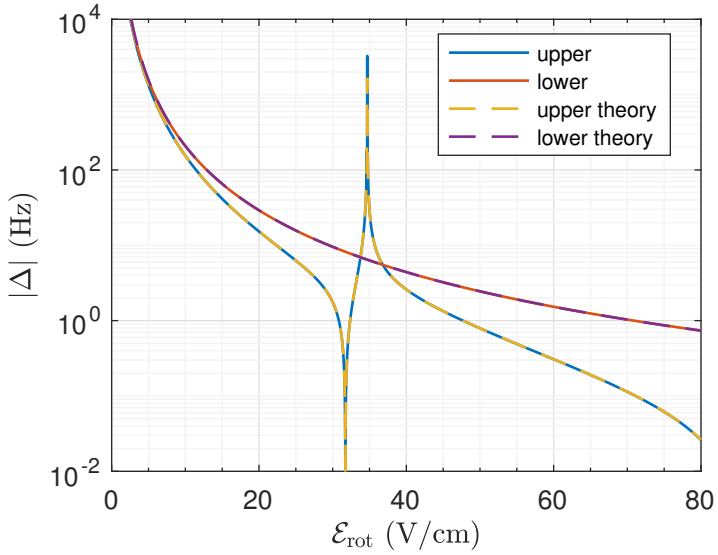

Figure 2.9: Energy difference between states of opposite m_F, but the same value of $m_F\Omega$ – i.e., states in the same Stark Doublet, versus $\mathcal{E}_{\rm rot}$, for $\mathcal{B}_{\rm rot} = 0$. This is the size of the avoided crossing $|\Delta|$ in units of Hz. Here $\omega_{\rm rot}/(2\pi) = 375$ kHz.

where the last equality is only true in the $^3\Delta_1$ state. We typically take the internuclear axis $\boldsymbol{n}$ to point from the Fluorine to the Hafnium nucleus, so that $D_\parallel \approx +1.8$ MHz/(V/cm). As a result, the internal electric field, which points from Hf to F, points against the internuclear axis. In Ref. [16], we took the eEDM energy shift to be

$$\left\langle F' M_F' \Omega' \right| H_d \left| F M_F \Omega \right\rangle = -d_e |\mathcal{E}_{\text{eff}}| \Omega \, \delta_{F'F} \, \delta_{M_F' M_F} \, \delta_{\Omega' \Omega} \tag{2.48}$$

to make all of these signs explicit and hopefully prevent confusion.

2.2.10 Differential g-factor

Conducting an eEDM measurement in a molecular state of nonzero Ω was first proposed by Dave DeMille for PbO in its metastable $^3\Sigma$ state Ref. [30], motivated by the desire to reverse the electric field experienced by a valence electron without reversing a laboratory electric field, which suppresses major systematics. John Bohn and Ed Meyer expanded on this idea to suggest the $^3\Delta_1$ state, which not only has the Ω-doublet feature, but also has a very small magnetic g-factor due to the cancellation of spin and orbital magnetic moments [87]. These proposals led to the use of the metastable $^3\Delta_1$ states of ThO and HfF^+ at Harvard and JILA, respectively, in what are presently the most sensitive eEDM searches.

While the magnetic g-factors of the Ω doublets in the $^3\Delta_1$ state of HfF^+ are very similar, they are not exactly equal, and their difference leads to some of the largest systematic effects that we are aware of. We parameterize their difference with the differential g-factor,

$$\delta g_F \equiv \frac{g_F^u - g_F^l}{2},$$

where $g_F^{u/l}$ are the g-factors of $M_F \, \Omega < 0$ and $M_F \, \Omega > 0$ states, respectively. We can obtain a good approximation for δg_F using perturbation theory on the effective Hamiltonian derived in the earlier sections of this chapter, accounting for two main contributions: the first is from Stark mixing of rotational levels $J = 1$ and $J = 2$ in $^3\Delta_1$, and the second is from a hyperfine-differential mixing of neighboring M_F sublevels within $^3\Delta_1$, $J = 1$, caused by the rotation of $\mathcal{E}_{\text{rot}}$. Here I will go through the derivations of each.

The contribution to δg_F arising from Stark mixing of $J = 1$ and $J = 2$ can be derived using 2nd order perturbation theory, where separate our Hamiltonian into a dominant term including tumbling and J-diagonal Stark contributions, and a perturbation including J-off-diagonal Stark and Zeeman contributions.

$$\begin{aligned} H_0 &= H_{\text{tum}} + H_{\text{hf}} + H_{\text{Stark}}\,\delta_{J'J}, \\ H_1 &= (H_{\text{Stark}} + H_{\text{Zeeman}})\,(1 - \delta_{J'J}). \end{aligned} \tag{2.49}$$

From standard 2nd order perturbation theory, the energy of a state $|i\rangle = |J = 1, \Omega, F, M_F\rangle$ will receive a correction

$$\Delta E_i^{(2)} = \sum_{n \neq i} \frac{\langle i|\, H_1\, |n\rangle \,\langle n|\, H_1\, |i\rangle}{\langle i|\, H_0\, |i\rangle - \langle n|\, H_0\, |n\rangle}. \tag{2.50}$$

Because $\mathcal{E}_{\text{rot}}$ acts along the laboratory z axis (in a rotating reference frame), it has only a $p = 0$ spherical component, and does not couple states of different M_F. In addition, $\mathcal{E}_{\text{rot}}$ can only couple states of the same Ω, because the molecule-frame dipole moment $D_\parallel$ has only a $q = 0$ spherical component. Therefore for a given $|J = 1, F, M_F, \Omega\rangle$ state, the sum in Eq. (2.50) contains only two terms. By substituting into Eq. (2.15) and a similar expression for the Zeeman Hamiltonian as described in Section 2.2.5, we obtain the relevant matrix elements

$$\begin{aligned} \left\langle 2, \frac{3}{2}, \frac{3}{2}, \pm 1 \right| H_1 \left| 1, \frac{3}{2}, \frac{3}{2}, \pm 1 \right\rangle &= \frac{\sqrt{3}}{10} \left(D_\parallel\, \mathcal{E}_{\text{rot}} \mp G_\parallel\, \mu_B\, \mathcal{B}_{\text{rot}} \right) \\ \left\langle 2, \frac{5}{2}, \frac{3}{2}, \pm 1 \right| H_1 \left| 1, \frac{3}{2}, \frac{3}{2}, \pm 1 \right\rangle &= -\frac{\sqrt{3}}{5} \left(D_\parallel\, \mathcal{E}_{\text{rot}} \mp G_\parallel\, \mu_B\, \mathcal{B}_{\text{rot}} \right) \end{aligned} \tag{2.51}$$

Substituting these matrix elements into the perturbation theory expression above, we find that the Stark contribution to the differential g-factor is

$$\delta g_F^{\text{Stark}} \approx \frac{\Delta E^{(2)}_{3/2,-1} - E^{(2)}_{3/2,+1}}{8B\, g_F\, \mu_B\, \mathcal{B}_{\text{rot}}\, M_F} = \frac{D_\parallel\, \mathcal{E}_{\text{rot}}\, G_\parallel}{20B\, g_F} = \frac{3D_\parallel\, \mathcal{E}_{\text{rot}}}{20B} \left(1 - \frac{g_N\, \mu_N}{3 g_F\, \mu_B} \right) \tag{2.52}$$

where $B = 0.29889(2)$ cm^{-1} is the $^3\Delta_1$ rotational constant, and I have substituted for the molecule-frame electronic g-factor $G_\parallel = 3g_F - g_N\, \mu_N/\mu_B$ in terms of the experimentally measurable value g_F and the Fluorine magnetic moment g_N.

The contribution to δg_F arising from the rotation of $\mathcal{E}_{\text{rot}}$ can be derived from second order perturbation theory, with H_{rot} as the perturbing Hamiltonian. The $M_F = \pm 3/2$ states gain some

admixture of their neighboring $M_F = 1/2$ states due to the rotating frame, which applies a slight change to their effective g-factor. The dominant change in the g-factor is common to both doublets, but the presence of hyperfine structure and the subsequent quadratic Stark shifts of the $F = 3/2$, $M_F = \pm 1/2$ states causes the degree of mixing of the upper doublet to be less than that of the lower doublet. The energy denominator $E_a - E_e$ from Eq. (2.50) applied to state $|a\rangle$ [Fig. (2.8)] can be expanded for small $\mathcal{B}_{\rm rot}$, and the resulting energy shift (for example in state $|a\rangle$) contains a term

$$\Delta E_a^{(2)} \subset \frac{3\hbar^2\omega_{\rm rot}^2\, g_N\, \mu_N\, \mathcal{B}_{\rm rot}}{D_\parallel\, \mathcal{E}_{\rm rot}\, A_\parallel}.$$

This energy shift is common to all four of the states a-d, but with a relative sign that depends on Ω. The g-factor of state $|a'\rangle$ thus contains a contribution

$$\delta g_F^{\rm rot} \approx \frac{2g_N\, \mu_N}{g_F\, \mu_B}\, \frac{\hbar^2\omega_{\rm rot}^2}{D_\parallel\, \mathcal{E}_{\rm rot}\, A_\parallel} \tag{2.53}$$

Note that this equation is slightly different from the result reported in Ref. [16]. That result contains an error that has been fixed here, and the result here has been verified by direct diagonalization of the full Hamiltonian. Thus to summarize, the total differential g-factor is

$$\frac{\delta g_F}{g_F} \approx \frac{2g_N\, \mu_N}{g_F\, \mu_B}\, \frac{\hbar^2\omega_{\rm rot}^2}{D_\parallel\, \mathcal{E}_{\rm rot}\, A_\parallel} + \frac{3D_\parallel\, \mathcal{E}_{\rm rot}}{20B}\left(1 - \frac{g_N\, \mu_N}{3g_F\, \mu_B}\right) \tag{2.54}$$

Figure 2.10 shows the upper and lower magnetic g-factors, as well as their difference, as a function of $\mathcal{E}_{\rm rot}$. The perturbation theory estimates show good agreement with a numerical diagonalization at $\mathcal{E}_{\rm rot} \gtrsim 10$ V/cm, however the mean value and difference do not agree well at low $\mathcal{E}_{\rm rot}$. This is due to higher-order coupling of M_F levels by $H_{\rm rot}$, which cannot be accounted for by second-order perturbation theory. It is worth noting that in exactly the range of $\mathcal{E}_{\rm rot}$ where the first term in Eq. (2.54) is supposed to dominate, namely at small values of $\mathcal{E}_{\rm rot}$, the mean value of g_F from perturbation theory is in complete disagreement with numerical diagonalization. As a result, the first term above is not particularly useful, and we are generally better off just relying on numerical diagonalization. It is also important to note that the differential g-factor given in Fig. 2.10 is not equivalent to the frequency channel f^D due to the effects of Δ and Δ^D. These effects are discussed in Chapter 3.

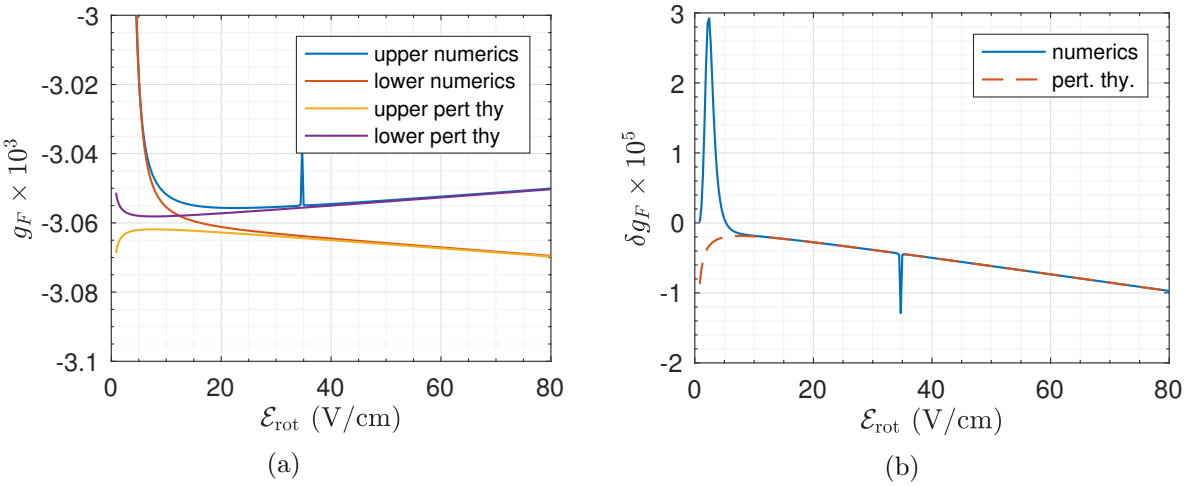

Figure 2.10: Magnetic g-factor of stretched states as a function of $\mathcal{E}_{\rm rot}$, at $f_{\rm rot} = 375$ kHz. The drop of the absolute g-factors to zero at low $\mathcal{E}_{\rm rot}$ results from mixing of M_F levels due to $H_{\rm rot}$ at order > 2 in perturbation theory. Note that we have not derived the absolute value of g_F from theory, but taken it from experiment.

Chapter 3

Generation 1 eEDM Measurement

3.1 Summary of the eEDM result

This section is a reproduction of the main text of Ref. [16].

A search for a nonzero permanent electric dipole moment of the electron (eEDM, d_e) constitutes a nearly background-free test for physics beyond the Standard Model (SM), since the SM predicts $|d_e| \lesssim 10^{-38}\, e\,\mathrm{cm}$ [102], while the natural scale of d_e in many proposed SM extensions is 10^{-27} to $10^{-30}\, e\,\mathrm{cm}$ [37]. Present experimental techniques now constrain these theories [6]; hence, there have been many recent efforts to measure an eEDM [6, 36, 60, 64, 79, 104, 137].

The most precise eEDM measurements to date were performed using beams of neutral atoms or molecules [6, 64, 104]. These experiments benefited from excellent statistical sensitivity provided by a high flux of neutral particles, and decades of past work have produced a thorough understanding of their common sources of systematic error. Nonetheless, a crucial systematics check can be provided by independent measurements conducted using different physical systems and experimental techniques. Moreover, techniques that allow longer interrogation times offer significant potential for sensitivity improvements in eEDM searches and other tests of fundamental physics [117].

In this Letter, we report on a precision measurement of the eEDM using molecular ions confined in a radio frequency (RF) trap, applying the methods proposed in Ref. [78] and demonstrated in Ref. [82]. We perform an electron spin precession experiment on $^{180}\mathrm{Hf}^{19}\mathrm{F}^{+}$ molecules in their metastable $^3\Delta_1$ electronic state, and extract the relativistically enhanced eEDM-induced energy shift $\sim 2d_e\mathcal{E}_{\mathrm{eff}}$ between stretched Zeeman sublevels, where $\mathcal{E}_{\mathrm{eff}} \approx 23$ GV/cm in HfF^{+} [44, 87, 98].

In addition to leveraging the high eEDM sensitivity and systematic error rejection intrinsic to a $^3\Delta_1$ state in a heavy polar molecule [36, 87], we use a unique experimental approach that is robust against sources of systematic error common to other methods. The 2.1(1) s lifetime of the $^3\Delta_1$ state in HfF^+ [91] and our use of an RF trap allow us to attain spin precession times in excess of 700 ms – nearly three orders of magnitude longer than in contemporary neutral beam experiments. This exceptionally long interrogation time allows us to obtain high eEDM sensitivity despite our lower count rate. In addition, performing an experiment on trapped particles permits the measurement of spin precession fringes at arbitrary free-evolution times, making our experiment relatively immune to systematic errors associated with imperfectly characterized state preparation.

Our apparatus and experimental sequence, shown schematically in Fig. 3.1, have been described previously [29, 78, 82, 83, 84, 91]. We produce HfF by ablation of Hf metal into a pulsed supersonic expansion of Ar and SF_6. The neutral beam enters the RF trap, where HfF is ionized with pulsed UV lasers to form HfF^+ in its ground vibronic state [83, 84]. The ions are stopped by a pulsed voltage on the radial trap electrodes, then confined by DC and RF electric quadrupole gradients (with RF frequency $f_{\rm rf} = 50$ kHz). We next adiabatically turn on a spatially uniform electric bias field $\mathcal{E}_{\rm rot} \approx 24$ V/cm that rotates in the radial plane of the ion trap with frequency $f_{\rm rot} \approx 250\,$kHz, causing the ions to undergo circular motion with radius $r_{\rm rot} \approx 0.5\,$mm. A pair of magnet coils aligned with the Z axis produce an axial magnetic gradient $\boldsymbol{\mathcal{B}} = \mathcal{B}'_{\rm axgrad}(2\boldsymbol{Z} - \boldsymbol{X} - \boldsymbol{Y})$ where $|\mathcal{B}'_{\rm axgrad}| \approx 40\,$mG/cm, which in the rotating frame of the ions creates a magnetic bias field $\mathcal{B}_{\rm rot} \equiv |\langle \boldsymbol{\mathcal{B}} \cdot \boldsymbol{\mathcal{E}}_{\rm rot}/\mathcal{E}_{\rm rot}\rangle| \simeq |\mathcal{B}'_{\rm axgrad} r_{\rm rot}|$ that is parallel (antiparallel) to $\mathcal{E}_{\rm rot}$ if $\mathcal{B}'_{\rm axgrad} > 0$ (< 0) [78, 82].

Our state preparation consists of population transfer to the eEDM-sensitive $^3\Delta_1$ state and selective depletion of magnetic sublevels to produce a pure spin state [Fig. 3.1(b-c)]. Two cw lasers co-propagating along the $\hat{Z}$ axis drive a Raman transition through a $^3\Pi_{0^+}$ intermediate state, transferring $\sim 40\%$ of the ground state population to the $^3\Delta_1$, $J = 1$, $F = 3/2$ state. Figure 3.2(a) shows the structure of this state in a rotating frame defined by $\boldsymbol{\mathcal{E}}_{\rm rot} \equiv \mathcal{E}_{\rm rot}\hat{z}$. It consists of four Stark doublets (pairs of magnetic sublevels) separated by $d_{\rm mf}\mathcal{E}_{\rm rot}/3h \approx 14$ MHz, where $d_{\rm mf}$ is the

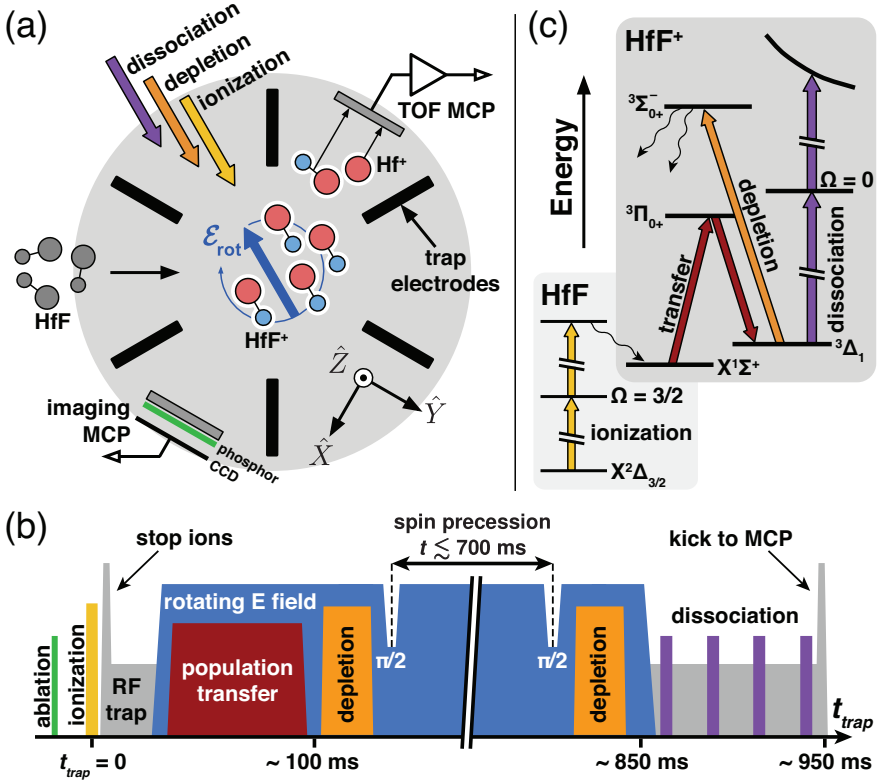

Figure 3.1: (a) Apparatus schematic, (b) experimental timing, and (c) relevant energy levels (not to scale) for an eEDM measurement using trapped ions. HfF is photoionized (yellow) to form HfF^+. A rotating electric bias field $\mathcal{E}_{\rm rot}$ (blue) polarizes the molecules, and transfer (red) and depletion (orange) lasers perform state preparation. The $\pi/2$ pulses are performed by modulating $\mathcal{E}_{\rm rot}$. Spin state populations are detected by depletion followed by photodissociation (purple) and counting the resulting Hf^+ ions on a microchannel plate (MCP).

$^3\Delta_1$ molecule-frame dipole moment and h is Planck's constant. The population transfer process produces an incoherent mixture of $M_F = \pm 3/2$ states in the upper or lower doublet, depending on the detuning of the second transfer laser. Selective depletion is then performed by a circularly polarized laser resonant with the $Q(1)$ line of a $^3\Sigma^-_{0^+} \leftarrow {}^3\Delta_1$ transition. The depletion laser is strobed synchronously with the rotating electric field so that its wavevector is either parallel or antiparallel to $\boldsymbol{\mathcal{E}}_{\rm rot}$, thus driving a $\sigma^{\pm}$ transition to an $F' = 3/2$ manifold and leaving one $M_F = \pm 3/2$ level populated in the $^3\Delta_1$ state.

Following strobed depletion, we perform a $\pi/2$ pulse to prepare an equal superposition of $M_F = \pm 3/2$ states. This is accomplished by reducing $\mathcal{E}_{\rm rot}$ for a brief interval, which increases a rotation-induced coupling $\Delta^{u/l}$ between $M_F = \pm 3/2$ states [Fig. 3.2(b)] and causes a pure spin state to evolve into an equal superposition in $\sim 1\,$ms [78, 82]. We return $\mathcal{E}_{\rm rot}$ to its nominal value and allow the phase of the superposition to evolve for a variable precession time, then apply a second $\pi/2$ pulse to map the relative phase of the superposition onto a population difference between $M_F = \pm 3/2$ states. A second set of strobed laser pulses again depletes all but one $M_F = \pm 3/2$ level. To selectively detect the remaining population in the $^3\Delta_1$, $J = 1$ state, we resonantly photodissociate HfF^+ using pulsed UV lasers [91]. We eject all ions from the trap, and count both Hf^+ and the temporally resolved HfF^+ using a microchannel plate (MCP) detector.

We interleave experimental trials where the two sets of strobed depletion pulses have the same or opposite phase with respect to $\mathcal{E}_{\rm rot}$ in order to alternately prepare and detect population in the $M_F = \pm 3/2$ states. Denoting by N_A (N_B) the measured population when the depletion phases are the same (opposite), we form the asymmetry $\mathcal{A} = (N_A - N_B)/(N_A + N_B)$, which normalizes drifts in absolute $^3\Delta_1$ population. The asymmetry forms an interference fringe that is well-approximated by a sinusoidal function of precession time t,

$$\mathcal{A}(t) \simeq -\mathcal{C}e^{-\gamma t}\cos(2\pi f t + \phi) + \mathcal{O}, \tag{3.1}$$

with frequency f proportional to the energy difference between the $M_F = \pm 3/2$ states, as shown in Fig. 3.2(c). The initial contrast $\mathcal{C}$, initial phase ϕ, offset $\mathcal{O}$, and decoherence rate γ parametrize

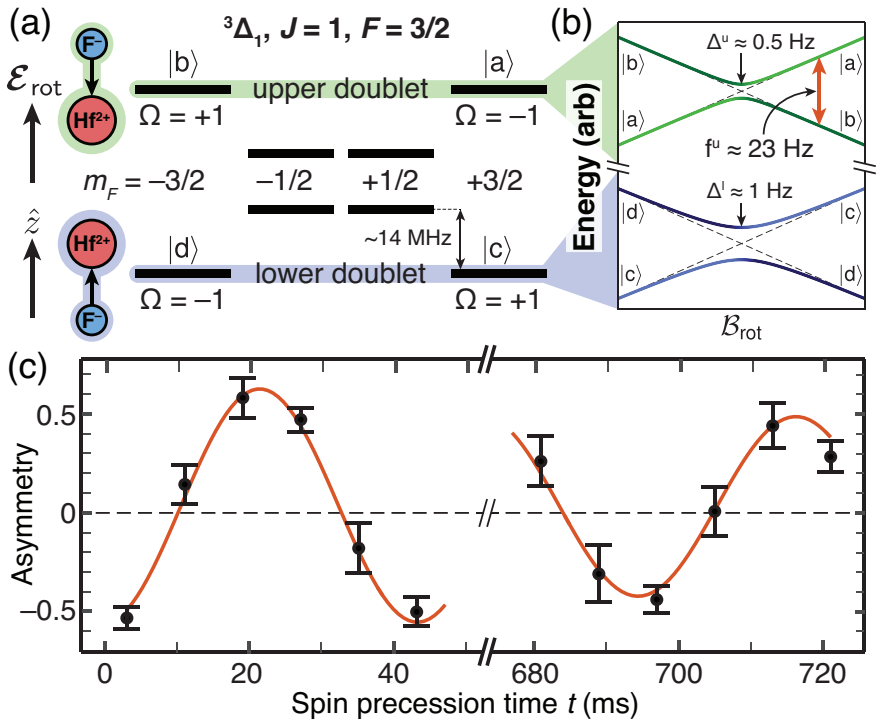

Figure 3.2: Electron spin resonance spectroscopy in HfF^+. (a) Level structure of the eEDM-sensitive $^3\Delta_1$, $F = 3/2$ state in an electric bias field $\mathcal{E}_{\rm rot}$. (b) Energies of $|M_F| = 3/2$ states as a function of magnetic bias field $\mathcal{B}_{\rm rot}$ (not to scale), showing an avoided crossing at $\mathcal{B}_{\rm rot} = 0$ due to a rotation-induced coupling $\Delta^{u/l}$. (c) Interference fringe with interrogation time $\sim 700\,$ms and decoherence rate $\gamma = 0.3(2)\,\mathrm{s}^{-1}$.

imperfect state preparation and the loss of coherence. We perform nonlinear least squares fitting of the asymmetry with Eq. (3.1), using $\mathcal{C}$, γ, f, ϕ, and $\mathcal{O}$ as fit parameters. Standard errors $\delta\mathcal{C}$, $\delta\gamma$, δf, $\delta\phi$, and $\delta\mathcal{O}$ are estimated from the Jacobian of the fit function at the optimum parameter values. The precession frequency contains the eEDM signal, while the other fit parameters are used to diagnose experimental imperfections and sources of systematic error.

To isolate an eEDM-dependent frequency shift and diagnose systematic errors, we form data "channels": components of a measurement that have a particular parity under a set of chosen "switches" – experimental parameters that are modulated between opposite values on a short timescale [1] . Our switches are the sign of the magnetic bias field $\tilde{B} = \mathrm{sgn}(\langle \boldsymbol{\mathcal{B}} \cdot \boldsymbol{\mathcal{E}}_{\mathrm{rot}} \rangle)$, the populated Stark doublet $\tilde{D} = -\mathrm{sgn}(M_F \Omega)$, and the sense of the electric bias field rotation $\tilde{R} = -\mathrm{sgn}(\boldsymbol{\omega}_{\mathrm{rot}} \cdot \hat{Z})$. We repeat our spin precession measurement in each of the eight unique "switch states" $\tilde{S} = (\tilde{B}, \tilde{D}, \tilde{R})$ to form a "block," and form channels X^s with parities $s \subset \{B, D, R\}$ from linear combinations of the eight measurements $X(\tilde{S})$, where $X \in \{\mathcal{C}, \gamma, f, \phi, \mathcal{O}\}$. We estimate the standard error δX by propagating the error estimates $\delta X(\tilde{S})$ resulting from the nonlinear least squares fit of Eq. (3.1).

If higher order effects are neglected, the measured spin precession frequency is dominated by the Zeeman shift between populated magnetic sublevels, and includes a BD-odd contribution from an eEDM:

$$\begin{aligned} hf(\tilde{S}) &\approx \left| -3 g_F \mu_B \tilde{B} \mathcal{B}_{\mathrm{rot}} + 2\tilde{D} d_e |\mathcal{E}_{\mathrm{eff}}| \right| \\ &= 3|g_F| \mu_B \mathcal{B}_{\mathrm{rot}} - 2\tilde{B}\tilde{D}\,\mathrm{sgn}(g_F)\, d_e |\mathcal{E}_{\mathrm{eff}}|. \end{aligned} \tag{3.2}$$

An eEDM signal thus appears as the lowest-order contribution to the f^{BD} frequency channel, while any non-ideal contributions to f^{BD} constitute sources of systematic error. The seven non-eEDM frequency channels contain information about experimental conditions such as non-reversing magnetic fields, and we use these channels to construct and confirm models of non-ideal experimental behavior and to correct for systematic shifts in f^{BD}. Some examples of frequency channels, their leading-order expressions in terms of experimental parameters, and their interpretations are shown

[1] Our notation for data channels closely follows that used by the authors of Refs. [6, 7].

Channel	Leading term	Interpretation
f^0	$3\lvert g_F\rvert\mu_B\mathcal{B}_{\rm rot}/h$	Avg. precession frequency
f^B	$3\lvert g_F\rvert\mu_B\mathcal{B}^{\rm nr}_{\rm rot}/h$	Non-reversing $\mathcal{B}_{\rm rot}$
f^D	$3\delta g_{\rm eff}\mu_B\mathcal{B}_{\rm rot}{\rm sgn}(g_F)/h$	Level-dependent g-factor
f^{BR}	$-3\langle\alpha\rangle f_{\rm rot}{\rm sgn}(g_F)$	Geometric phase
f^{BD}	$-2d_e\lvert\mathcal{E}_{\rm eff}\rvert\,{\rm sgn}(g_F)/h$	eEDM shift

Table 3.1: Selected frequency channels, their leading expression in terms of experimental parameters, and their interpretations. Here $\delta g_{\rm eff}$ is half the effective magnetic g-factor difference between Stark doublets, α is the tilt angle of $\boldsymbol{\mathcal{E}}_{\rm rot}$ above the radial plane of the ion trap, and $f_{\rm rot}$ is the rotation frequency of $\mathcal{E}_{\rm rot}$.

in Table 3.1.

Prior to eEDM data collection, we tuned a wide variety of experimental parameters over an exaggerated dynamic range and observed the response of the data channels to study non-ideal frequency shifts in our system that might affect an eEDM measurement. Two illustrative examples of these effects are shown in Fig. 3.3. Through this study, we developed a unified numerical model of our spin precession sequence. In this model, we integrate the classical motion of ions in simulated time-varying electric and magnetic fields, then propagate the internal quantum state of the molecules using an effective Hamiltonian that includes the two lowest rotational levels of $^3\Delta_1$. Using known experimental parameters and realistic estimates of construction imperfections, our model was able to reproduce all observed frequency shifts.

In total, we collected 1024 blocks (360.3 hours) of eEDM-sensitive data, with each block resulting in one value of f^{BD} and thus one eEDM measurement. Throughout the collection and analysis of this eEDM data, we added to the f^{BD} channel a hidden, computer-generated pseudo-random value drawn from a normal distribution with a standard deviation of $5\times10^{-28}\,e\,$cm. This "blind" allowed us to investigate systematic frequency shifts and perform statistical analysis while mitigating the effects of operator bias. We applied cuts to the blinded data based on non-eEDM channels indicating signal quality: blocks with $\mathcal{C}<0.1$ or $\mathcal{C}e^{-\gamma T}<0.1$ were cut due to low signal to noise (where T is the largest value of t sampled in a block). In addition, we cut data where shifts in the "co-magnetometer" channel f^B exceeded 0.4 Hz due to its contribution to systematic errors.

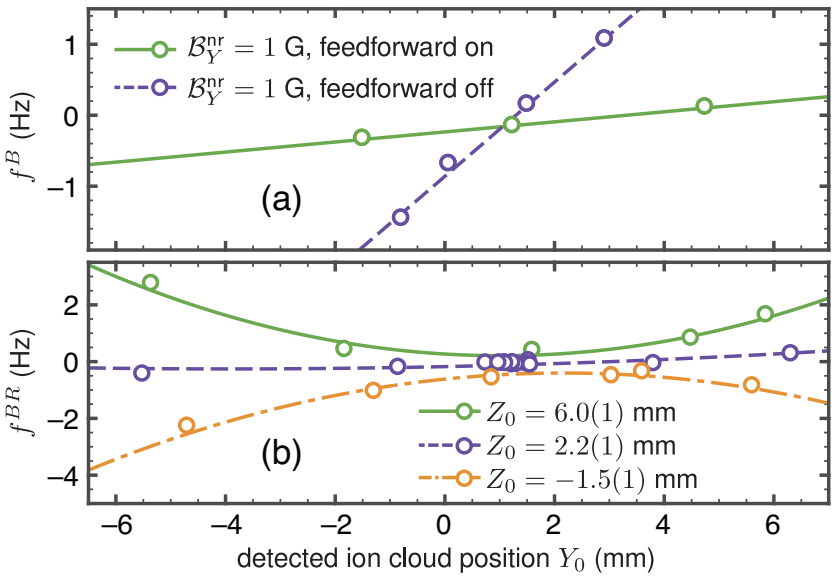

Figure 3.3: Frequency shifts in the f^B and f^{BR} channels due to a stray uniform magnetic field $\mathcal{B}_Y^{\rm nr}$ and ion displacements $Y_0\hat{Y}$ and $Z_0\hat{Z}$. (a) A shift in $f^B \propto \mathcal{B}_Y^{\rm nr} Y_0$ resulted from a contribution to $\mathcal{B}_{\rm rot}$ from an electric field gradient oscillating at $2f_{\rm rot}$, which we suppressed by reducing harmonic distortion in $\mathcal{E}_{\rm rot}$ via feedforward. (b) A shift in $f^{BR} = 3\langle\alpha\rangle f_{\rm rot} \propto Y_0^2 Z_0$ was well modeled by the known inhomogeneity in $\mathcal{E}_{\rm rot}$, and was suppressed by applying feedback to the ion position between eEDM measurements. Error bars are $\sim \pm 0.1$ Hz on all points.

After these cuts, our eEDM dataset consists of 903 blocks or 313.8 hours of data. The unblinded dataset is shown in Fig. 3.4(a-b). Normality tests and visual inspection of a normal probability plot indicate that the distribution of normalized and centered eEDM measurements $(f^{BD} - \langle f^{BD} \rangle)/\delta f$ is consistent with a normal distribution. The reduced chi-squared statistic for fitting a weighted mean to the eEDM dataset is $\chi^2_r = 1.22(5)$. This over-scatter is present in all frequency channels, and is attributable to non-reversing $\mathcal{B}'_{\mathrm{axgrad}}$ drifts on a timescale comparable to one data block. To compensate for this over-scatter, we scale our final statistical error bar by $\sqrt{\chi^2_r} \approx 1.1$.

During eEDM data collection, we suppressed sources of systematic error that appeared in our earlier model-building investigation by applying active feedback to relevant experimental parameters between the collection of data blocks. The only one of these that produced an observable shift in the f^{BD} channel was the combined effect of a non-reversing magnetic bias field $\mathcal{B}^{\mathrm{nr}}_{\mathrm{rot}}$ and the difference in effective magnetic g-factor between Stark doublets [78]. The f^B and f^D frequency channels, which are acquired concurrently with f^{BD}, provide direct measurements of these contributions. Since the value of $f^D \approx 10^{-3} f^0$ is fixed by the values of $\mathcal{E}_{\mathrm{rot}}$, $\mathcal{B}_{\mathrm{rot}}$, and f_{rot}, we suppress the systematic shift in the eEDM channel by applying a compensating $\mathcal{B}'_{\mathrm{axgrad}}$ to minimize $|f^B|$. We also apply a block-by-block correction to f^{BD} based on the measured values of f^B and f^D, the validity of which was verified in our earlier model-building study.

Though they were too small to be observed at our level of sensitivity, we predicted systematic shifts in the eEDM channel due to the frequency shifts in the f^B and f^{BR} channels shown in Fig. 3.3. We suppressed the first of these by adding a feedforward signal to $\mathcal{E}_{\mathrm{rot}}$ to cancel the harmonic distortion component at $2f_{\mathrm{rot}}$, reducing it from -48 dBc to -70 dBc, and by using magnet coils to null the ambient uniform magnetic field at the RF trap center to within $\sim \pm 30$ mG. To suppress the shift in f^{BR} caused by $\mathcal{E}_{\mathrm{rot}}$ inhomogeneity shown in Fig. 3.3(b), we measured the ion cloud position once per data block on a pair of MCPs, and applied DC potentials on the trap electrodes to position the ion cloud within $\sim 2\,\mathrm{mm}$ of the minimum of the quadratic shift. The residual offset of $f^{BR} \approx -100$ mHz and gradient of $\partial f^{BR}/\partial Y_0 \approx 20\,\mathrm{mHz/mm}$ shown in Fig. 3.3 are consistent with $\mathcal{E}_{\mathrm{rot}}$ inhomogeneity resulting from realistic machining, welding, and assembly imperfections in

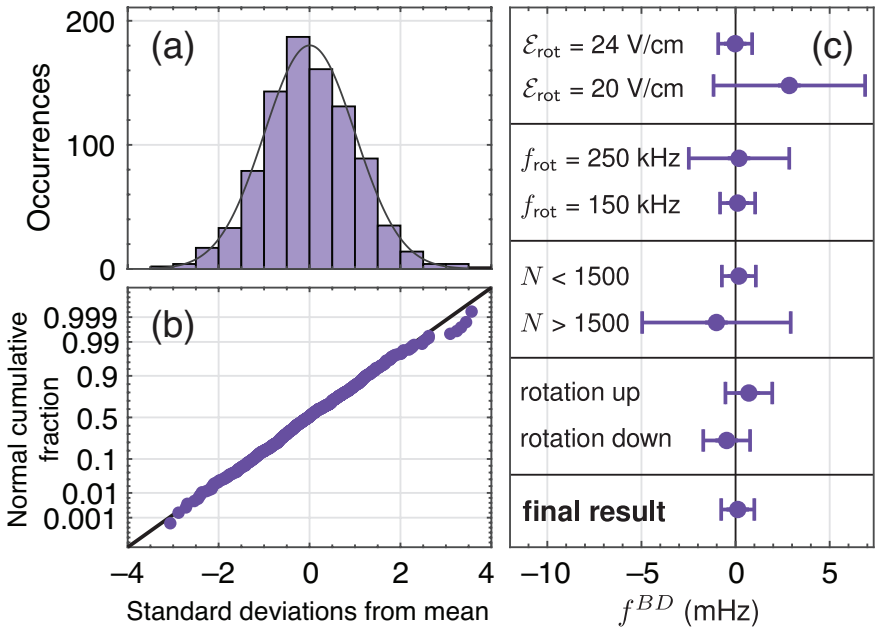

Figure 3.4: Summary of eEDM dataset after cuts and scaling δf by $\sqrt{\chi^2_r}$ to account for over-scatter. (a) Histogram of normalized, centered eEDM-sensitive frequency measurements $(f^{BD} - \langle f^{BD} \rangle)/\delta f$. (b) Normal probability plot of the same dataset, showing a linear trend suggesting that the data are consistent with a normal distribution. (c) Subsets of eEDM data taken under different values of experimental parameters, and the overall average of f^{BD}. Here N is the average number of trapped HfF^+ ions per run.

Effect	Correction	Uncertainty
Non-reversing $\mathcal{B}_{\mathrm{rot}}$	-1	5
Geometric phases		4
Axial secular motion		2
Rotation-odd $\mathcal{E}_{\mathrm{rot}}$		14
Doublet population background		195
Total systematic	-1	195
Statistical		868
Total uncertainty		890

Table 3.2: Systematic effects and corrections applied to the eEDM channel f^{BD}, in units of μHz.

the construction of our RF trap.

While collecting eEDM data, we also searched for new systematic errors correlated with parameters that could not be tuned over a significantly exaggerated dynamic range, including $\mathcal{E}_{\mathrm{rot}}$, f_{rot}, and the number of HfF^+ ions trapped per experimental trial [Fig. 3.4(c)]. We did not observe significant variation of f^{BD} with these parameters at our current level of precision. The variations of the non-eEDM frequency channels f^0 and f^D, in which we did anticipate variation with $\mathcal{E}_{\mathrm{rot}}$ and f_{rot}, were consistent with model predictions. Finally, we modified our data collection by randomizing the order of switch states in each block to search for and suppress systematic errors caused by parameter drifts correlated with our switches, and observed no significant variation of data channels. The final results of our systematic error searches and corrections are summarized in Table 3.2.

We removed our blind on 31 March 2017, and obtained a final value for the eEDM-sensitive frequency channel

$$f^{BD} = 0.10 \pm 0.87_{\mathrm{stat}} \pm 0.20_{\mathrm{syst}}\ \mathrm{mHz}. \tag{3.3}$$

Dividing by $-2|\mathcal{E}_{\mathrm{eff}}|\mathrm{sgn}(g_F)/h \approx 1.13 \times 10^{28}$ mHz/e cm [44, 98], we obtain a value for the eEDM

$$d_e = (0.9 \pm 7.7_{\mathrm{stat}} \pm 1.7_{\mathrm{syst}}) \times 10^{-29}\ e\,\mathrm{cm}, \tag{3.4}$$

which is consistent with zero within one standard error. The resulting upper bound is

$$|d_e| < 1.3 \times 10^{-28}\, e\,\mathrm{cm} \quad (90\%\ \text{confidence}). \tag{3.5}$$

Our result is consistent with the limit of $|d_e| < 9.3 \times 10^{-29}\ e\,\mathrm{cm}$ set by the ACME Collaboration [6, 7], and we have confirmed their result using a radically different experimental approach. Our measurement is limited by statistics, and our dominant source of systematic error can be further suppressed to the $10^{-30}\,e\,\mathrm{cm}$ level. Here we have assumed that parity and time-reversal violating effects arise purely from d_e. An additional contribution $\sim W_S C_S$ can arise from a pseudoscalar-scalar electron-nucleon coupling C_S [20, 32, 69, 113].

Since the completion of this first generation eEDM measurement, we have constructed a second generation ion trap that will confine ten times more ions over a one hundred times larger volume, and will provide a larger, more uniform rotating electric bias field. We estimate that these and other improvements should provide an order of magnitude higher eEDM sensitivity. In the further future, we plan to pursue a third generation eEDM measurement using $^{232}\mathrm{Th}^{19}\mathrm{F}^{+}$, in which the $^3\Delta_1$ ground electronic state with $\mathcal{E}_{\mathrm{eff}} \approx 36\,\mathrm{GV/cm}$ may allow a coherence time up to tens of seconds [32, 52, 116].

3.2 Data collection

This section is reproduced from the supplementary information of Ref. [16].

3.2.1 Switch state timing & control

As described in Section 3.1, a single eEDM measurement requires collecting one interference fringe in each of the eight unique switch states $(\tilde{B}, \tilde{D}, \tilde{R})$. As a compromise between signal to noise on a single fringe and reducing susceptibility to errors from drifting experimental conditions, we typically collect twelve points per fringe, with six points spanning one fringe period at short spin precession times $0 < t < 40$ ms and six more points spanning a second fringe period at long spin precession time, $(T - 40\ \mathrm{ms}) < t < T$, where during data collection we varied T between 200 and 700 ms. One measurement of the asymmetry $\mathcal{A}(t)$ requires two experimental trials, and we typically average eight measurements comprising sixteen trials at each value of t. As shown in Fig. 3.1, a single experimental trial is accompanied by approximately 300 ms of "dead time" spent on state

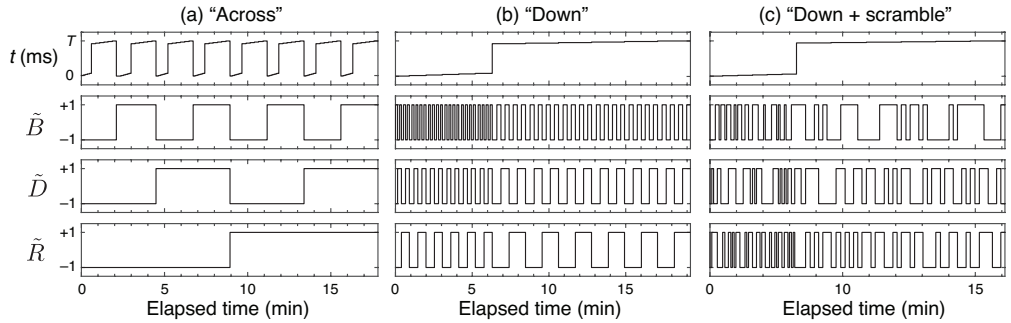

Figure 3.5: Relative timing of experimental configurations during the collection of one data block. (a) When taking data "across," we collect in each switch state an entire interference fringe as a function of t. (b) In the "down" configuration, we change the spin precession time t on a slower timescale than B, D, and R. (c) In the "down + scramble" configuration, we also re-randomize the order of switch states $(\tilde{B}, \tilde{D}, \tilde{R})$ at each value of t.

preparation, state readout, auxiliary measurements, and saving data. Thus, a single block requires a minimum of approximately 16 minutes to complete.

The timescale of data collection and the order of switch states and interrogation times can affect our statistical sensitivity, susceptibility to parameter drift, and sources of systematic error, depending primarily on the Fourier spectrum of $\mathcal{B}$ field drifts. We used three different ordering schemes, shown in Fig. 3.5, to investigate and mitigate these errors. The first, "across," makes up the smallest fraction of our eEDM dataset. We expect the "down" timing scheme to be less susceptible to drifts in experimental parameters on the few-minute timescale, for example due to temperature fluctuations or the accumulation of patch potentials on ion trap surfaces. The "down + scramble" timing scheme, in which the order of switch states is randomized in each block, should be still less susceptible to errors associated with both parameter drifts and systematic errors associated with the order of switch states.

As discussed in Section 3.1, the B, D, and R switches represent the sign of the axial magnetic gradient $\mathcal{B}'_{\mathrm{axgrad}}$ generating the rotating magnetic bias field, the populated Stark doublet, and the sense of electric bias field rotation, respectively. A National Instruments PCI-6733 digital-to-analog converter (DAC) supplies a control voltage to a bipolar current supply that powers the pair of magnet coils generating $\mathcal{B}'_{\mathrm{axgrad}}$, thus setting the value of $\tilde{B}$. The doublet switch $\tilde{D}$ is set

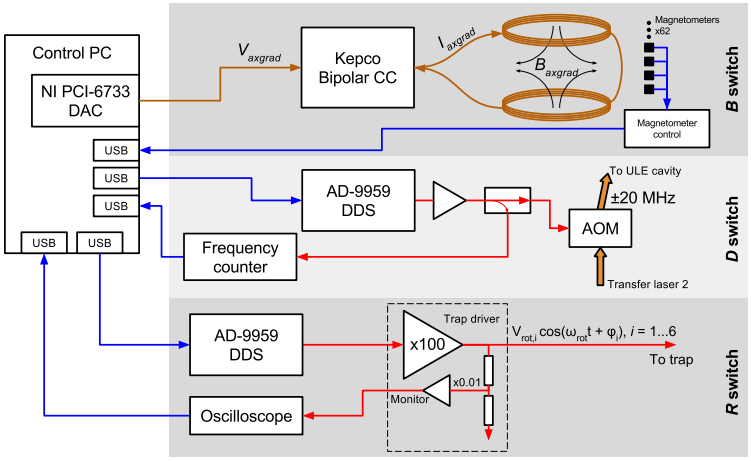

Figure 3.6: Schematic layout of control system for experimental switches. Blue traces indicate digital signals, gold traces indicated DC analog signals, and red traces indicate RF analog signals.

by adjusting the frequency output of an Analog Devices AD9959 direct digital synthesis (DDS) ASIC between two values separated by ~ 20 MHz. The amplified output drives an acousto-optic modulator that controls the frequency of the second of our Raman transfer lasers via a frequency offset lock to a stable optical cavity, thus tuning the laser to populate either the upper or lower Stark doublet. Finally, the value of $\tilde{R}$ is set by adjusting the relative phase of six DDS-generated sinusoidal signals that are amplified to produce the rotating electric bias field. These control systems are shown schematically in Fig. 3.6. None of our switches generate or require large currents or voltages, and each can be changed on a timescale that is short compared to collecting one 16-shot data point. Thus we are not restricted in their order due to dead-time considerations, and can randomize our switches without significant change in our duty cycle.

3.3 Data processing

This section is reproduced from the supplementary information of Ref. [16].

We use MATLAB to perform data analysis, which consists of counting Hf^+ ions at each time point in the fringe, calculating and fitting the asymmetry, forming data channels, blinding the eEDM channel, applying cuts, and searching for signs of systematic errors in the resulting data channels.

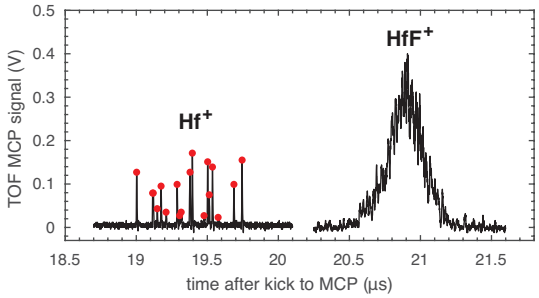

Figure 3.7: Typical raw data trace from the time-of-flight microchannel plate detector, showing time-resolved Hf^+ and HfF^+ signals. Red markers indicate counted Hf^+ ions contributing to the asymmetry signal.

A typical signal from our time-of-flight (TOF) microchannel plate (MCP) ion detector is shown in Fig. 3.7. The "signal" Hf^+ ions resulting from state-selective photodissociation and the "spectator" HfF^+ ions are temporally separated, and for numbers of Hf^+ ions below ~ 30, individual Hf^+ ion peaks are also well-resolved. We separately amplify the Hf^+ and HfF^+ signals to reduce noise on the Hf^+ signal while avoiding saturation of our transimpedance amplifier by the HfF^+ signal. We use a peak-finding algorithm to locate Hf^+ peaks of a specified prominence above the background value; typically 4 times the rms voltage of an empty trace.

We compute the asymmetry $\mathcal{A}(t)$ from the number of counted Hf^+ ions in runs of the experiment with opposite depletion phases. We fit the functional form of Eq. 3.1 to the measured asymmetry using MATLAB's Levenberg-Marquardt nonlinear least squares regression algorithm. Because measurements of the asymmetry do not follow a normal distribution (see e.g. Ref. [66]), we perform an unweighted regression, rather than binning measurements of $\mathcal{A}(t)$ for a given t and performing a weighted regression. Fitting simulated data with our analysis routine does not show any evidence of systematic shifts due to the non-gaussian distribution of $\mathcal{A}(t)$.

As discussed in Section 3.1 in the paragraph preceding Eq. 3.2, we form linear combinations of frequency measurements $f^{\tilde{B}\tilde{D}\tilde{R}} \equiv f(\tilde{B}, \tilde{D}, \tilde{R})$ to obtain frequency channels according to the

transformation

$$\begin{pmatrix} f^{0} \\ f^{B} \\ f^{D} \\ f^{BD} \\ f^{R} \\ f^{BR} \\ f^{DR} \\ f^{BDR} \end{pmatrix} = \frac{1}{8} \begin{pmatrix} + & + & + & + & + & + & + & + \\ + & - & + & - & + & - & + & - \\ + & + & - & - & + & + & - & - \\ + & - & - & + & + & - & - & + \\ + & + & + & + & - & - & - & - \\ + & - & + & - & - & + & - & + \\ + & + & - & - & - & - & + & + \\ + & - & - & + & - & + & + & - \end{pmatrix} \begin{pmatrix} f^{+++} \\ f^{-++} \\ f^{+-+} \\ f^{--+} \\ f^{++-} \\ f^{-+-} \\ f^{+--} \\ f^{---} \end{pmatrix}, \tag{3.6}$$

where $\pm$ signs represent ± 1. The standard error δf is equal for all frequency channels within one block, and is given by

$$\delta f = \frac{1}{8} \sqrt{\sum_{\tilde{B},\tilde{D},\tilde{R}=\pm} (\delta f^{\tilde{B}\tilde{D}\tilde{R}})^2}, \tag{3.7}$$

where $\delta f^{\tilde{B}\tilde{D}\tilde{R}}$ are the standard error estimates obtained from nonlinear least squares regression. We follow the same prescription to obtain the data channels for contrast, phase, decoherence rate, and offset parameters. Within the same MATLAB script that computes this linear transformation of measurements from the "state basis" to the "parity basis," we apply the blinding value to the f^{BD} channel. The pseudo-random blind value, which was previously generated and saved to a binary file, is read and added to the f^{BD} channel within a single line of code. Following systematics corrections (discussed in Section 3.5), we obtain the eEDM result by computing the weighted mean value of f^{BD} across all blocks (indexed by n),

$$\langle f^{BD} \rangle = \frac{\sum_n W_n f_n^{BD}}{\sum_n W_n}, \qquad \langle \delta f^{BD} \rangle = \frac{1}{\sqrt{\sum_n W_n}} \tag{3.8}$$

where we use weights $W_n = (\delta f_n)^{-2}$. To correct for the over-scatter of our data, we scale our final value of $\langle \delta f^{BD} \rangle$ by $\sqrt{\chi_r^2}$, where χ_r^2 is the reduced chi squared statistic of the distribution of normalized and centered eEDM measurements $(f^{BD} - \langle f^{BD} \rangle)/\delta f$. Typical values of data channels and other measured parameters are given in Table 3.3.

Table 3.3: Values of selected measured values from the portion of our eEDM dataset collected in 2017. For this data, $\mathcal{E}_{\mathrm{rot}} = 24$ V/cm and $f_{\mathrm{rot}} = 150$ kHz. For the values f^B, $\mathcal{C}^0$, and γ^0 that are subject to drift and therefore not normally distributed, we quote a range of observed values. For various values with either nonzero measured values, drift, or excess scatter, contributing factors are given.

Parameter	Mean or Range	Contributing factors
f^0	22.9985(13) Hz	Choice of $\mathcal{B}'_{\mathrm{axgrad}}$, $\mathcal{E}_{\mathrm{rot}}$, f_{rot}
f^B	−0.3 - 0.3 Hz	Drifting ambient $\mathcal{B}'^{\mathrm{nr}}_{\mathrm{axgrad}}$
f^D	−32.0(1.0) mHz	Choice of $\mathcal{B}'_{\mathrm{axgrad}}$, $\mathcal{E}_{\mathrm{rot}}$, f_{rot}
f^{BD}	−0.1(1.0) mHz	
f^R	3.1(1.1) mHz	
f^{BR}	−21.8(1.3) mHz	$\mathcal{E}_{\mathrm{rot}}$ inhomogeneity + ion position drift
f^{DR}	−0.8(1.0) mHz	
f^{BDR}	0.1(1.1) mHz	
$\mathcal{C}^0$	0.55 - 0.75	Photodissociation background
$\mathcal{C}^{BD}$	0.0065(69)	
γ^0	0.3 - 1.7 s^{-1}	Ion number, excess slosh and micromotion
γ^{BD}	0.0127(59) s^{-1}	
ϕ^0	0.2543(16) rad	Detuning of $\pi/2$ pulse due to nonzero $\mathcal{B}_{\mathrm{rot}}$
ϕ^{BD}	0.0021(15) rad	
$\mathcal{O}^0$	0.00416(50)	Detuning of $\pi/2$ pulse due to nonzero $\mathcal{B}_{\mathrm{rot}}$
$\mathcal{O}^{BD}$	0.00016(47)	

Over-dispersion appears in our frequency channels in a way that is consistent with it arising from a drifting ambient magnetic field gradient $\mathcal{B}'^{\mathrm{nr}}_{\mathrm{axgrad}}$. A drifting value of $\mathcal{B}'^{\mathrm{nr}}_{\mathrm{axgrad}}$ nominally only affects the f^B channel, however changes in $\mathcal{B}'^{\mathrm{nr}}_{\mathrm{axgrad}}$ on a timescale comparable to the collection of one data block causes over-scatter in all other data channels, including f^{BD}. In future measurements, we plan to mitigate this effect by removing sources of ambient $\mathcal{B}'^{\mathrm{nr}}_{\mathrm{axgrad}}$ and by collecting data blocks on a shorter timescale.

We chose our data cuts based on signal-to-noise considerations and the values of eEDM-insensitive data channels. The first data cut is performed at the ion counting level by a choice of a time-of-flight window and minimum pulse height for Hf^+ ion counting. Further cuts were based on initial and final contrast and on the value of the f^B data channel. We investigated the values of frequency channels as a function of the cut parameters, and found no worrisome dependencies.

3.4 Modeling frequency channels

This section is reproduced from the supplementary information of Ref. [16].

The high statistical sensitivity and the systematic error rejection features of our experimental approach come with an associated cost in the form of an increased level of complexity in modeling frequency measurements. The Ω-doublet structure of the $^3\Delta_1$ state, the nuclear hyperfine structure of HfF^+, our rotating quantization axis, and the motion of ions in inhomogeneous and time-dependent electric and magnetic fields all contribute to this complexity. As a result, we used a variety of numerical and perturbative techniques to analyze sources of non-ideal frequency shifts in our system. In this section we discuss our methods in general terms, and provide a list of observed frequency shifts. In Section 3.5 we describe in more detail effects that systematically affect the eEDM measurement channel f^{BD}.

3.4.1 Ion motion

The spin precession frequency of HfF^+ in our experiment is set by the electric and magnetic fields experienced by each ion. Since the electric and magnetic fields in the RF trap are inhomo-

geneous and (for the electric fields) time-varying, and the ions' trajectories are modified by the electric field (neglecting the Lorentz force), we must know the trajectories of the ions in order to determine their spin precession frequencies.

For our perturbative analysis of frequency channels, we use the standard approximation of harmonic motion with superimposed RF micromotion [9], and additionally superimpose rotating micromotion due to $\mathcal{E}_{\rm rot}$. In this case, the total electric field is

$$\boldsymbol{\mathcal{E}}(\boldsymbol{R},t) = \frac{V_{\rm rf}}{R_0^2}\cos(\omega_{\rm rf}t)(\boldsymbol{X}-\boldsymbol{Y}) + \frac{V_{\rm dc}}{Z_0^2}(\boldsymbol{X}+\boldsymbol{Y}-2\boldsymbol{Z}) + \mathcal{E}_{\rm rot}\left[\hat{X}\cos(\omega_{\rm rot}t) - \tilde{R}\hat{Y}\sin(\omega_{\rm rot}t)\right], \quad (3.9)$$

where $\omega_{\rm rot} \equiv 2\pi f_{\rm rot}$, $\omega_{\rm rf} \equiv 2\pi f_{\rm rf} \approx 50$ kHz, $\tilde{R}$ is the rotation switch sign, and R_0 and Z_0 are the effective radius and height of the RF trap. However, this approximation is not able to account for effects we observe due to electric field inhomogeneities of multipole order $l > 2$. We account for these higher order effects numerically by performing a multipole fit up to $l = 9$ of the electric field due to unit potential on each of the eight trap electrodes to obtain multipole coefficients c_{lm}^k (where $k = 1 \ldots 8$), which allows us to represent the total electric field in the ion trap as a function of the electrode voltages:

$$\boldsymbol{\mathcal{E}}(\boldsymbol{R},t) = \sum_{k=1}^{8} V_k(t) \sum_{lm} c_{lm}^k \left[-\boldsymbol{\nabla}\left(R^l\, Y_{lm}(\Theta,\Phi)\right)\right], \quad (3.10)$$

where (R,Θ,Φ) are spherical polar coordinates in the laboratory frame, and Y_{lm} are real spherical harmonics. We then numerically integrate the equations of motion for an ion to obtain $\boldsymbol{R}_{\rm ion}(t)$, and substitute back into Eq. (3.10) and a corresponding expression for $\boldsymbol{\mathcal{B}}(\boldsymbol{R})$ to obtain $\boldsymbol{\mathcal{E}}_{\rm ion}(t)$ and $\boldsymbol{\mathcal{B}}_{\rm ion}(t)$, the electric and magnetic fields at the location of the ion. Finally, we transform these fields into a rotating frame whose coordinate axes $\hat{x}$, $\hat{y}$, $\hat{z}$ are related to the laboratory frame axes $\hat{X}$, $\hat{Y}$, $\hat{Z}$ by

$$\hat{x} = -\hat{Z}, \qquad \hat{y} = \hat{Y}\cos(\omega_{\rm rot}t) + \tilde{R}\hat{X}\sin(\omega_{\rm rot}t), \qquad \hat{z} = \hat{X}\cos(\omega_{\rm rot}t) - \tilde{R}\hat{Y}\sin(\omega_{\rm rot}t). \quad (3.11)$$

In this frame, $\mathcal{E}_{\rm rot}$ nominally points along the $+\hat{z}$ axis. For this analysis, we neglect the effect of ion-ion interactions.

3.4.2 Effective Hamiltonian

Our modeling of frequency channels relies on an effective Hamiltonian description of HfF^+ molecules. We do not use optical pumping into dark states to perform $\pi/2$ pulses, so high-energy photons are not present, and coupling to other electronic states is absent throughout our spin precession sequence. As a result, we can build an effective Hamiltonian that includes only $^3\Delta_1$ sublevels. The $^3\Delta_1$ state is well-described by Hund's case (a) basis states with coupled nuclear spin,

$$|\Lambda = \pm 2, S = 1, \Sigma = \mp 1, J, \Omega = \pm 1, I = 1/2, F, M_F\rangle\,,$$

where $\Lambda = \mathbf{L}\cdot\mathbf{n}$ is the projection of the electronic orbital angular momentum $\mathbf{L}$ on the internuclear axis $\mathbf{n}$, $S = |\mathbf{S}|$ is the total electronic spin angular momentum, $\Sigma = \mathbf{S}\cdot\mathbf{n}$ is the electron spin projection on the internuclear axis, $J = |\mathbf{J}| = |\mathbf{L}+\mathbf{S}+\mathbf{R}|$ is the electronic plus rotational angular momentum, $\Omega = \mathbf{J}\cdot\mathbf{n}$ is the projection of the electronic angular momentum onto the internuclear axis, $I = |\mathbf{I}|$ is the ^{19}F nuclear spin, $F = |\mathbf{F}| = |\mathbf{J}+\mathbf{I}|$ is the total angular momentum of the molecule, and $M_F = \mathbf{F}\cdot\hat{z}$ is the projection of $\mathbf{F}$ on the rotating quantization axis [15]. We take the internuclear axis $\mathbf{n}$ to be directed from the ^{19}F nucleus to the ^{180}Hf nucleus. We model our spin precession experiment using an effective Hamiltonian that includes (in decreasing order of size) molecular rotation, the nuclear spin hyperfine interaction, the Stark effect, Ω-doubling, a rotating quantization axis, the electronic and nuclear Zeeman effects, and an eEDM:

$$H(\boldsymbol{\mathcal{E}},\boldsymbol{\mathcal{B}},\boldsymbol{\omega}_{\mathrm{rot}}) = H_{\mathrm{tum}} + H_{\mathrm{hf}} + H_{\mathrm{S}}(\boldsymbol{\mathcal{E}}) + H_{\Omega} + H_{\mathrm{rot}}(\boldsymbol{\omega}_{\mathrm{rot}}) + H_{\mathrm{Z},e}(\boldsymbol{\mathcal{B}}) + H_{\mathrm{Z},N}(\boldsymbol{\mathcal{B}}) + H_{\mathrm{edm}}. \quad (3.12)$$

We use the effective operators [2]

$$H_{\mathrm{tum}} = B_e\mathbf{J}^2, \qquad H_{\mathrm{hf}} = A_{\parallel}(\mathbf{I}\cdot\mathbf{n})(\mathbf{J}\cdot\mathbf{n}), \qquad H_{\mathrm{S}} = -d_{\mathrm{mf}}\mathbf{n}\cdot\boldsymbol{\mathcal{E}}, \qquad H_{\Omega} = \hbar\omega_{ef}\boldsymbol{\Omega}_x/2,$$
$$H_{\mathrm{rot}} = -\hbar\boldsymbol{\omega}_{\mathrm{rot}}\cdot\mathbf{F}, \quad H_{\mathrm{Z},e} = -G_{\parallel}\mu_B(\mathbf{J}\cdot\mathbf{n})(\boldsymbol{\mathcal{B}}\cdot\mathbf{n}), \quad H_{\mathrm{Z},N} = -g_N\mu_N\mathbf{I}\cdot\boldsymbol{\mathcal{B}}, \quad H_{\mathrm{edm}} = -d_e|\mathcal{E}_{\mathrm{eff}}|\Omega,$$

with constants listed in Table 3.4. The effective operator $\boldsymbol{\Omega}_x$ has matrix elements $\delta_{\eta',\eta}\delta_{\Omega',-\Omega}$ (where η represents all other quantum numbers).

[2] Matrix elements for each of these operators are discussed in Chapter 2.

Constant	Value	Description	Reference
B_e/h	8.983(1) GHz	Rotational constant	[29]
$A_\parallel/h$	−62.0(2) MHz	Hyperfine constant	This work
d_{mf}/h	1.79(1) MHz/(V/cm)	Molecule-frame electric dipole moment	This work
$\omega_{ef}/(2\pi)$	0.74(4) MHz	Ω-doubling constant	[29]
$\omega_{\mathrm{rot}}/(2\pi)$	250 kHz typ.	Rotation rate of $\mathcal{E}_{\mathrm{rot}}$	This work
g_F	−0.0031(1)	$F = 3/2$ state g-factor	[82][3]
g_N	5.25774(2)	Nuclear magnetic g-factor of ^{19}F	[119]
$\lvert\mathcal{E}_{\mathrm{eff}}\rvert/h$	5.63×10^{24} Hz/(e cm)	Effective electric field	[44]

Table 3.4: Constants used in the effective Hamiltonian of Eq. (3.12), for the calculation of frequency channels and systematic corrections. The total magnetic g-factor of $J = 1, F = 3/2$ states $g_F \equiv (G_\parallel + g_N\mu_N/\mu_B)/3$ results from the combination of nuclear and electronic Zeeman effects.

In our perturbative model of frequency channels, we treat the pairs of levels in either Stark doublet as a two-level system, and construct a 2×2 effective Hamiltonian for either doublet. We take the molecular rotation, Stark and Hyperfine Hamiltonian terms as an unperturbed Hamiltonian, then include the Zeeman, frame-rotation, Ω-doubling, and eEDM terms as perturbations. While the Zeeman effect of $\mathcal{B}_{\mathrm{rot}}$ is the dominant diagonal contribution to the two-level effective Hamiltonian, perpendicular electric and magnetic fields, rotation, Ω-doubling, and Stark mixing of rotational levels all contribute frequency shifts that are significant at the level of an eEDM search. In the basis of $F = 3/2$, $M_F = \pm 3/2$ states, the two-level effective Hamiltonian has the form

$$H_{\mathrm{eff}}^{u/l} = \frac{1}{2}\begin{pmatrix} -3(g_F \pm \delta g_F)\mu_B\mathcal{B}_{\mathrm{rot}} \pm 2d_e|\mathcal{E}_{\mathrm{eff}}| - 3\alpha h f_{\mathrm{rot}} + \ldots & h(\Delta \pm \Delta^D) \\ h(\Delta \pm \Delta^D) & 3(g_F \pm \delta g_F)\mu_B\mathcal{B}_{\mathrm{rot}} \mp 2d_e|\mathcal{E}_{\mathrm{eff}}| + 3\alpha h f_{\mathrm{rot}} + \ldots \end{pmatrix}, \tag{3.13}$$

where the u/l superscript and upper or lower signs correspond to the upper or lower Stark doublet, $\alpha \equiv \mathcal{E}_Z/\mathcal{E}_{\mathrm{rot}}$ is the tilt of the electric field away from the XY plane, and Δ is a rotation induced coupling with a Stark doublet-odd contribution Δ^D. Here the magnetic g-factor g_F results from the combined nuclear and electronic magnetic moments, which are coupled by the nuclear hyperfine Hamiltonian H_{hf}. Notable features of this two-level system are the difference in magnetic g-factor between Stark doublets δg_F, the rotation-induced coupling Δ, and the geometric frequency shift $3\alpha f_{\mathrm{rot}}$. The magnetic g-factor difference arises from Stark mixing of $J = 1$ with $J = 2$ and from

rotation-induced mixing of adjacent magnetic sublevels at second order in perturbation theory, and has the approximate form

$$\frac{\delta g_F}{g_F} \approx -\frac{3d_{\rm mf}\mathcal{E}_{\rm rot}}{20B_e}\left(1-\frac{g_N\mu_N}{3g_F\mu_B}\right)+\frac{3\hbar^2\omega_{\rm rot}^2}{d_{\rm mf}\mathcal{E}_{\rm rot}A_\parallel}\left(1-\frac{2g_N\mu_N}{3g_F\mu_B}\right)\approx -1\times10^{-3}. \tag{3.14}$$

The coupling Δ first arises at fourth order from the combined perturbations of $H_{\rm rot}$ and H_Ω, and breaks the degeneracy of the $|M_F|=3/2$ states in either Stark doublet at $\mathcal{B}_{\rm rot}=0$ [78, 88]. The fourth-order perturbation theory expression for Δ and its Stark doublet-odd component Δ^D are given by

$$h\Delta=\frac{3\hbar\omega_{ef}}{2}\left(\frac{\hbar\omega_{\rm rot}}{d_{\rm mf}\mathcal{E}_{\rm rot}}\right)^3\left(\frac{18A_\parallel^2-19d_{\rm mf}^2\mathcal{E}_{\rm rot}^2}{A_\parallel^2-d_{\rm mf}^2\mathcal{E}_{\rm rot}^2}\right),\qquad h\Delta^D=\frac{3\hbar\omega_{ef}}{2}\left(\frac{\hbar^3\omega_{\rm rot}^3}{d_{\rm mf}^2\mathcal{E}_{\rm rot}^2A_\parallel}\right)\left(\frac{9A_\parallel^2-8d_{\rm mf}^2\mathcal{E}_{\rm rot}^2}{A_\parallel^2-d_{\rm mf}^2\mathcal{E}_{\rm rot}^2}\right). \tag{3.15}$$

These expressions are valid as long as $d_{\rm mf}\mathcal{E}_{\rm rot}\gg\hbar\omega_{ef}$ and $d_{\rm mf}\mathcal{E}_{\rm rot}\gg\hbar\omega_{\rm rot}$. The strong scaling of Δ with $\mathcal{E}_{\rm rot}$ allows us to perform off-resonant $\pi/2$ pulses by modulating the magnitude of $\mathcal{E}_{\rm rot}$, as discussed in Section 3.1. Finally, the geometric phase shift arises from the fact that if $\mathcal{E}_Z$ is nonzero, the solid angle swept out by the rotating electric field differs from its nominal value of 2π. This effect is discussed extensively in Ref. [87]. Higher order contributions to $H_{\rm eff}^{u/l}$, denoted by ellipses in Eq. (3.13), are due to higher-order combinations of perturbing Hamiltonian components, and primarily result in small corrections to the terms already discussed.

For our numerical studies, we use $\boldsymbol{\mathcal{E}}_{\rm ion}(t)$ and $\boldsymbol{\mathcal{B}}_{\rm ion}(t)$ resulting from the simulated ion motion (Section 3.4.1) to construct $H_{\rm ion}(t)=H(\boldsymbol{\mathcal{E}}_{\rm ion}(t),\boldsymbol{\mathcal{B}}_{\rm ion}(t),\boldsymbol{\omega}_{\rm rot})$, and numerically integrate the Schrödinger equation for a single ion by exponentiating $H_{\rm ion}(t)$ at each value of t to obtain the time-evolution operator $U_{\rm ion}(t)$, which we apply to an initial state vector $|\psi_0\rangle$. For various sets of simulations we have either taken $|\psi_0\rangle$ to be one of states $|a\rangle$, $|b\rangle$, $|c\rangle$, or $|d\rangle$ [Fig. 3.2] and included realistic $\pi/2$ pulses by modulating the simulated value of $\mathcal{E}_{\rm rot}$, or we have assumed an ideal $\pi/2$ pulse by initializing $|\psi_0\rangle$ as an equal superposition of states $|a\rangle$ and $|b\rangle$ or $|c\rangle$ and $|d\rangle$. Finally, we construct the (simulated) asymmetry $\mathcal{A}(t)$ by projecting $|\psi(t)\rangle$ onto the upper or lower doublet states, and fit $\mathcal{A}(t)$ using the functional form of Eq. 3.1 in Section 3.1.

3.4.3 Mixing of frequency channels

The non-negligible size of Δ and Δ^D throughout our spin precession experiment produces a unique structure of frequency channels that affects our systematics analysis, and warrants describing in more detail. To do so, we parametrize the two-state effective Hamiltonian in terms of "diagonal" and "off-diagonal" parity components f_0^s and Δ^s,

$$H_{\text{eff}}(\tilde{S}) = \frac{h}{2}\begin{pmatrix} f_0^0 + \tilde{B}f_0^B + \tilde{D}f_0^D + \dots & \Delta + \tilde{B}\Delta^B + \tilde{D}\Delta^D \dots \\ \Delta + \tilde{B}\Delta^B + \tilde{D}\Delta^D + \dots & f_0^0 + \tilde{B}f_0^B + \tilde{D}f_0^D + \dots \end{pmatrix}. \tag{3.16}$$

Expanding the frequency channels obtained from this Hamiltonian about f_0^0, we obtain

$$f^0 = |f_0^0|\left(1 + \frac{\Delta^2 + (\Delta^B)^2 + (\Delta^D)^2 + \dots}{2|f_0^0|^2}\right) - f_0^B\frac{\Delta\Delta^B + \Delta^D\Delta^{BD} + \dots}{|f_0^0|^2} - f_0^D\frac{\Delta\Delta^D + \Delta^B\Delta^{BD} + \dots}{|f_0^0|^2} + \dots \tag{3.17}$$

$$f^B = f_0^B\left(1 - \frac{\Delta^2 + (\Delta^B)^2 + (\Delta^D)^2 + \dots}{2|f_0^0|^2}\right) + \frac{\Delta\Delta^B + \Delta^D\Delta^{BD} + \dots}{|f_0^0|} - f_0^D\frac{\Delta\Delta^{BD} + \Delta^B\Delta^D + \dots}{|f_0^0|^2} + \dots \tag{3.18}$$

$$f^D = f_0^D\left(1 - \frac{\Delta^2 + (\Delta^B)^2 + (\Delta^D)^2 + \dots}{2|f_0^0|^2}\right) + \frac{\Delta\Delta^D + \Delta^B\Delta^{BD} + \dots}{|f_0^0|} - f_0^B\frac{\Delta\Delta^{BD} + \Delta^B\Delta^D + \dots}{|f_0^0|^2} + \dots \tag{3.19}$$

$$f^{BD} = f_0^{BD}\left(1 - \frac{\Delta^2 + (\Delta^B)^2 + (\Delta^D)^2 + \dots}{2|f_0^0|^2}\right) + \frac{\Delta\Delta^{BD} + \Delta^B\Delta^D + \dots}{|f_0^0|} - f_0^B\frac{\Delta\Delta^D + \Delta^B\Delta^{BD} + \dots}{|f_0^0|^2} + \dots \tag{3.20}$$

with similar results for f^R, f^{BR}, f^{DR} and f^{BDR}. Thus the nonzero value of Δ, as well as any component of it that is odd under B, D, or R, causes mixing of "diagonal" parity components between measured frequency channels. This can cause systematic effects, the largest of which are described in Section 3.5. However, all B-odd components of Δ (Δ^B, Δ^{BD} etc.) are negligible, greatly reducing the number of terms that must be considered. The regular form of these frequency channels also allows a straightforward correction that removes mixing terms up to third order in perturbation theory of H_{eff},

$$f_0^{BD} = f^{BD} + f^B\left(\frac{f^D - f_0^D}{f^0}\right) + f^{BR}\left(\frac{f^{DR} - f_0^{DR}}{f^0}\right) + f^{BDR}\left(\frac{f^R - f_0^R}{f^0}\right) + \text{h. o.} \tag{3.21}$$

The frequency channels f^0, f^B, f^D, f^{BR}, f^{DR}, f^{BDR}, and f^R are measured simultaneously with f^{BD}, while the "diagonal" components f_0^D, f_0^{DR} and f_0^R must be estimated from theoretical models and auxiliary measurements. Note that in general the corrected value of f_0^{BD} includes terms in addition to $2d_e|\mathcal{E}_{\text{eff}}|$. The corrections in Eq. (3.21) account only for those systematics arising from the nonzero value of Δ, and does not include "diagonal" systematics such as those arising from a difference in magnetic g-factor between Stark doublets and a non-reversing magnetic bias field. Under typical experimental conditions, the above corrections cancel mixing to the level of ~ 10 μHz ($\sim 10^{-30}$ $e\,$cm). Correction terms are discussed in Section 3.5 and are included in our uncertainty budget.

3.4.4 Non-ideal frequency shifts

A detailed description of every non-ideal frequency shift observed during our model-building phase is beyond the scope of this supplement, and will be given in a future publication. Here we list the parameters and experimental imperfections we explored in Table 3.5, and list observed effects and their observation channels in Table 3.6. More detailed descriptions of effects included in our uncertainty budget are given in Section 3.5.

3.5 Systematics

This section is reproduced from the supplementary information of Ref. [16].

In perturbation theory of our effective Hamiltonian [Eq. (3.12)], an eEDM signal appears as the lowest-order contribution to the f^{BD} frequency channel, and its value is independent of all experimental parameters. Any other contributions to this channel constitute systematic errors and must be corrected if they are large enough to cause a significant shift. Systematic shifts can generally be grouped into one of two categories: real frequency shifts arising from higher-order terms in the effective Hamiltonian (introduced in Section 3.4.3), and apparent shifts arising from measurement errors. We have identified several possible sources of both types, and observed a frequency shift in f^{BD} due to one effect.

Description	Parameters	Study method
Rotating $\mathcal{E}$ field	$\mathcal{E}_{\rm rot}$, $\omega_{\rm rot}$	E,M
Axial magnetic bias gradient	$\mathcal{B}'_{\rm axgrad}$, $(\mathcal{B}_{2,m\neq 0}$, $\mathcal{B}_X$, $\mathcal{B}_Y$, $\mathcal{B}_Z)^4$	E,M
Non-reversing uniform $\mathcal{B}$ fields	$\mathcal{B}^{\rm nr}_X$, $\mathcal{B}^{\rm nr}_Y$, $\mathcal{B}^{\rm nr}_Z$	E,M
Non-reversing magnetic gradients	$\mathcal{B}^{\rm nr}_{2,m\neq 0}$	E,M
Ion cloud position	X_0, Y_0, Z_0	E,M
Ion cloud secular motion amplitude	X_1, Y_1, Z_1	E,M
Trap RF amplitude	$V_{\rm rf}$	E,M
Trap RF frequency	$\omega_{\rm rf}$	M
Number of trapped HfF^+ ions	N	E
$V_{\rm rot}$ harmonic distortion	V_{nf}, ϕ_{nf}, $n = 2 \ldots 6$	E,M
Currents in electrodes		E,M
Depletion laser polarization		E
Thermal drifts in trap amplifiers		E,M
Accumulating patch potentials		E,M

Table 3.5: Experimental parameters and imperfections explored as possible sources of systematic error. The letters E and M indicate that an effect was explored experimentally or through numerical and perturbative modeling, respectively.

Description	Channel	Scaling
RF micromotion in $\mathcal{B}'_{\rm axgrad}$	f^0	$g_F\mu_B\mathcal{B}'_{\rm axgrad}(X_0^2+Y_0^2)q/R_0$
Non-reversing $\mathcal{B}_{\rm rot}$	f^B	$g_F\mu_B\mathcal{B}^{\rm nr}_{\rm rot}$
	f^{BD}	$\delta g_{\rm eff}\mu_B\mathcal{B}^{\rm nr}_{\rm rot}$
$\mathcal{B}^{\rm nr}_{\rm rot}$ due to $\mathcal{E}_{\rm rot}$ 2nd harmonic, $\mathcal{B}^{\rm nr}_X$, $\mathcal{B}^{\rm nr}_Y$	f^B	$g_F\mu_B V_{2f}(\mathcal{B}^{\rm nr}_X X_0+\mathcal{B}^{\rm nr}_Y Y_0)/\mathcal{E}_{\rm rot}R_0^2$
	f^{BR}	$g_F\mu_B V_{2f}(\mathcal{B}^{\rm nr}_X Y_0-\mathcal{B}^{\rm nr}_Y X_0)/\mathcal{E}_{\rm rot}R_0^2$
Stark-induced D-odd g-factor	f^D	$g_F\mu_B\mathcal{B}_{\rm rot}d_{\rm mf}\mathcal{E}_{\rm rot}/B_e$
Rotation-induced D-odd g-factor	f^D	$g_F\mu_B\mathcal{B}_{\rm rot}(\hbar\omega_{\rm rot})^2/d_{\rm mf}\mathcal{E}_{\rm rot}A_\parallel$
Δ-induced effective D-odd g-factor	f^D	$\Delta^D\Delta/f^0$
Non-reversing axial $\mathcal{B}$-field	f^R	$(\Delta^2/f^0)(g_F\mu_B\mathcal{B}_Z/\hbar\omega_{\rm rot})$
	f^{DR}	$(\Delta^D\Delta/f^0)(g_F\mu_B\mathcal{B}_Z/\hbar\omega_{\rm rot})$
$\mathcal{E}_{\rm rot}$ inhomogeneity-induced geometric phase	f^{BR}	$f_{\rm rot}(X_0^2+Y_0^2)Z_0/R_0^3$
$\mathcal{B}_{\rm rot}$ due to electrode currents	f^{BR}	$g_F\mu_B\mu_0\omega_{\rm rot}C_{\rm elec}\mathcal{E}_{\rm rot}$
Axial secular motion frequency modulation	f^{BR}	$\beta Z_0 e\mathcal{E}_{\rm rot}/(m\omega_{\rm rot}\omega_Z T)$

Table 3.6: Observed frequency shifts and their scaling with selected experimental parameters (numerical factors are omitted). Here q is a dimensionless RF trap parameter [9], R_0 is the radius of the RF trap, Z_1 is the amplitude of the center-of-mass secular motion of the ion cloud along the Z axis, $C_{\rm elec}$ is the capacitance of an electrode, and $\beta \approx 1.4\times10^{-5}$ mm^{-2} is the fractional inhomogeneity of $\mathcal{E}_{\rm rot}$ along the Z axis.

We calculate systematic corrections according to a procedure similar to that of Ref. [6]. Parametrizing a systematic shift in the eEDM channel as $f^{BD}_{\mathrm{syst},i} = P_i S_i$ where P_i is a parameter and $S_i \equiv \partial f^{BD}/\partial P_i$, the corrected eEDM measurement in the n^{th} block is $f_n^{\mathrm{eEDM}} = f_n^{BD} + \sum_i f^{BD}_{\mathrm{corr},i,n} = f_n^{BD} - \sum_i P_{i,n} S_{i,n}$. We compute systematic corrections on a block-by-block basis, and we obtain the total i^{th} correction $\langle f^{BD}_{\mathrm{corr},i}\rangle$ and its uncertainty $\langle \delta f^{BD}_{\mathrm{corr},i}\rangle$ by propagating the standard errors $\delta P_{i,n}$ and $\delta S_{i,n}$ through the weighted averaging of blocks. For systematics that produced an observed shift in the eEDM channel (of which there was only one), we apply the correction and include $\langle \delta f^{BD}_{\mathrm{corr},i}\rangle$ in our uncertainty budget (Table II). For systematics that we did not observe directly in the eEDM channel, we include a systematic uncertainty $\langle \delta f^{BD}_{\mathrm{tot},i}\rangle \equiv \sqrt{\langle f^{BD}_{\mathrm{corr},i}\rangle^2 + \langle \delta f^{BD}_{\mathrm{corr},i}\rangle^2}$ in our uncertainty budget.

3.5.1 Doublet population contamination

When population is transferred from $^1\Sigma^+$ to $^3\Delta_1$, the detuning of the second transfer laser is set by an acousto-optic modulator to select either the upper or lower Stark doublet to be populated. The upper and lower Stark doublets are resolved by approximately nine times the 1σ Doppler width of each transfer resonance (Fig. 3.8), so population of the undesired Stark doublet is highly suppressed. During both population transfer and strobed depletion, however, spontaneous decay from the $^3\Pi_{0^+}$ and $^3\Sigma^-_{0^+}$ excited states to all hyperfine levels in $^3\Delta_1$, $J = 1$ can occur, albeit with a very small probability. Because our depletion and dissociation state readout processes are not Stark doublet-selective, population in the undesired Stark doublet will lead to uncharacterized beating in our interference fringes that will be misidentified as a loss of coherence and a frequency shift, as shown in Fig. 3.9. The effect of the apparent frequency shift is to suppress the measured value of f^D, leading to two sources of systematic error that we have identified.

The first systematic error arising from population in the wrong Stark doublet is that a suppressed value of f^D will suppress the correction of Eq. (3.26). Including this effect, we predict a value for f^D of

$$f^D_{\mathrm{meas}} = f^D_{\mathrm{true}} - \frac{w}{2\pi T}\sin\left(4\pi f^D_{\mathrm{true}} T\right), \tag{3.22}$$

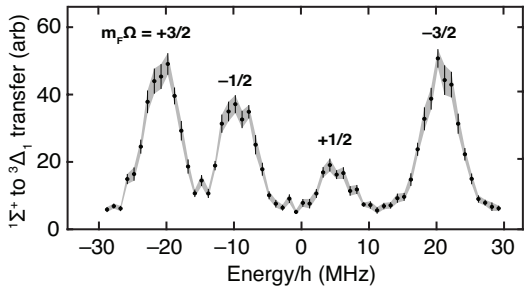

Figure 3.8: Stimulated Raman transfer from $^1\Sigma^+$, $J = 0$ to $^3\Delta_1$, $J = 1$, $F = 3/2$, showing Doppler-broadened resonances at the locations of Stark doublets.

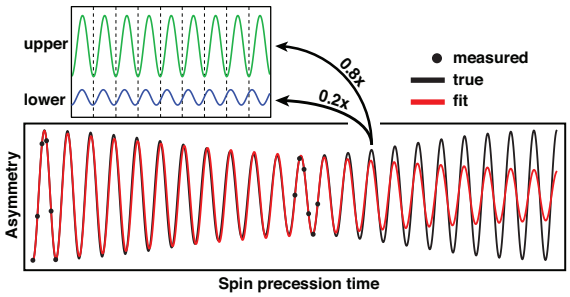

Figure 3.9: Simulated effect of doublet population contamination with a fraction $w = 0.2$ of the $^3\Delta_1$ population in the undesired Stark doublet. Green and blue traces in the inset illustrate the fractional contributions from the upper and lower doublet to the total true interference fringe (black line). Measuring the asymmetry at only short and long times (black points) leads to a misinterpretation of beating as a loss of coherence (red line), and results in an error in the fit frequency.

where T is the temporal separation between early and late time fringe measurements, and w is the fraction of the $^3\Delta_1$ state population in the lower (upper) Stark doublet when only the upper (lower) doublet should be populated. The resulting systematic error in the correction (3.26) is

$$f^{BD}_{\mathrm{syst},1} = \frac{w f^B}{2\pi f^0 T} \sin\left(4\pi f^D_{\mathrm{true}} T\right). \tag{3.23}$$

Using Eq. (3.22) and the difference between our measured and predicted values of f^D, we estimate $w = 0.02(1)$. However, w was not directly monitored during our data collection and systematic errors in the measured parameters contributing to the predicted value of f^D may dominate over any true population contamination. We estimate the total systematic error due to this effect to be $\langle \delta f^{BD}_{\mathrm{tot},1} \rangle = 8$ μHz.

While in neutral beam experiments, an uncharacterized ϕ^{BD} shift leads directly to a systematic frequency shift $\phi^{BD}/2\pi T$, our practice of measuring both early and late time phase nominally distinguishes ϕ^{BD} from f^{BD}. In the presence of population contamination, this systematic shift makes a small reappearance proportional to w. To derive the shift, we consider the sum of cosines with amplitudes $\mathcal{C}_+ = -(1-w)$ and $\mathcal{C}_- = -w$, and overall phases

$$\Phi_\pm(B,D) = (\omega^0 + B\,\omega^B \pm D\,\omega^D \pm BD\,\omega^{BD})t + (\phi^0 + B\,\phi^B \pm D\,\phi^D \pm BD\,\phi^{BD}),$$

where here we are neglecting the R switch. Assuming $w \ll 1$, the amplitude and phase of the sum are

$$\mathcal{C} \simeq \mathcal{C}_+ + w\cos\left[2(\Phi_+ - \Phi_-)\right], \qquad \Phi \simeq \Phi_+ - w\sin\left[2(\Phi_+ - \Phi_-)\right]. \tag{3.24}$$

We approximate our measured fringe frequency as $f \simeq (\Phi_T - \Phi_0)/2\pi T$, and upon transforming a block of phase measurements of the form of Eq. (3.24) to the parity basis according to Eq. (3.6), we obtain a systematic contribution to the f^{BD} channel

$$f^{BD}_{\mathrm{syst},2} \simeq \frac{w}{\pi T} \sin\left(2\phi^{BD}\right) \sin^2\left(2\pi f^D T\right). \tag{3.25}$$

We also obtain a similar term proportional to $\sin\left(2\phi^D\right)\sin^2\left(2\pi f^{BD} T\right)$, however we neglect it since it results in a multiplicative, rather than additive error on f^{BD} and because ϕ^D and f^{BD} are

uncorrelated in our eEDM dataset. Again, since w was not directly monitored during data collection, and since inconsistencies in our measured and predicted values of f^D could be due to other sources, we include a total systematic uncertainty $\langle f^{BD}_{\mathrm{tot},2}\rangle = 195$ μHz in our uncertainty budget. This contribution dominates over $f^{BD}_{\mathrm{tot},1}$, and is the largest contributor to systematic error in our experiment. Improved monitoring of w in the next generation of this experiment (via, e.g., microwave spectroscopy of the $^3\Delta_1$ $J = 1 \rightarrow J = 2$ transition), as well as operating in a regime of $\mathcal{E}_{\mathrm{rot}}$ and f_{rot} where f^D is suppressed, will reduce this systematic to the order of ~ 1 μHz.

3.5.2 Non-reversing $\mathcal{B}_{\mathrm{rot}}$ and effective differential g-factor

The simplest contributor to a non-reversing rotating magnetic bias field $\mathcal{B}^{\mathrm{nr}}_{\mathrm{rot}}$ is an imperfect reversal of the applied axial gradient $\mathcal{B}'_{\mathrm{axgrad}}$. Contributions can also arise from other sources, including for example higher order magnetic gradients or time-dependent magnetic fields. Figure 3.10 shows the only observed shift in the f^{BD} channel, caused by a non-reversing axial gradient $\mathcal{B}'^{\mathrm{nr}}_{\mathrm{axgrad}}$. Non-reversing $\mathcal{B}$ fields appear in the f^{BD} channel due to the difference in the magnetic g-factors of the upper and lower doublet states δg_F, and due to the non-negligible size of Δ and Δ^D compared to the Zeeman shift. Fortunately, an amplified shift appears in the simultaneously collected f^B channel, allowing us to apply a proportional correction. In terms of experimental parameters, the shift in the eEDM channel due to δg_F and Δ^D is

$$f^{BD}_{\mathrm{syst},3} = 3 g_F \mu_B \mathcal{B}^{\mathrm{nr}}_{\mathrm{rot}} \left(\frac{\delta g_F}{g_F} - \frac{\Delta \Delta^D}{|3 g_F \mu_B \mathcal{B}_{\mathrm{rot}}|^2} \right) + \mathrm{h.o.} \tag{3.26}$$

Under typical conditions, $f^{BD}_{\mathrm{syst},7}$ is of order $\sim 10^{-3} f^B$ and the sum of higher order terms is ~ 1 μHz. By comparison of the terms in Eq. (3.26) to the leading order expressions for frequency channels in Table I in Section 3.1, we find that we can apply a block-by-block correction (suppressing the subscript n)

$$f^{BD}_{\mathrm{corr},3} = f^B \frac{\delta g_{\mathrm{eff}}}{g_F} = f^B \left(\frac{f^D}{f^0} - 2 \frac{\delta g_F}{g_F} \right). \tag{3.27}$$

The typical value of f^B for a given block was $\lesssim 100$ mHz, and due to our applied feedback to reduce the value of $|f^B|$, its average value over many consecutive blocks was much smaller. The small value

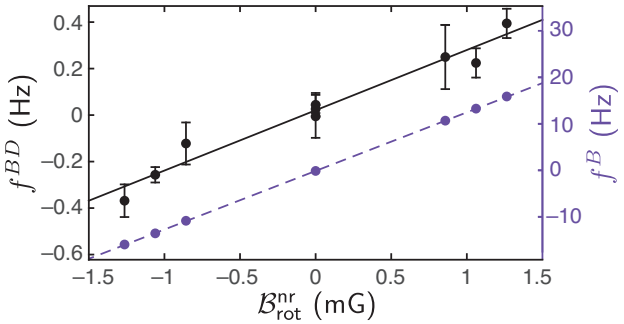

Figure 3.10: Systematic shift in the eEDM channel f^{BD} due to non-reversing $\mathcal{B}_{\rm rot}$ (left hand vertical axis, solid line), and a proportional shift in the f^{B} channel that we use to apply a correction (right hand vertical axis, dashed line). The constant of proportionality $f^{BD}/f^{B} = \delta g_{\rm eff}/g_F$ depends on $\mathcal{E}_{\rm rot}$ and $f_{\rm rot}$. The data shown here were taken under conditions chosen to make it particularly large ($\sim 10^{-2}$).

of $\delta g_{\rm eff}/g_F$ makes the correction to f^{BD} still smaller, with an average value of $\langle f^{BD}_{\rm corr,3}\rangle = -1(5)$ μHz over the entire eEDM dataset.

3.5.3 Geometric phase and axial magnetic field

While the six radial electrodes of our RF trap are designed to optimize uniformity of the rotating electric bias field, there nonetheless exist inhomogeneities in $\mathcal{E}_{\rm rot}$ that are well-described by spherical multipoles, as discussed in Section 3.4.1. The $(l, m) = (3, \pm 1)$ and $(5, \pm 1)$ spherical multipole components of $\mathcal{E}_{\rm rot}$ cause a nonzero time-average tilt of the rotating electric field $\langle\alpha\rangle = \langle\mathcal{E}_Z/\mathcal{E}_{\rm rot}\rangle$ and a corresponding geometric frequency shift $f^{BR} \approx 3\langle\alpha\rangle f_{\rm rot}$, shown in Fig. 3.3. Independently, a non-reversing axial magnetic field $\mathcal{B}^{\rm nr}_Z$ produces a nonzero value of Δ^{DR}, which forms the dominant contribution to the f^{DR} channel. The mixing mechanism described in Section 3.4.3 leads to a shift in f^{BD} equal to $-f^{BR}_0\Delta^{DR}\Delta/|f^0_0|^2$. Since $f^{BR} \approx f^{BR}_0 = 3\langle\alpha\rangle f_{\rm rot}$ and $f^{DR} \approx \Delta^{DR}\Delta/|f^0_0|$, we can in principle apply a corresponding correction

$$f^{BD}_{\rm corr,4} = \frac{f^{BR}f^{DR}}{f^0}, \tag{3.28}$$

which has an average value of $\langle f^{BD}_{\rm corr,4}\rangle = -3(2)$ μHz over the eEDM dataset. However, since this shift was too small for us to observe in the eEDM channel, we include a total systematic uncertainty $\langle\delta f^{BD}_{\rm tot,4}\rangle = 4$ μHz in our uncertainty budget.

Comparing Eqs. (3.21) and (3.28), we have neglected a contribution $-f^{BR}f_0^{DR}/|f_0^0|$ that cannot be obtained from our measured data channels. While f_0^{DR} is typically negligible, a contribution to this "diagonal" channel can arise from an R-odd contribution to $\mathcal{E}_{\rm rot}$, and is discussed in Section 3.5.6.

3.5.4 Harmonic distortion of $\mathcal{E}_{\rm rot}$

The systematic effects discussed in Sections 3.5.2 and 3.5.3 each arise from a single physical mechanism generating a frequency shift in f^B and f^{BR} respectively, which are subsequently "mixed" into f^{BD} by the nonzero values of δg_F, Δ^D, and Δ^{DR}. Other physical effects that generate "diagonal" frequency shifts in f^B and f^{BR} enter into f^{BD} in precisely the same way, and are thus contained in the corrections already applied. An illustrative example is the harmonic distortion of $\mathcal{E}_{\rm rot}$, which together with non-reversing uniform magnetic fields $\mathcal{B}_X^{\rm nr}$ and $\mathcal{B}_Y^{\rm nr}$ produces a $\mathcal{B}_{\rm rot}^{\rm nr}$ ($\equiv \mathcal{B}_{\rm rot}^{B}$) and a $\mathcal{B}_{\rm rot}^{BR}$ (an R-odd contribution to $\mathcal{B}_{\rm rot}^{\rm nr}$).

The rotating electric bias field $\mathcal{E}_{\rm rot}$ is generated by sinusoidal voltages of equal amplitude on each of the six radial electrodes, oscillating with a frequency of $f_{\rm rot}$ and with a relative phase of $\pi/3$ between adjacent electrodes. These voltages are generated by power operational amplifiers, which inevitably suffer from harmonic distortion. While exploring sources of systematic error, we observed frequency shifts up to several Hz in the f^B and f^{BR} channels. The observed shifts had a linear dependence on both transverse uniform magnetic fields and the equilibrium position of the ion cloud during the spin precession experiment. These shifts, shown in Fig. 3.2, were caused by a contribution to $\mathcal{B}_{\rm rot}^{\rm nr}$ from the combined effect of transverse magnetic fields and an oscillating electric field gradient generated by the second harmonic of $\mathcal{E}_{\rm rot}$. From a simple model of electric fields in the ion trap and using 2nd order perturbation theory of our effective Hamiltonian [5] , we obtained model expressions that matched the observed frequency shifts,

$$f^B = -\frac{3g_F\mu_B V_{2f}}{4\mathcal{E}_{\rm rot}R^2}(\mathcal{B}_X X_0 + \mathcal{B}_Y Y_0)\cos\phi_{2f}, \qquad f^{BR} = -\frac{3g_F\mu_B V_{2f}}{4\mathcal{E}_{\rm rot}R^2}(\mathcal{B}_X Y_0 - \mathcal{B}_Y X_0)\sin\phi_{2f}, \quad (3.29)$$

[5] See Section 3.6.1.

where V_{2f} and ϕ_{2f} are the amplitude and phase of the 2nd harmonic. During eEDM data collection, we suppressed V_{2f} to -70 dBc by adding a feedforward signal to the voltages generating $\mathcal{E}_{\rm rot}$, and canceled $\mathcal{B}_X$ and $\mathcal{B}_Y$ to within 30 mG of zero at the RF trap center using magnet coils. Both of these frequency shifts can cause a false eEDM; f^B through the effective differential g-factor, and f^{BR} through a shift in the f^{DR} channel. Both, however, are already corrected by $f^{BD}_{\rm corr,3}$ and $f^{BD}_{\rm corr,4}$. Higher harmonics of $f_{\rm rot}$ combined with magnetic gradients can contribute higher-order terms to Eq. (3.29), however the resulting shifts in the f^{BD} channel are similarly accounted for by the corrections already applied.

3.5.5 Frequency modulation due to axial secular motion

The geometric frequency shift $3\alpha f_{\rm rot}$ in Eq. (3.13) generates a BR-odd frequency contribution proportional to an axial electric field $\mathcal{E}_Z$, as was already discussed in the context of geometric phases. While coherent axial secular motion of the ion cloud at frequency $f_Z \gg f^0$ will not produce a time-average nonzero value of α, it does cause a BR-odd modulation of the instantaneous spin precession frequency, as shown for a deliberately large secular motion amplitude in Fig. 3.11. The ponderomotive potential associated with $\mathcal{E}_{\rm rot}$ inhomogeneity provides a source for axial secular motion, since our $\pi/2$ pulses involve modulating $\mathcal{E}_{\rm rot}$ and thus applying position-dependent impulses to the ion cloud. Further, we apply $\pi/2$ pulses of different lengths in the upper or lower Stark doublet, which can lead to a D-odd slosh amplitude and therefore a BDR-odd modulation.

We perform a frequency measurement by collecting a set of (typically) six equally spaced points at short interrogation time $t \lesssim 50$ ms and a second set at late time $t \lesssim 700$ ms, each set spanning approximately one period of spin precession. The frequency resulting from a nonlinear least squares fit to the functional form of Eq. 3.1 is approximately equal to the difference in phase between early and late time, $f \simeq (\phi_T - \phi_0)/2\pi T$. If aliasing this frequency modulation causes a systematic phase shift, a systematic frequency shift $f^{BR} = \Delta\phi^{BR}/2\pi T$ will result (with a similar frequency shift due to ϕ^{BDR}). To the extent that the spacing of our asymmetry points in interrogation time is incommensurate with $1/f_Z$, the shift in f^{BR} and f^{BDR} will be suppressed. However,

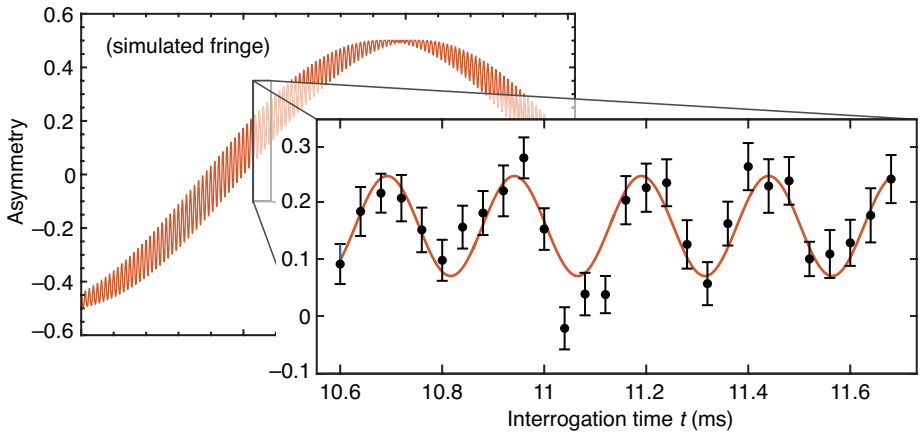

Figure 3.11: Phase modulation of an interference fringe at $f_Z = 4.01(7)$ kHz due to axial secular motion of the ion cloud with an intentionally exaggerated amplitude of ~ 3 mm, measured near the steepest portion of the fringe where $2\pi ft \approx \pi/2$.

we did not vary either f_Z or the spacing of our interrogation times during eEDM data collection in order to enhance this suppression. Thus a contribution to offsets in f^{BR} and f^{BDR} from this effect may be present.

While any BR-odd contribution from frequency modulation is a "diagonal" frequency shift and is accounted for by $f^{BD}_{\mathrm{corr},6}$, the BDR-odd frequency shift has not yet been accounted for. This is done so in the same manner as $f^{BD}_{\mathrm{corr},7}$ and $f^{BD}_{\mathrm{corr},6}$, as outlined in Section 3.4.3. The corresponding correction is

$$f^{BD}_{\mathrm{corr},5} = \frac{f^{BDR} f^{R}}{f^{0}}. \tag{3.30}$$

Since we did not observe a shift in the eEDM channel due to this systematic, we include an overall uncertainty $\langle \delta f^{BD}_{\mathrm{tot},5} \rangle = 2$ μHz. As in the case of $f^{BD}_{\mathrm{corr},6}$ where we neglected f^{DR}_0, here we have neglected f^{R}_0. The main known source of f^{R}_0 is discussed in the next section.

3.5.6 Rotation-odd $\mathcal{E}_{\mathrm{rot}}$

As discussed in Section 3.2, the R switch is controlled digitally by adjusting the relative phases of six DDS channels, each of which provides the $\mathcal{E}_{\mathrm{rot}}$ signal for one electrode. As a result, we expect an R-odd rotating electric field $\mathcal{E}^{R}_{\mathrm{rot}}$ to be very small, possibly dominated by RF pickup between neighboring amplifier circuits in our ion trap driver electronics. To the extent that $\mathcal{E}^{R}_{\mathrm{rot}}$ does exist, it could potentially cause a systematic error through accidental cancellation of the $\mathcal{B}^{\mathrm{nr}}_{Z}$-induced f^{R} and f^{DR} described in Section 3.5.3. This could occur because $\mathcal{E}^{R}_{\mathrm{rot}}$ produces R- and DR-odd "diagonal" frequency components,

$$f^{R}_0 = 3 g_F \mu_B \mathcal{B}^{R}_{\mathrm{rot}}, \qquad f^{DR}_0 = 3 \delta g_{\mathrm{eff}} \mu_B \mathcal{B}^{R}_{\mathrm{rot}}, \tag{3.31}$$

while the shifts in the same channels from $\mathcal{B}^{\mathrm{nr}}_{Z}$ arise from Δ^{R} and Δ^{DR}. The two sources of f^{R} and f^{DR} cannot be distinguished, and lead to systematic shifts of opposite sign in the eEDM channel. However, at our present level of sensitivity, all of these shifts were small compared to our statistical uncertainty. The resulting systematic frequency shifts in f^{BD} due to $\mathcal{E}^{R}_{\mathrm{rot}}$ are

$$f^{BD}_{\mathrm{syst},6} = f^{BR} \frac{\delta g_{\mathrm{eff}}}{g_F} \frac{\mathcal{E}^{R}_{\mathrm{rot}}}{\mathcal{E}_{\mathrm{rot}}}, \qquad f^{BD}_{\mathrm{syst},7} = f^{BDR} \frac{\mathcal{E}^{R}_{\mathrm{rot}}}{\mathcal{E}_{\mathrm{rot}}}. \tag{3.32}$$

Since we did not monitor $\mathcal{E}^R_{\rm rot}$ throughout data collection, we use a very conservative estimate of $\mathcal{E}^R_{\rm rot}/\mathcal{E}_{\rm rot} = 0.01$ with an uncertainty of $\delta\mathcal{E}^R_{\rm rot}/\mathcal{E}_{\rm rot} = 0.01$, and calculate systematic uncertainties $\langle \delta f^{BD}_{\rm tot,6}\rangle$ and $\langle \delta f^{BD}_{\rm tot,7}\rangle$ using the measured values of $\langle f^{BR}\rangle = -36.4(1.8)$ mHz and $\langle f^{BDR}\rangle = 0.55(93)$ mHz. The very small value of $\delta g_{\rm eff}/g_F \approx 10^{-3}$ suppresses $f^{BD}_{\rm tot,6}$ to ~ 1 μHz, so we include only $\langle \delta f^{BD}_{\rm tot,7}\rangle = 14$ μHz in our uncertainty budget.

3.6 Additional details on systematic effects

3.6.1 Harmonic distortion of $V_{\rm rot}$

Because we amplify our ion trap waveforms with op-amps rather than resonant circuits, harmonic distortion is an inevitability. We can generally anticipate spurious signals arising at frequencies satisfying

$$f_{\rm spur} = n\, f_{\rm rf} + m\, f_{\rm rot},$$

where n and m are integers. It so happens that certain ones of these are more prone to generating systematics than others, with $(n, m) = (0, 2)$ being a particularly interesting one! We can use the multipole fit coefficients of the electrodes in Table C.1 to predict the potential generated at the ion trap center by a particular configuration of voltages on the trap electrodes. We simply decide what configuration of voltages we are going to apply on each of the electrodes, and sum the multipole coefficients of each electrode (which have units of m^{-l}) multiplied by the voltage on that electrode,

$$c_{lm} = \sum_k V_k\, c^k_{lm}. \tag{3.33}$$

For the rotating electric field, the voltage applied on each of the electrodes is $V_{\rm rot}\, \cos(\omega_{\rm rot} t + \phi_{{\rm rot},k})$, with phase $\phi_{{\rm rot},k} = (9-2k)\pi/8 + \omega_{\rm rot} t$ for $\boldsymbol{\mathcal{E}}_{\rm rot}$ that initially points along $\hat{X}$ and rotates "up" in a right hand sense with respect to $\hat{Z}$. (For the opposite rotation sense, just flip the sign of the phase offsets $\sim 9 - 2k$). While we do not know in detail the specific mechanisms of harmonic distortion at work in our trap amplifiers (though Terry Brown certainly does), we are reasonably certain that they include some degree of slew rate limiting and voltage clipping. In general, we can parameterize

the voltage output of our amplifiers as a power series with a time delay,

$$V^{\text{actual}}(t) = V^{\text{nominal}}(t) + \alpha\,[V^{\text{nominal}}(t-\tau_2)]^2 + \beta\,[V^{\text{nominal}}(t-\tau_3)]^3 + \ldots. \tag{3.34}$$

Based on this parameterization and assuming the degree of harmonic distortion in all electrodes is the same, we can expect a term of the form

$$V_{2h,k}(t) = V_{2h,k}\cos\left[(9-2k)\pi/4 + 2\omega_{\text{rot}}t + \phi_{2h}\right]$$

Summing over electrodes, we find that to lowest order, the resulting multipole electric field in the ion trap is

$$\begin{aligned}\boldsymbol{\mathcal{E}}(\boldsymbol{R},t) = {}& \mathcal{E}_{\text{rot}}\left(\hat{X}\cos(\omega_{\text{rot}}t) + \hat{Y}\sin(\omega_{\text{rot}}t)\right) \\ & + \mathcal{E}_{2h}\left(\frac{X\hat{X}-Y\hat{Y}}{R_0}\cos(2\omega_{\text{rot}}t+\phi_{2h}) + \frac{X\hat{Y}+Y\hat{X}}{R_0}\sin(2\omega_{\text{rot}}t+\phi_{2h})\right),\end{aligned} \tag{3.35}$$

where $R_0 = 4.8$ cm is the radius of the ion trap. From the coefficients in Table C.1, I find $\mathcal{E}_{2h} \approx 0.8$ V/m per volt of second harmonic (amplitude). We can also parameterize the laboratory-frame magnetic field as $\boldsymbol{\mathcal{B}}(\boldsymbol{R},t) = \mathcal{B}_{\text{rot}}\,\hat{\mathcal{E}}_{\text{rot}}(t) + \mathcal{B}_X\,\hat{X} + \mathcal{B}_Y\,\hat{Y}$. We can use the transformation in Eq. (2.40) to transform the electric and magnetic fields into the rotating frame of the molecule. The results are

$$\begin{aligned}\boldsymbol{\mathcal{E}}(\boldsymbol{r},t) &= \mathcal{E}_{\text{rot}}\,\hat{z} + \mathcal{E}_{2h}\left(\frac{X\hat{z}-Y\hat{y}}{R_0}\cos(\omega_{\text{rot}}t+\phi_{2h}) + \frac{X\hat{y}+Y\hat{z}}{R_0}\sin(\omega_{\text{rot}}t+\phi_{2h})\right), \\ \boldsymbol{\mathcal{B}}(\boldsymbol{r},t) &= \mathcal{B}_{\text{rot}}\,\hat{z} + (\mathcal{B}_X\hat{z} + \mathcal{B}_Y\hat{y})\cos(\omega_{\text{rot}}t) + (\mathcal{B}_Y\hat{z} - \mathcal{B}_X\hat{y})\sin(\omega_{\text{rot}}t),\end{aligned} \tag{3.36}$$

where lowercase coordinate axes are in the in the rotating frame. Crucially, the $\hat{z}$ components of the 2nd harmonic electric field are completely dwarfed by $\mathcal{E}_{\text{rot}}$, and furthermore lead only to common-mode energy shifts for the M_F stretched states. Also crucially, moving to the rotating frame has reduced the frequency dependence of the 2nd harmonic electric field from $2\omega_{\text{rot}}$ to ω_{rot}. We can now perform perturbation theory to determine the frequency shift we will observe in Ramsey spectroscopy between states $|a\rangle$ and $|b\rangle$, for example. To perform perturbation theory, we need to know the contribution to the $^3\Delta_1$ Hamiltonian due to the electric and magnetic fields in Eq. (3.36). Fortunately, due to the work we did in deriving the matrix elements of various operators in earlier

chapters, this is quite straightforward. We can simply pull the relevant matrix elements from Eq. (2.30) and Table 2.1, finding

$$\begin{aligned}
\langle a|\, H_{\text{Zeeman}}\, |e\rangle &= \langle c|\, H_{\text{Zeeman}}\, |g\rangle = -\frac{\sqrt{3}}{2} g_F \mu_B \mathcal{B}_\perp, \\
\langle b|\, H_{\text{Zeeman}}\, |f\rangle &= \langle d|\, H_{\text{Zeeman}}\, |h\rangle = -\frac{\sqrt{3}}{2} g_F \mu_B \mathcal{B}_\perp, \\
\langle a|\, H_{\text{Stark}}\, |e\rangle &= \langle c|\, H_{\text{Stark}}\, |g\rangle = \frac{D_{||} \mathcal{E}_\perp}{2\sqrt{3}}, \\
\langle b|\, H_{\text{Stark}}\, |f\rangle &= \langle d|\, H_{\text{Stark}}\, |h\rangle = -\frac{D_{||} \mathcal{E}_\perp}{2\sqrt{3}},
\end{aligned} \tag{3.37}$$

where here $\mathcal{E}_\perp = \mathcal{E}_x - i\mathcal{E}_y$ and $\mathcal{B}_\perp = \mathcal{B}_x - i\mathcal{B}_y$. Using 2nd order perturbation theory with the perpendicular components of the Zeeman and Stark effects as our perturbing Hamiltonian H_1, we find the lowest-order contribution to the relative energy shift in the upper doublet,

$$\begin{aligned}
\Delta E_{ab}^{(2)} &= \frac{\langle a|\, H_1\, |e\rangle \langle e|\, H_1\, |a\rangle}{E_a - E_e} - \frac{\langle b|\, H_1\, |f\rangle \langle f|\, H_1\, |b\rangle}{E_b - E_f} \\
&= \frac{3 g_F \mu_B \mathcal{E}_{2h}}{2\mathcal{E}_{\text{rot}} R_0} \left[(\mathcal{B}_X\, X + \mathcal{B}_Y\, Y) \cos(\phi_{2h}) + (\mathcal{B}_X\, Y - \mathcal{B}_Y\, X) \sin(\phi_{2h}) \right].
\end{aligned} \tag{3.38}$$

Both the $\cos\phi_{2h}$ term and the $\sin\phi_{2h}$ term are odd with respect to $\tilde{B}$ and even with respect to $\tilde{D}$. With respect to $\tilde{R}$, however, the $\sin\phi_{2h}$ term is odd while the $\cos\phi_{2h}$ term is even. This is because fundamentally, ϕ_{2h} arises from something akin to a time-delay mechanism in the HV amplifiers and other synthesis electronics that generate $\mathcal{E}_{\text{rot}}$. Thus, we get contributions to the f^B and f^{BR} channels

$$\begin{aligned}
f^B &= \cdots + \frac{3 g_F \mu_B \mathcal{E}_{2h}}{2\mathcal{E}_{\text{rot}} R_0} (\mathcal{B}_X\, X + \mathcal{B}_Y\, Y) \cos(\phi_{2h}) + \ldots, \\
f^{BR} &= \cdots + \frac{3 g_F \mu_B \mathcal{E}_{2h}}{2\mathcal{E}_{\text{rot}} R_0} (\mathcal{B}_X\, Y - \mathcal{B}_Y\, X) \sin(\phi_{2h}) + \ldots.
\end{aligned} \tag{3.39}$$

3.7 Room for improvement

While the Generation 1 eEDM measurement with HfF^+ was in many ways a success, setting an upper bound on $|d_e|$ that was comparable to the ACME I experiment, it was clear that we would have to make significant gains in order to remain competitive in the next generation. That reality became even clearer all too soon, when the ACME II result of $|d_e| < 1.1 \times 10^{-29}$ e cm was released in Fall 2018 [2] – a full 12× more stringent than our Generation 1 result, and about 9× more

stringent than ACME I. Thus, we developed plans for improvements in the only two categories available: coherence time and count rate.

In the Generation 1 eEDM data, our spin coherence time was typically $\gamma^{-1} \approx 800$ ms. The methods for improving this were already well known to us, from early theory work by Eric and Aaron Leanhardt [78] and from experimental results in 2014, summarized in Kevin Cossel's thesis [28]: we should attempt to have lower ion cloud temperature for weaker collisions, lower density for a lower collision rate, and a larger value of $\mathcal{E}_{\text{rot}}$ to suppress the geometric phase accumulated in each collision. To achieve each of these goals, we needed to design and build a new ion trap. This step towards Generation 2 is described in Chapter 4.

How much room for sensitivity improvement was available from gains in coherence time? It is often approximated that precision scales inversely with interrogation time, however this is only true when the spin coherence time is short compared to dead time – time spent on state preparation and readout. In addition, in the HfF^+ experiment we suffer from both collisional dephasing parameterized by γ as well as loss of $^3\Delta_1$ population at a rate Γ due to spontaneous emission, which combine to give an effective coherence time of $\tau_{\text{eff}} = (\gamma + \Gamma/2)^{-1}$. Using an estimate that takes all of these effects into account [6] , I estimate that an improvement in γ^{-1} from 800 ms to 10 s would result in a factor of about 2.5× sensitivity gain.

The HfF^+ experiment had significantly more potential for improvement in the category of count rate. Increases in count rate can come from simply trapping a larger number of molecules per experiment cycle, which offers obvious gains but comes with drawbacks: Larger ion number in a fixed volume leads to a higher collision rate and thus faster collisional decoherence. We thus anticipated that we would like to "cash in" some of our gains that we expected to make in coherence time for an increase in count rate; in particular because the gains of improved spin coherence time are reduced once $\gamma \ll \Gamma$. Thus, the question becomes: What factor increase in ion number can we

[6] See Section 7.7.

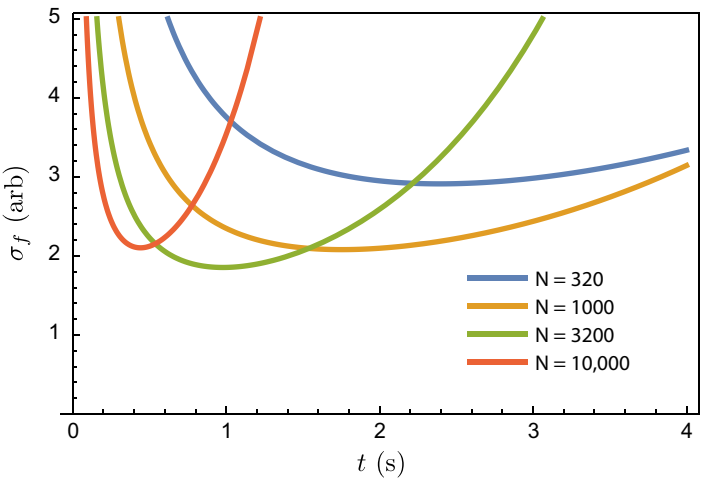

Figure 3.12: Attainable frequency precision for a Ramsey measurement σ_f (in arbitrary units) versus spin precession time for various numbers of trapped particles N, assuming that the decoherence rate γ scales proportionally with N. In this case, higher count rate is not always advantageous for precision when it leads to a loss of coherence.

attain and still maintain the $\gamma \ll \Gamma$? For example, if we assume the scaling

$$\gamma_{\text{new}} = \gamma_{\text{old}} \left(\frac{N_{\text{new}}}{N_{\text{old}}} \right), \tag{3.40}$$

we might find a behavior as shown in Fig. 3.12. In the end, this question will have to be answered empirically, because while the relation of γ to N at a fixed temperature is known approximately, the number of trapped ions affects the heating rate [19], and the temperature has a much stronger effect on the coherence time [78]. Fortunately, much like the result shown in Fig. 3.12, our frequency precision is generally a weak function of both the number and the interrogation time near the optimum value, so a crude optimization will be sufficient for our purposes.

A more fruitful but also more challenging avenue for improved precision is to improve the efficiency of our state preparation and readout processes, so that we could have larger signal sizes with the same number of trapped molecules, and thus the same decoherence rate. In this category, there was much to be gained at the conclusion of Generation 1, as shown in Table 3.7. In particular, if we are able to essentially lump together the ionization, transfer, and depletion processes in Table 3.7, we can imagine gaining up to a factor of ~ 10 in count rate, and thus about $3\times$ in precision, with no sacrifices made in coherence time. Our efforts in this direction are described in

Experiment step	Step efficiency	Overall efficiency
Ionization	0.2	0.2
Transfer	0.5	0.1
Depletion 1	0.5	0.05
Depletion 2	0.5	0.025
Dissociation	0.1	0.0025

Table 3.7: Experimental (in)efficiencies in Generation 1.

Chapter 5.

Chapter 4

Generation 2 Ion Trap

Even before the main thrust of Generation 1 eEDM data collection in 2017, it was clear that there was room for improvement upon that experiment in terms of both signal size and coherence time. To that end, we began design of a second generation ion trap and accompanying electronics, with a few goals in mind:

(1) Trap approximately 10× more ions for improved signal size. As it turns out, attaining this change was more a question of ionization laser beam shaping and pulse fluence than any property of the ion trap itself, but subsequently attaining long coherence times with those many ions depends on the trap parameters. To further increase our ion number substantially beyond the present value of $\lesssim 5 \times 10^4$, we would likely need to modify our pulsed molecular beam source to provide a higher density of neutral HfF.

(2) Eliminate the ellipsoidal mirrors from the Generation 1 ion trap, and redesign the electrode shape in order to have a more uniform $\mathcal{E}_{\mathrm{rot}}$ over a large volume. This should allow us to adiabatically expand the ion cloud (now with about 10^4 ions) and attain longer coherence times through colder temperatures and lower ion density [28].

(3) With new electronics, generate a much larger value of $\mathcal{E}_{\mathrm{rot}}$ to suppress collisional decoherence [28]. Also with the new electronics, suppress ground loops, which caused significant heating of the ion cloud in the Generation 1 trap.

This chapter centers around the latter two goals, which were carried out between Spring 2016 and

Fall 2017. In the next few sections, I discuss the design considerations and numerical optimization of the Generation 2 ion trap, as well as our benchmarking of the final product. This is followed by a brief discussion of the Generation 2 trap electronics, the design and construction of which was spearheaded by Matt Grau, Dan Gresh, Terry Brown, Felix Vietmayer, and Carl Sauer.

4.1 Design considerations

The main goal of our design for the Generation 2 ion trap was to obtain the trap parameters that would provide the most uniform $\boldsymbol{\mathcal{E}}_{\mathrm{rot}}$ over the largest possible volume. Not only do certain systematic errors depend on the uniformity of $\boldsymbol{\mathcal{E}}_{\mathrm{rot}}$ (see Chapter 3), but the ponderomotive potential

$$U_{\mathrm{pond}}(\boldsymbol{r}) = \frac{e^2}{4m\omega_{\mathrm{rot}}^2} \left|\boldsymbol{\mathcal{E}}_{\mathrm{rot}}(\boldsymbol{r})\right|^2 \tag{4.1}$$

tends to reduce the overall trap depth in a way that is very sensitive to the spatial uniformity of $\boldsymbol{\mathcal{E}}_{\mathrm{rot}}$. This tendency of the ponderomotive potential to reduce the trap depth was one of the primary motivations to move to eight radial electrodes over six: In the Generation 1 trap, the relative asymmetry between U_{pond} along the $\hat{X}$ and $\hat{Y}$ directions set a limit on the degree to which the trap could be "relaxed." A second motivation to move to eight electrodes was the increased optical access, in particular allowing us to use separate windows for the ionization and dissociation lasers, greatly simplifying our beam-overlapping optics [82] (and reducing the cost of replacement dichroics when the 266 nm laser inevitably burns everything in its path).

In addition to the chosen design constraint of using eight radial electrodes, we also assessed that to avoid making the distance from the pulsed valve to the trap center much longer (which would reduce the neutral HfF density at the point of ionization), we should attempt to make the Generation 2 trap fit in approximately the same size of vacuum chamber as the Generation 1 trap – i.e., one with 10CF flanges on top and bottom. Thus, the design choices to be made for the Generation 2 trap were relatively few:

(1) **Material:** The electrodes in the Generation 1 trap were fabricated from Stainless Steel

sheet metal, and were welded onto their supports. From the point of view of avoiding poorly characterized magnetic fields, this was not ideal. For Generation 2, we opted for Titanium, a very non-magnetic material which was favored by Kim Hagen for machining. We had some concerns about the UHV properties and electrical conductivity of Ti, but from various online databases these both appeared to be similar to SS, and we have had no issues.

(2) **Trap height:** For maximum trapping volume, this should be made as large as possible. As it turned out, a constraint was set on this parameter by the availability of 10CF-flanged, non-magnetic vacuum chambers. To reduce the presence of ferromagnetic material in the trap vicinity, we opted to purchase a custom Kimball Physics spherical octagon, which is machined directly from 316LN Stainless Steel and thus should avoid the phase changes and magnetism that unavoidably are present on welded chambers. The height of the chamber is 6.824" (see drawings in Appendix C), which we extended a further ~ 2" by adding 10CF double-sided flanges on top and bottom, sandwiched between the sealing 10CF flanges with feedthroughs.

(3) **Endcap electrode radius:** The endcap electrodes create the DC potential that confines the ions in the Z direction. The only hard constraint on their radius is that there remains adequate room outside for mounting of the radial electrodes. However, their potential is in general significantly shielded by the radial electrodes, and their radius was simply chose to be a convenient $R_{\mathrm{ec}} = 25$ mm (Fig. 4.1). Upon later consideration, it became evident that the finiteness of the radius of the endcaps, along with their shielding by the radial electrodes, contributes significantly to trap anharmonicity in the axial direction.

(4) **Inner and outer trap radius:** These parameters are set by the constraints that the trap must fit through the bore of a 10CF flange, that the inner radius should be as large as possible for a high degree of $\boldsymbol{\mathcal{E}}_{\mathrm{rot}}$ uniformity, and that the inside of the trap should be well-shielded from outside sources – e.g., patch charges on the chamber windows.

(5) **Radial electrode thickness:** The radial electrodes act as vertical supports for the trap, so they need to have some degree of rigidity. In addition, the flat surfaces of the machined tabs on the top and bottom of the electrodes serve to locate them. As a compromise between rigidity, ease of locating, and allowing optical access, we chose 4 mm thickness.

(6) **Radial electrode shape:** Having decided on the inner and outer trap radius, the number of electrodes, and the trap height, the shape of the radial electrodes' profile along the Z axis was the only remaining parameter that has an appreciable effect on the uniformity of $\boldsymbol{\mathcal{E}}_{\mathrm{rot}}$. This shape is the subject of our numerical optimization.

Key dimensions of the Generation 2 ion trap are shown in Figure 4.1. The dimensions shown were chosen to fit the design constraints described in the items above, and allow a starting point for the numerical optimization of $\mathcal{E}_{\mathrm{rot}}$ uniformity. The shape of the radial electrodes shown in the figure is as constructed.

4.2 Electrode shape optimization

We opted to parameterize the shape of the radial electrodes along the Z axis by a polynomial

$$X_{\mathrm{el}}(Z) = R_{\mathrm{in}}\left(1 - \sum_{n=1}^{n_{\max}} C_{2n}\left(\frac{Z}{Z_{\mathrm{el}}}\right)^{2n}\right), \tag{4.2}$$

where $Z_{\mathrm{el}} = 75$ mm is the maximum vertical extent of the radial electrodes, and $R_{\mathrm{in}} = 48$ mm is the inside radius of the trap at the $Z = 0$ plane (Fig. 4.1). To the extent that the trap is infinitely tall compared to its radius, optimal uniformity will be obtained with all $C_{2n} = 0$. We expect $C_{2n} < 1$ for all coefficients, and also $\sum_n C_{2n} < 1$ to prevent intersection of the radial electrodes in the computer model. In the design of the Generation 1 ion trap by Matt Grau in 2009, the electrodes had a parabolic shape – i.e., only the C_2 coefficient in Eq. (4.2) was nonzero. This allowed for the cancellation of $\mathcal{E}_{\mathrm{rot}}$ deviations up to 2nd order along the Z axis. In the Generation 2 trap, we allowed for coefficients up to C_{10}, which allows for cancellation of $\mathcal{E}_{\mathrm{rot}}$ inhomogeneity up to 10th order.

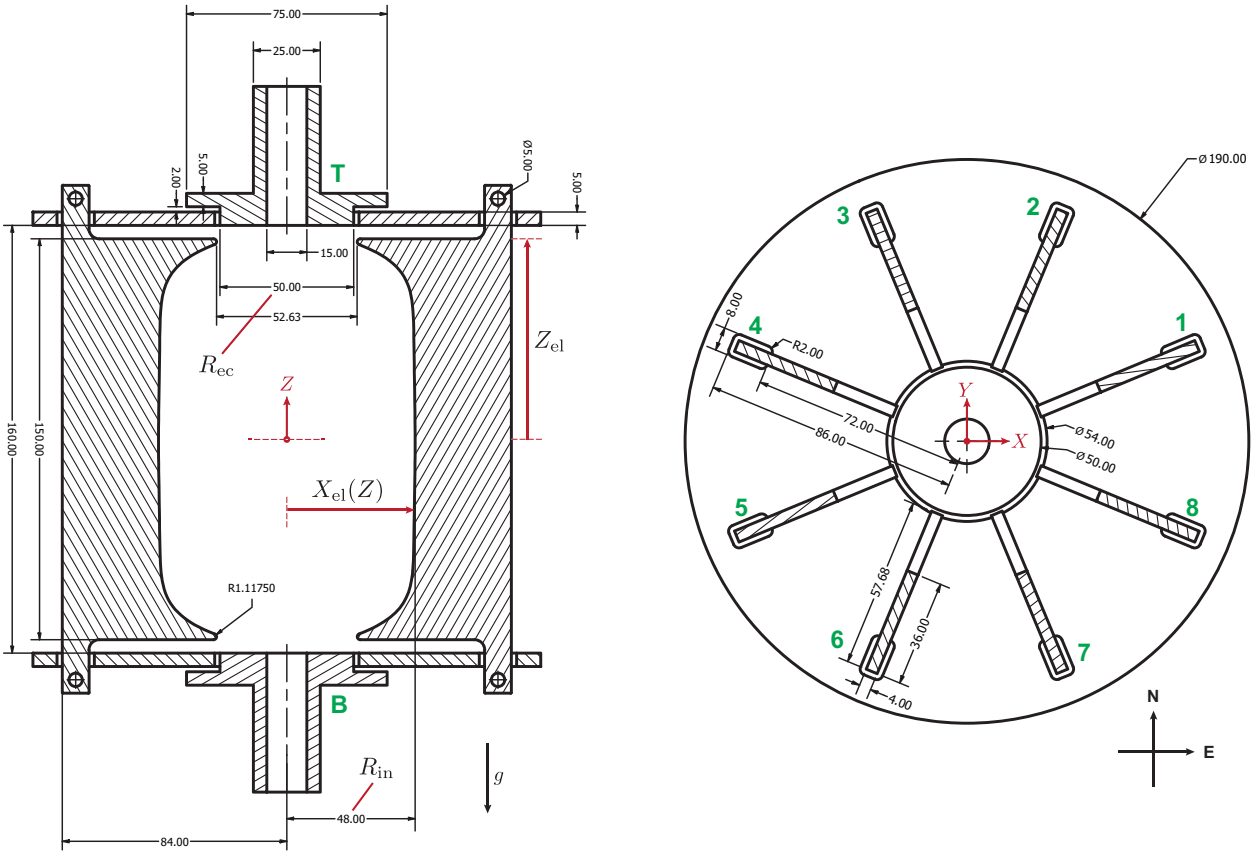

Figure 4.1: Key dimensions of Generation 2 ion trap. All dimensions in millimeters. Trap principal axes are indicated in red, and electode numbers are in green.

We typically characterize the degree of inhomogeneity in $\mathcal{E}_{\text{rot}}$ with a spherical multipole expansion about the ion trap center, which has the form of interior solutions to Laplace's equation $\Phi_{lm} \equiv r^l Y_{lm}(\theta, \phi)$. Through numerical electrostatics simulations in Comsol, we found that the changing the polynomial shape of the radial electrodes along the Z direction primarily affected the amplitudes of the multipole components having $(l, m) = (2n + 1, \pm 1)$. Along the line $(0, 0, Z)$, the norm of the electric field arising from these components behaves as $\mathcal{E} \sim Z^{l-1}$.

When optimizing the uniformity of $\mathcal{E}_{\text{rot}}$, we would like to prioritize a very high degree of flatness about the trap center; equivalent to weighting the coefficients C_n inversely with increasing n. We achieved this using a cost function

$$\text{Cost} = \int_{-Z_{\max}}^{Z_{\max}} \left[\mathcal{E}_{\text{rot}}(0,0,Z) - \mathcal{E}_{\text{rot}}(0,0,0)\right]^2 W(Z)\, dZ, \tag{4.3a}$$

$$W(Z) = \begin{cases} 1 - \sin^{10}\left(\frac{\pi Z}{2Z_{\max}}\right), & Z < Z_{\max} \\ 0, & Z \geq Z_{\max} \end{cases} \tag{4.3b}$$

where we took $Z_{\max} = 3$ cm, and $W(Z)$ is a weight function shown in Fig. 4.2. A drawback of this computationally inexpensive scheme is that in principle, this optimization attempts to minimize all terms $\mathcal{E}_{\text{rot}} \sim Z^{2n}$ rather than only up to Z^{10}. If we made $Z_{\max}$ too large, the values of $C_2 \ldots C_{10}$ would converge such that $\mathcal{E}_{\text{rot}}$ was on average flat over a larger region, but had high-order variations that would have created a significant ponderomotive potential. In the end, this choice of $Z_{\max}$ and weight function worked reasonably well, and succeeded at canceling terms up to $\mathcal{E}_{\text{rot}} \sim Z^{10}$ to the few percent level. The values of the optimized electrode shape coefficients are listed in Table 4.1, and the corresponding amplitudes of the multipole components for each electrode are given in Appendix C, Table C.1.

The optimization itself was carried out using the *Livelink for Matlab* add-on for the Comsol finite element analysis software suite. Livelink provides an application programming interface (API) – essentially a collection of functions callable from Matlab – that allows Comsol to be controlled programmatically from the Matlab command line, or better yet, from callable Matlab scripts and

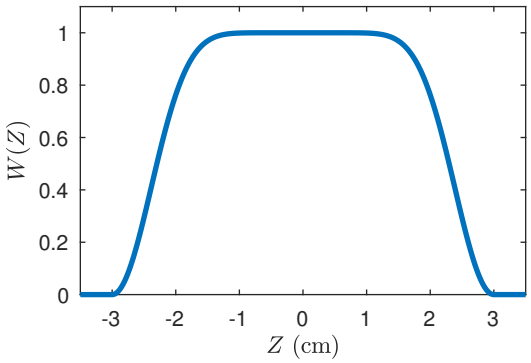

Figure 4.2: Weight function for electrode shape optimization, given by Eq. (4.3b)

C_2	0.067403
C_4	−0.119970
C_6	−0.167233
C_8	0.696342
C_{10}	0.092692

Table 4.1: Optimized polynomial coefficients for the radial electrodes' vertical profile for the Generation 2 ion trap.

functions. For iterative processes such as optimization, this is highly preferable to a GUI such as is available in standard Comsol. In Appendix A, I have included some example Matlab code for optimization, multipole fitting, and plotting of electrostatics results with Comsol via Livelink.

4.3 Results

We verified that our optimization of electrode shape had been successful through a variety of simulations, mechanical measurements, and experiments. The most straightforward verification that the optimization procedure has converged is to investigate the uniformity of $\mathcal{E}_{\mathrm{rot}}$, averaged over a single rotation period. Figure 4.3 shows the percent deviation of $\mathcal{E}_{\mathrm{rot}}$ in the XY and XZ planes, where deviations appear to be less than 0.5% over a cylinder of radius 20 mm and height 60 mm. Figure 4.4 compares the numerical results for $\mathcal{E}_{\mathrm{rot}}$ imported from Comsol with the multipole fit up to $l = 11$ along key trap directions: The X axis makes an angle $\pi/8$ with pairs of neighboring electrodes, while the line $X\cos(\pi/8) + Y\sin(\pi/8)$ runs along a line between opposing electrodes. The comparison confirms that the multipole fit to this order provides a reasonable approximation to the numerical results.

After assembling the ion trap but before installing in the vacuum chamber, Yuval and Kim Hagen conducted some measurements of the assembled trap using a dial indicator to verify the locations of the radial electrodes. First, they inserted the indicator along the Z axis of the trap with the top endcap removed, and after running the indicator along the inner edge of the top and bottom ground planes to verify that the trap was mounted flat, they then measured the differential radial displacement of each electrode near the midplane of the trap ("radial"). Second, they measured the relative vertical displacement of each of the electrodes' top surfaces, just inside the ground plane ("top"). Third, they ran the indicator along the back face of each electrode to check that they were mounted vertically ("back"). Finally, they ran the indicator vertically from top to bottom along either side of each electrode to measure their tilt ("side"). Kim recalled from the fabrication process that the back face was not particularly well registered to the mounting holes of the electrodes, so the "back" measurement is to be trusted least. With each measurement,

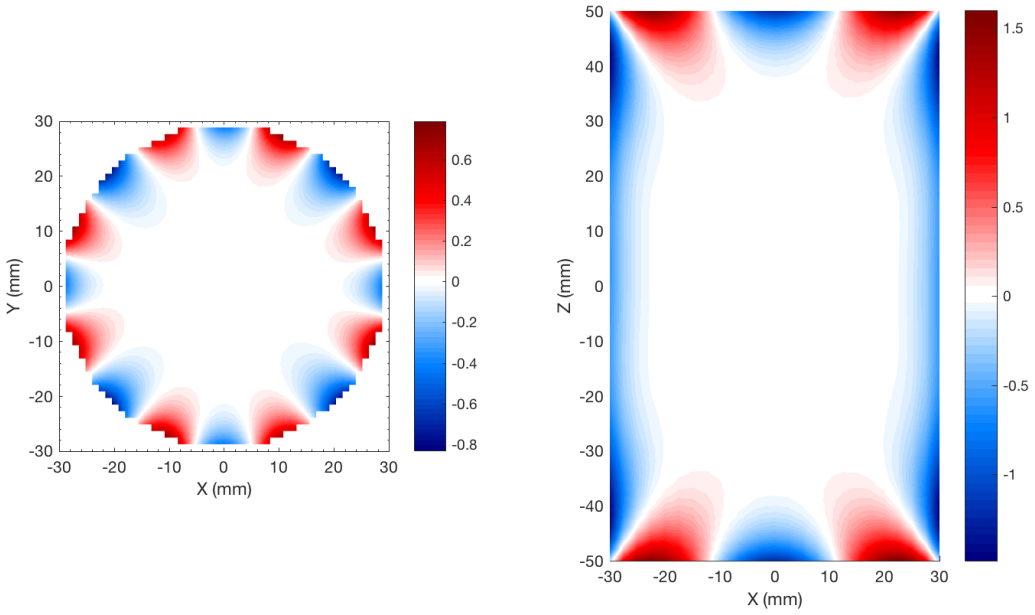

Figure 4.3: Percent deviation in $\mathcal{E}_{\text{rot}}$ in the XY and XZ planes in the Generation 2 ion trap, averaged over one rotation period. Plots generated using multipole fit, not direct Comsol solution.

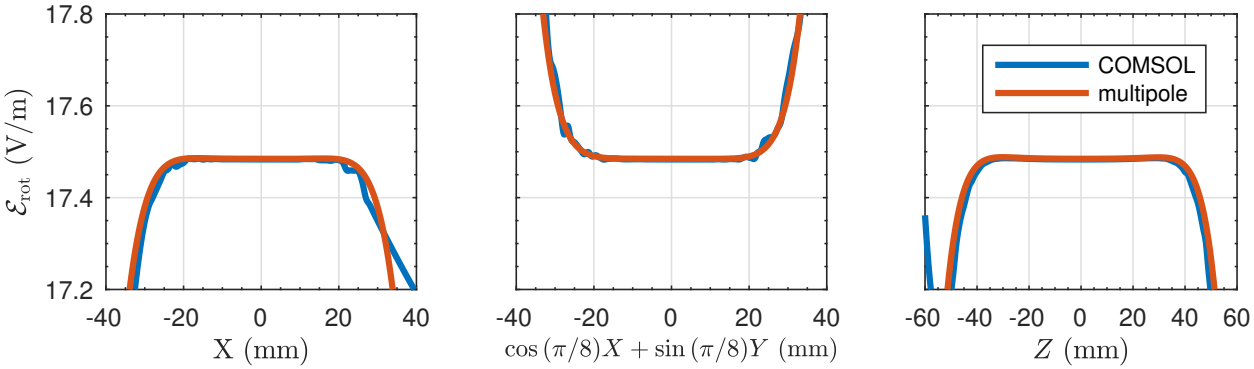

Figure 4.4: Comparison of Comsol solution for $\mathcal{E}_{\text{rot}}$ with multipole fit to $\ell = 9$, for $V_{\text{rot}} = 1$ V peak. Plots are for $\mathcal{E}_{\text{rot}}$ averaged over one rotation period.

electrode	radial	top	back	side
1	1.5	-1.5	3.5	4.25
2	0	-1.5	-3	4
3	0	-2.5	-2	2.25
4	0	-3	11	1.5
5	0	-3	-0.25	-0.75
6	0	-0.5	2	-0.5
7	0	-0.5	2	2
8	1.5	0	4	2

Table 4.2: Results of dial indicator measurements of the radial electrode positions by Yuval and Kim. The physical meaning of each measurement type is described in the text. All measurements are in mil (0.001 inch). The "back" measurement for electrode 4 has a large deviation, which was anticipated by Kim. However, the back of each electrode was not used as a mechanical reference; rather, the mounting holes are the references surfaces, so this measurement is not of concern.

they performed minor adjustments by slightly loosening and re-tightening the mounting bolts, in order to try to minimize the runout of each electrode relative to the average. The results of these measurements are listed in Table 4.2. Overall, the measurements indicate a $\cos^2\phi$ -like deviation of the height of the electrodes, and a slight overall twisting of the trap from top to bottom. While these deviations are likely too small to notice their effects on the trapping and ponderomotive potentials, these measurements may be important when considering geometric phase effects for the Generation 2 eEDM measurement.

Experimentally, we investigated the uniformity of $\mathcal{E}_{\mathrm{rot}}$ following the Generation 2 trap installation in Fall 2017 via its effects on ion motion through the ponderomotive potential [Eq. (4.1)], and through ion loss at the extremes of ion cloud position. Figure 4.5 shows potential energy surfaces along various trap axes, illustrating the anti-trapping behavior of $\mathcal{E}_{\mathrm{rot}}$. Evidently, a uniform applied electric field will result in a shift of the potential minimum away from $(0, 0, 0)$ and a reduction in the trap depth. A large enough applied field will result in loss of ions from the trap.

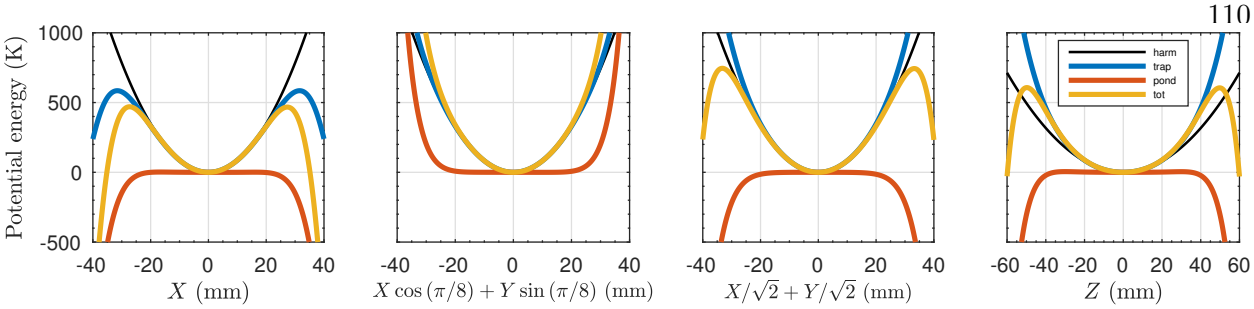

Figure 4.5: Potential energy surfaces for trapped HfF^+ ions in the Generation 2 ion trap, in units of Kelvin. The RF trapping ponderomotive potential (blue) closely approximates a harmonic trap (black) near the geometric center of the trap. The ponderomotive potential imposed by $\mathcal{E}_{\mathrm{rot}}$ inhomogeneity (red) distorts the total potential (yellow) and tends to decrease the trap depth. For this figure, $V_{\mathrm{rf}} = 15$ V peak, $V_{\mathrm{rot}} = 375$ V peak, and $V_{\mathrm{dc}} = 0.5$ V.

4.4 Trap driver electronics

In our studies of the effects of the effects of $\mathcal{E}_{\mathrm{rot}}$ amplitude and ion number on coherence time, we found that coherence time scales approximately as [28]

$$\tau \sim \frac{\mathcal{E}_{\mathrm{rot}}^{2.4}}{N_{\mathrm{HfF^+}}}, \tag{4.4}$$

for fixed values of the trap secular frequencies and ion cloud temperature. To improve our statistical sensitivity in Generation 2, we planned to increase $N_{\mathrm{HfF^+}}$ and decrease the trap frequencies, as discussed in Section 4.1. However, we also opted to improve our chances for long coherence times with high ion numbers by developing new ion trap driver electronics that could provide a higher value of $\mathcal{E}_{\mathrm{rot}}$. Additionally, we aimed to consolidate our trap controls and reduce RF pickup on the ion trap by developing new low-voltage trap waveform synthesis boards. We undertook these tasks with the help of Terry Brown, Felix Vietmayer, and Carl Sauer from the JILA electronics shop.

4.4.1 Synthesis boards

The design of our Generation 2 trap synthesis boards was initiated by Matt Grau before his graduation, and taken over and completed by Felix Vietmayer. The synthesis boards are built around the AD9959 direct digital synthesis (DDS) integrated circuit (IC) from Analog Devices, which is able to simultaneously generate four sinusoidal waveforms with digitally tunable amplitude,

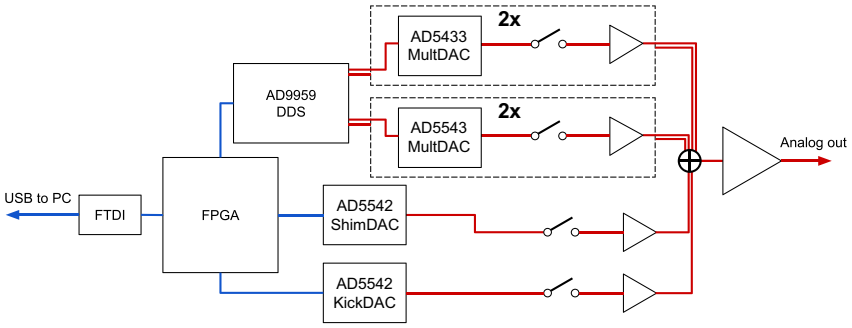

Figure 4.6: Schematic layout of the eEDM Generation 2 ion trap synthesis board. A Spartan 6 FPGA acts as a programmer and sequencer. We communicate with the FPGA via a USB-to-Serial interface chip from FTDI. The FPGA controls an AD9959 DDS, each of which has an AD5543 multiplying DAC, and two DACs to generate Shim and Kick voltages. Each channel has an analog switch to turn it on and off. All six channels are summed to produce a single analog output channel for each board.

phase, and frequency. Alongside the DDS IC, we have a pair of digital to analog converters (DACs) that generate DC signals for fine adjustments of ion cloud position ("shims") and sudden voltage jumps that suddenly impart a large velocity to the ion cloud ("kicks"). The DDS and DACs for each electrode are controlled by a field-programmable gate array (FPGA, one per electrode), which orchestrates the sequence of voltages to be applied. Our control software, which is based in Labview, communicates with the FPGA through a USB-to-serial interface chip from FTDI. The layout of the synthesis boards is shown schematically in Fig. 4.6.

Programming and testing of the synthesis boards was carried out by Felix Vietmayer and Dan Gresh in Summer 2017. To communicate with the synthesis boards, we use the functions `FT_Write` and `FT_Read` from the FTDI library `ftd2xx.dll`, which can be called from any Labview script (or from scripts written in C, C++ and a wide variety of other languages). Felix has programmed the FPGAs to expect data in a particular 7-byte format, implemented in Labview as shown in Fig. 4.7. We specify a "device" such as the AD9959 DDS, ShimDAC, or KickDAC; a memory address containing a parameter such as the start value of a voltage ramp or a DDS frequency; and finally the value to be assigned to that address. Using this tool, we write all of the sequence parameters to each board, then trigger all boards to output their sequence simultaneously using our Viewpoint DIO64. Documentation for the memory addresses of all sequencer parameters have

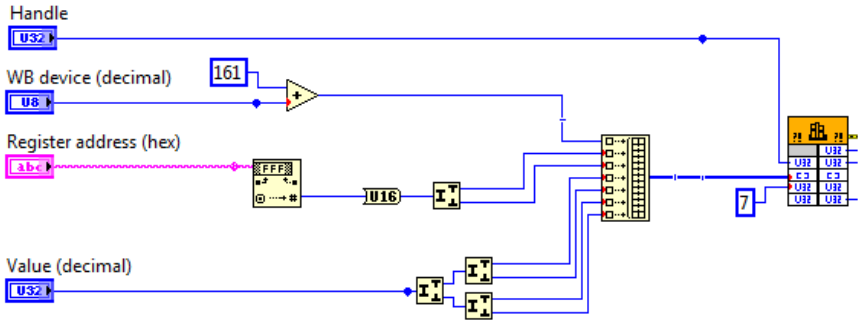

Figure 4.7: Labview code for writing to a Generation 2 ion trap synthesis board with identifier "handle." Each data packet contains 7 bytes. The first byte has the format `10YX XXXX`, where `Y` specifies read (0) or write(1), and `XXXXX` specifies a device numbered `0-31`. The second two bytes specify the memory address on the device, and the last four bytes carry the data to be written. The DLL function call on the right hand side is to the function `FT_write` in the FTDI library `ftd2xx.dll`.

been provided by Felix in a pair of documentation files, "wb_slave_AD9959.html" for the AD9959 (device 1) and "edm_seq register level documentation.html" for the sequencer and DACs (device 0).

4.4.2 Amplifiers

Terry Brown designed our Generation 2 trap driver amplifiers, which are built around the Apex PA94 op-amp. These op-amps can accommodate ±450 V rails, as compared to the ±200 V rails that were used in Generation 1 with PA98 op-amps [82]. Assuming that we operate with the rails set to 425 V for a margin of safety, and dedicate 25 V worth of amplitude to the RF trapping fields and shim voltages, the resulting $V_{\rm rot} = 400$ V will generate $\mathcal{E}_{\rm rot} = 69.9$ V/cm in the Generation 2 ion trap – a factor of 2.9 increase from Generation 1. The drawback of the PA94 is that it has a lower specified slew rate limit of $dV/dt = 700$ V/μs, as compared to 1000 V/μs specified for the PA98. In a basic amplifier design operating at $V_{\rm rot} = 400$ V, this would result in a maximum value of $\omega_{\rm rot} \approx 2\pi \times 280$ kHz. In Generation 1, our typical values of $\omega_{\rm rot}$ were between $2\pi \times 150$ kHz and $2\pi \times 250$ kHz, however for systematic checks we wanted as much simultaneous range on both $\mathcal{E}_{\rm rot}$ and $\omega_{\rm rot}$ as possible. To help in this area, Terry added two advanced design

features to the feedback loop built around the PA94. The following two paragraphs describing these features are essentially paraphrasing a discussion about these features.

The first feature Terry included in the Generation 2 trap amplifiers is a *composite amplifier*, which uses a pair of op-amps with different frequency response characteristics to improve the overall response of the amplifier as a whole [130]. Our amplifiers use the AD4898, which is a high-speed, low-noise op-amp that should improve the noise characteristics of the amplifier at low frequencies, and may also reduce harmonic distortion.

Secondly, Terry created a circuit design where current from the feedback loop is injected into the compensation pin (pin 6) of the PA94, whereas in their suggested design this pin is simply connected by a compensation capacitor to part of the input stage (pin 4). The compensation capacitor is typically chosen to maintain stability depending on the choice of gain, but also detrimentally affects the slew rate limit when the amplifier is driving a capacitive load. Terry's design essentially bypasses the input stage of the amplifier to drive the output stage directly, reducing crossover distortion and ringing in the step response when operating close to the slew rate limit. A limitation of this design is that the compensation pin can only access the output stage asymmetrically, so the slew rate limits for $dV/dt > 0$ and $dV/dt < 0$ are asymmetric in the final design. This asymmetry is visible on an oscilloscope trace of the amplifier output when attempting to drive the amplifier beyond the slew rate limit (or under normal conditions when the amplifier is not properly heat-sunk and begins to heat up).

Chapter 5

State preparation

One of the major inefficiencies of the Generation 1 eEDM experiment with HfF^+ was in state preparation, starting at the very beginning of the experiment sequence with the initial rotational distribution in the $^1\Sigma^+$ state. As shown in Table 3.7, the combined efficiency of ionization and Raman transfer was about 10%. Unfortunately, state preparation was also one of the areas where at the conclusion of the Generation 1 data collection, we had limited promising ideas for dramatic improvement. It took several unsuccessful attempts at coherent state preparation via stimulated Raman adiabatic passage (STIRAP) and adiabatic rapid passage (ARP) for us to realize that incoherent methods were not only easier to apply in our system, but dramatically more effective at concentrating population in the $^3\Delta_1$ state.

5.1 Coherent methods

Adiabatic techniques are widely applied for coherent internal state manipulation of atoms and molecules. Among the most commonly applied are ARP, which involves a frequency sweep of an electromagnetic driving field, and STIRAP, which involves amplitude modulation of a pair of lasers [126]. STIRAP was notably applied by the ACME Collaboration to improve their signal size by a factor of 14 in their second-generation measurement [2, 95]. As the name suggests, STIRAP involves adiabatically inducing a Raman transition between two low-lying states $|g_1\rangle$, $|g_2\rangle$ (Fig. 5.1) using a pair of phase-coherent lasers of different frequencies that are detuned from resonance with an excited state $|e\rangle$ that is subject to spontaneous decay with rate Γ. The intensities of the lasers

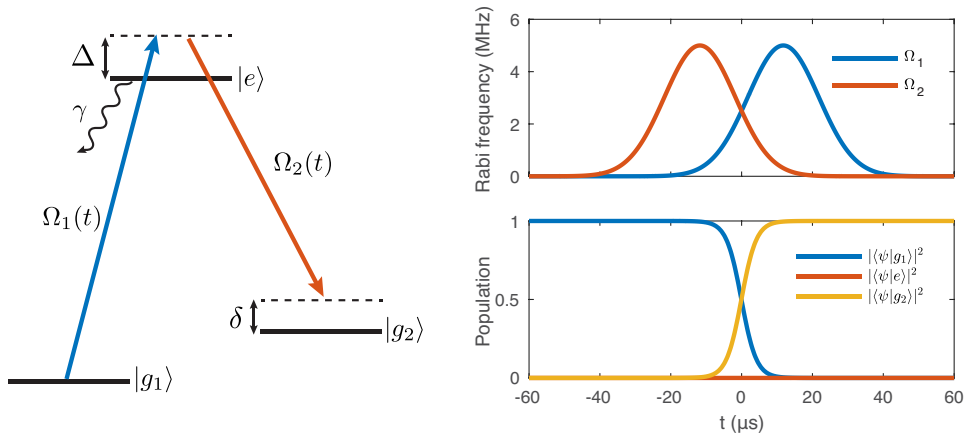

Figure 5.1: Simplified picture of STIRAP in a three-level system. Here $|g_1\rangle$ represents $^1\Sigma^+(v = 0, N = 0)$, while $|g_2\rangle$ represents $^3\Delta_1(v = 0, J = 1)$, and $|e\rangle$ represents $^3\Pi_{0^+}(v = 1, J = 0)$. The pump laser Ω_1 or "Stella" has $\lambda \approx 900$ nm, and the stokes laser Ω_2 or "Toptica" has $\lambda \approx 986$ nm.

are modulated, creating an intensity-dependent dark state that adiabatically changes character from $|g_1\rangle$ to $|g_2\rangle$, maintaining zero amplitude for populating $|e\rangle$ and thus avoiding spontaneous emission.

In HfF^+, the $^3\Pi_{0^+}$, $v = 1$, $J = 1$ state was chosen as an intermediate state for coherent transfer because it has a moderately strong coupling to both $^1\Sigma^+$, $v = 0$, $J = 0$ and $^3\Delta_1$, $v = 0$, $J = 1$, and because both of these transitions had been observed in near-IR survey spectroscopy of HfF^+ by Laura Sinclair, Kevin Cossel, and Dan Gresh [29]. These transitions have wavelengths of approximately 899.6665 nm and 986.4175 nm, respectively, both of which can be addressed with commercially available laser diodes. The details of our transfer laser setup and stabilization are described in Ref. [28].

Successful application of STIRAP can lead to population transfer efficiencies between low-lying states in excess of 90% [126], however it has stringent requirements that make it difficult to implement in general, and in our system in particular. Specifically, adiabaticity and phase coherence are the two main competing requirements for successful population transfer. Adiabaticity requires high Rabi frequencies and low rates of change of the Rabi frequencies, and can be roughly characterized by two requirements, one "local" and one "global." The local requirement, which

ensures the Rabi frequencies do not change too quickly, is

$$\Omega_{\text{eff}}(t) \gg \left[\Omega_1(t)\dot{\Omega}_2(t) + \dot{\Omega}_1(t)\Omega_2(t)\right]^{1/3}, \tag{5.1}$$

where $\Omega_{\text{eff}}(t) = \sqrt{\Omega_1(t)^2 + \Omega_2(t)^2}$. The global requirement, which ensures large enough pulse areas, is $\int_{-\infty}^{\infty} \Omega_{\text{eff}}(t)\, dt \gg \pi/2$ [127]. In the HfF^+ eEDM experiment, a major challenge for STIRAP is the high temperature of the ions, which creates Doppler widths of ≈ 40 MHz for near-infrared (NIR) one-photon transitions and ≈ 5 MHz for the $^1\Sigma^+ \rightarrow {}^3\Pi_{0^+} \rightarrow {}^3\Delta_1$ Raman transition. The ion velocities contributes to the two-photon detuning, increasing the intensity requirement for efficient STIRAP [127]. In our most recent STIRAP attempts led by Yan and Yuval in Summer 2017 following the completion of the Generation 1 eEDM measurement, we were not able to observe any coherent transfer, which is likely attributable to high ion temperatures and low Rabi frequencies.

We also attempted a Raman ARP, which potentially avoids the issues of temperature by sweeping the second transfer laser's frequency across the entire Doppler width, thereby addressing the entire molecular population with the full two-photon Rabi frequency. To sweep Toptica's frequency, we simply applied one period of a triangle wave to its external modulation port, which has a spec bandwidth of 5 MHz. Both Raman lasers were locked to the stable cavity, and Toptica's lock does not have the bandwidth to respond to the modulation on this timescale. We explored the parameter space of transfer fraction versus laser intensity and detuning as shown in Fig. 5.2. These tests were performed in the absence of $\mathcal{E}_{\text{rot}}$, so the maximum transfer fraction we could obtain with the incoherent method described in Ref. [28] is 2/3.

We fit the results of our ARP explorations with a semi-analytical model that combines the Landau-Zener transfer efficiency of ARP with the effects of decoherence due to laser phase noise or spontaneous scattering from the intermediate state, as described in Refs. [75, 93]. Following Ref. [93], we take the probability of transfer to be the sum of a contribution from incoherent transfer with a maximum probability of 2/3 given by the state degeneracy, and a coherent part proportional to the Landau-Zener transfer probability. Because in Fig. 5.2 we looked only for loss from $^1\Sigma^+(v = 0, J = 0)$, we also must multiply by a probability of spontaneous scattering. We

obtain a model equation for the population lost from ${}^1\Sigma^+(v=0, J=0)$ as a function of sweep rate,

$$P_{\text{loss}} = \left[\frac{2}{3}\left(1 - e^{-\pi\gamma\Omega/\alpha}\right) + e^{-\pi\gamma\Omega/\alpha}\left(1 - e^{-\frac{\pi\Omega^2}{2\alpha}}\right)\right] e^{-R_{\text{sc}}t}, \tag{5.2}$$

where α is the energy sweep rate of the second transfer laser, $\Omega = \Omega_1\Omega_2/(2\Delta)$ is the 2-photon Rabi frequency, Δ is the 1-photon detuning, and $\Omega_{1,2}$ are the 1-photon Rabi frequencies. The spontaneous scattering rate is

$$R_{\text{sc}} = \left(\frac{\Gamma}{2}\right) \frac{I/I_0}{1 + (2\Delta/\Gamma)^2 + I/I_0}, \tag{5.3}$$

with excited state linewidth Γ, first photon (Stella or Ω_1) laser intensity I, and saturation intensity I_0.

Throughout Fig. 5.2, we plot the fraction of molecules lost from ${}^1\Sigma^+(v=0, J=0)$ as a function of the sweep duration $T_{\text{sweep}} \propto 1/\alpha$. In Fig. 5.2a, we assumed a flat intensity profile across the ion cloud, and fit the transferred fraction with γ, Ω_1, and Ω_2 as free parameters. Then in Fig. 5.2b, we reduced both laser powers by half, and found that the experimental results for transfer fraction as a function of sweep time did not qualitatively match the model expectation. Dashed lines in parts (a) and (b) of Fig. 5.2 also show the factors contributing to the overall probability, including the probability of surviving spontaneous emission and the Landau-Zener probability. Fig. 5.2c-5.2d, we found significantly better agreement between our model and the experiment by including the effects of finite laser beam size and finite ion cloud size. We expressed the overall transfer probability as an integral over the X-Y plane, where $\Omega_1(X, Y)$ and $\Omega_2(X, Y)$ are 2D Gaussian functions and the transfer probability is weighted by the ion density $\rho(X, Y)$.

In all of our model fits to attempted ARPs, the parameter γ characterizing decoherence would essentially diverge. We interpreted this to mean that we were far from the region of parameter space where we could attain high efficiency transfer. This can also be anticipated from the fact that we attained our highest transfer fractions in the vicinity of 1 ms sweep duration, which is long enough that the ions' velocities would undergo a full cycle of oscillation in the Z axis. In this regime, we expect the model of Eq. (5.2) to break down, and we cannot reasonably expect high

transfer efficiency. However, the good agreement between experiment and our model in the short transfer duration region near 0.1 ms, where transfer is well approximated by the Landau-Zener formula alone, can help us to conclude that to achieve high transfer efficiency we would need orders of magnitude more laser intensity or a stronger transition. Unfortunately, higher intensity is not available, and we soon found that incoherent transfer was a better option.

5.2 Rotational cooling & vibrational decay

Upon ionization, the HfF^+ population is spread approximately equally over rotational levels $J = 0$ through $J = 2$, plus a little bit in $J = 3$ – comprising 32 total quantum states, when nuclear spin is accounted for. About 20% of the total HfF^+ population is in $^1\Sigma^+$, $v = 0$, $J = 0$, which has two nuclear spin states. If we use only coherent methods of state preparation, we can expect to prepare at best 10% of the total ion population in a single $|F, M_F, \Omega\rangle$ state of $^3\Delta_1$, $v = 0$, $J = 1$. With a single quantum projection step and unit detection efficiency, we could then in principle detect 5% of the total ion population as eEDM signal. On the other hand, if we use a form of dissipative state preparation that removes entropy from the initial ion ensemble through spontaneous emission, we might hope to significantly improve our overall efficiency. Vibrational branching ratios are not in our favor in HfF^+, so tasks requiring thousands of photon cycles such as laser cooling are certainly out of the question. However, in the eEDM spirit of trying new things, in Summer 2017 after the completion of the Generation 1 dataset, we decided to try some basic rotational cooling in $^1\Sigma^+$, $v = 0$, using the $^3\Sigma^-_{0^+}$, $v = 0$, $J = 1$ excited state. The motivations for attempting rotational cooling through $^3\Sigma^-_{0^+}$ were

- It has a strongly allowed electric dipole transition with $^1\Sigma^+$ ($D = 0.23\, e\, a_0$ theoretically [28]) and a weak electric dipole transition with $^3\Delta_1$ ($D = 0.08\, e\, a_0$ theoretically). Thus, contamination of $^3\Delta_1$ excited vibrational states should in theory be kept to a minimum.
- It has relatively favorable Franck-Condon overlap with $^1\Sigma^+$, as shown in Table 5.1.
- It is an $\Omega = 0$ state of definite parity, so only P and R branches exist in the transition

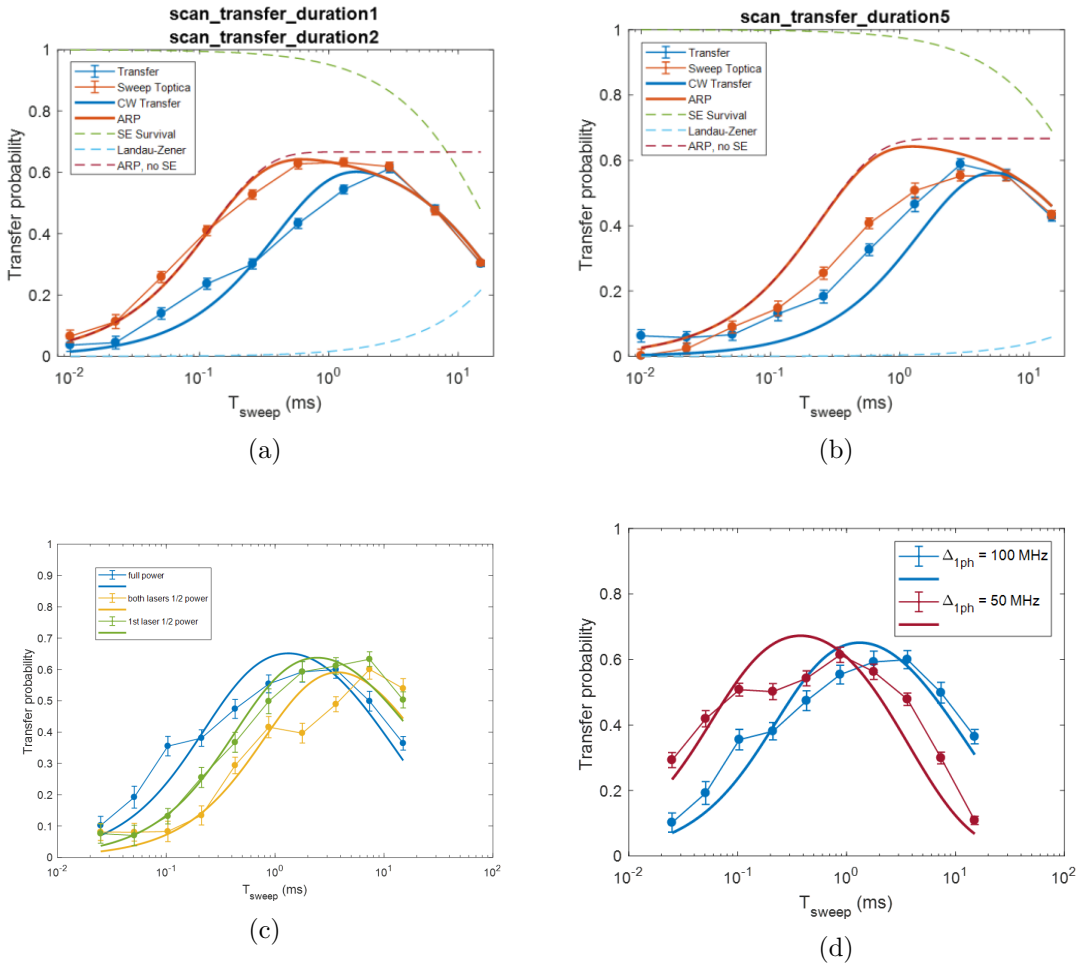

Figure 5.2: Tests of the model from Eq. (5.2) for chirped Raman adiabatic rapid passage with HfF^+. In (a) and (b), we did not account for the cloud side and laser beam profile. In (a), we calibrated the parameters of Eq. (5.2). In (b), we reduced each laser power by half and found that the model did not fit observations. In (c) and (d), integrating Eq.(5.2) over a spatially varying laser intensity and ion density was able to account for the observed variation in transfer probability with laser power and detuning.

	v'		
v''	0	1	2
0	0.6648	0.2641	0.0595
1	0.2771	0.2298	0.3245
2	0.0519	0.3619	0.0430
3	0.0057	0.1222	0.3364

Table 5.1: Franck-Condon factors for the $^1\Sigma^+ \leftrightarrow {}^3\Sigma^-_{0^+}$ system of HfF^+, assuming a Morse potential. Spectroscopic constants for both electronic states are given in Ref. [28].

with $^1\Sigma^+$. This removes one possible decay path, allowing for higher-efficiency rotational cooling.

- The $^1\Sigma^+ \leftarrow {}^3\Sigma^-_{0^+}$ $(0,0)$ transition has wavelength $\lambda \approx 754$ nm, which can be reached by our cw Ti:Sapph laser, as well as a diode available from Toptica.

The $^1\Sigma^+ \leftarrow {}^3\Sigma^-_{0^+}$ $(0,0)$ transition was observed and fitted in Comb-vms survey spectroscopy of HfF^+ conducted by Laura Sinclair, Kevin, and Dan. The fit constants, found in Ref. [28], Table 5.2 line 12, give that the desired $P(2)$ line will be found at $\nu = 13253.053(7)$ cm^{-1}. By scanning the Ti:Sapph by hand while monitoring the dissociated population from $^1\Sigma^+$, $v = 0$, $J = 2$, we found the $P(2)$ transition at $\nu = 13253.059(1)$ cm^{-1}, or $\lambda = 754.54280(6)$ nm, consistent with the fit within the reported 1σ statistical error bar. In addition to a laser resonant with the $P(2)$ transition, we also added microwaves (with frequencies in multiples of 18277.55 GHz) to couple the $J = 1, 2, 3$ states of $^1\Sigma^+$, $v = 0$, causing the entire population of these three rotational states to be electronically excited and (potentially) decay to $J = 0$. While in molecular laser cooling experiments, this method of microwave remixing can be detrimental to MOT performance because it reduces the scattering rate [26, 134], this slowdown is relatively small compared to our coherence times of ~ 2 s, and should not significantly impact our statistical sensitivity.

The results of rotation cooling with and without microwave remixing are shown in Fig. 5.3. With microwave remixing, we attained about a factor of 2 increase in the $J = 0$ population. This represented a modest win, and was our first foray into incoherent state preparation. At this early point in the Generation 2 experiment, we had not yet returned to dissociation of the $^3\Delta_1$ state,

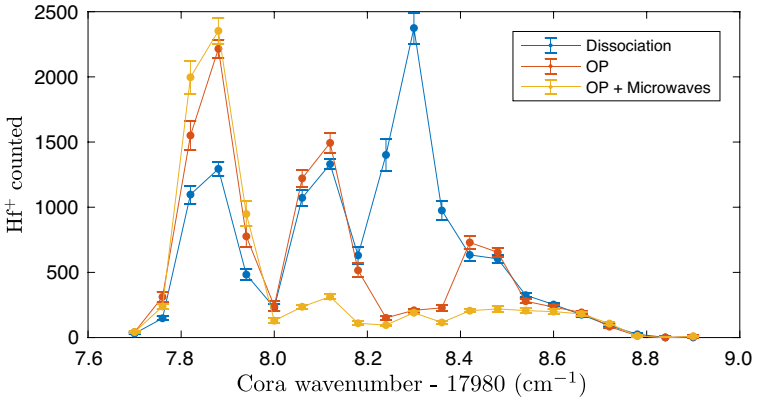

Figure 5.3: R branch of the REMPD spectrum of HfF^+ from its $^1\Sigma^+$ ground state through an $\Omega' = 0$ intermediate state at $\nu_0 \approx 35976$ cm^{-1} , with chops showing rotational cooling. Not shown: enormous background in $^3\Delta_1$, $v = 0$, $J = 1$.

and so we did not yet know of the unfortunate news waiting for us there – vibrational decay!

As discussed in Section 2.2.4 and in early theoretical work by Petrov *et al.* [99], the spontaneous decay lifetimes of excited vibrational states of $^3\Delta_1$ have lifetimes on the order of ~ 100 ms (Fig. 5.4). By contrast, the lifetime for decay of $^3\Delta_1$ to $^1\Sigma^+$ manifold is on the order of 3 s, from our latest measurements. Any population reaching the excited vibrational states of $^3\Delta_1$ early in the experiment sequence will tend to decay to $^3\Delta_1$, $v = 0$ by the end of an experiment cycle ~ 1.5 s later, and some of this population will end up in $J = 1$. That population will be dissociated, and detected as a background, reducing the contrast of our eEDM signal and hurting our signal-to-noise ratio. This was precisely the situation we found upon performing optical pumping through $^3\Sigma^-_{0^+}$. Even with the 814.5 nm depletion laser depopulating $^3\Delta_1$, $v = 0$, $J = 1$ for the first ~ 100 ms of trap time, hundreds of ions would again be detected in $^3\Delta_1$, $v = 0$, $J = 1$ several hundred ms later – a sure sign that population was reaching excited vibrational states. This was a substantial disappointment, and essentially put a stop to 754 nm rotational cooling. Fortunately, this initial investigation into incoherent state preparation inspired bigger and better ideas in first the ThF^+ experiment and subsequently in HfF^+.

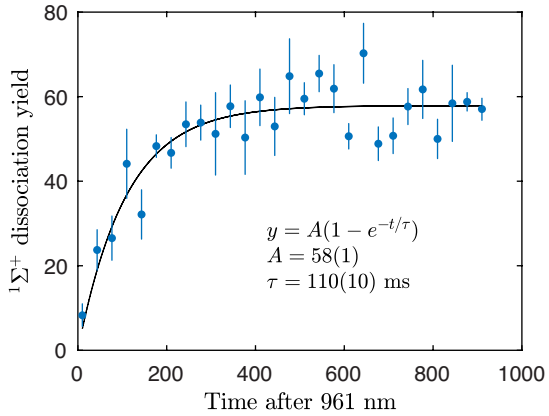

Figure 5.4: Repopulation of $^1\Sigma^+(v = 0,\ N = 0)$ by vibrational decay after laser depletion, detected by photodissociation. A similar repopulation will occur in $^3\Delta_1(v = 0,\ J = 1)$, leading to a spurious background in an eEDM measurement.

5.3 Incoherent state preparation

While our rotational cooling on the $^3\Sigma^-_{0^+} \leftarrow {}^1\Sigma^+$ (0,0) P(2) transition was a limited success, it provided the inspiration for a more extensive optical pumping-based state preparation scheme in ThF^+ by Yan and Kia Boon, which we readapted for use in HfF^+ (Fig. 5.5). The general idea of this scheme in HfF^+ is to drive the $^3\Pi_{0^+} \leftarrow {}^1\Sigma^+$ (0,0) P(1) transition at 961.434 nm with simultaneous application of microwaves that link $N = 0$ through $N = 3$ in $^1\Sigma^+$, thereby removing all $^1\Sigma^+$, $v = 0$ population and nominally transferring it to $^3\Delta_1$, $v = 0$. In reality, of course, some decay from $^3\Pi_{0^+}$, $v = 0$ will end up in excited vibrational levels of both $^1\Sigma^+$ and $^3\Delta_1$. Population in excited vibrational levels of $^1\Sigma^+$ will simply be lost, but the excited vibrational levels of $^3\Delta_1$ must be depleted to prevent background due to their decay. We do this through the P(1) rotational lines of $\Delta v = 0$ transitions to the $^3\Sigma^-_{0^+}$ state, which primarily sends the population back to $^1\Sigma^+$ and eliminates the risk of background. To develop this scheme, we had to search for several new transitions that had not previously been observed in HfF^+, and build or acquire cw lasers at several new NIR wavelengths.

For the first step of this state preparation scheme, no new lasers were required. We simply tuned our Toptica laser that had previously been driving the $^3\Pi_{0^+} \leftarrow {}^3\Delta_1$ (1,0) Q(1) transition at 986.4 nm over to the $^3\Pi_{0^+} \leftarrow {}^1\Sigma^+$ (0,0) band at 961.4 nm, which had been observed in comb-vms (Ref. [28], Table 5.2). We also already had microwaves set up to address the $N = 0 \leftrightarrow 1$, $1 \leftrightarrow 2$, and $2 \leftrightarrow 3$ transitions in the ground vibrational level of $^1\Sigma^+$ at multiples of 18277.55 MHz. We verified that this optical pumping was successful by REMPD of $^1\Sigma^+$, $v = 0$ at a first dissociation photon wavelength of 27154 cm^{-1} while chopping the 961 nm laser and the microwaves on and off, as shown in Fig. 5.6.

Between Generations 1 and 2, the experiment underwent simultaneous changes to both our state preparation method and our REMPD transition, and thus we cannot exactly distinguish the improvement in state preparation and the slight decrease in our readout efficiency (discussed in Section 6). Nonetheless, we can compare the number of ions we detected in $^3\Delta_1(v = 0, J = 1)$

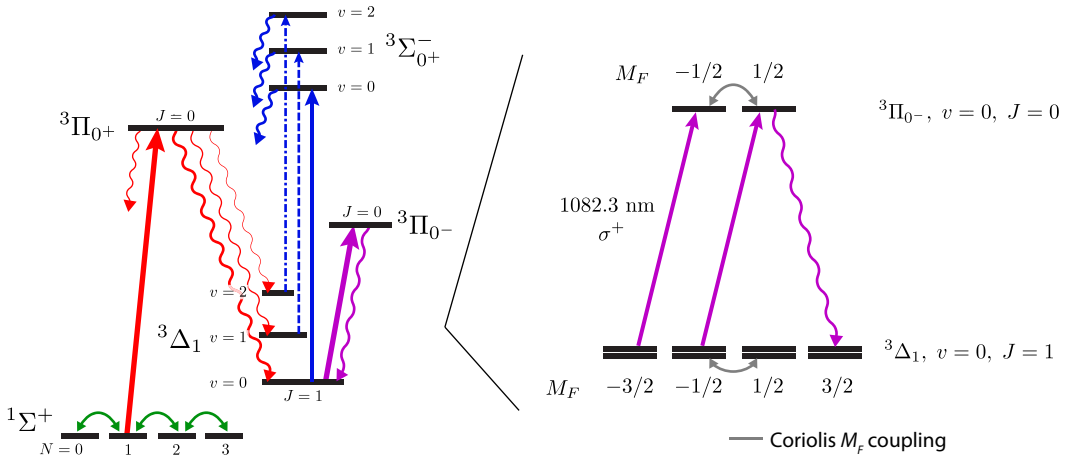

Figure 5.5: Incoherent state preparation scheme for HfF^+. Population is pumped out of $^1\Sigma^+$ using a combination of laser light on the $^3\Pi_{0^+} \leftarrow {}^1\Sigma^+$ (0,0) P(1) transition (red) and microwaves connecting rotational levels in $^1\Sigma^+$, $v = 0$ (green). Population in excited vibrational states of $^3\Delta_1$ is cleaned up by lasers on the $^3\Sigma^-_{0^+} \leftarrow {}^3\Delta_1$ (1,1) and (2,2) transitions (blue dash and dash-dot). In the ground rovibrational state of $^3\Delta_1$, quasi-cycling M_F pumping is performed on the $^3\Pi_{0^-} \leftarrow {}^3\Delta_1$ (0,0) P(1) transition (purple), and depletion is performed on the $^3\Sigma^-_{0^+} \leftarrow {}^3\Delta_1$ (0,0) Q(1) transition (blue).

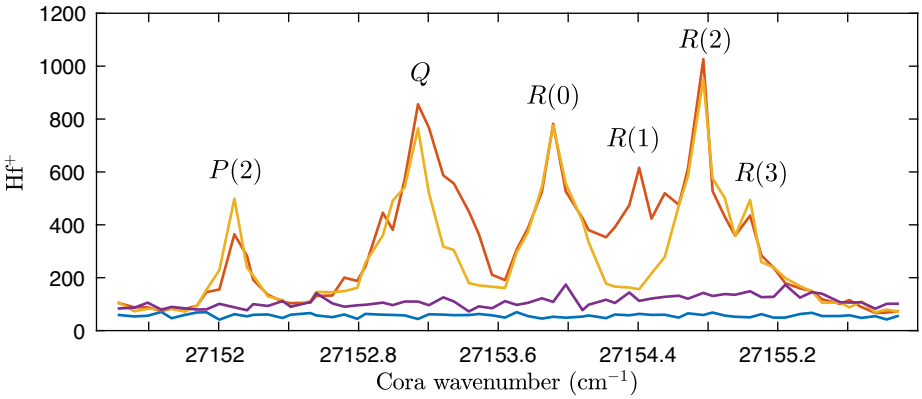

Figure 5.6: REMPD spectrum of $^1\Sigma^+$, $v = 0$ through an $\Omega = 1$ intermediate state. Red shows the initial distribution, with population distributed from $N = 0$ to $N = 3$. Adding the 961 nm transfer laser on the P(1) line to $^3\Pi_{0^+}$ causes depletion of $N = 1$, evidenced by disappearance of the R(1) line. Further adding microwaves gives the purple trace, where only a broad background is visible. We believe this background arises from vibrational decay that occurs between the end of transfer and dissociation.

before M_F pumping. In Generation 1, this number was on the order of 50 detected ions spread between two M_F levels, while in Generation 2 we detect about 2500 ions spread amongst 12 M_F sublevels.

5.3.1 M_F pumping with $^3\Pi_{0^-}$

To prepare a pure M_F state in $^3\Delta_1$, we need to do further optical pumping with strobed, circularly polarized light applied from the side of the ion trap. In Generation 1, this was done only on the $^3\Sigma^-_{0^+} \leftarrow {}^3\Delta_1$ (0,0) P(1) transition at 814.5463 nm. However, a greater population in $^3\Delta_1$, $v = 0$, $J = 1$ can be maintained if we instead use the $^3\Pi_{0^-}$, $v = 0$ state, which due to parity selection rules, forms an electronically closed system with $^3\Delta_1$. We therefore decided to locate the $^3\Pi_{0^-} \leftarrow {}^3\Delta_1$ (0,0) transition, which had not been previously observed in velocity modulation spectroscopy as at about 1083 nm, it was too far into the infrared.

While the ground vibrational state of $^3\Pi_{0^-}$ had not been observed, the comb-vms results in Kevin's thesis [28] do list the $^3\Pi_{0^-} \leftarrow {}^3\Delta_1$ (1,0) transition with $\nu_0 = 9948.624(6)$ cm^{-1}. The $\Delta G_{1/2}$ value (the energy difference between the first two vibration levels) for $^3\Pi_{0^-}$ is not known, however assuming it is approximately the same as $^3\Pi_{0^+}$, we would expect to find the $^3\Pi_{0^-} \leftarrow {}^3\Delta_1$ transition at $\nu_0 = 9235.694(16)$ cm^{-1} or $\lambda_0 = 1082.756(2)$ nm. This is a very fortunate wavelength, as DBR lasers designed for metastable Helium spectroscopy are readily available in the 1083 nm region from Eagleyard and Photodigm. Also fortunately, $^3\Pi_{0^-} \leftarrow {}^3\Delta_1$ is a strongly allowed electric dipole transition with favorable Franck-Condon factors (Table 5.2), so a few tens of mW from a DBR laser is acceptable for depletion, in contrast to the hundreds of mW needed for depletion at 814.5 nm.

We first attempted to find the $^3\Pi_{0^-} \leftarrow {}^3\Delta_1$ (0,0) transition with a DBR laser borrowed from Yuval's former group, that of Edvardas Narevicius at the Weizmann Institute. We populated $^3\Delta_1$ using 961 nm laser light, then looked for depletion of the $^3\Delta_1$, $v = 0$ population detected via dissociation as a function of the DBR laser wavelength. Unfortunately, the DBR laser from the Narevicius group was centered too far towards the red, and we were unable to find the transition

	v'		
v''	0	1	2
0	0.6916	0.2422	0.0540
1	0.2658	0.2726	0.3045
2	0.0395	0.3745	0.0699
3	0.0001	0.0006	0.1635

Table 5.2: Franck-Condon factors for the $^3\Pi_{0^-} \leftrightarrow {}^3\Delta_1$ system, assuming a Morse potential. Here I have used the known value of $\Delta G_{1/2} = 716.0$ cm^{-1} for $^3\Pi_{0^-}$ and assumed that $\omega_e x_e$ has the same value as for $^3\Pi_{0^+}$, approximately 3.3 cm^{-1}. Molecular constants are found in Ref. [28].

without pulling the laser temperature dangerously close to the dew point, around 10 Celsius. We then purchased a DBR centered around a bluer wavelength, and we were able to locate the band in the vicinity of 1082.3 nm. The precise values of the P(1), Q(1) and R(1) lines are recorded in Table 5.3. From these values, we find that the band origin is $\nu_0 = 9239.2090(7)$ for this transition, and $\Delta G_{1/2} = 709.415(6)$ cm^{-1} for the $^3\Pi_{0^-}$ state. Having only observed a pair of vibrational transitions, we cannot estimate ω_e and $\omega_e\, x_e$ for the $^3\Pi_{0^-}$ state, but if $\omega_e\, x_e \approx 3.3$ cm^{-1} (the same value as $^3\Pi_{0^+}$), then $\omega_e = \Delta G_{1/2} + 2\omega_e\, x_e \approx 716.0$ cm^{-1}. This result is in agreement with the theory from Skripnikov *et al.* in Ref. [29].

Having found the $^3\Pi_{0^-}$ transition, we can then use the P(1) line to perform quasi-cycling optical pumping of M_F in order to accumulate population in a single stretched M_F level of $^3\Delta_1$, $v = 0$, $J = 1$, as illustrated in Fig. 5.5. Using the P(1) transition keeps the transition closed with respect to the rotational degree of freedom, and prevents population from decaying to $J = 2$. Due to the presence of Ω doubling, both Stark doublets in $^3\Delta_1$ (which have completely mixed parity in the presence of $\mathcal{E}_{\rm rot}$) are populated equally by decay from $^3\Pi_{0^-}$. While this would have presented an issue in the Generation 1 experiment, it works well in combination with our Stark doublet-selective

Line	λ (nm)	ν (cm^{-1})
P(1)	1082.4137(1)	9238.6118(9)
Q(1)	1082.3472(1)	9239.1794(9)
R(1)	1082.2139(1)	9240.3174(9)

Table 5.3: Observed line positions for the $^3\Pi_{0^-} \leftarrow {}^3\Delta_1$ (0,0) band.

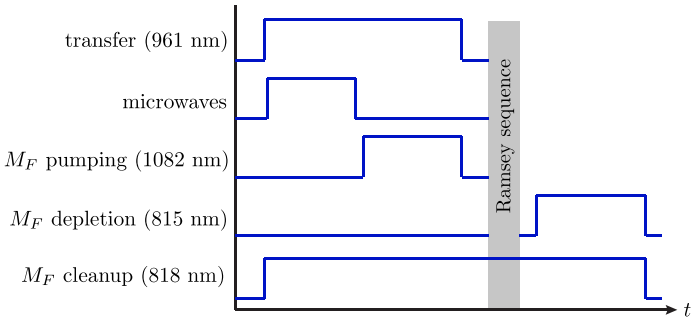

Figure 5.7: Timing of state preparation and readout. The 961 nm laser and microwaves transfer population to $^3\Delta_1$, and remain on during M_F pumping to send any population that returns to $^1\Sigma^+$ (for example from vibrational decay) back to $^3\Delta_1$. After the Ramsey sequence, the 814.5 nm laser depletes all but one M_F level in $^3\Delta_1$.

readout, which is decribed in Section 6.

5.3.2 Polarization measurement

While the $^3\Pi_{0^-}$ state is ideal for preparation of a large population in a single M_F level, its quasi-cycling nature is not optimal for readout of the M_F level populations. For state readout, we would like to be able to selectively remove population from $^3\Delta_1$, $J = 1$ via an electronic state that has a very small probability of returning via spontaneous emission. The best accessible state for this purpose in HfF^+ is $^3\Sigma^-_{0^+}$, which is predicted theoretically to decay with 88% probability to $^1\Sigma^+$ rather than $^3\Delta_1$ [28] (in the approximation that these are the only states it decays to). We have performed depletion through $^3\Sigma^-_{0^+}$, $v = 0$ with considerable success for several years [52], using the Coherent cw Ti:sapphire previously used by Dan, Kevin, and Laura in the discharge lab tuned to the transition at 814.5463(1) nm. Due to the usefulness of the Ti:sapph as a tunable laser for spectroscopy work, we purchased a new Toptica TA Pro system at 814.5 nm for the Generation 2 experiment. While previously this transition was used both for state preparation (before the Ramsey sequence) and readout, we now use it only for readout after the 2nd $\pi/2$ pulse.

Figure 5.7 shows the timing sequence of our state preparation and readout. First, 961 nm and microwaves are applied to transfer population to $^3\Delta_1$, as described in Section 5.3. We then perform M_F pumping with 1082 nm, which pumps all population in $^3\Delta_1$, $v = 0$, $J = 1$ into a single

M_F level in each stretched Stark doublet. Figure 5.8 shows the dissociation yield from $^3\Delta_1$ $J = 1$ as a function of M_F pumping and depletion durations. The cycling nature of the 1082 nm transition is visible in the increase of dissociation yield in the $\sigma^+\sigma^+$ chop as a function of pumping duration. The comparable timescales of each process despite the very different laser powers highlight the very different transition strengths of $^3\Pi_{0^-} \leftrightarrow {}^3\Delta_1$ and $^3\Sigma^-_{0^+} \leftrightarrow {}^3\Delta_1$.

5.3.3 Vibrational cleanups

The excited vibrational states of $^3\Delta_1$ are populated by decay of $^3\Pi_{0^+}$ in proportion to the $(0, v'')$ Franck-Condon factors given in Table 5.7 of Ref. [28]. Because we drive only the P(1) line with our 961 nm laser in transferring population from $^1\Sigma^+$ to $^3\Delta_1$, only the $J = 1$ levels of each vibrational state in $^3\Delta_1$ should initially be populated. As discussed in Section 2.2.4, these levels decay with lifetimes on the order of ~ 100 ms, which presents a source of background for our second-scale eEDM measurement. Happily, the progression of $\Delta v = 0$ transitions to the $^3\Sigma^-_{0^+}$ state all have similarly favorable wavelengths to our projection laser at 814.5 nm, with the (1,1) and (2,2) transitions being found at approximately 818.4 nm and 822.4 nm, respectively. The AR-coated laser diodes from Eagleyard can easily be tuned to these wavelengths in a homebuilt ECDL, and because we are simply performing incoherent optical pumping on a timescale of many milliseconds, a few mW of each to the chamber is enough for our purposes. We implemented two vibrational cleanup lasers for these purposes, which enabled the high depletion contrast shown in Fig. 5.8b.

Our initial vibrational repump scheme as shown in Fig. 5.9a has us driving the P(1) lines to $^3\Sigma^-_{0^+}(v = 1, 2)$ out of $^3\Delta_1(v = 1, 2)$, respectively. We chose these transitions based on the idea that maintaining rotational closure is very important to attaining high overall efficiency. While this is generally true, we have not yet implemented any repumping lasers to recover the population initially sent to excited vibrational levels of $^3\Delta_1$, and this population is essentially just considered to be lost. As a result, we are not particularly concerned with driving only P(1) transitions, and we realized that we can in theory do better at preventing background by driving the P(1) and P(2) transitions from $^3\Delta_1(v = 1)$, as shown in Fig. 5.9b. Empirically, we have not observed a significant

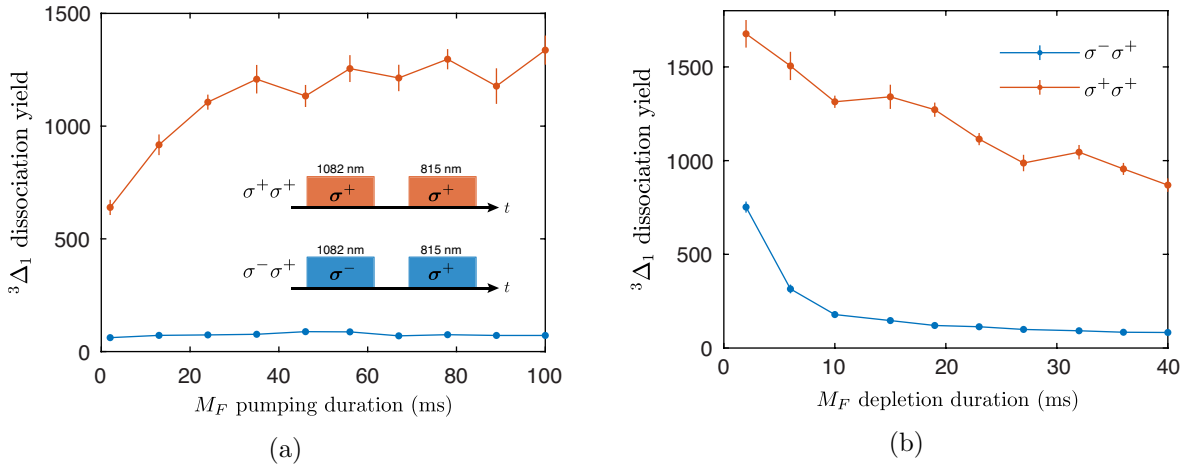

Figure 5.8: Timescale of strobed circularly polarized state preparation and readout. (a) M_F pumping on the $^3\Pi_{0^-} \leftarrow {}^3\Delta_1$ (0,0) P(1) transition with about 50 mW of 1082.3 nm laser light, with a fixed duration of M_F depletion of 40 ms. Inset: Timing sequence of $\sigma^+\sigma^+$ and $\sigma^+\sigma^-$ chops. (b) M_F depletion on the $^3\Sigma^-_{0^+} \leftarrow {}^3\Delta_1$ (0,0) P(1) transition using about 400 mW of 814.5 nm laser light, with a fixed duration of M_F pumping of 60 ms. Both beam waists are roughly 5 mm.

difference between these two methods, in particular because the dissociation background is a much stronger function of the intensity of the two REMPD lasers.

There remains one background phenomenon related to our incoherent state preparation that is not well understood. This is a REMPD background that is independent of the first REMPD photon wavelength, leading us to think that it is off-resonant 2-photon dissociation of excited molecules by 266 nm. This background appears only if the 961 nm laser drives the $^3\Pi_{0^+} \leftarrow {}^1\Sigma^+$ transition, and it is larger if we drive the R branch of this transition than if we drive the P branch. All of this is consistent with the idea that vibrationally excited $^3\Delta_1$ molecules can be off-resonantly dissociated by two photons of 266 nm, however the more mysterious part is illustrated in Fig. 5.10: The 818 nm vibrational cleanup lasers tend to reduce this background substantially. To my eyes, the most probable explanation for this is that these vibrationally excited $^3\Delta_1$ molecules can be dissociated by Cora+266 or by 266+266, so that both the sharp transitions shown in Fig. 5.10 and the broad background arise from the same population.

5.4 Sensitivity improvement

In the HfF^+ eEDM experiment, absolutely efficiencies are often slightly squirrely quantities. Even when pulsed laser fluences are carefully measured, the beam profiles tend to change dramatically upon dye laser realignment, and beam pointing is only controlled on the millimeter scale; the same scale as the ion cloud size. The nonlinear nature of frequency doubling of pulsed lasers also tends to exacerbate intensity inhomogeneities across beam profiles, which are further convolved with their overlap with the ion density. As a result of all these factors, the overall efficiency of our state preparation and detection is most easily characterized by the number of Hf^+ ions detected as eEDM signal, and is least subject to errors when averaged over days or even weeks. Thus, our sensitivity improvement in going from Generation 1 to Generation 2 can be summed up in the comparison of two numbers: Averaged over the Generation 1 eEDM dataset, our Hf^+ signal was about 7 ions per experiment cycle at late Ramsey times (where we get most of our phase sensitivity). In Generation 2 as of May 2019, we typically count about 400 ions per experiment cycle at late

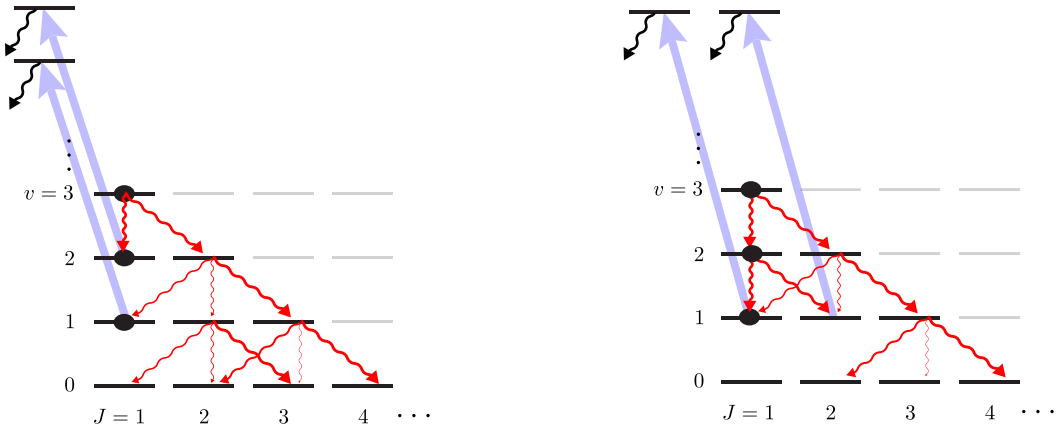

(a) Original scheme (b) Improved scheme

Figure 5.9: Paths of rovibrational spontaneous decay from initially populated $J = 1$ levels in the $^3\Delta_1$ electronic state of HfF^+, showing (a) original and (b) improved vibrational cleanup schemes for preventing background in $^3\Delta_1(v = 0, J = 1)$. The $J = 1$ levels in several vibrational states are populated by transfer from $^1\Sigma^+$ and M_F pumping in $^3\Delta_1$. In the original scheme, some population could still reach $v = 0, J = 1$. In the improved scheme, cleanup lasers (blue) driving the $^3\Sigma^-_{0^+} \leftarrow {}^3\Delta_1$ (1,1) P(1) and P(2) transitions prevent any decay to $^3\Delta_1(v = 0, J = 1)$ and reduce the decay to $^3\Delta_1(v = 0, J = 2)$.

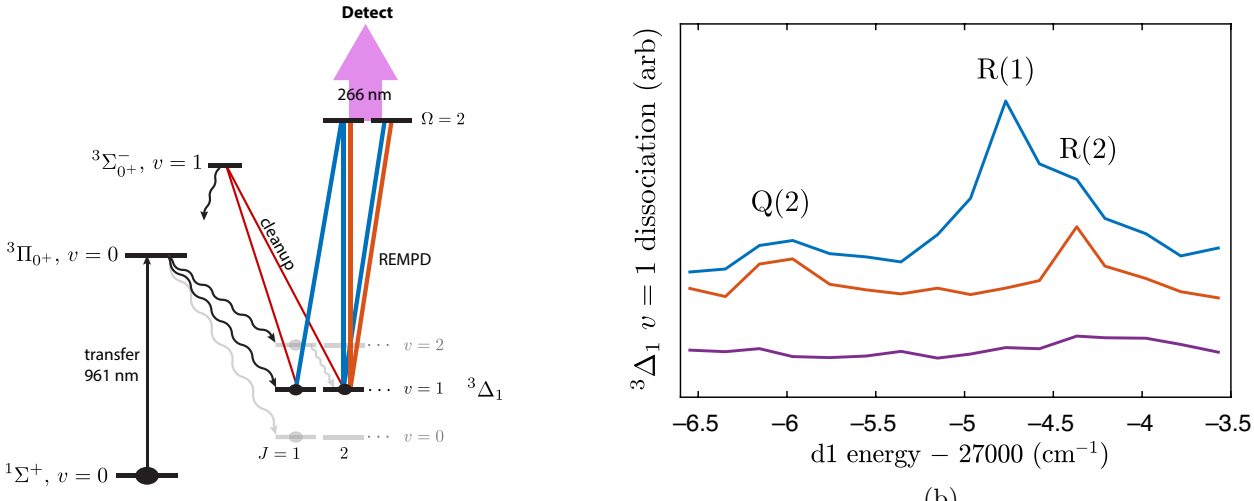

(a) (b)

Figure 5.10: Depletion spectroscopy of $^3\Delta_1(v = 1)$ using "cleanup" lasers driving the $^3\Sigma^-_{0^+} \leftarrow {}^3\Delta_1\,(1,1)$ transition at 818.4 nm. Population is transferred from $^1\Sigma^+(v = 0, J = 0)$ with 961 nm laser light driving the $^3\Pi_{0^+} \leftarrow {}^1\Sigma^+\,(0,0)$ transition, causing some spontaneous emission into $^3\Delta_1(v = 1)$. In the blue trace, no cleanup lasers are applied, so three rotational lines are observed in the REMPD spectrum (b). In the red trace, the $J = 1$ state is depleted, and in purple, both $J = 1$ and $J = 2$ are depleted.

Ramsey time. We have thus attained a factor of about 50 in count rate, or about a factor of 7 in overall sensitivity based on count rate alone.

Chapter 6

Oriented photodissociation

6.1 Photodissociation before Generation 2

Until Fall 2018, we performed resonance-enhanced multiphoton dissociation (REMPD) in the same way as described in Refs. [82, 91]: We use a pair of UV lasers, one a tunable grating-stabilized dye laser that is frequency doubled with a nonlinear crystal (See Appendix C) and one a fixed-frequency 266 nm quadrupled YAG, to photodissociate HfF^+ into Hf^+ and F. The Hf^+ are then detected on an MCP (Fig. 6.1). The "resonance-enhanced" aspect of REMPD allows us to resolve rotational states of HfF^+ with the first photon. The second photon dissociates the molecule from the intermediate state, and its resonance width is essentially determined by the width of the vibrational wavefuction of the intermediate state (Fig. 6.2, [61]).

Very little is known qualitatively about the states of HfF^+ in the vicinity of 30000 cm^{-1}, where our REMPD intermediate state is located. In the group's initial studies, performed by Huanqian, Kang-Kuen, Matt, and Kevin, essentially every available laser was sent through the chamber simultaneously, and the frequency of one laser was tuned while monitoring for photodissociation [82]. The survey scan found several transitions, all of which had intermediate states with quantum number $\Omega = 0$. Due to the large number of electronic states in HfF^+ and the high degree of mixing, particularly amongst excited states, J and Ω are expected to be the only good quantum numbers for REMPD intermediate states. Some of the observed transitions appeared to follow a vibrational progression with $\omega_e \approx 600$ cm^{-1}, some variation in relative coupling strength to $^1\Sigma^+$ vs. $^3\Delta_1$ was observed.

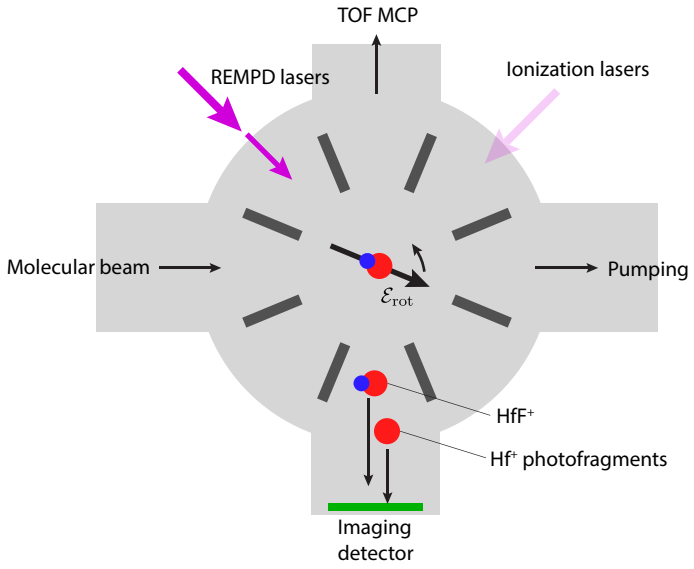

Figure 6.1: Top view of the Generation 2 ion trap, showing the locations of REMPD lasers and the imaging MCP detector. Space constraints prevent us from having perfectly $\sigma^{\pm}$-polarized REMPD lasers while also having $\mathcal{E}_{\rm rot}$ parallel to the MCP face for optimal imaging.

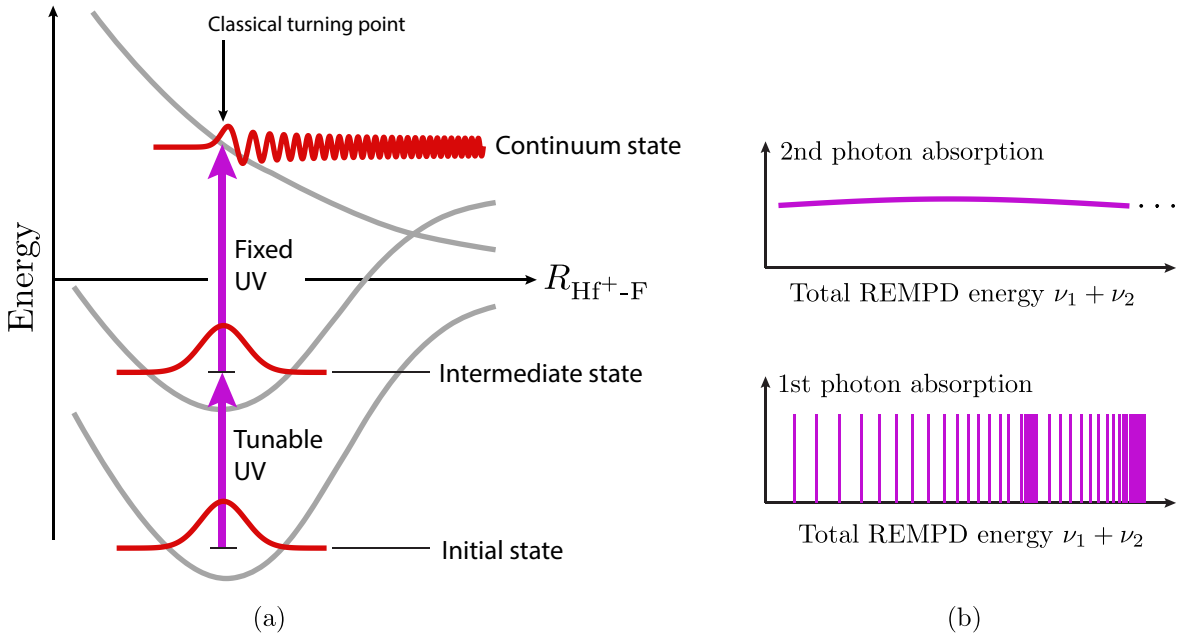

Figure 6.2: (a) Energy levels and (b) qualitative 1st and 2nd photon absorption in REMPD, as described in Section 6.1. One tunable UV laser drives a bound-bound transition in HfF^+, and a fixed UV laser drives the bound intermediate state into the continuum of dissociating states. The absorption spectrum of the tunable UV laser is typical of bound-bound transitions in diatomics, while the absorption of the second photon is a very slowly varying function of energy, determined by the Franck-Condon overlap of the intermedate and final state wavefunctions (the *reflection approximation* [61]).

The Generation 1 REMPD scheme has the advantage of very high quantum efficiency, but its drawback is excess noise arising from our grating-stabilized pulsed dye laser. The particular variety of dye laser we use for REMPD lases on several longitudinal modes simultaneously, leading to a spectral width on the order of 0.06 cm^{-1} or 1.8 GHz. Worse still is that the relative strength of these longitudinal modes varies stochastically from one laser pulse to the next. We believe this broad spectral width is the cause of excess noise we observe in our photodissociation yield. A comparable situation was considered in a 1988 theory [56], where the authors considered the excess noise that would be observed in the intensity of resonance fluorescence of an atomic vapor in the presence of laser phase noise. Their model, shown in Fig. 6.3, qualitatively agrees with the behavior of our observed excess noise as a function of the first REMPD laser detuning.

While in the Generation 1 eEDM measurement, this excess noise was undoubtedly present, it was simply drowned out by the shot noise on our $\lesssim 10$ ions per experiment cycle. Now with hundreds to thousand of detected Hf^+ per cycle, excess noise has become impossible to ignore. After struggling against this and other sources of noise for several months, we decided to pursue a scheme for a differential measurement that had been floating around the lab for a few months: oriented photodissociation. With a single-shot differential measurement of relative ion populations, all noise arising from pulsed lasers (include ablation, ionization, and dissociation) becomes common mode, and is greatly suppressed. In this chapter, I describe the implementation of this scheme, which has been a resounding success.

6.2 Imaging photofragments & new ideas

In Fall 2017, led by Yuval, we implemented imaging of Hf^+ ions via rapidly ($\lesssim 500$ ns) switching off the high voltage bias on the phosphor screen in between the arrival times of Hf^+ and HfF^+. Upon our first imaging of dissociation from $^1\Sigma^+$, $v = 0$, $J = 0$, we observed a distinctive dipolar pattern of the photofragments, shown in Fig. 6.4. Our immediate thoughts were along the lines of "that's cool" and "is that useful?" Some thought led us to the conclusion that it might be possible for the orientation of the molecules set by $\boldsymbol{\mathcal{E}}_{\text{rot}}$ to be preserved through the

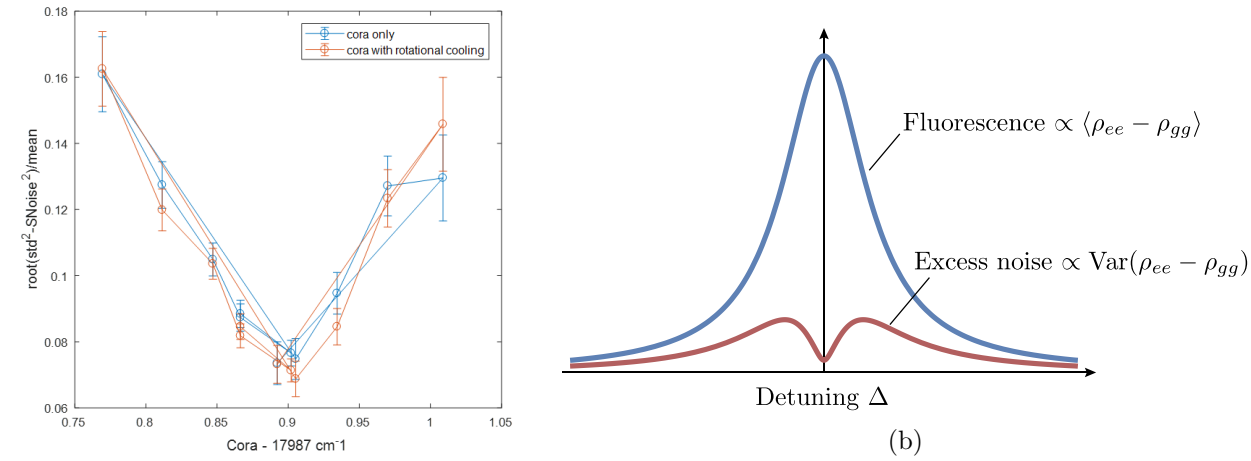

(a) (b)

Figure 6.3: (a) Observed excess noise as a function of first dissociation laser ("Cora") detuning from resonance. (b) Theoretical model of fluorescence of an atomic transition and excess noise in photon counts as a function of laser detuning, using a phase diffusion model of laser linewidth, from Ref. [56].

photodissociation process, resulting in a distribution of photofragments that depended on the Stark doublet, i.e., on $M_F\Omega$.

The initial outlook for the usefulness of this sort of oriented photodissociation seemed discouraging, as we were under the impression that a simultaneous detection was of limited usefulness, unless it was a simultaneous detection of both $M_F = \pm 3/2$ states in the same Stark doublet. However, as discussed in Chapter 7, this is not the case. In fact, a simultaneous measurement of a single M_F state in both Stark doublets is extremely useful for removing excess noise due to ion creation, state preparation, and photodissociation. Until fully appreciating this fact somewhat later, my personal motivation for pursuing the theoretical development described in Section 6.3 was simply that it was interesting.

The primary outcome of the theoretical and numerical investigation detailed in Section 6.3 was the conclusion that in order to attain this doublet-resolved photodissociation, we needed an intermediate state for REMPD that had total angular momentum projection quantum number $|\Omega| > 0$. At that time, all observed intermediate states for photodissociation had $|\Omega| = 0$; they were the results of the investigation described in Refs. [82, 91]. To find at state with $|\Omega| > 0$, we would need to perform more survey spectroscopy. Embarking on several weeks of survey spectroscopy can seem like a daunting task at the outset, and much of the delay between having this idea and completing our survey scan was due to the discouraging prospect that we might not find any states with the desired property. A further concern was the fact that the only practical direction available for us to scan was towards lower total dissociation energy (a redder first photon), resulting inevitably in lower-energy products and degraded radial resolution set by the finite temperature of our ion cloud. The reason for this limitation is that the scans in Ref. [82] cover the spectral region from frequency doubled 548 nm (~ 36500 cm^{-1}) to about 618 nm (~ 32360 cm^{-1}). Generating shorter wavelengths than 548 nm with a dye laser necessitates pumping with 355 nm light, and dealing with shorter dye degradation times – something we were not willing to do, as the eEDM experiment is sufficiently bogged down by equipment maintenance as it is.

Fortunately, we received a push in the right direction from Prof. Tanya Zelevinsky from

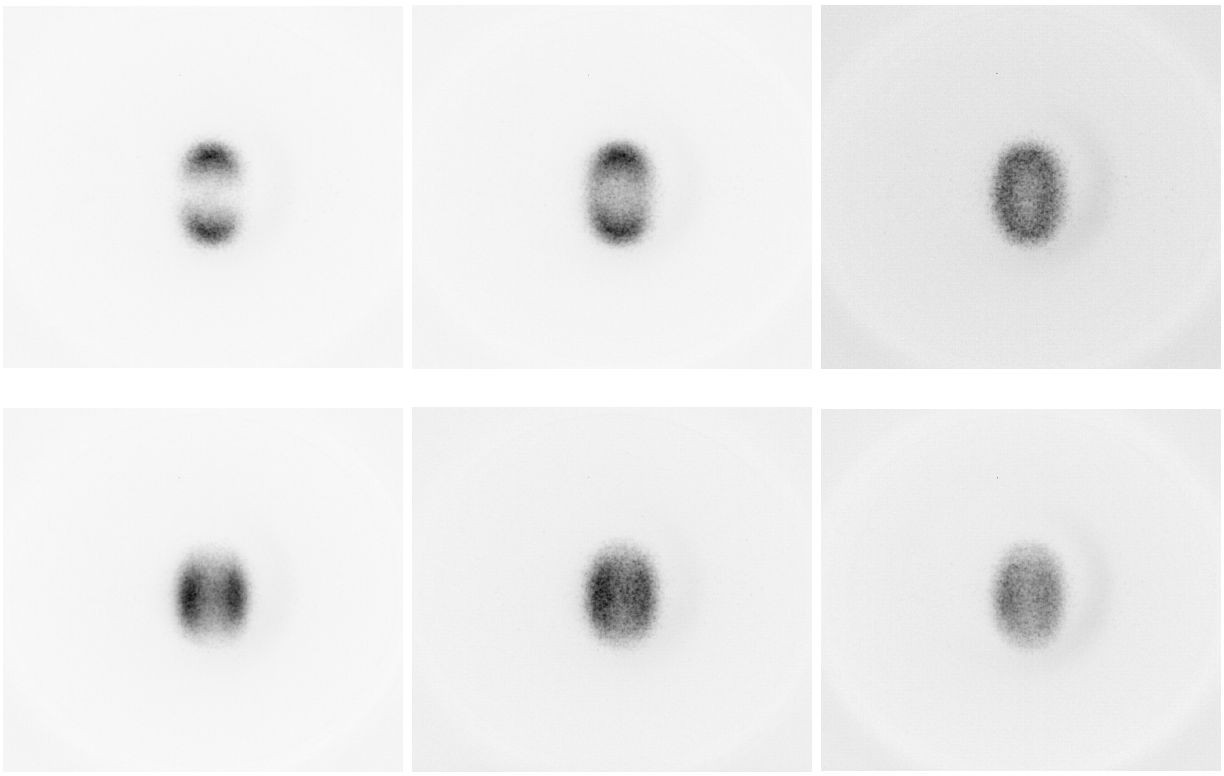

Figure 6.4: Imaged angular distribution of photofragments resulting from REMPD of HfF^+ ions initially in the $^1\Sigma^+$ state, with the first transition tuned to the R(0), R(1), and P(1) rotational lines in the left, middle, and right columns respectively. Average of about 25 shots. In the top row, the 266 nm laser is horizontally polarized, while in the bottom row, 266 nm is vertically polarized. This shows that the bound-to-continuum transition is perpendicular ($\Delta\Omega = \pm 1$).

Columbia University, who visited Jun's group in Summer 2018. Her group has had considerable success studying photodissociation of ultracold $^{88}Sr_2$ [86], and her familiarity with the theory provided us with confidence in an idea that we did not have much background knowledge on. She felt strongly that the doublet-resolved dissociation should work, as our theory (and the semiclassical approximation) predicted. Motivated by her expertise, we collected several thousand cm^{-1} worth of spectra in Fall 2018, as described in Section 6.4.

6.3 Theory

After our initial observation of the dumbbell-like angular distribution of photofragments resulting from dissociation of $^1\Sigma^+$ molecules, we applied the well-established theory of photofragmentation to address one central question: How does the angular distribution of photofragments in the lab frame $I(\theta, \phi)$ depend on the quantum numbers of the initial, intermediate, and final states, and on the laser polarizations? As discussed in Section 2.1, the high Z of the Hf nucleus, the presence of f-shell electrons in Hf, and the ionic nature of the $Hf^{2+} - F^-$ bond led us to expect that the high-lying and dissociating states of HfF^+ are many in number and complex in structure. We therefore do not expect to be able to make any predictions of the radial distribution of the photofragments beyond the maximum value of their kinetic energy, which is set by the UV lasers' wavelengths compared to the dissociation threshold.

Photofragment distributions are particularly pretty to look at, and they have been studied in some detail since initial work by Zare and others in the 1960s, summarized in the review in Ref. [135]. Due to the very large multiplicity of possible interfering channels in a photofragmentation process, the application of a fully quantum mechanical theory is quite complicated. This has motivated quasiclassical expressions, which were explored in some detail for homonuclear molecules in recent work from Prof. Tanya Zelevinsky's group [85].

Because the theory side of photofragmentation I describe here is primarily motivational rather than quantitative, I will make essentially every available approximation, retaining only what is necessary to determine the requirements for orienting the photofragments. We begin with Eq. (7)

of Ref. [10], and adapt it to describe the angular distribution of photofragments from a two-photon dissociation process. We take our initial state to be a mixture of magnetic sublevels in a single rotational level represented by a density matrix ρ, our intermediate states are denoted $|J_n\Omega_n M_n\rangle$ where we fix J_n and Ω_n, and our final states are denoted by a subscript f. We assume the final state has a well-defined value of $|\Omega_f|$ (the axial recoil approximation), but multiple J and M levels are accessible. The resulting formula for the photofragment distribution is

$$\begin{aligned} I(\theta,\phi) \propto & \sum_{\pm|\Omega_f|} \sum_{J'_f\, J_f} \sum_{M'_F\, M_F} \mathcal{D}^{J_f\,*}_{M_f\Omega_f}(\phi,\theta,0)\, \mathcal{D}^{J'_f}_{M'_f\Omega_f}(\phi,\theta,0) \sqrt{(2J'_f+1)(2J_f+1)} \\ & \sum_{(\Omega_n M_n)} \sum_{(\Omega'_n M'_n)} \sum_{(\Omega_i M_i)} \sum_{(\Omega'_i M'_i)} \langle J_f\Omega_f M_f|\, T_2\, |J_n\Omega_n M_n\rangle \, \langle J_n\Omega_n M_n|\, T_1\, |J_i\Omega_i M_i\rangle \\ & \times \left\langle J_i\Omega'_i M'_i\right|\, T_1^\dagger\, \left|J_n\Omega'_n M'_n\right\rangle \left\langle J_n\Omega'_n M'_n\right|\, T_2^\dagger\, \left|J'_f\Omega_f M'_f\right\rangle \left\langle J_i\Omega'_i M'_i\right|\, \rho\, |J_i\Omega_i M_i\rangle\,, \end{aligned} \tag{6.1}$$

where the parentheses under the summation signs indicate that this sum simply runs over magnetic sublevels and parity doublet states within a single rotational level. Note that because REMPD is able to resolve rotational levels of the initial and intermediate states, there is no summation over J_i or J_n. The spherical tensor operators T_1 and T_2 represent electric dipole transition operators, and their matrix elements are given by

$$\begin{aligned} \left\langle J'\Omega' M'\right|\, (-\boldsymbol{D}\cdot\boldsymbol{\mathcal{E}})\, |J\Omega M\rangle = & -\sum_p (-1)^p\, \mathcal{E}_{-p}\, (-1)^{M'-\Omega'} \begin{pmatrix} J' & 1 & J \\ -M' & p & M \end{pmatrix} \\ & \times \sum_q \begin{pmatrix} J' & 1 & J \\ -\Omega' & q & \Omega \end{pmatrix} \sqrt{(2J+1)(2J'+1)}\, D_q, \end{aligned} \tag{6.2}$$

where $\mathcal{E}_{-p}$ should be replaced with the appropriate components for the corresponding dissociation laser polarization.

In this treatment, I have not included nuclear spin. However, as long as we are primarily interested in the angular distribution created by a single $|J_i\Omega_i M_i\rangle$ or an incoherent mixture of the same M_i and opposite Ω_i (and thus opposite Stark doublet), the angular distribution will be the same as if we were considering a single $|F\Omega M_F\rangle$ level including nuclear spin. Alternatively, if the hyperfine structure is not resolved by the first dissociation laser (which is the situation in the HfF^+

eEDM experiment), then we can simply trace over the nuclear spin degree of freedom to obtain the matrix elements of the density matrix $\langle J_i \Omega_i' M_i' | \, \rho \, | J_i \Omega_i M_i \rangle$, as discussed in Ref. [10].

In late 2017, I implemented Eq. (6.1) in Matlab in order to generate simulated angular distribution images [1] . The adjustable parameters when generating an angular distribution are the initial, intermediate, and final state quantum numbers $|\Omega_i|$, J_i, $|\Omega_n|$, J_n, and $|\Omega_f|$; the REMPD laser electric fields $\boldsymbol{\mathcal{E}}_{1,2}$; and the rotating electric field $\boldsymbol{\mathcal{E}}_{\rm rot}$, which sets the quantization axis with respect to which we define the density matrix elements. In the rotating wave approximation, and since the intensity distribution is unnormalized (so the magnitude of $\boldsymbol{\mathcal{E}}$ does not matter), the electric fields of the lasers can simply be represented as complex unit vectors similar to Jones vectors [58]. For example $\boldsymbol{\mathcal{E}} = (\hat{X} + i\hat{Y})/\sqrt{2}$ represents a circularly polarized laser propagating along $\hat{Z}$. For the transition dipole matrix elements, the choice of $|\Omega|$ for each of the initial, intermediate, and final states sets ahead of time whether a given transition is parallel or perpendicular, and we can simply set $q = \Omega' - \Omega$ and $D_q = 1$ in Eq. (6.2). In order to reduce the enormous multiplicity of possible channels [suggested by the number of summation symbols in Eq. (6.1)], I first eliminated possible combinations of quantum numbers that would be zero by standard selection rules such as angular momentum conservation in 3j symbols. I then evaluated Eq. (6.1), with the summations essentially restricted to the nonzero channels.

Figure 6.6 shows simulated photofragment angular distributions arising from REMPD of $^1\Sigma^+$, generated using Eq. (6.1). I show photofragment distributions for a selection of REMPD rotational lines with $\Omega_n = 0$ and $|\Omega_f| = 1$, which is the choice of intermediate and final Ω that shows good agreement with our experimental observations. In all of the images in Fig. 6.6, I calculated the distribution for an incoherent mixture of initial magnetic sublevels M_i in order to match our experimental conditions immediately after REMPI of HfF to form HfF^+ in the ion trap.

[1] Strictly speaking, I implemented a simulation that was equivalent to Eq. (6.1) but not exactly the same. In order to account for nuclear spin, I simulated the first transition using a master equation approach for the bound-bound system. I then traced over nuclear spin degrees of freedom and applied Eq. (7) of Ref. [10] for the bound-continuum transition. The problem with this implementation is that if the first transition is completely forbidden (for example due to poor choice of laser polarization), the intermediate state will remain empty. Then since I renormalized the intermediate state wavefunction for the bound-continuum transition, the results would essentially be junk. In a more recent implementation, I used Eq. (6.1) directly, which gives the same results in all situations where the first transition is allowed.

$\lvert\Omega_i\rvert$	$\lvert\Omega_n\rvert$	$\lvert\Omega_f\rvert$	Line	$\lvert\Omega_i\, M_i\rangle$	$\boldsymbol{\epsilon}_1$	$\boldsymbol{\epsilon}_2$	$I(\theta,\phi)$
0	0	1	R(0)	Mixed	$\sigma^{\pm}$	π	$\sin^4\theta\,\cos^2\phi$
			P(1)				$\sin^2\theta$
1	2	3	R(1)	$\lvert-1,1\rangle$	σ^+	σ^+	$\sin^{12}(\theta/2)$
				$\lvert1,1\rangle$			$\cos^{12}(\theta/2)$
1	2	1	R(1)	$\lvert-1,1\rangle$	σ^+	σ^-	$\sin^{12}(\theta/2)$
				$\lvert1,1\rangle$			$\cos^{12}(\theta/2)$
1	1	1	Q(1)	$\lvert-1,1\rangle$	π	π	$\cos^2\theta\,\sin^4(\theta/2)$
				$\lvert1,1\rangle$			$\cos^2\theta\,\cos^4(\theta/2)$

Table 6.1: Selected analytical expressions for the angular distribution of photofragments, resulting from Eq. (6.1). In the oriented cases $|\Omega_i| > 0$, $\boldsymbol{\mathcal{E}}_{\rm rot}$ is directed along $\theta = 0$. The laser polarizations $\boldsymbol{\epsilon}_{1,2}$ are represented in standard atomic notation, and $\sigma^{\pm} = \sigma^+ + \sigma^-$, with the quantization axis set by $\mathcal{E}_{\rm rot}$ as shown in Fig. 6.5. Note that the angular distributions are unnormalized.

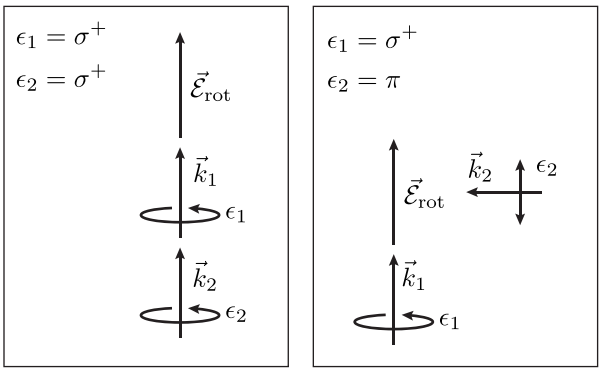

Figure 6.5: Examples of possible laser polarizations for oriented REMPD. Note that due to the availability of optical access in our vacuum chamber and the location of the ion detector, not all configurations of lasers and quantization axis (set by $\mathcal{E}_{\rm rot}$) are practical.

Apart from the aspect ratio, which is set by the relative trap secular frequencies and the time between dissociation and detection, the results match our experimental observations in Fig. 6.4 qualitatively very well.

Figure 6.7 shows simulated photofragment distributions arising from REMPD of oriented populations [2] in the stretched magnetic sublevels of $^3\Delta_1$, $J = 1$. The selection of transitions shown illustrates the main finding of this theoretical investigation, which is that an oriented photofragment distribution can only be obtained when $|\Omega_n| > 0$. By eye, the theoretically "most oriented" distribution is obtained when $|\Omega_n| = 1$, $|\Omega_f| = 1$, and REMPD is performed on the Q(1) line. However, as shown in Fig. 6.8, this distribution in fact has a small amplitude for photofragments to be ejected in the "wrong" hemisphere. If we define the doublet contrast as

$$\mathcal{K} = \left| \frac{N_1 - N_2}{N_1 + N_2} \right| \tag{6.3}$$

where $N_{1,2}$ are

$$N_1 = \frac{N}{4\pi} \int_0^{2\pi} \int_0^{\pi/2} I(\theta, \phi) \sin\theta \, d\theta \, d\phi, \qquad N_2 = \frac{N}{4\pi} \int_0^{2\pi} \int_{\pi/2}^{\pi} I(\theta, \phi) \sin\theta \, d\theta \, d\phi,$$

then we find a theoretical maximum value of $15/16 \approx 0.94$ for the $|\Omega_f| = 1$ case. Experimentally, Q branch transitions are problematic because they are likely to be contaminated with background from population in higher J levels. The recipe for the overall best contrast in dissociation of $^3\Delta_1$ (albeit by a slim margin) is to use the R(1) line of a transition where $|\Omega_n| = 2$ and $|\Omega_f| = 1$ or 3, attaining a theoretical value $\mathcal{K} = 63/64 \approx 0.98$. In reality, of course, there are other factors that go into the choice of an intermediate state for oriented photodissociation, which are discussed in the next section.

6.4 Survey spectroscopy

In Fall 2018, we decided to pursue oriented photodissociation in HfF^+, and therefore we had to perform survey spectroscopy in order to find an appropriate transition. Our search was subject

[2] By "oriented populations," I mean a pure quantum state with a well-defined orientation of the Hf and F nuclei in the laboratory frame.

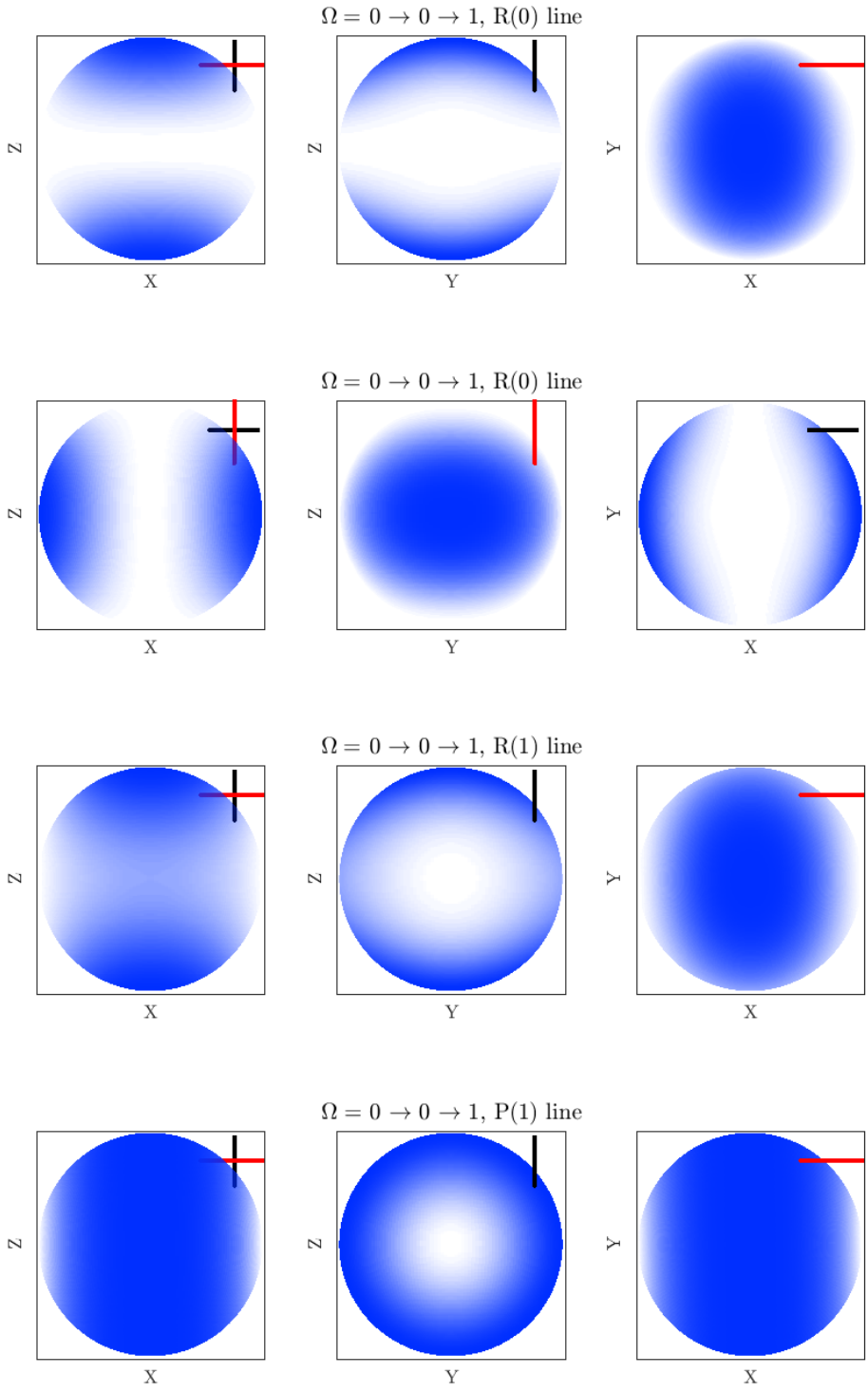

Figure 6.6: Simulated photofragment angular distributions resulting from REMPD of HfF^+ in the $^1\Sigma^+$ electronic state in an incoherent mixture of all magnetic sublevels, calculated using Eq. (6.1). The black and red lines in the top right indicate the polarization of the first and second dissociation photons, respectively. Three views are shown for each distribution to give a sense of the 3D shape.

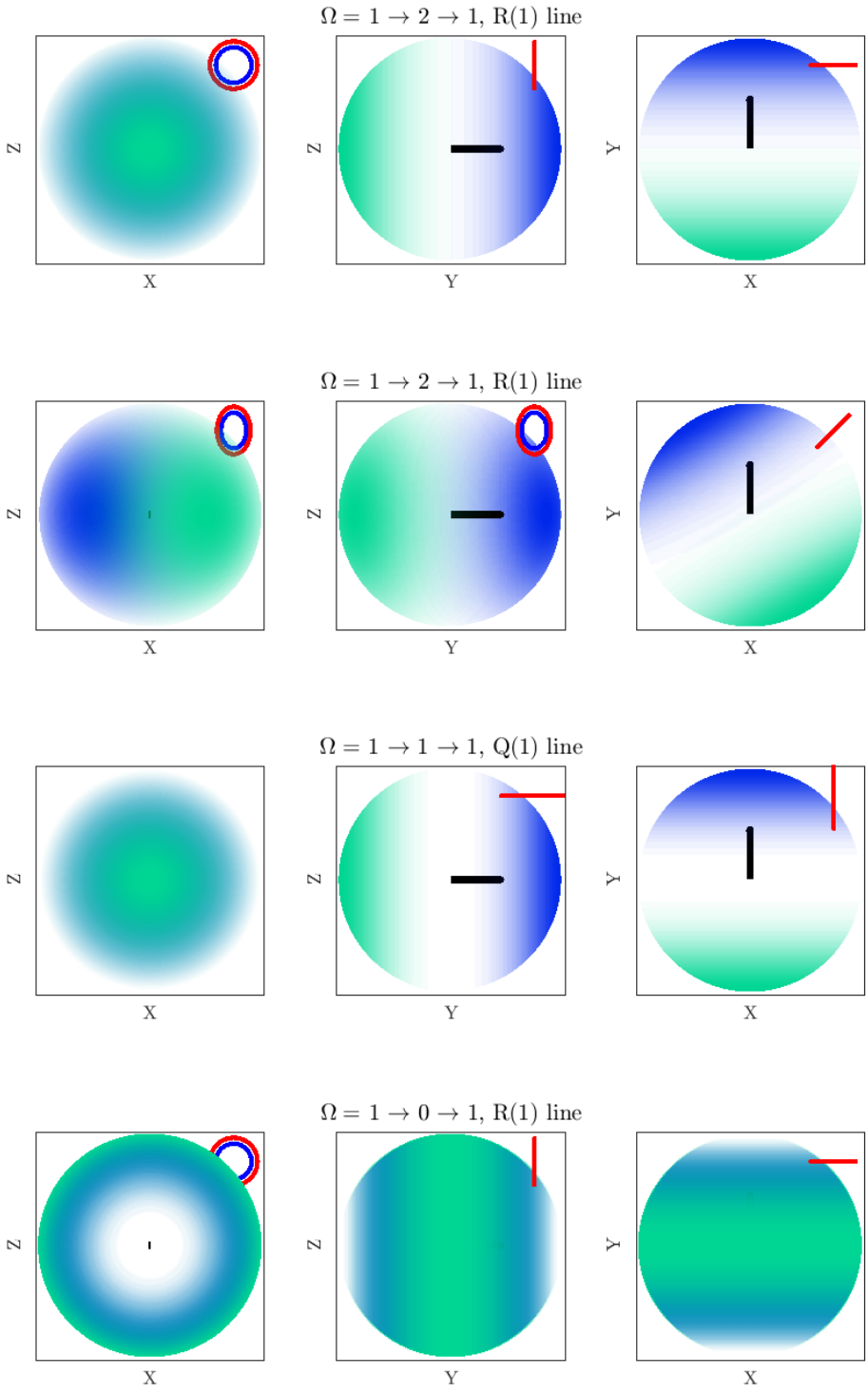

Figure 6.7: Simulated photofragment distributions resulting from REMPD of HfF^+ in the $^3\Delta_1$ electronic state, with opposite Stark doublets populated. The blue and red lines in the top right indicate the polarization of the first and second dissociation photons, respectively, while the thick black arrow indicates the direction of $\boldsymbol{\mathcal{E}}_{\mathrm{rot}}$. Oriented distributions are obtained only when $\Omega_n \neq 0$.

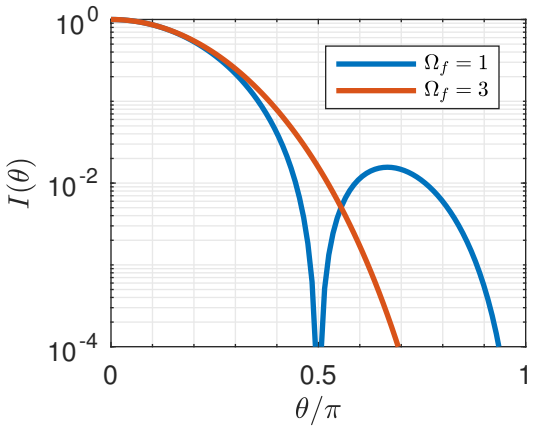

Figure 6.8: Comparison of theoretical oriented photofragment distributions $I(\theta)$ for REMPD transitions $\Omega = 1 \rightarrow 2 \rightarrow 1$ and $\Omega = 1 \rightarrow 2 \rightarrow 3$, each with the corresponding optimal polarizations. Initial population is only in one Stark doublet. Expressions are listed in Table 6.1, lines 4 and 8. In the case $\Omega_f = 1$, an additional lobe of photofragments appears on the "wrong" hemisphere, reducing the attainable contrast.

to several constraints, some of which were self-imposed: Firstly, the second photon must be either 266 nm, or have the same frequency as the first. This is because 266 nm is the highest energy photon we can straightforwardly produce with our existing lasers, and we would like the photofragments to have as much kinetic energy as possible, both for the purposes of spatially separating the oriented photofragments in time of flight, and to decrease the probability of predissociation. Secondly, the first photon, which drives a bound-bound transition in HfF^+, must be a wavelength that we can produce with our Sirah Cobra-Stretch dye laser, pumped with 532 nm light from our Spectra-Physics LAB-170 pulsed YAG. Thus, it must lie between 274 nm ($\sim$ 36500 cm^{-1}) and about 380 nm ($\sim$ 26300 cm^{-1}). The region from 274 nm to 309 nm ($\sim$ 32400 cm^{-1}) was surveyed by Matt Grau, Huanqian Loh, Kevin Cossel, and Kang-Kuen Ni in Refs. [82, 91] with no $|\Omega_n| > 0$ transitions found, so this left us only with the region 26300-32400 cm^{-1} to search.

Aside from the technical requirements, there are other qualitative features that are desirable in an oriented REMPD transition. The most obvious is strength: We would like the largest signal possible, and we are restricted to a single dissociation laser pulse in order to image oriented photofragments. Thus, the strongest transition is desirable. Unfortunately, this desirable property runs counter to the necessity of scanning at a lower first photon energy than had been done in Ref. [91], because a lower energy bound-free transition will result in a higher probability of predissociation. The effects of total dissociation energy on the strength and angular distribution of a REMPD transition are shown in Figure 6.9. In red, a low energy above threshold results in a higher probability of predissociation and radiative decay back to bound states and thus a weaker transition, as well as lower kinetic energy of the photofragments. A higher energy above threshold (green) results in a stronger dissociation transition, as more kinetic energy is gained by the nuclei before they encounter an avoided crossing and have the potential to undergo radiative decay. An additional qualitative feature of REMPD transitions shown in Fig. 6.9 is the possibility of multiple dissociation channels resulting in different kinetic energies of the products, and potentially even different angular distributions.

Before beginning survey scans, we had to implement a frequency doubling and pointing

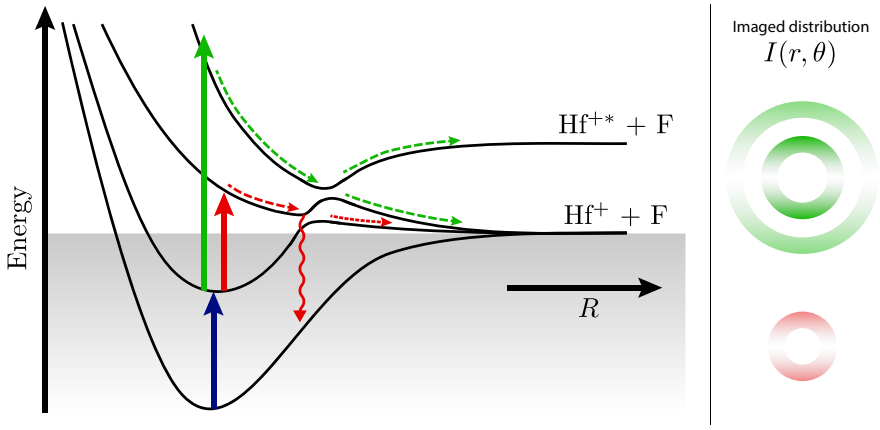

Figure 6.9: Schematic potential energy curves showing the effect of total dissociation energy on photofragment distributions. Red: low energy above threshold results in a high probability of radiative decay. Green: high kinetic energy results in a lower probability of radiative decay. Different energies above threshold may also result in multiple dissociation channels becoming available, resulting in concentric rings of photofragments.

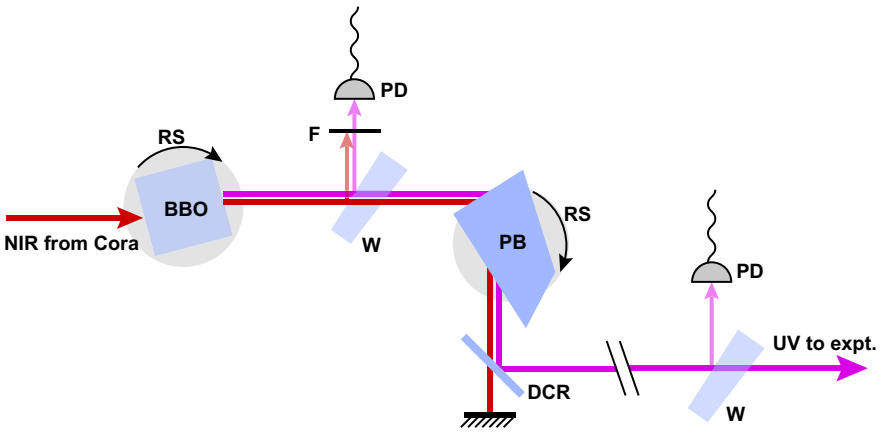

Figure 6.10: Schematic layout of the frequency doubling and pointing compensation setup for the Cobra-Stretch dye laser, which provides the first UV photon for REMPD. The first rotation stage optimizes the phase matching of the BBO for UV production, while the second rotation stage compensates for changes in beam pointing due to the BBO rotation. Abbreviations: BBO, β-barium borate crystal; RS, rotation stage; W, wedged pickoff; F, UV-passing filter; PD, photodiode; DCR, dichroic mirror.

compensation setup for the Cobra-Stretch dye laser (Cora), which is approximately equivalent to the commercial autotracker we have for the PrecisionScan dye laser (Bertha). This setup is shown schematically in Fig. 6.10. Visible to NIR light produced by the dye laser is sent through a BBO crystal mounted on a rotation stage (RS) to produce UV light. A wedged glass pickoff (W) and photodiode (PD) with a UV-passing filter positioned close to the BBO detects the UV light, providing information on the optimal angle of the BBO. A second pickoff and photodiode positioned close to the experiment provides information on the UV pointing, which is fed back to the angle of a Pellin-Broca prism (PB) mounted on a second rotation stage. All feedback is performed in a Labview script of the "state machine" type described in Matt Grau's thesis [49] running on a control PC (Pikachu). While in principle the photodiodes and rotation stages could be used in a closed-loop control system to servo Cora's UV fluence being provided to the experiment, we found it more useful and straightforward to create a lookup table of BBO and PB angles versus Cora wavelength, then use that lookup table during the scan. The procedure for calibrating the angles is as follows:

(1) Go to the next Cora resonator position in the scan.

(2) Perform a 1D scan of the BBO angle and find the maximum UV energy measured by PD1. Go to this angle with the BBO.

(3) Perform a 1D scan of the PB angle and find the maximum UV energy measured by PD2. Go to this angle with the PB.

(4) Record the wavelength as measured by the Bristol wavemeter, as well as the two rotation stage angles.

We found that the positions of the rotation stages were sufficiently repeatable and the pointing of the vis-NIR light from the dye laser was sufficiently stable that a single coarse scan over the lasing range of a dye would remain valid essentially indefinitely (months and counting), requiring only occasional small adjustments to the pointing of the fundamental light into the BBO.

We performed REMPD scans over the 26300-32400 cm^{-1} range using Rhodamine 640, Pyridine 1, Pyridine 2, and Styryl 8 dyes[3] . An approximately 800 cm^{-1} region from 30000-30800 cm^{-1} was inaccessible with these dyes, and would only have been accessible with DCM dye in DMSO solvent, which we were hesitant to use due to the dye's probable carcinogenic nature [132] and the propensity of DMSO solvent to transport dye molecules through the skin [63]. Figure 6.11 shows the raw survey spectroscopy data from the coarse scans, which were performed at a resolution of about 0.2 cm^{-1} . We performed three main "chops" to distinguish transitions originating from different low-lying states of HfF^+: dissociation products in the "ionization only" chop can arise only from the $^1\Sigma^+$, $v = 0$ state, as our REMPI process is vibronically selective by energy conservation. In the "754 nm" chop, we applied cw laser light to drive the $^3\Sigma^-_{0^+} \leftarrow {}^1\Sigma^+$ $(0, 0)$ transition for a few tens of milliseconds, causing population to decay into excited vibrational levels of $^1\Sigma^+$ and $^3\Delta_1$ with a slight preference for $^1\Sigma^+$, which can subsequently be photodissociated. In the "961 nm" chop, we applied cw light to drive the $^3\Pi_{0^+} \leftarrow {}^1\Sigma^+$ $(0, 0)$ transition, which leads to decay primarily to the $^3\Delta_1$ state, albeit to multiple vibrational levels as dictated by Franck-Condon factors (see Ref. [28], Table 5.7).

[3] These are Sirah Lasertechnik brand names for dyes. Their proper chemical names are much less concise.

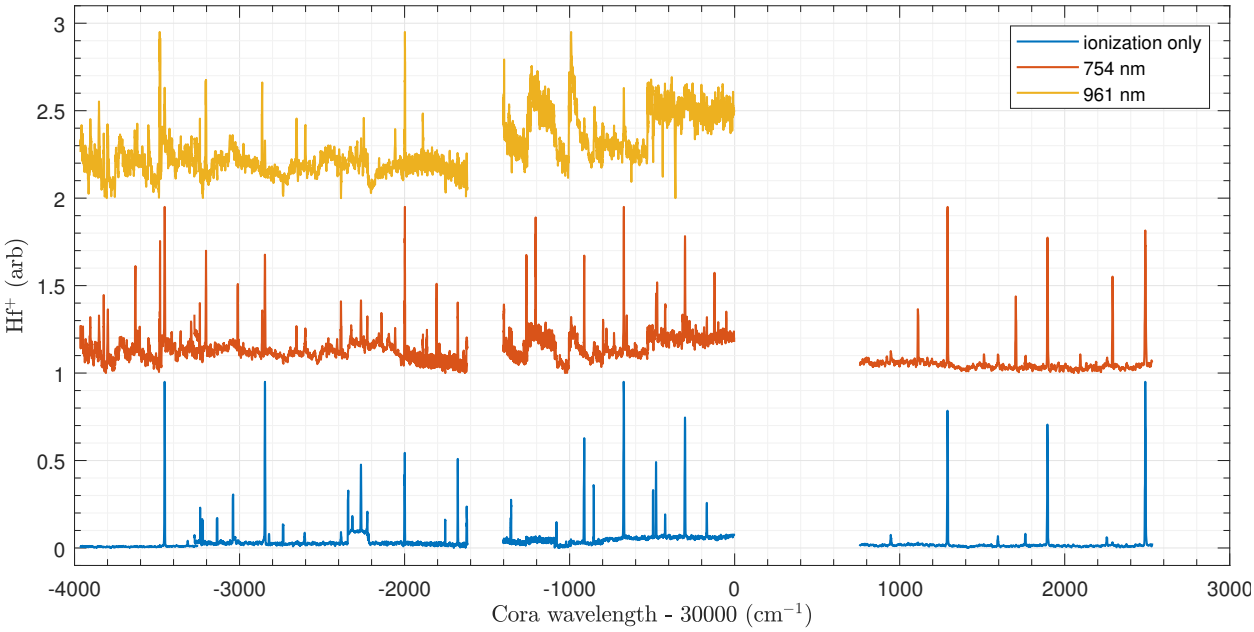

Figure 6.11: REMPD survey spectroscopy of HfF^+ in the 26000-32500 cm^{-1} region for the first photon. The second photon wavelength is 266 nm for all observed transitions.

For all of the strong transitions we observed in the coarse REMPD survey scans, we performed fine scans in order to identify the Ω value of the intermediate state. For transitions originating from $^1\Sigma^+$, we know that the only possible values of $|\Omega_n|$ were 0 and 1, so we needed only to look for a Q branch in the rotational band to identify the character of the intermediate state. For transitions originating from $^3\Delta_1$, we identified $|\Omega_n|$ by optical pumping from $^1\Sigma^+$ using the 961 nm laser (Toptica) driving the $^3\Pi_{0^+} \leftarrow {}^1\Sigma^+$ $(0,0)$ transition to populate the lowest rotatioal levels of $^3\Delta_1$. The lowest allowed value of J is Ω, so if $\Omega_n = 0$, 1, or 2, there should be 3, 2, or 1 line(s), respectively, visible in the dissociation spectrum of $^3\Delta_1$, $J = 1$. Successively more lines become visible if $^3\Delta_1$ is populated via the P(1), R(1), or R(2) lines of the $^3\Pi_{0^+} \leftarrow {}^1\Sigma^+$ $(0,0)$ band. Figure 6.12 shows this process for a transition to an $\Omega = 2$ state observed at a first dissociation photon energy ≈ 27752 cm^{-1} .

A table of observed dissociation transitions and their Ω values (where identified) is given in Table D.1 in Appendix D. The most important results of our search are an $\Omega = 2$ transition at 27137 cm^{-1} and an $\Omega = 1$ transition at 26516 cm^{-1} both originating from $^3\Delta_1$, $v = 0$. Also important is an $\Omega = 1$ transition at 27154 cm^{-1} originating from $^1\Sigma^+$, $v = 0$, which is useful for diagnostic purposes, for example for checking the efficiency and timescale of our microwave and optical pumping-based transfer scheme.

6.5 Imaging oriented photodissociation

Having performed survey spectroscopy and found a few candidate REMPD transitions for oriented detection, we then had to attempt to observe oriented photofragments, and find the set of experimental parameters that provides the best separation of the Stark doublets for eEDM spectroscopy. In contrast to the conditions in the experiments described in Ref. [85] and other works from the Zelevinsky lab, our molecules are not particularly cold or tightly confined. As a result, the effects of finite temperature may degrade our ability to resolve the Stark doublets.

Photodissociation imparts the Hf^+ molecules with a momentum kick with an angular probability distribution given by $I(\theta, \phi)$ of the form discussed in Section 6.3. Thus at zero elapsed

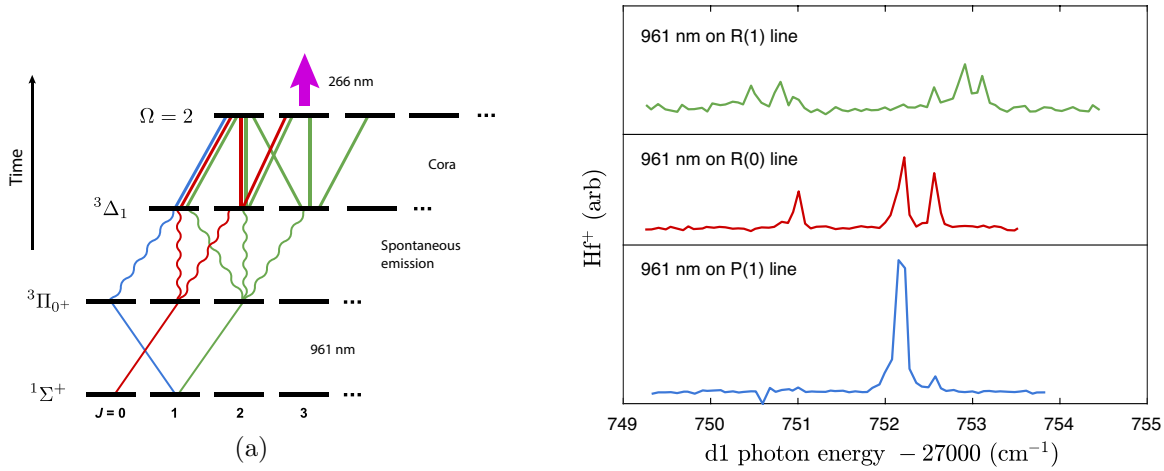

Figure 6.12: Identification of the Ω value of a REMPD intermediate state by selective population of $^3\Delta_1$ through $^3\Pi_{0^+}$. Part (a) shows the trajectories of population through rotational levels of electronic states, while part (b) shows the resulting REMPD spectrum. A single strong line when populating on the P(1) line with 961 nm indicates that this is an $\Omega = 2$ transition.

time after REMPD, the ion cloud (now composed of HfF^+ + Hf^+) would be indistinguishable from the distribution before dissociation. In theory, to observe $I(\theta, \phi)$, we should wait a time $\pi/(2\omega_{sec})$ where ω_{sec} is the trap secular frequency (assumed isotropic). In reality, however, the trap secular frequencies are not typically isotropic, and the travel time of the ion cloud to the imaging MCP detector is not infinitesimal compared to a trap secular period. Furthermore, we need to temporally separate Hf^+ from HfF^+ by ≈ 1 μs in order to image only Hf^+ and prevent contamination of our images by a HfF^+ background. Thus, the optimal imaging of Stark doublets could not be "dialed in," and involved some searching in the parameter space spanned by the time of dissociation, the phase of the trap rf, and the duration and strength of the kick to the imaging MCP.

The Imaging MCP kick settings were set roughly by hand in order to temporally resolve Hf^+ and HfF^+, and the timing of dissociation was scanned (via serial communication with the DDG controlling Olga's flashlamps and Q-switch) to find the maximum contrast, as shown in Fig. 6.13. The fact that the asymmetry plateaus for a range of Cora delay while the number of counted Hf^+ ions is not depleted indicates that we have overcome the limitation set by the ion cloud's initial size and temperature, and are instead limited by some other factor setting our doublet contrast. A reduction of the number of counted Hf^+ accompanied by a plateau of the contrast would indicate that we are losing Hf^+ ions off the side of the detector.

Figure 6.14 shows images of photofragment distributions resulting from REMPD of the upper and lower Stark doublets using the transition at 27137 cm^{-1} . Conditions in these images in terms of energy resolution are about as good as we could achieve. Two distinct radii of photofragments are visible, showing that (at least) two channels are populated by the 266 nm dissociation transition – a possibility described in Fig. 6.9. The inner radius (lower energy) photofragments have a much less shell-like and more spherical appearance, which is likely a result of the convolution of the finite initial ion cloud size and temperature with the kick imparted by photodissociation.

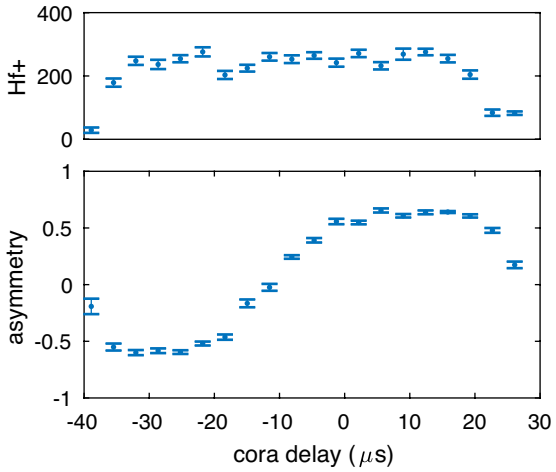

Figure 6.13: Left-right asymmetry $\mathcal{K}$ of oriented photofragments as a function of dissociation laser timing. The offset of the horizontal axis is arbitrary; the fall of trap time occurs around 30 μs. The flat sections indicate that our peak asymmetry is no longer limited by the ion cloud temperature.

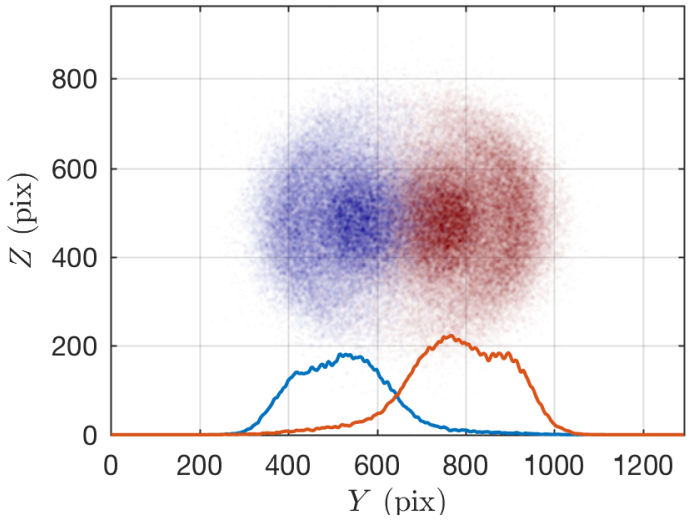

Figure 6.14: Images and integrated distributions of upper and lower Stark doublets using the oriented REMPD transition at a first photon wavelength of $\sim$ 27137 cm^{-1} .

6.5.1 Doublet depletion

Our first studies of oriented dissociation were performed using our old "semi-coherent" Raman transfer with Stella (899.7 nm) and Toptica (tuned to 986.4 nm), where we can selectively populate a single Stark doublet. While this technique is good for populating only one doublet, it is not particularly good for attaining high signal-to-noise. Subsequently, we were able to produce population in a single doublet by first populating all of $^3\Delta_1$ by optical pumping, then performing our 1083 nm M_F pumping to push all of the $^3\Delta_1$ population to the same M_F level in both Stark doublets, and finally depleting one doublet using an 814.5 nm beam tuned to the $^3\Sigma^-_{0^+} \leftarrow {}^3\Delta_1$ $(0,0)$, Q(1) transition (Fig. 6.15a). This doublet depletion beam is picked off from the 814.5 nm depletion laser and sent along the $-\hat{Z}$ direction via the breadboard above the chamber in order to avoid the Doppler shifts caused by the RF trap and $\mathcal{E}_{\text{rot}}$. At early trap time, our Doppler FWHM is on the order of 40 MHz, so with $\mathcal{E}_{\text{rot}} \approx 60$ V/cm, the Stark separation of ~ 110 MHz allows us to selectively deplete either the upper or lower doublet.

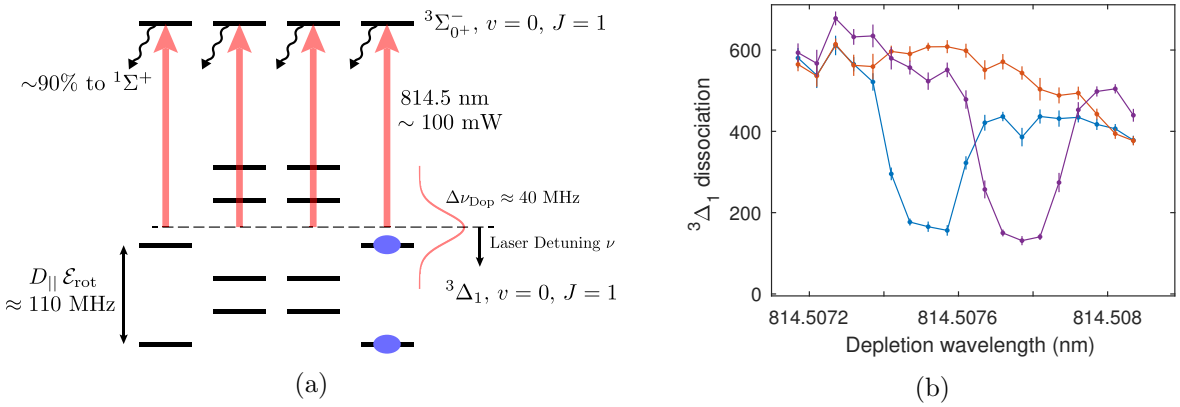

Figure 6.15: Laser depletion of Stark doublets to verify orientation-selective dissociation and to measure the doublet contrast $\mathcal{K}$. A portion of the 814.5 nm light usually used for strobed M_F depletion is picked off and applied vertically down the trap axis to attain the minimum Doppler width of about 40 MHz. While π polarization is shown in (a), the laser does not in fact have a well-defined polarization with respect to the quantization axis set by $\mathcal{E}_{\mathrm{rot}}$, so which M_F levels are depleted is set by energy alone. (b) Observed reduction in $^3\Delta_1$ dissociation yield as a function of 814.5 nm laser detuning, showing population depletion of each Stark doublet.

Chapter 7

Generation 2 eEDM signal

In the Generation 2 eEDM measurement with HfF^+, we have made significant improvements to our signal size, at the cost of increased complexity of analysis. In addition, with our increased signal size, sources of excess noise are no longer drowned out by the shot noise on Hf^+. As a result, we will need to be much more quantitative in our understanding of sources of excess noise and systematic effects arising from incorrect signal parameterization. In this chapter, I provide some preliminary thoughts in the direction of signal parameterization for Generation 2, consider the fundamental limits to our measurement precision, and estimate our statistical sensitivity based on present performance and known sources of excess noise. These ideas are by no means complete, and I hope they will simply contribute as a jumping off point for what will certainly be a challenging analysis.

7.1 Center cut

In our Generation 1 eEDM experiment with HfF^+, we would intentionally populate only one Stark doublet at a time, and our analysis in fact relied on this assumption to the extent that we had to include a "doublet contamination" systematic to account for spurious population in the "wrong" Stark doublet (See supplemental material of Ref. [16]). Now in our Generation 2 measurement, we are populating both Stark doublets by design, and doublet contrast $\mathcal{K}$ is never perfect. As a result, our analysis must take into account the doublet contamination that will always be present, in order to prevent a host of dangerous systematic effects.

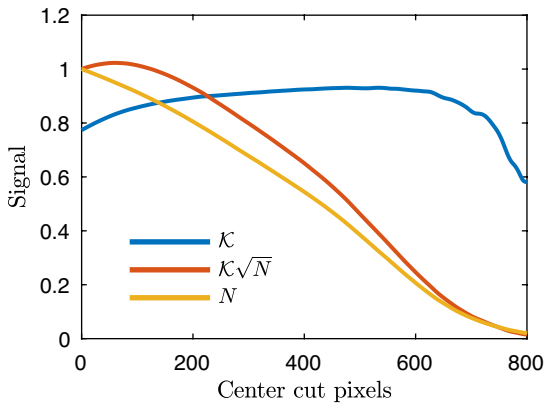

Figure 7.1: Effect of a central signal cut on doublet contrast $\mathcal{K}$, signal size N, and frequency sensitivity $\mathcal{K}\sqrt{N}$. The horizontal axis is the width of a rectangular region, centered around $Y = 650$ pixels in Fig. 6.14. The lines $\mathcal{K}\sqrt{N}$ and N are normalized to 1 at zero cut pixels.

One step we can take in the early stages of data processing to suppress the effects of finite doublet contrast is to make a signal cut in the region of our Hf^+ images where an ion has approximately equal probability of belonging to either Stark doublet, and so cannot meaningfully contribute to a doublet-odd signal such as the eEDM. Such a cut must be made after many images are collected at different Ramsey times, so that averaged over all images, the doublet populations will be very nearly equal. We can then average together all images and take the center of mass in order to find the central Y value, Y_0. We then reprocess each image, throwing away ion counts that occurred within a band $|Y - Y_0| \leq Y_{\text{cut}}/2$. The remaining ion counts N, doublet contrast $\mathcal{K}$, and sensitivity $\mathcal{K}\sqrt{N}$ resulting from this "center cut" procedure is shown in Fig. 7.1. A center cut of about 60 pixels results in a slight increase in eEDM sensitivity, but the doublet contrast $\mathcal{K}$ increases significantly. To suppress systematic effects, we will likely want to cut even more than the value of Y_{cut} that gives the highest sensitivity.

7.2 Parameterizing the eEDM signal

In order to fit our Ramsey fringes and extract an eEDM signal, we need to develop a parameterized model of the fringes' functional form. Just as in Generation 1, the population in each of

the M_F levels after the Ramsey sequence can be parameterized as

$$\begin{aligned} N_{a/b} &= \frac{N_0\, e^{-\Gamma t}}{2}\left(1 \mp \mathcal{C}^u e^{-\gamma t}\cos\Phi^u \pm \mathcal{O}^u\right), \\ N_{c/d} &= \frac{N_0\, e^{-\Gamma t}}{2}\left(1 \mp \mathcal{C}^l e^{-\gamma t}\cos\Phi^l \pm \mathcal{O}^l\right), \end{aligned} \tag{7.1}$$

where t is the Ramsey time, $\Gamma \approx (2\text{ s})^{-1}$ is the $^3\Delta_1$ decay rate, γ is the spin coherence decay rate, $\mathcal{C}^{u/l}$ is the fringe contrast, N_0 is the initial Ramsey-phase-averaged ion number, and $\Phi^{u/l}$ is the Ramsey phase. I have allowed some parameters to have a doublet dependence (for example $\mathcal{C}^{u/l}$), but kept others such as γ and N_0 with only an average value. The ion numbers in each state from Equation (7.1) can also be expressed in the form

$$N_a = N_t\, p_u, \qquad N_b = N_t\,(1-p_u), \qquad N_c = N_t\, p_l, \qquad N_d = N_t\,(1-p_l) \tag{7.2}$$

where $N_t = N_0\, e^{-\Gamma t}$, which more clearly expresses the fact that the Ramsey experiment has a binomially distributed outcome.

At this stage, our finite doublet contrast presents a complication: we cannot directly detect the populations N_{abcd}, but only mixtures $N_{a/c}$ and $N_{b/d}$. I will refer to the detected ion number mostly consisting of state a with an uppercase subscript N_A, and similarly for the other states. Using our existing definition of the doublet contrast from Eq. (6.3), the detected number in each of these populations is

$$\begin{aligned} N_{A/B} &= \left(\frac{1+\mathcal{K}}{2}\right) N_{a/b} + \left(\frac{1-\mathcal{K}}{2}\right) N_{c/d} \\ N_{C/D} &= \left(\frac{1-\mathcal{K}}{2}\right) N_{a/b} + \left(\frac{1+\mathcal{K}}{2}\right) N_{c/d} \end{aligned} \tag{7.3}$$

From each of these populations, we form an asymmetry $\mathcal{A} = \pm(2N/N_t - 1)$, where $N_t = N_0\, e^{-\Gamma t}$, and the upper and lower signs depend on the sign of the nominal M_F of the state detected. The asymmetries resulting from states in the same Stark doublet are nominally equal, so we are left with two asymmetries that are each a sum of interference fringes of the form familiar from our Generation 1 eEDM measurement, $\sim -\mathcal{C}e^{-\gamma t}\cos\Phi + \mathcal{O}$, with weights $(1 \pm \mathcal{K})/2$. We then separate the contrast, offset, and phase into their doublet-even and doublet-odd parts, e.g. $\mathcal{C}^{u/l} = \mathcal{C}^0 \pm \mathcal{C}^D$,

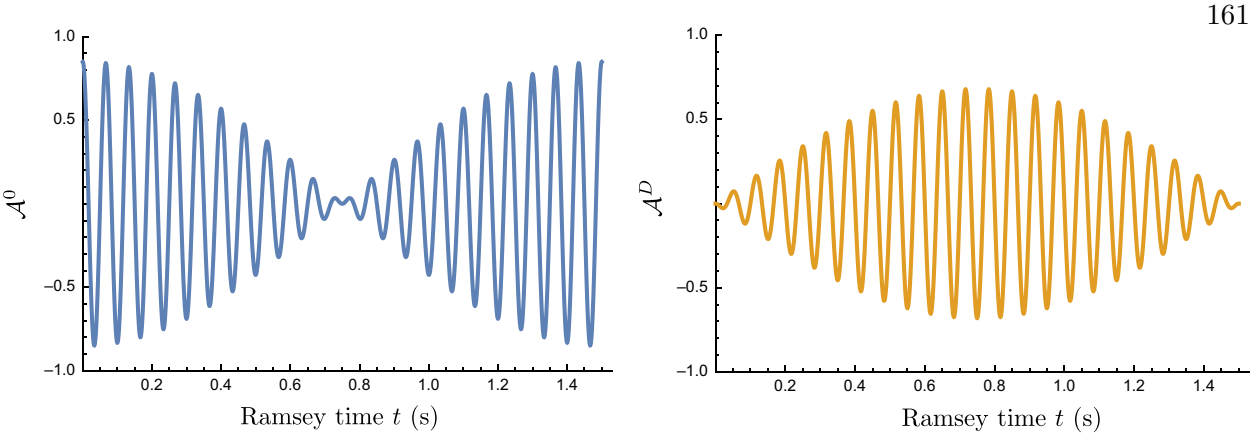

Figure 7.2: Typical appearance of doublet-even and doublet-odd asymmetry signals. The peak-to-peak value of $\mathcal{A}^0$ is $\mathcal{C}$ (with a typical value of ~ 0.8) in the present parameterization, while the peak-to-peak value of $\mathcal{A}^D$ is $\mathcal{CK}$, where $\mathcal{K}$ has a typical value of ~ 0.75. I have reduced the value of f^0 to 15 Hz to more clearly show the Ramsey fringe, and I have taken $f^D = 0.33$ Hz. Here I have neglected decoherence and set $\gamma = 0$.

and rearrange the asymmetries to the doublet-even and doublet odd forms,

$$\begin{aligned}\mathcal{A}^0 &= \mathcal{C}^0 e^{-\gamma t}\cos\Phi^0\,\cos\Phi^D - \mathcal{C}^D e^{-\gamma t}\sin\Phi^0\,\sin\Phi^D + \mathcal{O}^0,\\ \mathcal{A}^D &= \mathcal{C}^D\mathcal{K} e^{-\gamma t}\cos\Phi^0\,\cos\Phi^D - \mathcal{C}^0\mathcal{K} e^{-\gamma t}\sin\Phi^0\,\sin\Phi^D + \mathcal{K}\mathcal{O}^D.\end{aligned} \tag{7.4}$$

With a parameterized model for our Ramsey signal, we can investigate the effects of fundamental and technical noise sources, and develop a data collection scheme to extract a quiet measurement of Φ^D, which contains the eEDM signal.

7.3 Limits to precision

The form of the doublet-even and -odd asymmetries given in Eq. (7.4) is somewhat hairy, and error propagation on these expressions will quickly become a mess. In this section, I will step back from a full error propagation calculation to think about the limits to the precision of a basic Ramsey measurement [1] . I then investigate the effects of some realistic experimental imperfections such as noisy particle number, and finite and noisy state preparation and detection efficiency. These simpler situations will introduce standard mathematical tools for propagation of uncertainties,

[1] Strictly I will be discussing the standard quantum limit (SQL), which is less fundamental than the Heisenberg limit. Experiments that do not utilize spin-spin correlations cannot beat the SQL.

identify some reasonable approximations we should make in subsequent calculations, and highlight the ways in which experimental imperfections limit our precision.

7.3.1 Noise in an ideal Ramsey experiment

For experiments on single trapped atomic ions, where essentially an infinite number of photons can be scattered from a trapped ion and its presence in the trap can be determined with extremely high fidelity, the fundamental limit to the measurement of a quantum phase is *quantum projection noise*. Quantum projection noise for a single trapped ion is the variance in the number of "successes" (say, finding the particle in the state $|a\rangle$) for a given number of trials N,

$$\mathrm{E}\left(N_a\right) = Np, \qquad \mathrm{Var}\left(N_a\right) = Np(1-p), \tag{7.5}$$

where $\mathrm{E}\left(\right)$ and $\mathrm{Var}\left(\right)$ denote the expectation and variance, $p = \cos^2(\phi/2)$ is the probability of finding the state $|a\rangle$ after a Ramsey sequence that starts in $|b\rangle$, and where $\phi = \omega t$ is the quantum phase evolved between states $|a\rangle$ and $|b\rangle$.

Of course, N repeated Ramsey experiments on a single particle is equivalent to one Ramsey experiment on an ensemble of a fixed number of particles N, where both N_a and N_b can be measured with perfect fidelity. In this situation, if we to form the asymmetry (sometimes also called the polarization or the visibility) $\mathcal{A} = (N_a - N_b)/(N_a + N_b)$, we would find

$$\mathcal{A} = 2p - 1 = \cos\phi, \qquad \mathrm{Var}\left(\mathcal{A}\right) = \frac{4p(1-p)}{N} = \frac{\sin^2\phi}{N}. \tag{7.6}$$

In an experiment where we would like to measure an energy splitting $\hbar\omega = \Delta E$ with the highest precision possible, we should repeat trials with the Ramsey time t chosen so that $\mathrm{E}\left(\phi\right) = \pi/2$. (This fact is fairly intuitive, but it is also discussed in the context of maximum likelihood estimation in Ref. [133]). At $\phi \approx \pi/2$, the variance of the asymmetry is $\mathrm{Var}\left(\mathcal{A}\right) \approx 1/N$, leading to $\mathrm{Var}\left(\phi\right) = \frac{1}{N}$. In the case that the Ramsey fringe has imperfect contrast characterized by $0 < \mathcal{C} < 1$, we simply obtain $\mathrm{Var}\left(\phi\right) = (\mathcal{C}^2 N)^{-1}$. The variance on ϕ leads to an uncertainty on ω and thus and uncertainty on the measured energy ΔE,

$$\mathrm{Std}\left(\Delta E\right) = \frac{\hbar}{\mathcal{C}t\sqrt{N}}. \tag{7.7}$$

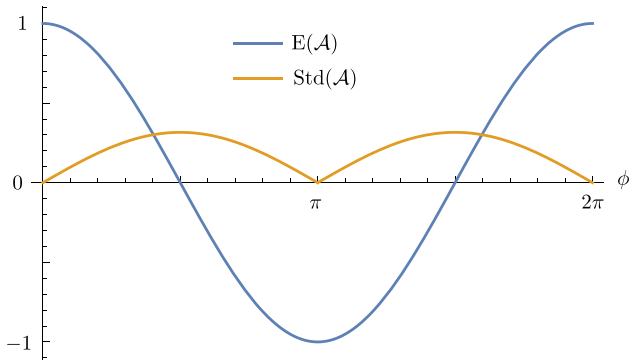

Figure 7.3: Mean and standard deviation of the asymmetry for a single experimental trial with $n = 10$ particles and perfect detection efficiency. The behavior of the standard deviation as a function of Ramsey phase ϕ is characteristic of quantum projection noise.

This result is known as the *standard quantum limit* or the quantum projection noise limit, and can be beaten by techniques such as spin squeezing, which take advantage of correlations between particles [14].

7.3.2 Varying particle number

In contrast to the situation in experiments with one or a few trapped atomic ions, our state detection on the HfF^+ eEDM experiment is destructive, and we must produce a new sample with every experimental cycle. The number of ions we create and trap is probabilistic, and has an unknown distribution. In the most optimistic scenario, where we produce molecules from a much larger sample with a small probability, we should expect $N \sim \text{Poisson}\left(\overline{N}\right)$. However, due to a variety of factors including fluctuations in ionization laser intensity and frequency, we instead observe a distribution that can be approximated as a Gaussian with a mean $\mathrm{E}(N) = \overline{N}$ and variance $\mathrm{Var}(N) = \overline{N} + (\alpha\overline{N})^2$. We refer to the parameter α as "fractional noise," and it typically takes a value between 0.2 - 0.4 for our HfF^+ creation.

We might want to ask how a varying particle number affects our ability to reach the quantum projection noise limit $\mathrm{Var}(\phi) = 1/(\mathcal{C}^2\overline{N})$. In particular, investigating this question will introduce several useful concepts, which we can then apply to questions of how more complex and realistic effects affect our measurement noise on the HfF^+ eEDM experiment. When N is a random vari-

able, the number of particles ending up in state $|a\rangle$ can be thought of as a sum over N independent Bernoulli distributed variables d_i, where i runs from 1 to N. For a Bernoulli variable with probability p, we have $\mathrm{E}(d_i) = p$ and $\mathrm{Var}(d_i) = p(1-p)$. The total number of particles ending up in state $|a\rangle$ and $|b\rangle$ is $N_{a/b} = \sum_{i=1}^{N} d_i$, but now N is *also* a random variable. We can evaluate the mean and variance of $N_{a/b}$ using *Wald's lemma* and the *law of total variance* [12],

$$\begin{aligned} \mathrm{E}(N_a) &= \mathrm{E}\left(\sum_{i=1}^{N} d_i\right) = \mathrm{E}(N)\,\mathrm{E}(d) = \overline{N}p \\ \mathrm{Var}(N_a) &= \mathrm{E}(\mathrm{Var}(N_a|N)) + \mathrm{Var}(\mathrm{E}(N_a|N)), \\ &= \overline{N}p(1-p) + p^2\mathrm{Var}(N) \end{aligned} \tag{7.8}$$

where the vertical bar notation in $\mathrm{E}(N_a|N)$ means "the expectation of N_a conditional on a fixed value of N." The law of total variance is used when random variables depend on the values of other random variables: the *total* variance of N_a depends on the fact that it is a Binomially distributed variable in its own right, and would have a variance $Np(1-p)$ for a fixed value of N – this accounts for the first term in Eq. (7.8). The second term arises from the random variation in N. Similarly, the total variance on N_b is

$$\mathrm{Var}(N_b) = \overline{N}p(1-p) + (1-p)^2\mathrm{Var}(N), \tag{7.9}$$

where $1-p$ has replaced p since particles that are not projected onto state $|a\rangle$ end up in state $|b\rangle$. When calculating the asymmetry, it's therefore also important to consider the covariance between the populations in state $|a\rangle$ and $|b\rangle$, which we can do with the *law of total covariance*,

$$\begin{aligned} \mathrm{Cov}(N_a, N_b) &= \mathrm{E}(\mathrm{Cov}(N_a, N_b|N)) + \mathrm{Cov}(\mathrm{E}(N_a|N), \mathrm{E}(N_b|N)). \\ &= -\overline{N}p(1-p) + p(1-p)\mathrm{Var}(N). \end{aligned} \tag{7.10}$$

The first term in Eq. (7.10) is the covariance of successes and failures in a binomial, and is negative because of the inherent anticorrelation between N_a and N_b.

Now, armed with expressions for the means, variances, and covariance of N_a and N_b in terms of the ion number and projection probability, we can express the variance of $\mathcal{A}$ similarly. Strictly speaking, $\mathcal{A}$ is a ratio of random variables and follows a *ratio distribution*, which has fairly nasty

properties [66, 76]. Provided $\overline{N}$ is large enough, we can approximate $\mathrm{Var}(\mathcal{A})$ with a Taylor series expansion, obtaining

$$\mathrm{Var}(\mathcal{A}) \approx \frac{4\overline{N}_a^2 \mathrm{Var}(N_b) + 4\overline{N}_b^2 \mathrm{Var}(N_a) - 8\overline{N}_a \overline{N}_b \mathrm{Cov}(N_a, N_b)}{(\overline{N}_a + \overline{N}_b)^4}. \tag{7.11}$$

Substituting in our expressions from Eqs. (7.8) to (7.10), we again find the same result as Eq. (7.6), $\mathrm{Var}(\mathcal{A}) = 4p(1-p)/\overline{N}$. Thus we see that measuring the populations of states $|a\rangle$ and $|b\rangle$ simultaneously in an idealized experiment allows for normalization of fluctuations in particle number, even in the presence of excess noise on ion production.

What if we cannot simultaneously detect states $|a\rangle$ and $|b\rangle$ in a single experimental cycle? In this case, the ion number is essentially uncorrelated from one experimental cycle to the next, and we can take $\mathrm{Cov}(N_a, N_b) = 0$. We will no longer have the favorable cancellation of excess noise that we had due to the covariance in Eq. (7.11), and instead we get

$$\mathrm{Var}(\mathcal{A}) = \frac{4p(1-p)}{\overline{N}} + 8\alpha^2 p^2 (1-p)^2 = \frac{\sin^2\phi}{\overline{N}} + \frac{\alpha^2 \sin^4\phi}{2}. \tag{7.12}$$

While the first term decreases with increasing $\overline{N}$, the second term is independent of $\overline{N}$ and thus represents a limit to measurement precision. We see that if we cannot simultaneously measure both spin states in order to normalize away ion number noise, the fractional noise will become dominant when $(\alpha\overline{N})^2 \gg 2\overline{N}$, which for our typical values of $\alpha \approx 0.3$ occurs by about $\overline{N} \approx 50$. While in the Generation 1 eEDM experiment with HfF^+ we had $\overline{N} \lesssim 10$ so that quantum projection noise was dominant, in the Generation 2 experiment with $\overline{N} \gtrsim 500$, excess noise will easily dominate. Figure 7.4 shows the behavior of the signal-to-noise ratio (SNR) $1/\sigma_{\mathcal{A}}$ as a function of $\overline{N}$ (assuming perfect contrast).

One aspect of Eq. (7.12) worth mentioning is that even in the limit $\alpha \to 0$, we have required two separate experimental cycles to obtain a measurement of $\mathcal{A}$. We can no longer think of $\overline{N}$ as the number of particles detected in a single experiment cycle; rather it is the average number detected in *two* experimental cycles. To obtain the same number of measurements of $\mathcal{A}$, we must run the experiment for twice as long.

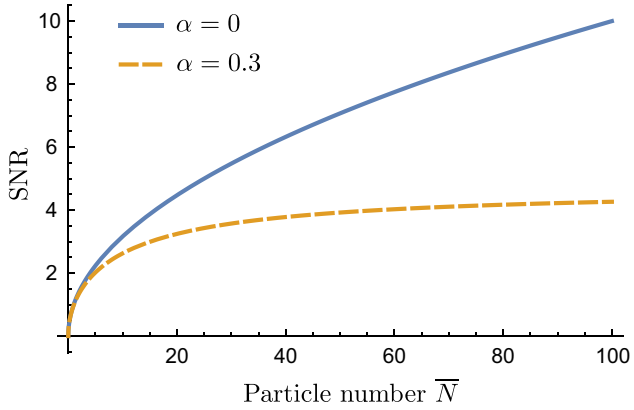

Figure 7.4: Signal-to-noise ratio (SNR) of a Ramsey phase measurement as a function of particle number, in the case where both spin state populations cannot be measured simultaneously. In the presence of excess noise α, the SNR approaches a constant value with increasing signal.

7.3.3 State preparation and detection efficiency

In Sections 7.3.1 and 7.3.2, we considered an experiment with perfect state preparation and detection efficiency, but in Section 7.3.2 allowed the particle number to be a random variable. What are the effects of finite state preparation and detection efficiency? We should expect that finite state preparation efficiency behaves in the same way as ion creation, since our only mathematical description of ion production so far has been to assign a mean $\overline{N}$ and variance $\overline{N} + (\alpha\overline{N})^2$ to the number of particles taking part in the Ramsey sequence. Indeed, this is the case: if we begin with our excessively noisy ion creation and follow this with a state preparation step with efficiency p_T (with subscript T alluding to transfer to the $^3\Delta_1$ state), we can use the law of total variance to obtain the mean and variance of the number N_u of molecules that participate in the Ramsey sequence in the upper Stark doublet,

$$\begin{aligned}
\mathrm{E}\left(N_u\right) &= \overline{N}\overline{p}_T \equiv \overline{N}_T \\
\mathrm{Var}\left(N_u\right) &= \overline{N}\overline{p}_T(1-\overline{p}_T) + \overline{p}_T^2\mathrm{Var}\left(N\right) + \overline{N}^2\mathrm{Var}\left(p_T\right) \\
&= \overline{N}_T + \overline{N}_T^2\left(\alpha^2 + \frac{\mathrm{Var}\left(p_T\right)}{\overline{p}_T^2}\right) \\
&= \overline{N}_T + \left(\alpha_T\overline{N}_T\right)^2,
\end{aligned} \tag{7.13}$$

where in contrast to the previous two sections, I have now allowed the probability of transfer p_T to have a variance, which could arise from laser intensity or frequency noise. In the last line, I have defined a new effective ion number $\overline{N}_T$ and a new fractional noise parameter $\alpha_T^2 = \alpha^2 + \mathrm{Var}\left(p_T\right)/\overline{p}_T^2$. Evidently, adding a binomial state preparation step has not changed the general characteristics of our ion number distribution, but has only reduced the mean ion number by its efficiency and added in quadrature to the fractional noise parameter. Thus, from now on we can lump together all ion creation and state preparation processes, and just take the number of ions participating in the Ramsey sequence to have a mean $\overline{N}$ and variance $\overline{N} + (\alpha\overline{N})^2$, as in the previous two sections.

What about a finite (and potentially varying) detection efficiency p_{det}? We can start here with Eqs. (7.8)-(7.10), and investigate the variance on the asymmetry calculated from N_a^{det} and N_b^{det}, the detected ion numbers in states $|a\rangle$ and $|b\rangle$. Again using the law of total variance, and

continuing under the assumption that N_a and N_b can only be measured on separate experimental trials, we find

$$\mathrm{Var}\left(\mathcal{A}\right) = \frac{4p(1-p)}{\overline{N}\overline{p}_{\mathrm{det}}} + 8p^2(1-p)^2\left(\alpha^2 + \frac{\mathrm{Var}\left(p_{\mathrm{det}}\right)}{\overline{p}_{\mathrm{det}}^2}\right), \tag{7.14}$$

where as before, $p = \cos^2(\phi/2)$ is the probability of projection onto state $|a\rangle$. Thus in the case that N_a and N_b can only be detected on separate trials, finite and noisy detection efficiency has essentially the same effects as state preparation efficiency: it reduces the effective number of particles that participate in the Ramsey experiment through the denominator $\overline{N}\overline{p}_{\mathrm{det}}$, and it contributes to excess noise that is independent of $\overline{N}$.

7.3.4 Thoughts on "the QPN limit"

In experiments with optical cycling, the effects of finite detection efficiency can be overcome, and it is possible to achieve $\sigma_\phi = (\mathcal{C}\sqrt{N})^{-1}$ even without collecting every photon emitted by the atoms or molecules, where N is the number of particles participating in the Ramsey sequence. However, the requirements on how many photons must be scattered by each particle are quite onerous, and there are some surprising requirements – for example, scattering photons until there is a high probability that each particle in the experiment will reach a dark state is in fact detrimental to the final SNR [76, 77].

On the HfF^+ eEDM experiment, we cannot presently detect via optical cycling, and the limit to our variance on the asymmetry is given by the first term in Eq. (7.14). In light of the progress we have made on differential detection as discussed in Chapter 6, the quantitative effects of which are discussed in the next few sections, we have been motivated to ask ourselves questions like "What is the standard quantum limit for our experiment?", and "If we measure $\sigma_\phi = (\mathcal{C}\sqrt{N_{\mathrm{d}}})^{-1}$ where N_{d} is the number of particles *detected* [in two experiment cycles, see discussion below Eq. (7.12)], is this the quantum projection noise limit?" Having seen the essentially interchangeable nature of finite state preparation and detection efficiency in the preceding two sections, my answer to this question is that yes, we can consider $\sigma_\phi = (\mathcal{C}\sqrt{N_{\mathrm{d}}})^{-1}$ to be limited by quantum projection noise. This is because our finite detection efficiency is interchangeable with a finite state preparation efficiency,

and due to this fact, the total number of particles participating in the Ramsey sequence is not a particularly important concept. Of course, our precision is also very much limited by our finite state preparation and detection efficiency! This is a semantic point, but the real takeaway is that when we find $\sigma_\phi = (\mathcal{C}\sqrt{N_\mathrm{d}})^{-1}$, we should be happy that technical noise sources are not contributing significantly to our measurement noise.

7.4 Methods of estimating Ramsey phase

In the preceding section, I used a form of the asymmetry

$$\mathcal{A} = \frac{N_a - N_b}{N_a + N_b}, \tag{7.15}$$

assuming that N_a and N_b could result from any pair of experimental cycles. However, other methods of assembling the asymmetry are possible. In particular, since the number of HfF^+ ions created (and thus Hf^+ detected) in neighboring experimental cycles are essentially uncorrelated, there is no reason to choose any particular pair of N_a and N_b. For this reason, we considered various possibilities for calculating $\mathcal{A}$ using various combinations of averaged values of N_a and N_b. For example, we can define two versions of the asymmetry,

$$\mathcal{A}_a = 2\frac{N_a}{\overline{N}} - 1, \qquad \mathcal{A}_b = 1 - 2\frac{N_b}{\overline{N}}, \tag{7.16}$$

where $\overline{N}$ is the total average number of particles taking part in the experiment. Both of these functions take the same value on average as $\mathcal{A}$. Of course, in reality, we cannot know the true mean $\overline{N}$ exactly, and must estimate it with a sample mean. We can then aggregate the datasets $\mathcal{A}_a$ and $\mathcal{A}_b$ together to form $\mathcal{A}$.

In the past, we have considered other forms of the asymmetry. Take, for example, the form

$$\mathcal{A}'_a = \frac{N_a - \overline{N}_b}{N_a + \overline{N}_b}, \qquad \mathcal{A}'_b = \frac{\overline{N}_a - N_b}{\overline{N}_a + N_b}. \tag{7.17}$$

The variance on $\mathcal{A}'_{a/b}$ is smaller than on the form in Eq. (7.16) by a factor of two, and for large numbers of trials so that $\mathrm{Var}\left(\overline{N}_{a/b}\right)$ is small, the mean is nearly identical. However, through

Monte-Carlo simulation, we have found that this form of the asymmetry is pathological: it is always over-scattered, i.e., the reduced χ^2 statistic is much greater than 1 for typical parameters. While I have not been able to show this analytically, for the rest of this thesis I will stick to the form of Eq. (7.16).

7.5 Noise on Generation 2 eEDM signal

Returning at last to the full form of the asymmetry from Section 7.2, we have that the doublet-even and doublet-odd asymmetries can be expressed in terms of the counted ion numbers in groups A through D as

$$\mathcal{A}^0 = \frac{N_A - N_B + N_C - N_D}{2N_t}, \qquad \mathcal{A}^D = \frac{N_A - N_B - N_C + N_D}{2N_t}, \tag{7.18}$$

where $N_t = \mathrm{E}\left(N_A + N_B + N_C + N_D\right)/2$ is the average number of ions in a *shot* at a given Ramsey time t, where there are two groups per shot as in Fig. 6.14. Fortunately, error propagation on these expressions is very straightforward, and we obtain

$$\begin{aligned} \mathrm{Var}\left(\mathcal{A}^0\right) &= \frac{1}{(2N_t)^2}\left[\sum_s \mathrm{Var}\left(N_s\right) + 2\mathrm{Cov}\left(N_A, N_C\right) + 2\mathrm{Cov}\left(N_B, N_D\right)\right] \\ \mathrm{Var}\left(\mathcal{A}^D\right) &= \frac{1}{(2N_t)^2}\left[\sum_s \mathrm{Var}\left(N_s\right) - 2\mathrm{Cov}\left(N_A, N_C\right) - 2\mathrm{Cov}\left(N_B, N_D\right)\right], \end{aligned} \tag{7.19}$$

where s runs over A-D. At this stage, we need to account for finite doublet contrast, which causes group A to consist of ions derived from both states $|a\rangle$ and $|c\rangle$. In $\mathrm{Var}\left(\mathcal{A}^0\right)$ above, we simply replace $N_A \to N_a$, $N_B \to N_b$ and so on, where N_a is the number of detected ions from state $|a\rangle$. For the variance on the doublet-odd asymmetry, we obtain

$$\begin{aligned} \mathrm{Var}\left(\mathcal{A}^D\right) = \frac{1}{(2N_t)^2}&\left[(N_a + N_c)(1 - \mathcal{K}^2) + \mathcal{K}^2(\mathrm{Var}\left(N_a\right) + \mathrm{Var}\left(N_c\right) - 2\mathrm{Cov}\left(N_a, N_c\right))\right] \\ &+ \text{identical term with } a \to b \text{ and } c \to d, \end{aligned} \tag{7.20}$$

where $\mathcal{K}$ is the doublet contrast, as defined in Eq. (6.3).

The variances and covariances on the number of detected ions from each M_F state can be derived by considering a series of cascaded binomial processes shown in Fig. 7.5. As discussed in

Sections 7.3.2 and 7.3.3, all of this apparent complexity boils down to the result that each state remains approximately Poisson distributed, with an effective fractional noise constant α_{eff} that receives contributions from the fractional variance of each binomial process. We can therefore take the number variances to have a simple form:

$$\begin{aligned}
\text{Var}\,(N_a) &= N_t p_u(1-p_u) + p_u^2 \text{Var}\,(N_t) + N_t^2 \text{Var}\,(p_u)\,, \\
\text{Var}\,(N_c) &= N_t p_l(1-p_l) + p_l^2 \text{Var}\,(N_t) + N_t^2 \text{Var}\,(p_l)\,, \\
\text{Cov}\,(N_a, N_c) &= \text{Cov}\,(p_u, p_l)\,\text{Var}\,(N_t) + p_u p_l \text{Var}\,(N_t) + N_t \text{Cov}\,(p_u, p_l)\,,
\end{aligned} \tag{7.21}$$

and we can then substitute in $\text{Var}\,(N_t) = N_t + \alpha_{\text{eff}}^2 N_t^2$ to account for fractional noise. The variances of N_b and N_d can be obtained from Eq. (7.21) with the replacements $a \to b$, $c \to d$, $p_u \to 1 - p_u$, and $p_l \to 1 - p_l$. Here p_u and p_l are the binomial probabilities of quantum projection onto state $|a\rangle$ or $|c\rangle$ in the upper or lower-doublet Ramsey sequence, as defined in Eqs. (7.1), (7.2).

For simplicity, I will assume that the upper and lower Stark doublets have the same contrast and coherence time, and call the contrast as a function of time $\mathcal{C}_t \equiv \mathcal{C}^0\, e^{-\gamma t}$. Substituting Eqs. (7.21) into Eqs. (7.19) and neglecting higher order terms, we obtain estimates for the variances of the doublet-even and doublet-odd asymmetries,

$$\begin{aligned}
\text{Var}\,(\mathcal{A})^0 &\approx \frac{1}{2N_t} + \frac{\alpha_{\text{eff}}^2}{2}\left[1 + \mathcal{C}_t^2 \cos^2(\Phi^0)\cos^2(\Phi^D)\right] + \frac{\mathcal{C}_t^2}{2}\text{Var}\,(\Phi)\sin^2(\Phi^0)\cos^2(\Phi^D), \\
\text{Var}\,(\mathcal{A})^D &\approx \frac{1}{2N_t} + \frac{(\mathcal{C}_t \mathcal{K} \alpha_{\text{eff}})^2}{2}\sin^2(\Phi^0)\sin^2(\Phi^D) + \frac{(\mathcal{C}_t \mathcal{K})^2}{2}\text{Var}\,(\Phi)\cos^2(\Phi^0)\sin^2(\Phi^D).
\end{aligned} \tag{7.22}$$

The first term in both equations arises from quantum projection noise. The second term in each expression arises from fractional noise α_{eff}, which may arise from variations in ablation, ionization, transfer, or photodissociation yield. The last term in each expression arises from phase noise, parameterized by $\text{Var}\,(\Phi)$ – it may arise from magnetic field noise, or jitter of the ion cloud position in the trap. We see that when Φ^D is a multiple of π, meaning the upper and lower doublet Ramsey fringes are in phase, $\sin^2\Phi^D$ vanishes and we are left with $\text{Var}\left(\mathcal{A}^D\right) \approx 1/(2N_t)$, which is the shot-noise limit.

Figure 7.6 shows the standard deviation of $\mathcal{A}^0$ and $\mathcal{A}^D$ as a function of Φ^D, with $\Phi^0 = 10\Phi^D$. The analytical expressions in Eq. (7.22) agree well with Monte Carlo simulation results, and show

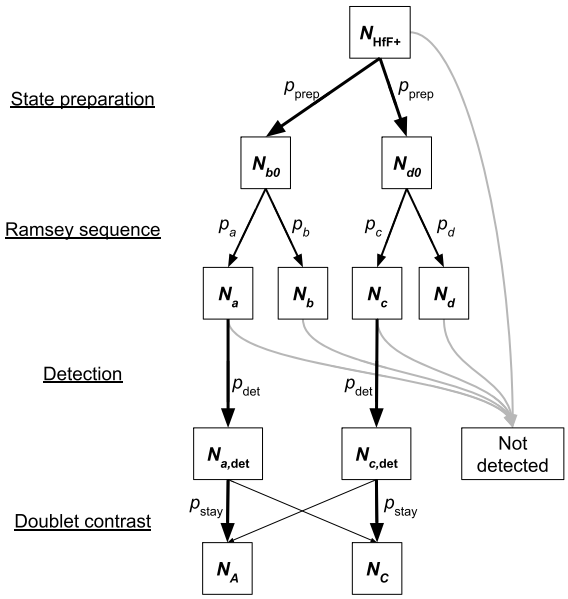

Figure 7.5: Sequence of probabilities in one experimental cycle of the HfF^+ eEDM experiment, from creation of N_{HfF^+} to simultaneous detection of N_A and N_C Hf^+ ions on the imaging MCP detector. Here p_{prep} is the probability of a molecule being prepared in $^3\Delta_1(v = 0, J = 1, F = 3/2, M_F = 3/2)$ rather than lost to other states via spontaneous decay, p_a-p_d are the probabilities of surviving the Ramsey sequence in one of states $|a\rangle$-$|d\rangle$, p_{det} is the detection probability, and $p_{stay} = (1 + \mathcal{K})/2$ (where $\mathcal{K}$ is the doublet contrast) is the probability of a detected ion being assigned to the correct doublet group.

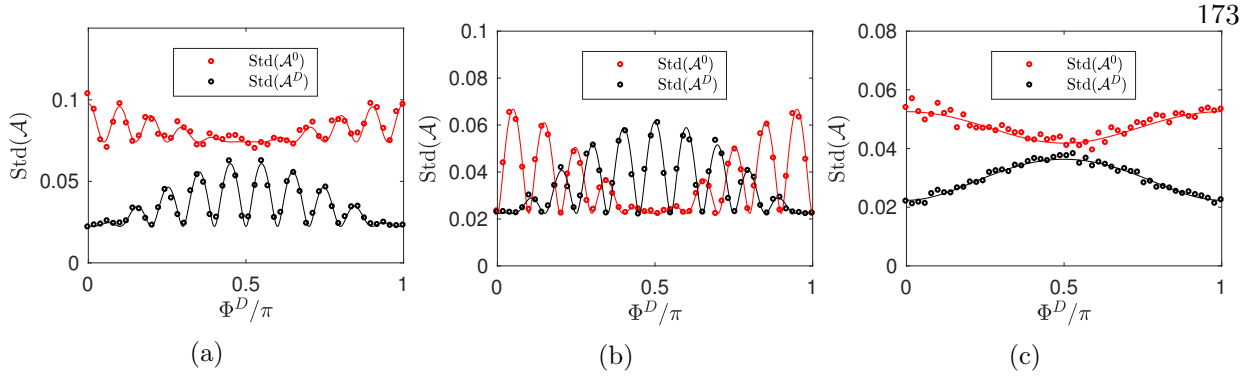

Figure 7.6: Standard deviation of doublet-even and doublet-odd asymmetries $\mathcal{A}^0$ and $\mathcal{A}^D$ as a function of Φ^D, with 1000 ions detected per experiment cycle (shot noise limit $1/\sqrt{2N_t} \approx 0.02$). Points are Monte Carlo simulation results, while lines are from Eq. (7.22). Three regimes of excess noise are shown: In (a), $\alpha_{\text{eff}} = 0.1$ and $\text{Var}(\Phi) = 0$ so that fractional noise dominates. In (b), $\alpha_{\text{eff}} = 0$ and $\text{Var}(\Phi) = (0.1)^2$, so that phase noise dominates. In (c), $\alpha_{\text{eff}} = 0.05$ and $\text{Var}(\Phi) = (0.05)^2$, so that both contribute equally.

that when $\Phi^D = 0$ or π, the differential asymmetry is able to achieve the shot noise limit even in the presence of both phase noise and ion number noise. Thus, as long as we measure Φ^D in the vicinity of these values, we should feel reassured that we can take $\text{Var}\left(\mathcal{A}^D\right) \approx 1/(2N_t)$ when estimating the Generation 2 eEDM sensitivity.

7.6 Effect of ion cloud jitter

While we have shown in the preceding section that our differential measurement is robust to technical noise in ion number and photodissociation efficiency, it is not robust to jitter in the ion cloud position along the axis separating the upper and lower doublets, which is typically the Y axis in the lab frame (horizontal in Fig. 6.14). Technical noise of this type produces negative correlation between the populations detected in each Stark doublet, which leads to noise on the difference $N_A - N_C$ and thus on the eEDM signal.

After imaging photodissociation products, we assign each of the imaged ions to the left or right group depending on their position in the image. As in earlier sections, I will label these groups A and C, corresponding to the phase of the depletion lasers where only states $|a\rangle$ and $|c\rangle$ are detected (Fig. 2.8). Ions coming from state $|a\rangle$ have a probability $p_s = \int_{-\infty}^{Y_0} dY\, P(Y)$ of

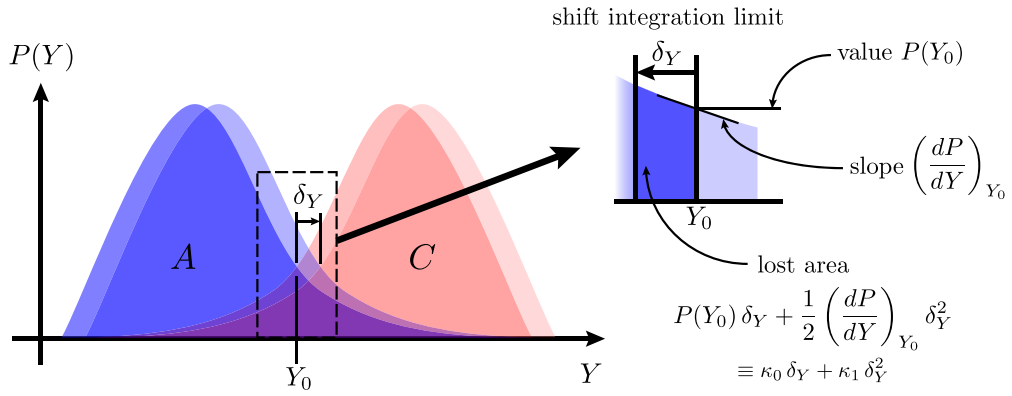

Figure 7.7: Effect of ion cloud jitter on assignment of ions to doublet groups, here labeled A and C. A shift of the ion cloud in the positive Y direction by an amount δ_Y relative to the mean position Y_0 causes a loss of an area $\kappa_0\delta_Y + \kappa_1\delta_Y^2$.

being assigned to group A, and a probability $p_g = 1 - p_s$ of being assigned to group C. We can parameterize jitter of the ion cloud along Y by the random variable δ_Y, such that $\mathrm{E}(\delta_Y) \equiv 0$ and $\mathrm{E}(\delta_Y^2) \equiv \mathrm{Var}(Y)$, as shown in Fig. 7.7. A jitter of the ion cloud in the $+Y$ direction effectively corresponds to a shift of the integration limit in the $-Y$ direction, away from Y_0. As a function of δ_Y, the numbers of ions counted in groups A and C in a single shot are thus

$$\begin{aligned} N_A &= N_a^{\mathrm{d}}(p_s - \kappa_0\delta_Y - \kappa_1\delta_Y^2) + N_c^{\mathrm{d}}(1 - p_s - \kappa_0\delta_Y + \kappa_1\delta_Y^2), \\ N_C &= N_c^{\mathrm{d}}(p_s + \kappa_0\delta_Y - \kappa_1\delta_Y^2) + N_a^{\mathrm{d}}(1 - p_s + \kappa_0\delta_Y + \kappa_1\delta_Y^2), \end{aligned} \tag{7.23}$$

where I have defined the parameters κ_0 and κ_1 as the value and half the derivative of the Hf^+ probability density function at Y_0, as shown in Fig. 7.7. Here N_a^{d} and N_c^{d} are the numbers of ions detected from states $|a\rangle$ and $|c\rangle$, respectively.

Using the definitions of the variance and covariance [2] along with our chosen properties of δ_Y, we can derive the variances and covariances of N_A and N_C. The results are quite messy and not extremely illuminating. More interesting is the variance of the population difference, since near $\phi^D = n\pi$, the doublet-odd asymmetry (for one choice of depletion laser phase) is approximately

[2] For any two random variables X and Y,

$$\begin{aligned} \mathrm{Var}(X) &\equiv \mathrm{E}\left((X - \mathrm{E}(X))^2\right) \\ \mathrm{Cov}(X,Y) &\equiv \mathrm{E}\left((X - \mathrm{E}(X))(Y - \mathrm{E}(Y))\right). \end{aligned}$$

equal to

$$\mathcal{A}^D(\Phi^D \approx n\pi) \approx \frac{N_A - N_C}{N_t}. \tag{7.24}$$

I find an excess noise contribution due to jitter of

$$\begin{aligned}\mathrm{Var}\left(\mathcal{A}^D\right) \approx \frac{\mathrm{Var}\left(N_A - N_C\right)}{N_t^2} &= \kappa_0^2 \mathrm{Var}\left(Y\right) + \frac{2\kappa_1 \mathrm{Var}\left(Y\right)}{N_t}(\mathcal{K} - \kappa_1 \mathrm{Var}\left(Y\right)) \\ &+ 4\kappa_1^2 \frac{(N_a^{\mathrm{d}} - N_c^{\mathrm{d}})^2}{N_t^2}(\mathrm{Kurt}\left(Y\right) - \mathrm{Var}\left(Y\right)^2) \\ &+ \text{terms not dependent on } Y,\end{aligned} \tag{7.25}$$

where $\mathrm{Kurt}\left(X\right) = \mathrm{E}\left((X - \mathrm{E}\left(X\right))^4\right)$ is the kurtosis. We find that nonzero jitter in the ion cloud position contributes excess noise directly to our eEDM measurement, and it can be suppressed by having better resolved Stark doublets, characterized by the parameters κ_0 and κ_1. The most concerning of these effects is the first term, which can limit our signal to noise independent of $\overline{N}$ if $\mathrm{Var}\left(Y\right)$ is large.

Using Fig. 6.14, we can make an estimate of the contribution of $\kappa_0^2 \mathrm{Var}\left(Y\right)$ to our excess noise: Very roughly, the ions in one doublet are spread over about 300 pixels on the detector, so we can take $\kappa_0 \approx 0.003$ pix^{-1}. The ion trap is approximately a harmonic oscillator, but by very long confinement times the ion cloud position has essentially dephased. The probability density for the cloud center position in a single shot Y is thus

$$\rho = \frac{1}{\pi}\sqrt{\frac{1}{Y_{\mathrm{max}}^2 - Y^2}}, \tag{7.26}$$

where Y_{max} is the maximum excursion in Y, which depends on the ion cloud's energy. This gives a mean square value $\mathrm{Var}\left(Y\right) = Y_{\mathrm{max}}^2/2$. A typical value for Y_{max} is perhaps 20 pixels (≈ 1 mm, corresponding to an energy of about $k_B \times (4$ Kelvin) – about the HfF^+ temperature), so that we obtain an excess noise contribution $\mathrm{Std}\left(\mathcal{A}^D\right)_{\mathrm{excess}} \approx 0.05$. Given that we typically have about 1000 detected ions per shot leading to shot noise of ≈ 0.02, this contribution may well dominate over shot noise.

7.7 Generation 2 sensitivity estimate

Assuming that we are able to attain the shot noise limit, we would like to know (a) what is the optimal Ramsey time given our counts per shot, decoherence and loss rates, and dead time, and (b) what is our expected precision after a given data collection time? We can safely assume that much like in the Generation 1 experiment described in Chapter 3, we will measure the Ramsey phase Φ at short and long Ramsey times ≈ 0 and t, and extract the spin precession frequency $f \approx \Delta\Phi/(2\pi t)$. However, in contrast to Generation 1, we can now measure both the Stark doublet-even and doublet-odd components of the phase Φ^0 and Φ^D simultaneously. So from each measured sum and difference Ramsey fringe $\mathcal{A}^0$ and $\mathcal{A}^D$, we will extract

$$\begin{aligned} f^0 &= \frac{\Phi^0(t) - \Phi^0(0)}{2\pi t}, \\ f^D &= \frac{\Phi^D(t) - \Phi^D(0)}{2\pi t}. \end{aligned} \tag{7.27}$$

The phases Φ^0 and Φ^D will likely be extracted from a nonlinear least squares fit of $\mathcal{A}^0$ and $\mathcal{A}^D$, as in the Generation 1 measurement. We will then repeat the Ramsey measurement for opposite signs of $\mathcal{B}'_{\mathrm{axgrad}}$ to extract the eEDM channel frequency f^{BD}, as discussed in Section 3.3.

In order to determine the optimal parameters for data collection, we can estimate $\mathrm{Var}\left(f^{BD}\right) \approx \mathrm{Var}\left(f^{D}\right)$ by straightforward error propagation on Eq. (7.27). Assuming the variance of $\mathcal{A}^D$ is dominated by shot noise, and by propagating uncertainty on Eq. (7.4), we can relate $\mathrm{Var}\left(\Phi^D(t)\right)$ to $\mathrm{Var}\left(\mathcal{A}^D\right)$:

$$\mathrm{Var}\left(\mathcal{A}^D\right) = \frac{1}{2N_0 e^{-\Gamma t}} \approx (\mathcal{C}^0 \mathcal{K} e^{-\gamma t})^2 \mathrm{Var}\left(\Phi^D\right). \tag{7.28}$$

Propagating errors on Eq. (7.27) and using $f^{BD} \approx 2d_e\mathcal{E}_{\mathrm{eff}}/h$, we find a shot noise limited uncertainty on d_e of

$$\begin{aligned} \sigma_{d_e} &= \frac{\hbar}{2\mathcal{E}_{\mathrm{eff}} t} \sqrt{\mathrm{Var}\left(\Phi_0^D\right) + \mathrm{Var}\left(\Phi_t^D\right)} \\ &= \frac{\hbar}{2\mathcal{E}_{\mathrm{eff}} t \mathcal{K}\mathcal{C}^0\sqrt{N_0}} \sqrt{\left(\frac{1}{s_{\mathrm{e}}} + \frac{e^{(2\gamma+\Gamma)t}}{1-s_{\mathrm{e}}}\right)\left(\frac{t(1-s_{\mathrm{e}}) + t_{\mathrm{d}}}{T_{\mathrm{tot}}}\right)}, \end{aligned} \tag{7.29}$$

where N_0 is the average number [3] of detected Hf^+ per shot at $t = 0$ (before any loss), Γ and γ are the Hf^+ loss and decoherence rates, T_{tot} is the total amount of data collection time, t_{d} is the "dead

[3] I have skipped several steps of algebra in writing down Eq.(7.29). More explicitly, starting with the first line of

Parameter	Value	Units	Description
N_0	10^3		Initial detected Hf^+
Γ	$1/2$	s^{-1}	Hf^+ loss rate
γ	$1/5$	s^{-1}	Spin decoherence rate
t_d	0.4	s	Dead time
$\mathcal{E}_{eff}$	23×10^9	V/cm	Effective electric field
$\mathcal{C}^0$	0.85		Initial spin contrast
$\mathcal{K}$	0.8		Doublet contrast

Table 7.1: Typical experimental parameters for the Generation 2 eEDM experiment with HfF^+. N_0 is the total number of Hf^+ detected (in both Stark doublets) in one experimental cycle near $t = 0$ on the side of a fringe, i.e., when $\Phi^0 \approx \pi/2$.

time" spent on state preparation and readout rather than phase evolution, and s_e is the fraction of experiment cycles where we choose $t \approx 0$ in order to measure $\Phi^D(0)$. We can optimize Eq. (7.29) with respect to s_e, finding

$$s_{e,best} = \frac{1}{1 + e^{(\gamma+\Gamma/2)t}\sqrt{(1-D)}}, \tag{7.31}$$

where $D \equiv t/(t + t_d)$ is the duty cycle; the fraction of total data collection time spent on spin precession.

Optimization of Eq. (7.29) with respect to t is easily done graphically. It so happens that σ_{d_e} is quite insensitive to the choice of t, as shown in Fig. 7.8, for the typical experimental parameters listed in Table 7.1. I find that for an approximately optimal choice of t, the shot noise limit for our statistical sensitivity is about 3×10^{-29} e cm for 1 hour of data collection. Comparing to the ACME II statistical error bar of 3.6×10^{-30} e cm for 350 hours of data collection, we should be able to do about as well in 100 hours. Of course, this strongly depends on whether we can acheive shot noise limited sensitivity! As of this writing, we have observed shot noise limited measurements of $\mathcal{A}^D$ at $t \approx 1.5$ s, but challenges continue with extracting shot noise limited phase measurements.

Eq. (7.29), we have

$$\frac{\hbar}{2\mathcal{E}_{eff}t}\sqrt{\mathrm{Var}\left(\Phi_0^D\right) + \mathrm{Var}\left(\Phi_t^D\right)} = \frac{\hbar}{2\mathcal{E}_{eff}t\mathcal{K}\mathcal{C}^0\sqrt{2N_0\,S}}\sqrt{\frac{1}{s_e} + \frac{1}{(1-s_e)e^{-2\gamma t}e^{-\Gamma t}}}, \tag{7.30}$$

where S is the total number of phase measurements performed. The total time taken for S is $T_{tot} = 2S\left[s_e t_d + (1-s_e)(t+t_d)\right]$, where the factor of 2 accounts for the fact that we need two experiment cycles to measure the populations of all four states $|a\rangle$ - $|d\rangle$. Solving this expression for S and substituting the result into Eq. (7.30) gives Eq.(7.29).

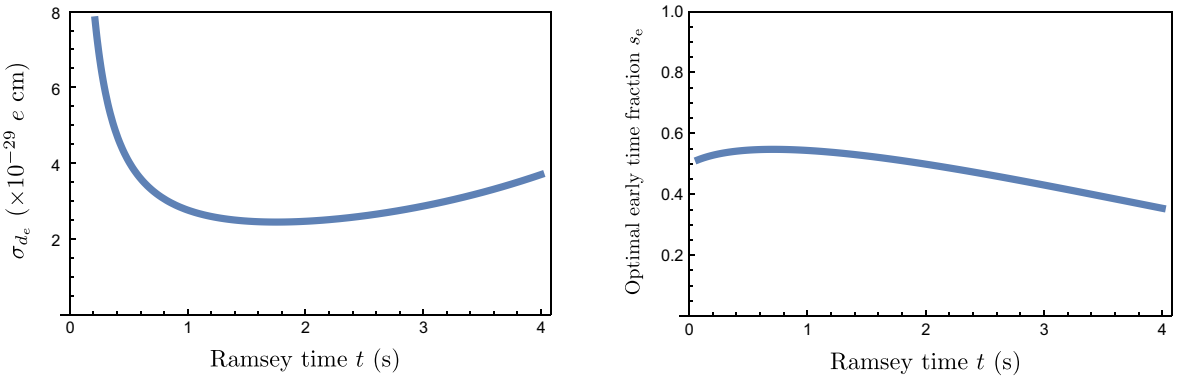

Figure 7.8: (a) Statistical sensitivity for $T_{\rm tot} = 1$ hour of data collection with the experimental parameters listed in Table 7.1. (b) Optimal fraction of data to be collected at $t \approx 0$, versus Ramsey time.

Chapter 8

Looking forward

This section is reproduced from Ref. [17].

Searches for electric dipole moments and other T-violating interactions in atoms and molecules have great potential to host some of the first signs of microscopic BSM physics. Their high sensitivity, relatively low cost and short time between successive measurements (when compared to collider experiments) has brought them to the forefront of new physics searches, particularly in view of the non-detection of new TeV-scale particles at the LHC.

The opposing requirements of high absolute frequency precision and strong relativistic effects for EDM-sensitive systems have pushed experimenters to use specialized approaches that are often distinct from what is applicable in systems chosen for other precision applications, such as atomic clocks, gyroscopes, and accelerometers. However, these challenging systems inspire innovation, which can contribute to advancement in other fields – laser cooling of polyatomic molecules for ultracold chemistry, for example [72].

While the careful approach that is required of experimenters in EDMs and other precision measurements does not generally result in overnight advances, the past decade has seen dramatic improvements to EDM bounds both in paramagnetic and diamagnetic systems. For diamagnetic systems in particular, the abundance of BSM parameter sensitivities encourages a wide variety of approaches: the most stringent constraints will likely require combined results from Hg, Xe, Rn, TlF, and the neutron. For paramagnetic systems, attaining orders of magnitude further improvement will necessitate systems that achieve both high count rate and long coherence times. The

confluence of techniques required to improve both paramagnetic and diamagnetic EDM bounds will require drawing from, and contributing to, advances in techniques in the broader world of AMO physics and emerging quantum technologies.

8.1 Future techniques in AMO EDM experiments

This section is reproduced from Ref. [17].

The near future holds great potential for improvements to EDM experiments. Further development of the ^{225}Ra apparatus with established techniques can be expected to lead straightforwardly to orders of magnitude higher statistical sensitivity, and improvements in quantum state control of molecules will allow the application of laser cooling and trapping techniques to both diamagnetic and paramagnetic EDM-sensitive molecular species. Also being developed are additional experiments on paramagnetic atoms Cesium and Francium [68, 137], a paramagnetic molecule experiment using a Stark-decelerated beam of BaF [25], and a diamagnetic molecule experiment using TlF in collaboration between Yale, Columbia, and the University of Massachusetts Amherst [31]. At present, molecules appear to provide the highest raw sensitivity to paramagnetic and diamagnetic EDMs, so essentially all near-future techniques focus on improving statistical sensitivity through higher count rates and longer coherence times. Long coherence times provide another important advantage in significantly suppressing systematic effects.

One possibility for improving global constraints on BSM physics parameters without dramatically changing the absolute precision of an individual EDM experiment is through the nuclear magnetic quadrupole moment (MQM, M) in isotopologues with spin $I > 1/2$ for the heavy nucleus [40]. The operators giving rise to a MQM are complementary to those constrained by diamagnetic systems: the dimension-four CP-violating QCD parameter θ and the proton EDM d_p [40]. Species such as ^{177}HfF$^+$ and ^{181}Ta^{16}O$^+$ have accessible $^3\Delta_1$ states and comparable sensitivity to d_e, C_S and M [42, 117]. The neutral species ^{173}YbF and the isovalent triatomic molecule ^{173}YbOH are expected to have comparable sensitivity to a MQM [40, 73].

In HfF$^+$, the eEDM search already underway at JILA has the potential to search for a MQM

without significant changes to the experimental approach. However, the experimental sensitivity required for a nuclear MQM measurement to improve upon constraints to the underlying BSM physics parameters is on the order of 30 μHz; approximately 20$\times$ smaller than the 1σ uncertainty in the most recent eEDM measurement using HfF^+. Particularly in view of multiple parameter sensitivities and the necessity of a global analysis, ion trap measurements must improve by at least an order of magnitude in order to constrain BSM physics. This goal could be within reach in the second generation JILA eEDM experiment.

Apart from direct BSM physics sensitivity resulting from a choice of molecule, there are several possible routes to improved precision in molecular ion EDM experiments. The JILA group has improved the spin coherence time in HfF^+ to $\sim$ 2.3 s through adiabatic expansion cooling, reducing decoherence due to ion-ion collisions. Significant further improvements will require a cryogenic environment to reduce the vibrational excitation rate from blackbody radiation, and the use of a $^3\Delta_1$ ground state molecule, which the JILA group is also pursuing in a separate eEDM search using ThF^+. For a MQM search, the $^3\Delta_1$ ground state molecule TaO^+, possibly in a cryogenic environment, may attain coherence times on the scale of many seconds [42].

EDM experiments with coherence times on the scale of seconds operate in a regime where the experimental repetition rate is limited by spin interrogation time, rather than dead time. In this regime, experimental sensitivity scales as $1/\sqrt{\tau}$ for a fixed total data collection time (which is often constrained by practicality). Both the HfF^+ eEDM search and the ^{225}Ra EDM search are approaching this limit. Substantial improvement could be attained by multiplexing experiments in a conveyor-belt style apparatus (Fig. 8.1a): Simultaneous interrogation of 100 bunches of 10^3 (detected) particles with τ = 10 s and a repetition rate of 10 Hz would result in a sensitivity of approximately $\sigma_f \sim 10$ μHz in one hour of data collection, or $\sigma_d \sim 10^{-31}$ e cm for $\mathcal{E}_{\text{eff}} = 35$ GV/cm (Fig. 8.1a). Such techniques are likely more straightforward to apply in an ion-trapping experiment, where the technical challenges will primarily be centered around development of electronics. The JILA group is investigating this possibility for the ThF^+ eEDM search.

Ideas are also being pursued for attaining long coherence times with neutral molecules

through laser cooling and trapping. Magneto-optical traps (MOTs) have been an essential tool in AMO experiments for several decades, and show promise for application to EDM experiments with molecules. These non-conservative traps allow population to be accumulated from a slowed atomic beam or a vapor, and in atomic systems reach $\sim 10^9$ atoms at temperatures on the order of ~ 100 μK. The first MOTs for diatomic molecules have been demonstrated since 2011, for the species SrF, CaF and YO [1, 8, 26, 125]. These molecules were chosen for their decoupling of vibrational and electronic degrees of freedom, and their low mass, which allows the molecules to be slowed to MOT capture velocities with as few scattered photons as possible while maintaining optical cycling. The molecules used in EDM experiments are typically very heavy (~ 200 u), however YbF in particular is isovalent with SrF and CaF, and is thus reasonably well-suited to laser cooling. The Imperial College group has demonstrated one-dimensional laser cooling for YbF [81], and has proposed a molecular fountain design for measuring the eEDM [123]. They estimate over 100 ms coherence time will be achievable with packets of 10^5 molecules, leading to an estimated sensitivity in the 10^{-30} e cm range.

In a recent proposal [73], the triatomic molecule YbOH is proposed as a species that is amenable to both laser cooling and high eEDM sensitivity, while maintaining the systematic-suppressing properties of $^3\Delta_1$ states that are being applied in the ThO, HfF^+ and ThF^+ eEDM searches (Fig. 8.1b). YbOH has a similar electronic structure to YbF, SrF and CaF, leading to a low probability of vibrational excitation in electronic decay, and the possibility of laser slowing and trapping. Experiments sensitive to BSM physics would take place in the first excited state of the bending vibrational mode, using its parity doublet structure to allow full polarization in small laboratory electric fields and suppress systematic effects. As it is isovalent with YbF, YbOH is also anticipated to be sensitive to a nuclear MQM at a similar level to YbF and HfF^+ [40]. A MQM search is under development in the Hutzler group at Caltech [90], along with a parallel effort to implement laser cooling and trapping for a future eEDM measurement (Fig. 8.1b).

In upcoming experiments using molecules and atoms with ground or low-lying EDM-sensitive states (e.g. ^{225}Ra, ThF^+, YbF, and YbOH), the spin precession time will likely not be limited by

spontaneous decay. For YbF and YbOH in CBGBs, for example, the spin interrogation time will be limited by the length of the apparatus and the beam velocity. In this regime, spin-squeezing techniques that use quantum correlations between particles to overcome the quantum projection noise limit become applicable [14, 65, 101]. To our knowledge, these techniques have not yet been demonstrated with cold molecules, but they have the potential to further improve the precision of future EDM experiments.

Several past EDM searches have used solid-state systems [36, 60], which have exceptionally high statistical sensitivity due to their sample sizes of order 10^{20} particles. However, these experiments have faced challenges with diagnosing and suppressing systematic effects. Other proposals have suggested performing an EDM measurement on molecules confined in inert gas matrices [71, 128], which has the potential to combine very high count rate with coherence times on the order of 100 ms, and robustness against systematic effects through highly variable experimental parameters (Fig. 8.1c). Such an experiment would yield a statistical sensitivity on the order of 10^{-36} e cm in 100 hours – a value beyond any other proposed technique. The more recent proposal suggests using fluorescence detection and an orientation-dependent hyperfine structure [129] to both prepare and read out individual molecules in an orientation-specific way. The proposal [128] is currently under development at York University and the University of Toronto.

8.2 Towards eEDM Generation 2 with HfF^+

I recall saying to Matt Grau and Kevin Cossel in 2014, just as I was learning to operate the HfF^+ apparatus, that I thought our experiment was "designed into a corner," and that I couldn't think of a single way we could do things differently and still have the experiment work at all. At that time, I had evidently not yet meditated enough on the ways of eEDM. Much of this thesis has been about revisiting aspects of the experiment that seemed to me as a first year graduate student to be written in stone, and thinking hard about whether they could be done differently.

Chapters 2 and 3 of this thesis covered basic aspects of HfF^+ and progress in the lab until 2017, which to me feels like just the beginning. The Generation 1 result, while competitive at the

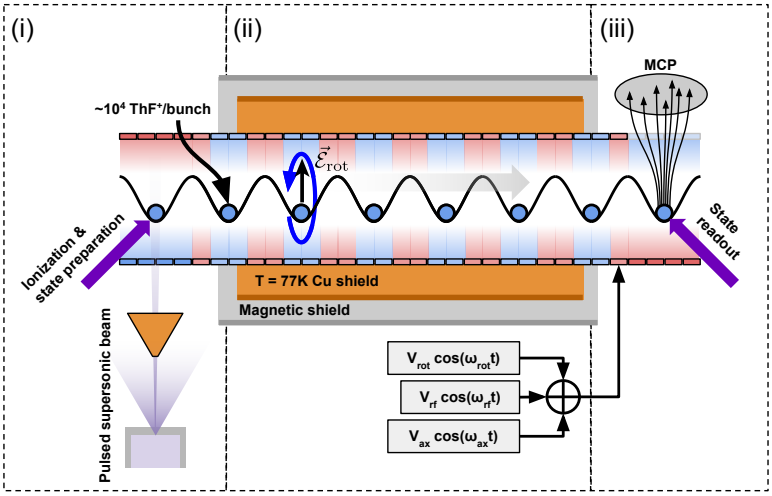

(a)

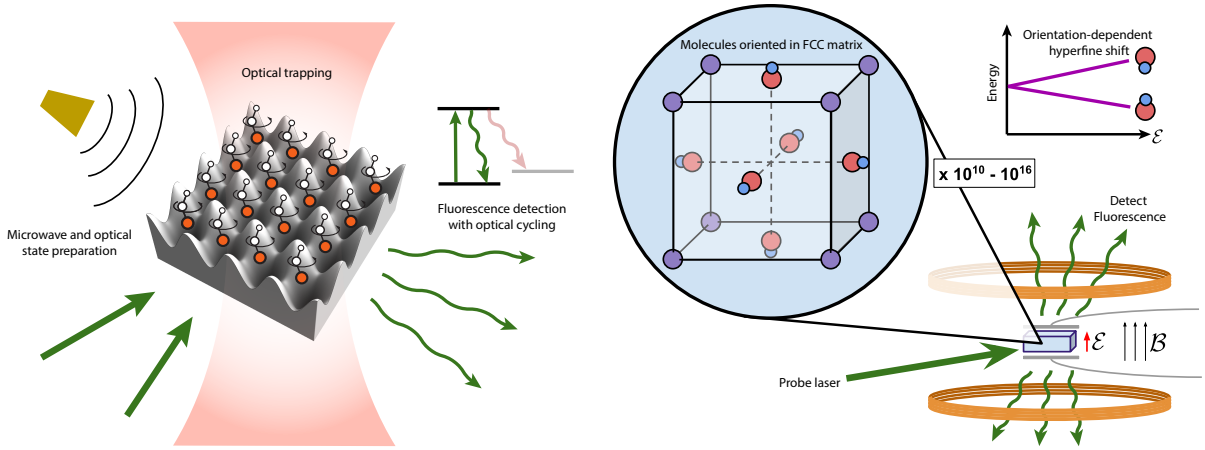

(b) (c)

Figure 8.1: Future methods for electric dipole moment searches. (a) A "conveyor belt" of trapped ions for attaining long coherence time and high repetition rates, in development at JILA. (b) Laser cooled and trapped YbOH, a long-term goal for the PolyEDM Collaboration between Caltech, Harvard, and University of Toronto. (c) The EDM3 method for molecules in inert gas matrices, in development at York University and the University of Toronto.

time, has now been thoroughly left in the dust by ACME II, and we once again need to catch up. Our 1σ statistical error bar for Generation 1 with HfF^+ was 8.7×10^{-29} e cm, while ACME II had $\sigma_{\text{stat}} = 3.6 \times 10^{-30}$ e cm; a factor of 24 better. Fortunately, thanks to recent developments, catching up remains a possibility.

In Chapter 4, we discussed the design and implementation of the Generation 2 RF trap. The trap, built by the JILA machine shop and powered by drivers from the JILA electronics shop, has been happily confining ions for nearly 2 years. The ideas going into the design of the Generation 2 trap were essentially the same as for the Generation 1 trap designed by Matt Grau, minus the ellipsoidal mirrors for laser-induced fluorescence detection of HfF^+. The main goal was that $\mathcal{E}_{\text{rot}}$ should be uniform over a large region so that the ion cloud can have very low density for long coherence times. I think it has met that goal.

In Chapter 5, we discussed our old and new state preparation in HfF^+, with a few central lessons that are all too obvious in retrospect:

(1) a low-tech solution is often the best one,

(2) a molecule does not need to be laser-coolable for optical pumping to work well, and

(3) in an ion trap, we have time to spare.

For years, we worked under the impression that the electronic and vibrational branching ratios for spontaneous emission in HfF^+ were too poor, so that resonantly driving electronic transitions would immediately lead to our molecules being "lost in Hilbert space," never to be seen again, except perhaps as incoherent background. Then in Summer 2017, thanks to our privilege of owning a widely tunable cw Ti:sapphire laser, we tried on a whim to rotationally cool $^1\Sigma^+$ molecules via the $^3\Sigma^-_{0^+}$ state as discussed in Section 5.3, and had a modest success. From there, Yan and Kia Boon decided to perform all-incoherent state preparation in ThF^+, and we on the HfF^+ side – not being so proud as to not adopt a good idea when we see it – followed suit. We begged and borrowed laser diodes from all around JILA, hacked together lasers, and in the course of a few days in 2018 were able to observe as many as 4000 Hf^+ ions as dissociation products of $^3\Delta_1$ – an

unprecedented yield for our experiment. Better still, our incoherent state preparation has very low requirements for laser stability and power: we presently have 7 lasers stabilized to about 20 MHz with our HighFinesse wavemeter, and some send as little as 10 mW to the experiment.

The developments described in Chapter 6 and 7, all of which transpired in 2018-2019, have been some of the most exciting of my PhD. I hope that this work may be valuable for future experiments with molecules beyond eEDM, such as quantum information studies [18, 92]. As discussed in Section 6.1, the signal gains we reaped from the Generation 2 ion trap and incoherent state preparation would be essentially useless if we continued to be hampered by excess noise from our multimode pulsed dye lasers. Inspired by classic work in photofragmentation from the chemical physics community [135] and new work with ultracold molecules [85], we developed a new state detection technique that provides us with a differential quantum phase measurement in a single experiment cycle. This means that noise in ion production, state preparation, and dissociation are all common-mode and can be normalized away, leaving only the fundamental quantum projection noise. I believe that without this development, which came about thanks to our collaboration with Tanya Zelevinsky, we would have had a long and arduous battle against virtually endless sources of excess noise.

I am sometimes asked by others in the AMO field if it is dull working on a precision measurement experiment, where we spend years at a time studying excess noise and systematic effects, with the likely outcome of these years of effort being a measurement of a quantity that is consistent with zero. My answer is emphatically "no." Why? In precision measurement, life is always better than it used to be. In 2013, a typical Ramsey fringe had about 5 signal Hf^+ ions per shot, and had a coherence time on the order of 150 ms. Now in 2019, our Ramsey fringes have about 1000 signal Hf^+ ions per shot, and we have coherence times of order 5 s. Not only do these gains keep us in the running for record sensitivity, they allow us to perform diagnostic studies with unprecedented ease. In 2013, I could not have imagined where we would be today.

Bibliography

[1] L. Anderegg, B. L. Augenbraun, E. Chae, B. Hemmerling, N. R. Hutzler, A. Ravi, A. Collopy, J. Ye, W. Ketterle, and J. M. Doyle. Radio Frequency Magneto-Optical Trapping of CaF with High Density. Physical Review Letters, 119(10):103201, 9 2017.

[2] V. Andreev, D. G. Ang, D. DeMille, J. M. Doyle, G. Gabrielse, J. Haefner, N. R. Hutzler, Z. Lasner, C. Meisenhelder, B. R. OLeary, C. D. Panda, A. D. West, E. P. West, and X. Wu. Improved limit on the electric dipole moment of the electron. Nature, 562(7727):355–360, 2018.

[3] T. Appelquist and J. Carazzone. Infrared singularities and massive fields. Physical Review D, 11(10):2856–2861, 1975.

[4] N. Auerbach, V. V. Flambaum, and V. Spevak. Collective T- and P-odd electromagnetic moments in nuclei with octupole deformations. Physical Review Letters, 76(23):4316–4319, 6 1996.

[5] S. Ban, J. Dobaczewski, J. Engel, and A. Shukla. Fully self-consistent calculations of nuclear Schiff moments. Physical Review C, 82(1):15501–15507, 7 2010.

[6] J. Baron, W. C. Campbell, D. DeMille, J. M. Doyle, G. Gabrielse, Y. V. Gurevich, P. W. Hess, N. R. Hutzler, E. Kirilov, I. Kozyryev, B. R. O'Leary, C. D. Panda, M. F. Parsons, E. S. Petrik, B. Spaun, A. C. Vutha, and A. D. West. Order of magnitude smaller limit on the electric dipole moment of the electron. Science, 343(6168):269–272, 1 2014.

[7] J. Baron, W. C. Campbell, D. DeMille, J. M. Doyle, G. Gabrielse, Y. V. Gurevich, P. W. Hess, N. R. Hutzler, E. Kirilov, I. Kozyryev, B. R. O'Leary, C. D. Panda, M. F. Parsons, B. Spaun, A. C. Vutha, A. D. West, and E. P. West. Methods, analysis, and the treatment of systematic errors for the electron electric dipole moment search in thorium monoxide. New Journal of Physics, 19(7):73029–73068, 5 2017.

[8] J. F. Barry, D. J. McCarron, E. B. Norrgard, M. H. Steinecker, and D. DeMille. Magneto-optical trapping of a diatomic molecule. Nature, 512(7514):286–289, 8 2014.

[9] D. J. Berkeland, J. D. Miller, J. C. Bergquist, W. M. Itano, and D. J. Wineland. Minimization of ion micromotion in a Paul trap. Journal of Applied Physics, 83(10):5025–5033, 1 1998.

[10] J. A. Beswick and R. N. Zare. On the quantum and quasiclassical angular distributions of photofragments. Journal of Chemical Physics, 129(16):164310–164315, 10 2008.

[11] M. Bishof, R. H. Parker, K. G. Bailey, J. P. Greene, R. J. Holt, M. R. Kalita, W. Korsch, N. D. Lemke, Z. T. Lu, P. Mueller, T. P. O'Connor, J. T. Singh, and M. R. Dietrich. Improved limit on the ^{225}Ra electric dipole moment. Physical Review C, 94(2):25501, 8 2016.

[12] J. K. Blitzstein and J. Hwang. Introduction to Probability. Chapman & Hall/CRC Texts in Statistical Science. CRC Press/Taylor & Francis Group, 2014.

[13] G. Bollen. FRIB - Facility for Rare Isotope Beams. In AIP Conference Proceedings, volume 1224, pages 432–441. American Institute of Physics, 5 2010.

[14] B. Braverman, A. Kawasaki, and V. Vuletić. Impact of non-unitary spin squeezing on atomic clock performance. New Journal of Physics, 20(10):103019, 10 2018.

[15] J. M. Brown and A. Carrington. Rotational Spectroscopy of Diatomic Molecules. Cambridge University Press, 2003.

[16] W. B. Cairncross, D. N. Gresh, M. Grau, K. C. Cossel, T. S. Roussy, Y. Ni, Y. Zhou, J. Ye, and E. A. Cornell. Precision Measurement of the Electron's Electric Dipole Moment Using Trapped Molecular Ions. Physical Review Letters, 119(15), 2017.

[17] W. B. Cairncross and J. Ye. Atoms and molecules in the search for time-reversal symmetry violation. Nature Reviews Physics, submitted, 2019.

[18] S. L. Campbell, R. B. Hutson, G. E. Marti, A. Goban, N. Darkwah Oppong, R. L. McNally, L. Sonderhouse, J. M. Robinson, W. Zhang, B. J. Bloom, and J. Ye. A Fermi-degenerate three-dimensional optical lattice clock. Science, 358(6359):90–94, 2017.

[19] K. Chen, S. T. Sullivan, W. G. Rellergert, and E. R. Hudson. Measurement of the Coulomb logarithm in a radio-frequency Paul trap. Physical Review Letters, 110(17), 2013.

[20] T. Chupp, P. Fierlinger, M. Ramsey-Musolf, and J. Singh. Electric Dipole Moments of the Atoms, Molecules, Nuclei and Particles. Reviews of Modern Physics, 10 2017.

[21] T. Chupp and M. Ramsey-Musolf. Electric Dipole Moments: A Global Analysis. Physical Review C, 91(3):035502, 3 2014.

[22] T. E. Chupp, P. Fierlinger, M. J. Ramsey-Musolf, and J. T. Singh. Electric dipole moments of atoms, molecules, nuclei, and particles. Reviews of Modern Physics, 91(1):015001, 1 2019.

[23] A. Collaboration. Observation of a new particle in the search for the Standard Model Higgs boson with the ATLAS detector at the LHC. Physics Letters B, 716(1):1–29, 9 2012.

[24] C. Collaboration. Observation of a new boson at a mass of 125 GeV with the CMS experiment at the LHC. Physics Letters B, 716(1):30–61, 9 2012.

[25] T. N.-e. collaboration. Measuring the electric dipole moment of the electron in BaF. 4 2018.

[26] A. L. Collopy, S. Ding, Y. Wu, I. A. Finneran, L. Anderegg, B. L. Augenbraun, J. M. Doyle, and J. Ye. 3D Magneto-Optical Trap of Yttrium Monoxide. Physical Review Letters, 121(21):213201, 11 2018.

[27] E. D. Commins, J. D. Jackson, and D. P. DeMille. The electric dipole moment of the electron: An intuitive explanation for the evasion of Schiff's theorem. American Journal of Physics, 75(6):532–536, 6 2007.

[28] K. C. Cossel. Techniques in molecular spectroscopy: from broad bandwidth to high resolution. PhD thesis, University of Colorado Boulder, 10 2014.

[29] K. C. Cossel, D. N. Gresh, L. C. Sinclair, T. Coffey, L. V. Skripnikov, A. N. Petrov, N. S. Mosyagin, A. V. Titov, R. W. Field, E. R. Meyer, E. A. Cornell, and J. Ye. Broadband velocity modulation spectroscopy of HfF^+: Towards a measurement of the electron electric dipole moment. Chemical Physics Letters, 546(C):1–11, 9 2012.

[30] D. DeMille. Search for the electric dipole moment of the electron using metastable PbO. AIP Conference Proceedings, 596:72–83, 1 2001.

[31] D. DeMille. Towards a new generation of EDM experiments using molecules. Bulletin of the American Physical Society, 62, 2017.

[32] M. Denis, M. S. Norby, H. J. A. Jensen, A. S. P. Gomes, M. K. Nayak, S. Knecht, and T. Fleig. Theoretical study on ThF^+, a prospective system in search of time-reversal violation. New Journal of Physics, 17(4):43005–43014, 4 2015.

[33] M. Dine and A. Kusenko. Origin of the matter-antimatter asymmetry. Reviews of Modern Physics, 76(January):1–30, 2004.

[34] P. A. M. Dirac. The principles of quantum mechanics. Clarendon Press, Oxford, 1958.

[35] J. Dobaczewski and J. Engel. Nuclear time-reversal violation and the schiff moment of 225Ra. Physical Review Letters, 94(23):232502, 2005.

[36] S. Eckel, A. O. Sushkov, and S. K. Lamoreaux. Limit on the electron electric dipole moment using paramagnetic ferroelectric Eu 0.5Ba 0.5TiO 3. Physical Review Letters, 109(19):193003, 11 2012.

[37] J. Engel, M. J. Ramsey-Musolf, and U. Van Kolck. Electric dipole moments of nucleons, nuclei, and atoms: The Standard Model and beyond. Progress in Particle and Nuclear Physics, 71:21–74, 7 2013.

[38] J. L. Feng. Naturalness and the Status of Supersymmetry. Annual Review of Nuclear and Particle Science, 63(1):351–382, 10 2013.

[39] V. V. Flambaum. Enhanced nuclear Schiff moment and time reversal violation in ^{229}Th-containing molecules. arXiv.org, page 1808.03629, 2018.

[40] V. V. Flambaum, D. Demille, and M. G. Kozlov. Time-reversal symmetry violation in molecules induced by nuclear magnetic quadrupole moments. Physical Review Letters, 113(10):103003, 2014.

[41] V. V. Flambaum and V. G. Zelevinsky. Enhancement of nuclear Schiff moments and time-reversal violation in atoms due to soft nuclear octupole vibrations. Physical Review C, 68(3):7, 2003.

[42] T. Fleig. TaO^+ as a candidate molecular ion for searches of physics beyond the standard model. Physical Review A, 95(2):022504, 2017.

[43] T. Fleig and M. Jung. Model-independent determinations of the electron EDM and the role of diamagnetic atoms. Journal of High Energy Physics, 2018(7):718–795, 7 2018.

[44] T. Fleig and M. K. Nayak. Electron electric-dipole-moment interaction constant for HfF^+ from relativistic correlated all-electron theory. Physical Review A, 88(3):32514–32516, 9 2013.

[45] T. Fleig and M. K. Nayak. Electron electric dipole moment and hyperfine interaction constants for ThO. Journal of Molecular Spectroscopy, 300(C):16–21, 6 2014.

[46] T. Fleig, M. K. Nayak, and M. G. Kozlov. TaN, a molecular system for probing P, T -violating hadron physics. Physical Review A, 93(1):810–873, 1 2016.

[47] L. L. Foldy and S. A. Wouthuysen. On the Dirac theory of spin 1/2 particles and its non-relativistic limit. Physical Review, 78(1):29–36, 4 1950.

[48] B. Graner, Y. Chen, E. G. Lindahl, and B. R. Heckel. Reduced Limit on the Permanent Electric Dipole Moment of ^{199}Hg. Physical Review Letters, 116(16):161601, 4 2016.

[49] M. Grau. Measuring the Electron Electric Dipole Moment with Trapped Molecular Ions. PhD thesis, University of Colorado Boulder, 1 2016.

[50] M. Grau, A. E. Leanhardt, H. Loh, L. C. Sinclair, R. P. Stutz, T. S. Yahn, and E. A. Cornell. Near-infrared LIF spectroscopy of HfF. Journal of Molecular Spectroscopy, 272(1):32–35, 2 2012.

[51] D. Gresh. The first precision measurement of the electron electric dipole moment in trapped molecular ions. PhD thesis, University of Colorado Boulder, 2018.

[52] D. N. Gresh, K. C. Cossel, Y. Zhou, J. Ye, and E. A. Cornell. Broadband velocity modulation spectroscopy of ThF^+ for use in a measurement of the electron electric dipole moment. Journal of Molecular Spectroscopy, 319(C):1–9, 1 2016.

[53] B. Grzadkowski, M. Iskrzyński, M. Misiaka, and J. Rosieka. Dimension-six terms in the Standard Model Lagrangian. Journal of High Energy Physics, 2010(10):75018–75021, 10 2010.

[54] D. Hanneke, S. Fogwell, and G. Gabrielse. New Measurement of the Electron Magnetic Moment and the Fine Structure Constant. Physical Review Letters, 100(12):120801, 2008.

[55] A. Hansson and J. K. Watson. A comment on Hönl-London factors. Journal of Molecular Spectroscopy, 233(2):169–173, 2005.

[56] T. Haslwanter, H. Ritsch, J. Cooper, and P. Zoller. Laser-noise-induced population fluctuations in two- and three-level systems. Physical Review A, 38(11):5652–5659, 1988.

[57] W. C. Haxton and E. M. Henley. Enhanced T-nonconserving nuclear moments. Physical Review Letters, 51(21):1937–1940, 11 1983.

[58] E. Hecht. Optics. Pearson education. Addison-Wesley, 2002.

[59] F. Hehl and W. Ni. Inertial effect of a dirac particle. Physical Review D, 42(6):2045, 1 1990.

[60] B. J. Heidenreich, O. T. Elliott, N. D. Charney, K. A. Virgien, A. W. Bridges, M. A. McKeon, S. K. Peck, D. Krause, J. E. Gordon, L. R. Hunter, and S. K. Lamoreaux. Limit on the electron electric dipole moment in gadolinium-iron garnet. Physical Review Letters, 95(25):253004, 12 2005.

[61] G. Herzberg. Molecular Spectra and Molecular Structure. Prentice-Hall, Inc., New York, 1939.

[62] E. a. Hinds. Testing time reversal symmetry using molecules. Physica Scripta, T70:34–41, 1 1997.

[63] A. Horita and L. J. Weber. Skin penetrating property of drugs dissolved in dimethylsulfoxide (DMSO) and other vehicles. Life Sciences, 3(12):1389–1395, 12 1964.

[64] J. J. Hudson, D. M. Kara, I. J. Smallman, B. E. Sauer, M. R. Tarbutt, and E. A. Hinds. Improved measurement of the shape of the electron. Nature, 473(7348):493–496, 4 2011.

[65] S. F. Huelga, C. Macchiavello, T. Pellizzari, A. K. Ekert, M. B. Plenio, and J. I. Cirac. Improvement of frequency standards with quantum entanglement. Physical Review Letters, 79(20):3865–3868, 1997.

[66] N. R. Hutzler. A New Limit on the Electron Electric Dipole Moment. PhD thesis, Harvard University, 3 2014.

[67] N. R. Hutzler, H.-i. Lu, and J. M. Doyle. The Bu ff er Gas Beam : An Intense , Cold , and Slow Source for Atoms and Molecules. Chemical Reviews, 112(9):4803–4827, 4 2012.

[68] T. Inoue, S. Ando, T. Aoki, H. Arikawa, S. Ezure, K. Harada, T. Hayamizu, T. Ishikawa, M. Itoh, K. Kato, H. Kawamura, A. Uchiyama, T. Aoki, K. Asahi, T. Furukawa, A. Hatakeyama, K. Hatanaka, K. Imai, T. Murakami, H. S. Nataraj, T. Sato, Y. Shimizu, T. Wakasa, H. P. Yoshida, A. Yoshimi, and Y. Sakemi. Experimental search for the electron electric dipole moment with laser cooled francium atoms. Hyperfine Interactions, 231(1-3):157–162, 12 2015.

[69] M. Jung. A robust limit for the electric dipole moment of the electron. Journal of High Energy Physics, 2013(5):71805–71815, 5 2013.

[70] I. B. Khriplovich and S. K. Lamoreaux. CP Violation Without Strangeness. Springer, Berlin, 1997.

[71] M. G. Kozlov and A. Derevianko. Proposal for a sensitive search for the electric dipole moment of the electron with matrix-isolated radicals. Physical Review Letters, 97(6):63001, 8 2006.

[72] I. Kozyryev, L. Baum, K. Matsuda, and J. M. Doyle. Proposal for Laser Cooling of Complex Polyatomic Molecules. ChemPhysChem, 17(22):3641–3648, 11 2016.

[73] I. Kozyryev and N. R. Hutzler. Precision Measurement of Time-Reversal Symmetry Violation with Laser-Cooled Polyatomic Molecules. Physical Review Letters, 119(13):133002–133006, 9 2017.

[74] F. Kuchler, E. Babcock, M. Burghoff, T. Chupp, S. Degenkolb, I. Fan, P. Fierlinger, F. Gong, E. Kraegeloh, W. Kilian, S. Knappe-Grüneberg, T. Lins, M. Marino, J. Meinel, B. Niessen, N. Sachdeva, Z. Salhi, A. Schnabel, F. Seifert, J. Singh, S. Stuiber, L. Trahms, and J. Voigt. A new search for the atomic EDM of 129Xe at FRM-II. Hyperfine Interactions, 237(1):1–5, 12 2016.

[75] X. Lacour, S. Guérin, L. P. Yatsenko, N. V. Vitanov, and H. R. Jauslin. Uniform analytic description of dephasing effects in two-state transitions. Physical Review A, 75(3), 2007.

[76] Z. Lasner. Order-of-magnitude-tighter bound on the electron electric dipole moment. PhD thesis, Yale University, 2019.

[77] Z. Lasner and D. Demille. Statistical sensitivity of phase measurements via laser-induced fluorescence with optical cycling detection. Physical Review A, 98(5):53823, 2018.

[78] A. E. Leanhardt, J. L. Bohn, H. Loh, P. Maletinsky, E. R. Meyer, L. C. Sinclair, R. P. Stutz, and E. A. Cornell. High-resolution spectroscopy on trapped molecular ions in rotating electric fields: A new approach for measuring the electron electric dipole moment. Journal of Molecular Spectroscopy, 270(1):1–25, 11 2011.

[79] J. Lee, J. Chen, L. V. Skripnikov, A. N. Petrov, A. V. Titov, N. S. Mosyagin, and A. E. Leanhardt. Optical spectroscopy of tungsten carbide for uncertainty analysis in electron electric-dipole-moment search. Physical Review A, 87(2):22512–22516, 2 2013.

[80] T. D. Lee and C. N. Yang. Question of parity conservation in weak interactions. Physical Review, 104(1):254–258, 1 1956.

[81] J. Lim, J. R. Almond, M. A. Trigatzis, J. A. Devlin, N. J. Fitch, B. E. Sauer, M. R. Tarbutt, and E. A. Hinds. Laser Cooled YbF Molecules for Measuring the Electron's Electric Dipole Moment. Physical Review Letters, 120(12):123201, 3 2018.

[82] H. Loh. Search for an electron electric dipole moment with trapped molecular ions. PhD thesis, University of Colorado Boulder, University of Colorado Boulder, 7 2013.

[83] H. Loh, R. P. Stutz, T. S. Yahn, H. Looser, R. W. Field, and E. A. Cornell. REMPI spectroscopy of HfF. Journal of Molecular Spectroscopy, 276-277(1):49–56, 7 2012.

[84] H. Loh, J. Wang, M. Grau, T. S. Yahn, R. W. Field, C. H. Greene, and E. A. Cornell. Laser-induced fluorescence studies of HfF produced by autoionization. Journal of Chemical Physics, 135(15):154308, 1 2011.

[85] M. McDonald. High Precision Optical Spectroscopy and Quantum State Selected Photodissociation of Ultracold $^{88}Sr_2$ Molecules in an Optical Lattice. PhD thesis, Columbia University, 2017.

[86] M. McDonald, B. H. McGuyer, F. Apfelbeck, C. H. Lee, I. Majewska, R. Moszynski, and T. Zelevinsky. Photodissociation of ultracold diatomic strontium molecules with quantum state control. Nature, 534(7610):122–126, 7 2016.

[87] E. R. Meyer, J. L. Bohn, and M. P. Deskevich. Candidate molecular ions for an electron electric dipole moment experiment. Physical Review A, 73(6):62108–62110, 6 2006.

[88] E. R. Meyer, A. E. Leanhardt, E. A. Cornell, and J. L. Bohn. Berry-like phases in structured atoms and molecules. Physical Review A, 80(6):62110–62113, 12 2009.

[89] W. Nagourney, J. Sandberg, and H. Dehmelt. Shelved optical electron amplifier: Observation of quantum jumps. Physical Review Letters, 56(26):2797–2799, 1986.

[90] S. Nakhate, T. C. Steimle, N. H. Pilgram, and N. R. Hutzler. The pure rotational spectrum of YbOH. Chemical Physics Letters, 715:105–108, 1 2019.

[91] K. K. Ni, H. Loh, M. Grau, K. C. Cossel, J. Ye, and E. A. Cornell. State-specific detection of trapped HfF^+ by photodissociation. Journal of Molecular Spectroscopy, 300:12–15, 3 2014.

[92] K. K. Ni, T. Rosenband, and D. D. Grimes. Dipolar exchange quantum logic gate with polar molecules. Chemical Science, 9(33):6830–6838, 8 2018.

[93] T. Noel, M. R. Dietrich, N. Kurz, G. Shu, J. Wright, and B. B. Blinov. Adiabatic passage in the presence of noise. Physical Review A, 85(2):23401, 2012.

[94] E. B. Norrgard, E. R. Edwards, D. J. McCarron, M. H. Steinecker, D. DeMille, S. S. Alam, S. K. Peck, N. S. Wadia, and L. R. Hunter. Hyperfine structure of the $B^3\Pi_1$ state and predictions of optical cycling behavior in the $X \rightarrow B$ transition of TlF. Physical Review A, 95(6):062506, 2017.

[95] C. D. Panda, B. R. O'Leary, A. D. West, J. Baron, P. W. Hess, C. Hoffman, E. Kirilov, C. B. Overstreet, E. P. West, D. DeMille, J. M. Doyle, and G. Gabrielse. Stimulated Raman adiabatic passage preparation of a coherent superposition of ThO $H^3\Delta_1$ states for an improved electron electric-dipole-moment measurement. Physical Review A, 93(5):052110, 5 2016.

[96] R. H. Parker, M. R. Dietrich, M. R. Kalita, N. D. Lemke, K. G. Bailey, M. Bishof, J. P. Greene, R. J. Holt, W. Korsch, Z. T. Lu, P. Mueller, T. P. O'Connor, and J. T. Singh. First measurement of the atomic electric dipole moment of ^{225}Ra. Physical Review Letters, 114(23):233002, 6 2015.

[97] E. Petrik West. A Thermochemical Cryogenic Buffer Gas Beam Source of ThO for Measuring the Electric Dipole Moment of the Electron. PhD thesis, Harvard University, 2017.

[98] A. N. Petrov, N. S. Mosyagin, T. A. Isaev, and A. V. Titov. Theoretical study of HfF^+ in search of the electron electric dipole moment. Physical Review A, 76(3):30501–30504, 9 2007.

[99] A. N. Petrov, N. S. Mosyagin, and A. V. Titov. Theoretical study of low-lying electronic terms and transition moments for HfF^+ for the electron electric-dipole-moment search. Physical Review A, 79(1):607–608, 1 2009.

[100] A. N. Petrov, L. V. Skripnikov, and A. V. Titov. Zeeman interaction in the $^3\Delta_1$ state of HfF^+ to search for the electron electric dipole moment. Physical Review A, 96(2):22508, 4 2017.

[101] L. Pezzè, A. Smerzi, M. K. Oberthaler, R. Schmied, and P. Treutlein. Quantum metrology with nonclassical states of atomic ensembles. Reviews of Modern Physics, 90:035005, 2016.

[102] M. E. Pospelov and I. B. Khriplovich. Electric dipole moment of the W boson and the electron in the Kobayashi-Maskawa model. Sov. J. Nucl. Phys., 53:638–640, 1991.

[103] E. M. Purcell and N. F. Ramsey. On the Possibility of Electric Dipole Moments for Elementary Particles and Nuclei.pdf. Physical Review, 78(6):807, 1 1950.

[104] B. C. Regan, E. D. Commins, C. J. Schmidt, and D. DeMille. New limit on the electron electric dipole moment. Physical Review Letters, 88(7):718051–718054, 2 2002.

[105] M. S. Safronova, D. Budker, D. DeMille, D. F. J. Kimball, A. Derevianko, and C. W. Clark. Search for New Physics with Atoms and Molecules. Reviews of Modern Physics, 90(2):025008, 6 2017.

[106] A. D. Sakharov. Violation of CP-Invariance, C-Asymmetry, and Baryon Asymmetry of the Universe. ZhETF Pis'ma, 5:24, 1 1967.

[107] J. J. Sakurai and S. F. Tuan. Modern quantum mechanics. Addison-Wesley Pub. Co, 1994.

[108] P. G. Sandars. The electric dipole moment of an atom. Physics Letters, 14(3):194–196, 2 1965.

[109] H. Schall, M. Dulick, and R. W. Field. The electronic structure of LaF: A multiconfiguration ligand field calculation. The Journal of Chemical Physics, 87(5):2898–2912, 1987.

[110] L. I. Schiff. Measurability of nuclear electric dipole moments. Physical Review, 132(5):2194–2200, 1 1963.

[111] E. Schmutzer and J. Plebanski. Quantum mechanics in non inertial frames of reference. Fortschritte der Physik, 25(1):37–82, 1 1977.

[112] L. C. Sinclair. Development of Frequency Comb Velocity-Modulation Spectroscopy, Spectroscopy of HfF^+ and the JILA eEDM Experiment. PhD thesis, University of Colorado Boulder, 2012.

[113] L. V. Skripnikov. Combined 4-component and relativistic pseudopotential study of ThO for the electron electric dipole moment search. Journal of Chemical Physics, 145(21):214301–214311, 12 2016.

[114] L. V. Skripnikov. Communication: Theoretical study of HfF^+ cation to search for the T,P-odd interactions. Journal of Chemical Physics, 147(2):1–5, 7 2017.

[115] L. V. Skripnikov, A. N. Petrov, and A. V. Titov. Communication: Theoretical study of ThO for the electron electric dipole moment search. Journal of Chemical Physics, 139(22):0–4, 1 2013.

[116] L. V. Skripnikov and A. V. Titov. Theoretical study of ThF^+ in the search for T,P-violation effects: Effective state of a Th atom in ThF^+ and ThO compounds. Physical Review A, 91(4), 1 2015.

[117] L. V. Skripnikov, A. V. Titov, and V. V. Flambaum. Enhanced effect of CP -violating nuclear magnetic quadrupole moment in a HfF^+ molecule. Physical Review A, 95(2):1220, 2017.

[118] J. Smith, E. Purcell, and N. Ramsey. Experimental measurement to the electric dipole moment of the neutron. Physical Review, 108(1):120–122, 1 1957.

[119] N. J. Stone. Table of nuclear magnetic dipole and electric quadrupole moments. Atomic Data and Nuclear Data Tables, 90(1):75–176, 1 2005.

[120] R. P. Stutz. Towards Measuring the Electron Electric Dipole Moment Using Trapped Molecular Ions. PhD thesis, University of Colorado Boulder, University of Colorado Boulder, 8 2010.

[121] O. P. Sushkov and V. V. Flambaum. Parity breaking effects in diatomic molecules. Sov. Phys. JETP, 48(4):608, 1978.

[122] P. Sushkov, V. V. Flambaum, and I. B. Khriplovich. Possibility of investigating P-and T-odd nuclear forces in atomic and molecular experiments. Zh. Eksp. Teor. Fiz., 87(November 1984):1521–1540, 1984.

[123] M. R. Tarbutt, B. E. Sauer, J. J. Hudson, and E. A. Hinds. Design for a fountain of YbF molecules to measure the electron's electric dipole moment. New Journal of Physics, 15(5):53018–53034, 5 2013.

[124] E. R. Tardiff, E. T. Rand, G. C. Ball, T. E. Chupp, A. B. Garnsworthy, P. Garrett, M. E. Hayden, C. A. Kierans, W. Lorenzon, M. R. Pearson, C. Schaub, and C. E. Svensson. The radon EDM apparatus. In ISAC and ARIEL: The TRIUMF Radioactive Beam Facilities and the Scientific Program, volume 225, pages 197–206. Springer Netherlands, 1 2014.

[125] S. Truppe, H. J. Williams, M. Hambach, L. Caldwell, N. J. Fitch, E. A. Hinds, B. E. Sauer, and M. R. Tarbutt. Molecules cooled below the Doppler limit. Nature Physics, 13(12):1173–1176, 8 2017.

[126] N. V. Vitanov, T. Halfmann, B. W. Shore, and K. Bergmann. Laser-induced population transfer by adiabatic passage techniques. Annual Review of Physical Chemistry, 52(1):763–809, 3 2001.

[127] N. V. Vitanov, A. A. Rangelov, B. W. Shore, and K. Bergmann. Stimulated Raman adiabatic passage in physics, chemistry, and beyond. Reviews of Modern Physics, 89(1):015006, 3 2017.

[128] A. C. Vutha, M. Horbatsch, and E. A. Hessels. Oriented polar molecules in a solid inert-gas matrix: a proposed method for measuring the electric dipole moment of the electron. Atoms, 6(1):3–10, 3 2017.

[129] A. C. Vutha, M. Horbatsch, and E. A. Hessels. Orientation-dependent hyperfine structure of polar molecules in a rare-gas matrix: a scheme for measuring the electron electric dipole moment. Physical Review A, 98:032513, 2018.

[130] J. Williams. Application Note 21 - Composite Amplifiers. Technical Report July, Linear Technology, 1986.

[131] C. S. Wu, E. Ambler, R. W. Hayward, D. D. Hoppes, and R. P. Hudson. Experimental test of parity conservation in beta decay. Physical Review, 105(4):1413–1415, 1 1957.

[132] B. J. Y. Wuebbles and J. S. Felton. Evaluation of laser dye mutagenicity using the ames/salmonella microsome test. Environmental Mutagenesis, 7(4):511–522, 1985.

[133] Y. X. Yao and S. M. Pandit. Cramér-Rao Lower Bounds for a Damped Sinusoidal Process. IEEE Transactions on Signal Processing, 43(4):878–885, 4 1995.

[134] M. Yeo, M. T. Hummon, A. L. Collopy, B. Yan, B. Hemmerling, E. Chae, J. M. Doyle, and J. Ye. Rotational State Microwave Mixing for Laser Cooling of Complex Diatomic Molecules. Physical Review Letters, 114(22):223003–223004, 2015.

[135] R. N. Zare. Photoejection Dynamics. Molecular Photochemistry, 4(1):1–37, 1 1972.

[136] R. N. Zare. Angular momentum: understanding spatial aspects in chemistry and physics. Wiley, New York, 1988.

[137] K. Zhu, N. Solmeyer, C. Tang, and D. S. Weiss. Absolute polarization measurement using a vector light shift. Physical Review Letters, 111(24):243005–243006, 12 2013.

Appendix A

Simulations

The goal of this section is to make a selection of past simulations and numerical calculations accessible to future generations of students on the EDM experiment.

A.1 Spherical multipole fitting

Since 2015, we have used a simple suite of tools in Matlab for linear least squares fitting of interior spherical multipole solutions to the Laplace equation,

$$-\nabla^2 \Phi(\boldsymbol{r}) = 0. \tag{A.1}$$

Here "interior" refers to the fact that the potential $\Phi(\boldsymbol{r})$ remains finite as $r \to 0$. The potential Φ can be decomposed into multipole components,

$$\Phi(\boldsymbol{r}) = \sum_{l=0}^{\infty} \sum_{m=-l}^{l} c_{lm}\, \Phi_{lm}(\boldsymbol{r}) \tag{A.2}$$

The multipole components of the potential are

$$\Phi_{lm}(r, \theta, \phi) = r^l\, Y_{lm}(\theta, \phi), \tag{A.3}$$

each of which is itself a solution to the Laplace equation. For the spherical harmonics Y_{lm}, we use a semi-normalized real form

$$Y_{lm} = \sqrt{\frac{4\pi}{2l+1}} \times \begin{cases} \frac{i}{\sqrt{2}} \left(Y_l^m - (-1)^m Y_l^{-m}\right) & \text{if } m < 0, \\ Y_l^0 & \text{if } m = 0, \\ \frac{1}{\sqrt{2}} \left(Y_l^{-m} + (-1)^m Y_l^m\right) & \text{if } m > 0, \end{cases} \tag{A.4}$$

which are convenient in that the first few multipole components are easy to memorize. Some examples of these are shown in Table A.1.

As can be seen from Table A.1, when expressed in Cartesian coordinates, the potentials $\Phi_{lm}(\boldsymbol{r})$ take the form of polynomials where the exponents in each term sums to l. This makes a particularly convenient form for creating a lookup table, rather than evaluating them in spherical coordinates (which is computationally expensive). I used Mathematica to generate tables of coefficients as shown in Table A.2, and imported these into Matlab for fitting and further use.

To fit with multipoles, we perform linear regression using QR decomposition. The total potential is to be expressed as a sum over components as in Eq. (A.2). Accounting for errors and noise, we can write this as a matrix equation,

$$\underline{\Phi} = \underline{\underline{M}}\,\underline{C} + \underline{\epsilon}, \tag{A.5}$$

where the observed potential is

$$\underline{\Phi} = \left[\Phi(\boldsymbol{r}_0)\ \Phi(\boldsymbol{r}_1)\ \ldots\right]^T,$$

the coefficient vector is

$$\underline{C} = \left[c_{0,0}\ c_{1,-1}\ c_{1,0}\ \ldots\right]^T,$$

and the design matrix is

$$\underline{\underline{M}} = \begin{bmatrix} \Phi_{0,0}(\boldsymbol{r}_0) & \Phi_{1,-1}(\boldsymbol{r}_0) & \Phi_{1,0}(\boldsymbol{r}_0) & \ldots \\ \Phi_{0,0}(\boldsymbol{r}_1) & \Phi_{1,-1}(\boldsymbol{r}_1) & \Phi_{1,0}(\boldsymbol{r}_1) & \ldots \\ \Phi_{0,0}(\boldsymbol{r}_2) & \Phi_{1,-1}(\boldsymbol{r}_2) & \Phi_{1,0}(\boldsymbol{r}_2) & \ldots \\ & \vdots & & \end{bmatrix}$$

We evaluate $\underline{\underline{M}}$ and use QR factorization in Matlab to solve the least squares problem, with the solution for the coefficients

$$\underline{C} = \underline{\underline{R}}^{-1}\,\underline{\underline{Q}}^T\,\underline{\Phi}. \tag{A.6}$$

We have also implemented regression using observations of the *fields* $\vec{\mathcal{E}} = -\nabla\Phi$, by simply concatenating the observations of the X, Y, and Z components of the fields, and evaluating a $3\times$

l	m	Φ_{lm}	$\boldsymbol{\mathcal{E}}_{lm,X}$	$\boldsymbol{\mathcal{E}}_{lm,Y}$	$\boldsymbol{\mathcal{E}}_{lm,Z}$
0	0	1	0	0	0
1	1	X	1		
1	0	Z			1
1	-1	Y		1	
2	2	$\frac{\sqrt{3}}{2}(X^2 - Y^2)$	$\sqrt{3}X$	$-\sqrt{3}Y$	
2	1	$\sqrt{3}XZ$	$\sqrt{3}Z$		$\sqrt{3}X$
2	0	$\frac{1}{2}\left(2Z^2 - X^2 - Y^2\right)$	$-X$	$-Y$	$2Z$
2	-1	$\sqrt{3}YZ$		$\sqrt{3}Z$	$\sqrt{3}Y$
2	-2	$\sqrt{3}XY$	$\sqrt{3}Y$	$\sqrt{3}X$	
3	1	$-\sqrt{\frac{3}{8}}X\left(X^2 + Y^2 - 4Z^2\right)$	$-\sqrt{\frac{3}{8}}\left(3X^2 + Y^2 - 4Z^2\right)$	$-\sqrt{\frac{3}{2}}XY$	$2\sqrt{6}XZ$
4	1	$-\sqrt{\frac{5}{8}}XZ\left(3X^2 + 3Y^2 - 4Z^2\right)$	$\sqrt{\frac{5}{8}}Z\left(-9X^2 - 3Y^2 + 4Z^2\right)$	$-3\sqrt{\frac{5}{2}}XYZ$	$-\sqrt{\frac{45}{8}}X\left(X^2 + Y^2 - 4Z^2\right)$

Table A.1: Unnormalized real spherical harmonics used in spherical multipole fitting in this thesis. The (lack of) normalization is chosen so that the $(l = 1, m)$ and $(l = 2, m = 0)$ components have the form conventionally used in past eEDM work.

0	0	0	2	2	2	2	2
0	0	0	-2	-1	0	1	2
0	0	2	0	0	1	0	0
0	1	1	0	1.732	0	0	0
1	0	1	0	0	0	1.732	0
0	2	0	0	0	-0.5	0	-0.866
1	1	0	1.732	0	0	0	0
2	0	0	0	0	-0.5	0	0.866

Table A.2: Example of a table of multipole potential data for $l = 2$. The first two rows contain l and m values, however the first three columns of the first two rows are ignored. The remaining rows of the first three columns indicate exponents of the X, Y, and Z coordinates. Each of the remaining columns contains coefficients of the Φ_{lm} indicated by the first two rows. For example, reading from this table, we obtain $\Phi_{2,-2} = 1.732\,X\,Y$, in agreement with Table A.1.

larger design matrix using the analytical form of the gradient of the potentials, which can be easily obtained by matrix operations on the Mathematica output shown in Table A.2.

As of July 2019, these functions are available on the JILA network drive in the directory `smb:\\jilafile\scratch\cornell\common\edm\MATLAB\multipole` , which includes a Mathematica script to generate text files, and Matlab scripts to process the text files into `.mat` files that contain the same information. It also takes an analytical derivative of the tabular data to obtain lookup tables for the multipole fields.

A.2 Space charge & thermometry

In Fall 2017, just after installing the Generation 2 ion trap, we were creating about 10^4 HfF^+ ions per shot, and we wanted to know their temperature. We calibrated the MCP transfer functions as described in Section B.1 (as well as in Huanqian's thesis), but found that our fitted ion cloud temperatures were quite high, on the order of 30 to 50 Kelvin. This caused us to suspect significant space charge effects, which tends to make the peak density lower and the width higher than for a non-interacting gas. We subsequently investigated the temperature and the presence of space charge effects through three main avenues:

- The profile of the ion cloud in time of flight

- Frequency and damping of breathing modes of the ion cloud
- Depletion spectroscopy of $^1\Sigma^+[0,0]$

A.2.1 Ion cloud profile

The mutual Coulomb repulsion between the HfF^+ ions in our RF trap affects the density distribution of the ion cloud $n(\boldsymbol{r})$. In the extreme limit of low temperatures, the ion cloud crystallizes into a Coulomb crystal, but even at much higher temperatures, the effects of interactions should be visible in the density profile. However there are several confounding factors: we only observe the ion cloud in time of flight, the ions may be flying through a distorting potential landscape, and there are other HfF^+ isotopes present in the trap. Altogether, the ion cloud profile is likely the least reliable way of characterizing the temperature and the extent of space charge effects.

To try to back out the temperature, I wrote a simulation in Matlab that uses successive relaxation to obtain the equilibrium density distribution in a given trapping potential. In fact, this simulation was initially motivated by my brief forays into molecular dynamics simulations, where I have found that one of the most time-consuming steps in a Coulomb problem is allowing the ensemble to reach an equilibrium spatial distribution. In future simulations of Ramsey fringes, when the effects of space-charge on fringe frequencies may become noticeable, it will likely be desirable to simulate the electric fields experienced by a small fraction of some $\sim 10^4$ ions whose trajectories are simulated. In this case, we probably will want to start from approximately an equilibrium configuration.

To solve for the equilibrium distribution $n(\boldsymbol{r})$, I begin with a guess $n_0(\boldsymbol{r})$, which is usually either a Gaussian corresponding to a non-interacting cloud, or a flat-top distribution (which of these converges faster depends on the Coulomb interaction energy compared to kinetic energy). From our initial guess, we can solve the discrete Poisson equation with a simple matrix inversion to obtain the electric potential,

$$\Phi(\boldsymbol{r}) = -\frac{e}{\epsilon_0}\frac{1}{\nabla^2}n(\boldsymbol{r}), \tag{A.7}$$

where $1/\nabla^2$ denotes the inverse of the discrete Laplacian operator. I then update the density distribution according to

$$n(\boldsymbol{r}) \rightarrow (1-\alpha)n(\boldsymbol{r}) + \alpha\, n_{\mathrm{new}}(\boldsymbol{r}), \tag{A.8}$$

where $0 < \alpha < 1$ is a constant chosen to decide how quickly the solution attempts to converge, and the "new" density distribution is

$$n_{\mathrm{new}}(\boldsymbol{r}) = n_0 \exp\left\{-\frac{V(\boldsymbol{r}) + e\Phi(\boldsymbol{r})}{k_B T}\right\}, \tag{A.9}$$

where n_0 is a normalization factor chosen so that the new density distribution integrates to N, the total ion number. If α is too large, the solution will become unstable; typically $\alpha \approx 0.1$ is a good choice. The updated density distribution is then used to solve for $\Phi(\boldsymbol{r})$, and the process is repeated until a stationary solution is reached. An example result is shown in Fig. A.1, where even at a temperature of 5 K, a cloud of 10^4 ions shows significant effects of reduced density due to space charge.

A.2.2 Ion cloud breathing modes

A useful way to inquire about the relative energy scales of Coulomb interactions versus thermal motion is via the collective normal modes of "breathing" or "jiggling" of the ion cloud. In a hot and therefore weakly interacting cloud of ions, collisions have a relatively small effect on the secular (sloshing) motion of each ion in the trap. In this limit, the apparent breathe frequency of the ion cloud along trap axis i is $\omega_{\mathrm{breathe}} = 2\omega_{\mathrm{sec},i}$, and energy is very slow to transfer between principal axes. Here, the breathe modes of the ion cloud are not collective modes in the true sense, but just single particle motion of many independent particles in the trap with some degree of phase coherence.

In a cold ion cloud, the Coulomb potential energy of the cloud is not small compared to its thermal kinetic energy. In this limit, collective breathing modes of the ions clouds exist, with frequencies $\omega_{\mathrm{breathe}} < 2\omega_{\mathrm{sec},i}$. Experimentally, we investigated the "axgrad" mode, which is shown schematically in Fig. A.2(a). We adjusted the trap parameters so that the secular frequencies were

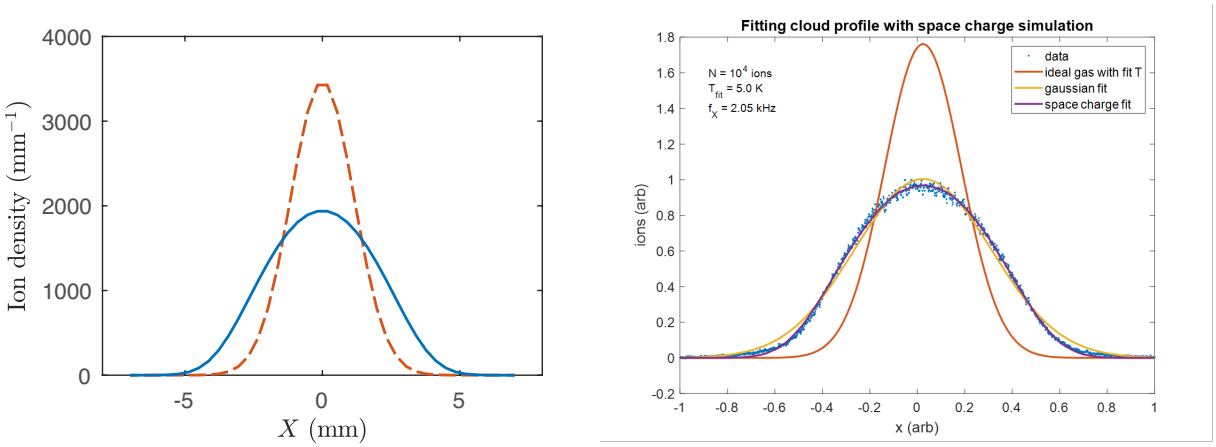

(a) (b)

Figure A.1: (a) Simulated integrated density profile of an ion cloud with (blue) and without (red dashed) space charge effects. Here $N = 10^4$ ions, $T = 5$ K, and the cloud is confined in a spherically symmetric harmonic potential with $\omega = 2\pi \times 2$ kHz. The Y and Z axes have been integrated out, so that this is what we would see as a voltage trace on an MCP detector – i.e., this is not a slice through the density distribution. (b) Experimentally observed time of flight profile of the ion cloud density, with overlays of various simulated profiles. Assuming a temperature of 5 K and 10^4 ions, a profile that accounts for the space charge effects provides the best fit.

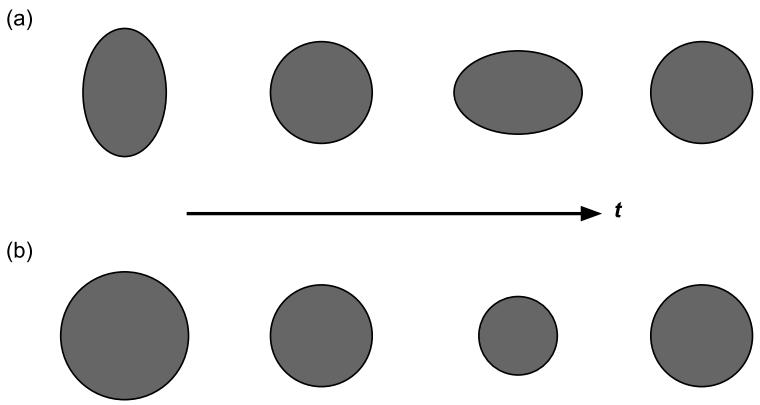

Figure A.2: Examples of normal modes of a cold ion cloud. In the "axgrad" mode (a), the axial direction is out of phase with the radial directions, and oscillates with twice the amplitude. In the "breathe" mode (b), the cloud widths along all three principal axes oscillate in phase.

nearly equal at $\omega_{\rm sec} = 2.05(1)$ Hz, and excited the "axgrad" mode by applying a simultaneous voltage pulse of equal magnitude on the endcap electrodes. The observed oscillation is shown in Fig. A.3. The $1/e$ time of the oscillation is of order 2 ms, and the oscillation frequency is about 3 kHz – significantly less than $2\omega_{\rm sec}$. Qualitatively, this shows that space charge effects are significant in our HfF^+ cloud. Comparison with a numerical simulation of the cloud breathe frequencies could extract the temperature, however we have not yet performed such a simulation, as we found Doppler thermometry to be more straightforward.

A.2.3 Doppler thermometry

Having found that the spatial width of the cloud in time of flight was not representative of the temperature (unless space charge is accounted for), we found that the simplest way to perform thermometry is by measuring the Doppler width of the cloud via laser spectroscopy. For this purpose, we primarily used the 961 nm laser ("Toptica") driving the $^3\Pi_{0^+} \leftarrow {}^1\Sigma^+$ (0,0) $P(1)$ transition, and tuned its wavelength via the lock to our HighFinesse wavemeter. The intensity of the 961 nm laser had to be reduced significantly to prevent saturation of the transition. With a few millisecond probe time, we observed widths between $\sigma_n u \approx 10$ MHz and 30 MHz, corresponding to temperatures in the 3 K to 30 K range.

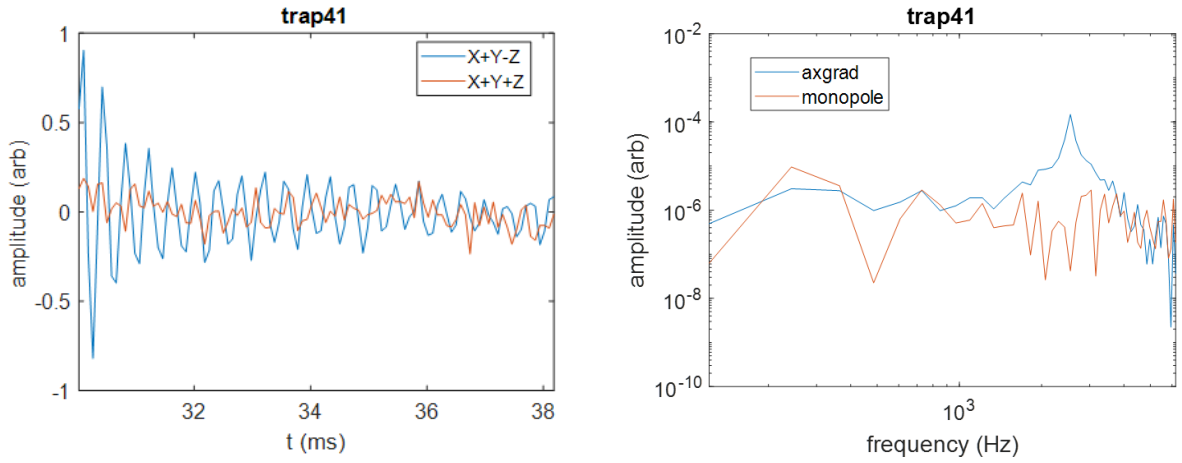

(a) (b)

Figure A.3: (a) Damping of the "axgrad" and "breathe" collective modes of oscillation of the HfF^+ cloud, after excitation by a kick applied to both endcaps. (b) FFT of the data from part (a), showing the frequency of the "axgrad" mode, which is approximately $1.7\omega_{\mathrm{sec}}$. This indicates that space charge effects are significant in the ion cloud.

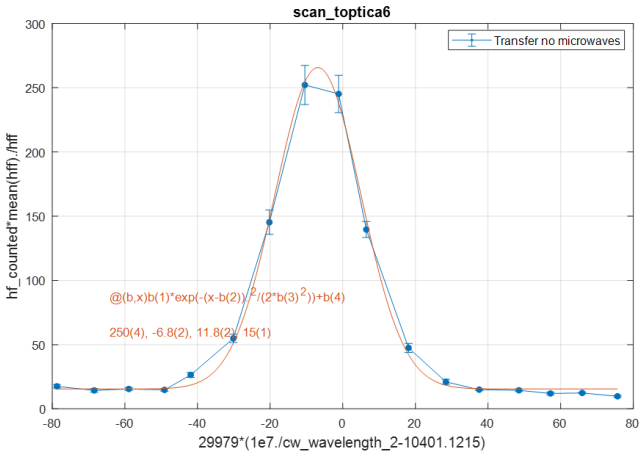

Figure A.4: Population detected by photodissociation of $^3\Delta_1(v=0, J=1)$ versus frequency of the 961 nm laser driving the $^3\Pi_{0^+} \leftarrow {}^1\Sigma^+$ (0,0) $P(1)$ transition, showing the one-photon Doppler width of the HfF^+ cloud. The 961 nm laser is stabilized to the HighFinesse wavemeter. The measured width is $\sigma_\nu = 11.8(2)$ MHz, corresponding to a temperature of $T = m\sigma_\nu^2\lambda^2/k_B = 3.1(1)$ K.

A.3 Trap design

Here I include a my Matlab code for optimization of the Generation 2 ion trap geometry. This may serve as a useful reference for future use of the Livelink for Matlab toolbox for Comsol, as the documentation for this Comsol add-on is somewhat limited. The Matlab script below programmatically generates a basic version of the Generation 2 ion trap geometry with certain predefined parameters (such as the ion trap height and radius) and numerically optimizes the electrode shapes as described in Chapter 4.

First, one needs to start the Comsol Server and Livelink for Matlab. On a PC with Comsol installed, the Comsol Server application can be found in the directory

`C:\Program Files\COMSOL\COMSOL53a\Multiphysics\COMSOL Launchers`

where 5.3a is replaced by the Comsol version installed. Then in Matlab we add paths to the Livelink API functions and start the Livelink interface using the following commands:

```
import com.comsol.model.*;
import com.comsol.model.util.*;
addpath('C:\Program Files\COMSOL\COMSOL53a\Multiphysics\mli\');
mphstart();
```

I then initialize the Comsol model with the following:

```
function model = model_init(mesh_size)

% dependencies
import com.comsol.model.*;
import com.comsol.model.util.*;
% addpath('C:\Program Files\COMSOL\COMSOL52\Multiphysics\mli\');

% input arguments
if nargin<1
    mesh_size = 7;
end

params = trap_geom_param_defaults();
filename = ['trap_' datestr(today,'YYmmDD')];
model = mphopen('optimization_models/chamber_simple_160901.mph');
% model = ModelUtil.create(filename);
model.name([filename '.mph']);

% set model parameters
```

```
20      model = set_model_params(model,params);
21
22      % build geometry
23      [model,rad_elec_domains] = build_trap_geom(model);
24
25      % assign materials
26      model = set_trap_materials(model,rad_elec_domains);
27
28      % add electrostatics & define potentials
29      model = set_electrostatics(model);
30
31      % build mesh
32      model = build_mesh(model,mesh_size);
33
34      % don't show progress bar
35      ModelUtil.showProgress(false);
36
37      figure(1); clf;
38      mphviewselection(model,'geom1',[rad_elec_domains],'entity','domain',...
39          'facemode','off');
40
41      end
```

The function `mphopen` is part of the Livelink API, and takes as an argument an `.mph` file path as a string. I then pass the variable `model` into and out of various functions that initialize different aspects of the geometry, materials, and mesh. I set certain default parameters with the following code:

```
1       params.pi = pi;
2       params.N_elec = 8;
3
4       params.Vrot = 1;
5       params.phi_rot = 0;
6       params.Vtrap = 0;
7       params.phi_trap = 0;
8       params.Vtop = 0;
9       params.Vbot = 0;
10
11      params.c2 = 0.053811014;
12      params.c4 = -0.114742513;
13      params.c6 = -0.149448808;
14      params.c8 = 0.693544237;
15      params.c10 = 0.099128725;
16
17      params.r_trap_inner = 0.048;
18      params.r_trap_outer = 0.084;
19      params.w_elec_tab = 0.010;
20      params.h_elec_tab = 0.020;
21      params.h_rad = 0.150;
22      params.t_rad = 0.004;
23
24      params.fillet_radius = 0.001;
25
26      f = fields(params);
27      for i = 1:numel(f)
```

```
28          model.param.set(f{i},params.(f{i}));
29      end
```

The function `build_trap_geom` defines the geometry of the ion trap in terms of the existing parameters.

```
1       function [model,rad_elec_domains] = build_trap_geom(model)
2
3       import com.comsol.model.*;
4       import com.comsol.model.util.*;
5       % addpath('C:\Program Files\COMSOL\COMSOL52\Multiphysics\mli\');
6
7       if nargin<1 || isempty(model)
8           filename = ['trap_' datestr(today,'YYmmDD')];
9           model = ModelUtil.create(filename);
10      end
11
12      % set model params just in case
13      params = get_model_params(model);
14
15      % create geometry
16      try
17          geom = model.geom('geom1');
18      catch
19          geom = model.geom.create('geom1',3);
20      end
21
22      % parametric definitions of radial electrode geometry
23      for i = 1:params.N_elec
24
25          % define a workplane
26          workplane_tag = char(geom.feature.uniquetag('workplane'));
27          workplane = geom.feature.create(workplane_tag,'WorkPlane');
28          workplane.set('planetype', 'quick');
29          workplane.set('quickplane', 'xz');
30          workplane.set('quicky','t_rad/2');
31
32          % define a bezier polygon that outlines the electrodes
33          rad_elec_body_tag = ...
                char(workplane.geom.feature.uniquetag('rad_elec_body'));
34          rad_elec_body = ...
                workplane.geom.feature.create(rad_elec_body_tag,'BezierPolygon');
35          rad_elec_body.set('type','open');
36          rad_elec_body.set('degree',1);
37          rad_elec_body.set('p',...
38              {
39              'r_trap_inner*(1-c2-c4-c6-c8-c10)','r_trap_outer-w_elec_tab',...
40                  'r_trap_outer-w_elec_tab','r_trap_outer','r_trap_outer',...
41                  'r_trap_outer-w_elec_tab','r_trap_outer-w_elec_tab',...
42                  'r_trap_inner*(1-c2-c4-c6-c8-c10)';
43              '-h_rad/2','-h_rad/2','-(h_rad/2+h_elec_tab)','-(h_rad/2+h_elec_tab)',...
44              'h_rad/2+h_elec_tab','h_rad/2+h_elec_tab','h_rad/2','h_rad/2'
45              });
```

```
46          rad_elec_body.set('createselection','on');
47
48          % front face of the electrode -- a polynomial
49          rad_elec_front_tag = ...
                char(workplane.geom.feature.uniquetag('rad_elec_front'));
50          rad_elec_front = ...
                workplane.geom.feature.create(rad_elec_front_tag,'ParametricCurve');
51          rad_elec_front.set('rtol',1e-9);
52          rad_elec_front.set('parname','s');
53          rad_elec_front.set('parmin',-1);
54          rad_elec_front.set('parmax',1);
55          rad_elec_front.set('coord',{'r_trap_inner*(1 - c2*s^2 - c4*s^4 - c6*s^6 ...
                - c8*s^8 - c10*s^10)','h_rad/2*s'});
56          rad_elec_front.set('createselection','on');
57
58          % turn the line defining the electrode into a surface
59          rad_elec_surf_tag = ...
                char(workplane.geom.feature.uniquetag('rad_elec_surf'));
60          rad_elec_surf = workplane.geom.feature.create(rad_elec_surf_tag, ...
                'ConvertToSolid');
61          rad_elec_surf.selection('input').set({rad_elec_front_tag,...
62              rad_elec_body_tag});
63          rad_elec_surf.set('createselection','on');
64
65          % fillet some of the corners
66          fillet_tag = workplane.geom.feature.uniquetag('fillet');
67          fillet = workplane.geom.feature.create(fillet_tag,'Fillet');
68          fillet.selection('point').set([rad_elec_surf_tag '(1)'],[1 2 4 5]);
69          fillet.set('radius','fillet_radius');
70
71          % define an extrusion to make the electrode 3D
72          rad_elec_ext_tag = char(geom.feature.uniquetag('rad_elec_ext'));
73          rad_elec_ext = geom.feature.create(rad_elec_ext_tag, 'Extrude');
74          rad_elec_ext.set('distance','t_rad');
75          rad_elec_ext.selection('input').set({workplane_tag});
76          rad_elec_ext.set('createselection','on');
77
78          % rotate the 3D shape into its final position
79          rad_elec_tag = geom.feature.uniquetag('rad_elec');
80          rad_elec = geom.feature.create(rad_elec_tag,'Rotate');
81          rad_elec.selection('input').set({rad_elec_ext_tag});
82          rad_elec.set('keep','off');
83          rad_elec.set('createselection','on');
84          rad_elec.set('pos',{'0','0','0'});
85          rad_elec.set('rot',['(360/N_elec)*' num2str(i-1) '+(360/(2*N_elec))']);
86      end
87
88      % build geometry
89      model.geom.run();
90
91      % get domain numbers
92      rad_elec_domains = double(arrayfun(@(i) model.selection(['geom1_rad_elec',...
93          num2str(i) '_dom']).inputEntities,1:params.N_elec));
94
95      end
```

Then we define the materials of the electrodes:

```
mat = model.material.create('steel');
mat.materialModel('def').set('relpermittivity',1);
mat.materialModel('def').set('electricconductivity','4.032e6[S/m]');
mat.selection.set(rad_elec_domains);
```

We then introduce a stationary study with electrostatics physics, and assign potentials to the electrodes:

```
function model = set_electrostatics(model)

params = get_model_params(model);

% create a study, as in the Comsol GUI
study = model.study.create('study');
study.feature.create('stationary', 'Stationary');

% if electrostatics physics has not been defined, do that
try
    es = model.physics('es');
catch
    es = model.physics.create('es','Electrostatics','geom1');
end

% numbers of the electrodes
n_el = 1:params.N_elec;

% loop through electrodes and assign potentials
for i = 1:params.N_elec
    pot_tag = ['Vrad' num2str(i)];

    % create the potential object
    pot = es.feature.create(pot_tag, 'ElectricPotential', 2);

    % set the potential value
    pot.set('V0',['Vrot*cos(phi_rot-' num2str(i-1+1/2) '*2*pi/N_elec) + ...
        Vtrap*cos(phi_trap-4*' num2str(i-1+1/2) '*pi/N_elec)']);

    % create a named selection for this potential
    pot.selection.named({['geom1_rad_elec' num2str(i) '_bnd']});
end

end
```

We then build the mesh:

```
try
    mesh = model.mesh('mesh1');
catch
    mesh = model.mesh.create('mesh1','geom1');
end
```

```
6       mesh.run();
7       mesh.feature('size').set('hauto',mesh_size);
8       mesh.run();
```

Then finally we execute the code below for optimization. Here the only new commands used are `model.study('study').run` and `mphinterp`, which runs the computation of the electric potential and imports the results to Matlab, interpolated on a grid.

```
1       % regression setup
2       z = linspace(-zmax,zmax,Nz)';
3       powers = 0:2:fit_poly_order;
4       VanderM = bsxfun(@power,z/zmax,powers);
5       [VanderQ,VanderR] = qr(VanderM,0);
6
7       % optimization
8       optim_table = table();
9       weight_fun = 1e6*(1-cos(linspace(0,pi,numel(z))').^10);
10
11      old_data = dirfun(@(x) readtable(x),'optimization_results','pattern','.csv');
12      old_data = vertcat(old_data{:});
13      if isempty(C_guess)
14          if ~isempty(old_data)
15              C_init = old_data{old_data.resid==min(old_data.resid),...
16                  {'c2','c4','c6','c8','c10'}};
17              C_init = C_init(1:round(elec_poly_order/2));
18          else
19              C_init = zeros(1,round(elec_poly_order/2));
20          end
21      else
22          C_init(1:numel(C_guess)) = C_guess;
23      end
24
25      iter = 1;
26      C_final = fminsearchbnd(@optimfun,C_init,C_init-0.02,C_init+0.02,...
27          optimset('Disp','iter','maxiter',1));
28
29          function resid = optimfun(C)
30              for j = 1:numel(C)
31                  model.param.set(['c' num2str(2*j)],C(j));
32              end
33
34              model.study('study').run;
35              Enormz = mphinterp(model,'es.normE','coord',[0*z 0*z z]')';
36              pfit = VanderR\(VanderQ'*Enormz);
37              Enormz_fit = VanderM*pfit;
38
39              resid = simps(z,(Enormz_fit-Enormz_fit(z==0)).^2.*weight_fun);
40
41              figure(2); clf;
42              subplot(2,1,1);
43              plot(z,Enormz,z,Enormz_fit,'linewidth',2);
44              title(['Iteration ' num2str(iter)]);
```

```
45              ylabel('|E_{rot}| (V/m)');
46              xlabel('z (m)');
47
48              subplot(2,1,2);
49              plot(z,(Enormz_fit-Enormz_fit(z==0)).^2.*weight_fun,'linewidth',2);
50              title(['Iteration ' num2str(iter)]);
51              ylabel('cost function');
52              xlabel('z (m)');
53              drawnow();
54
55              C = padarray(C,[0 5-numel(C)],0,'post');
56              optim_table = [optim_table; array2table([iter C ...
                    resid],'variablenames',{'iter','c2','c4','c6','c8','c10','resid'})];
57              writetable(optim_table,results_filename);
58
59              iter = iter+1;
60
61              if mod(iter-1,10)==0
62                  mphsave(model,[pwd filesep filename '.mph']);
63              end
64          end
65
66      % plot results
67      for k = 1:numel(C_final)
68          model.param.set(['c' num2str(2*k)],C_final(k));
69      end
70      model.geom('geom1').run;
71      model.mesh('mesh1').run;
72      model.study('study').run;
73
74      pg = model.result.create('pg', 'PlotGroup3D');
75      slice = pg.feature.create('slice', 'Multislice');
76      slice.set('expr', 'V');
77      mphplot(model,'pg');
78
79      set(gcf,'units','normalized','position',[0.3536    0.0787    0.2917    ...
            0.8259]);
80      view([0 90])
81
82      % save model
83      mphsave(model,[pwd filesep folder filesep filename '.mph']);
```

A.4 Optical pumping

Prior to implementing optical pumping state preparation, I performed a simple rate equation simulation to estimate our overall efficiency for preparing population in ${}^3\Delta_1(J=1)$. I used the set of first order differential equations for state populations n_i,

$$\frac{dn_i}{dt} = \sum_{j\neq i} \Omega_{i\leftarrow j}\, n_j + A_{i\leftarrow j} n_j - \Gamma_i n_i \tag{A.10}$$

Typically, the matrix $\boldsymbol{A}$ of Einstein A coefficients will look something like

$$\boldsymbol{A} = \begin{pmatrix} 0 & A_{1\leftarrow 2} & A_{1\leftarrow 3} \\ 0 & -\Gamma_2 & A_{2\leftarrow 3} \\ 0 & 0 & -\Gamma_3 \end{pmatrix}, \tag{A.11}$$

where $\Gamma_j = \sum_i A_{ij}$ is the total decay rate of state j. Here I have imagined that the energies of the states are ordered $E_1 < E_2 < E_3$, and that E_1 is the ground state and does not decay. The matrix $\boldsymbol{\Omega}$ represents light absorption and thus depends on which lasers are present. For example, it might look like

$$\boldsymbol{\Omega} = \begin{pmatrix} 0 & 0 & 0 \\ B_{2\leftarrow 1}\rho(\omega_{21}) & 0 & 0 \\ B_{3\leftarrow 1}\rho(\omega_{31}) & B_{3\leftarrow 2}\rho(\omega_{32}) & 0 \end{pmatrix}, \tag{A.12}$$

if we have laser fields driving every transition, where $B_{i\leftarrow j}$ are Einstein B coefficients and $\rho(\omega_{ij})$ is the spectral energy density of radiation at angular frequency $\omega_{ij} = (E_i - E_j)/\hbar$. In terms of molecular parameters and constants, the Einstein coefficients are

$$\begin{aligned} A_{i\leftarrow j} &= \frac{\omega_{ij}^3 |\boldsymbol{D}_{ij}|^2}{3\pi\epsilon_0\hbar c^3}, \\ B_{i\leftarrow j} &= \frac{\pi^2 c^3}{\hbar\omega_{ij}^3} A_{j\leftarrow i}, \end{aligned} \tag{A.13}$$

where $\boldsymbol{D}$ is the electric dipole matrix element between states i and j.

This model neglects all coherences and thus of course cannot produce phenomena such as Rabi flopping. However (due to Doppler broadening) we are also unable to observe any Rabi flopping in the experiment, so this does not seem like a significant limitation. I estimated the electric dipole matrix elements between various electronic and vibrational states according to the methods described in Chapter 2, and solved the rate equations in Matlab. For molecule-frame dipole matrix elements, I used the data from Kevin's thesis and Ref. [99] in order to include as many electronic states as possible. Rate equation simulation results are shown in Fig. A.5.

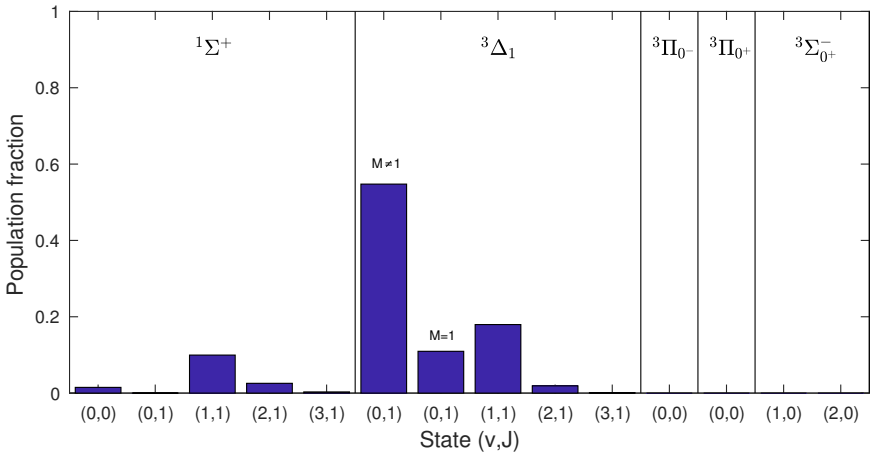

(a)

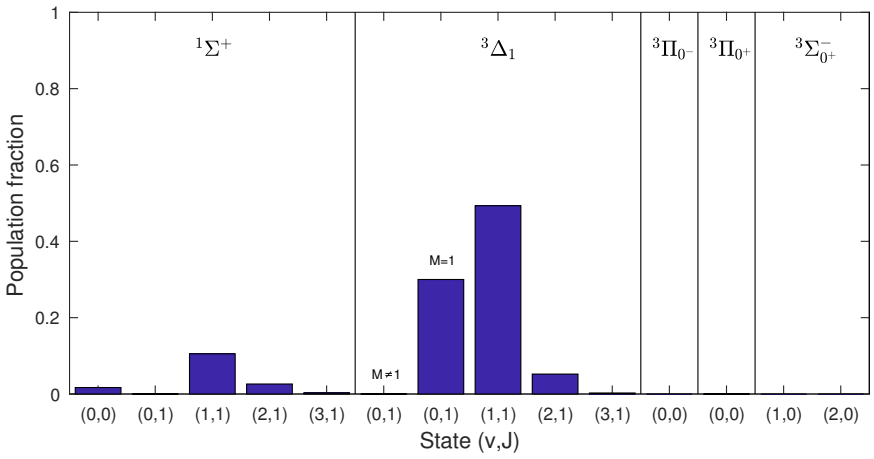

(b)

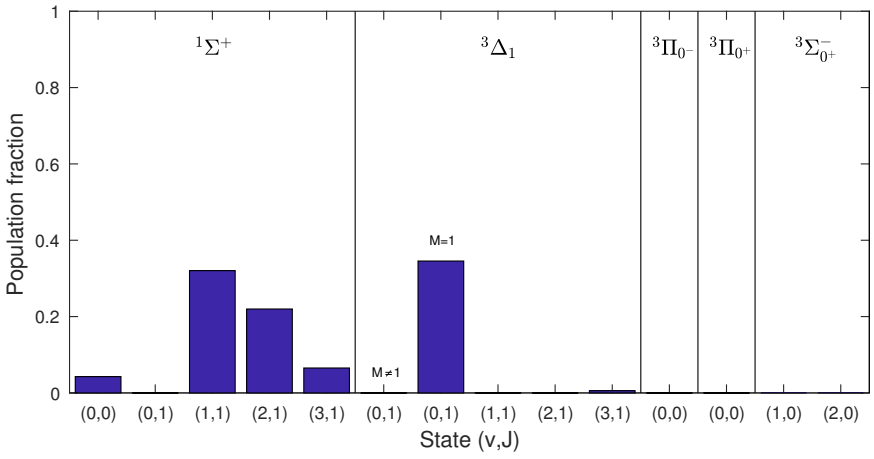

(c)

Figure A.5: Rate equation prediction for state populations after optical pumping state preparation. (a) Transfer from $^1\Sigma^+$ only via $^3\Pi_{0^+}$, (b) with M_F pumping through $^3\Pi_{0^-}$, (c) with vibrational cleanups through $^3\Sigma^-_{0^+}$. Part (b) indicates that the best route to improved signal size is with a repump from $^3\Delta_1(v=1)$ through $^3\Pi_{0^-}$ (1178.7 nm).

A.5 Magnetic fields

In the Generation 2 experiment with HfF^+, we have implemented magnetometry using a network of eight Bartington Instruments fluxgate sensors mounted to the vacuum chamber. Much more details about the hardware aspects of the magnetometry will be included in a future work (likely Tanya Roussy's thesis), but here I provide a brief overview of the process of fitting magnetometer data.

The positions of the magnetometers are registered to the vacuum chamber via the mounting holes machined by Kimball physics. We have a CAD model of the Generation 2 chamber along with the magnetometers located in

`X:\Magnetometers Mark_2\Inventor\gen2_chamber_with_mags.iam`

for which I wrote a VBA macro (quoted below) to export the magnetometers' coordinates and orientations [in the form of a rotation matrix *a la* Eq. (2.40)]. An example of the output of this script is shown in Table A.3.

```
Public Sub PrintMagCoordsGen2()

    ' Get the active assembly.
    Dim oAsmDoc As AssemblyDocument
    Set oAsmDoc = ThisApplication.ActiveDocument

    'Set up the CSV output file
    Dim OutputFile As String
    OutputFile = "X:\Magnetometers_Mark 2\Inventor\sensor_coordinates.csv"
    Open OutputFile For Output As #1

    ' Generate header text
    Dim FileHeader As String
    FileHeader = "sensor" & ", "
    Dim i As Integer
    Dim j As Integer
    ' Rotation matrix elements (9 columns)
    For i = 1 To 3
        For j = 1 To 3
            FileHeader = FileHeader & "R_" & i & j & ", "
        Next
    Next
    ' Origin coordinates (3 columns)
    j = 4
    For i = 1 To 3
        FileHeader = FileHeader & "O_" & i & ", "
```

```
27      Next
28      ' Trim final comma and space
29      FileHeader = Left(FileHeader, Len(FileHeader) - 2)
30
31      ' Print header to file
32      Debug.Print FileHeader
33      Print #1, FileHeader
34
35      Dim oOcc As ComponentOccurrence
36      For Each oOcc In oAsmDoc.ComponentDefinition.Occurrences
37          ' Loop through sensor assemblies
38          If InStr(oOcc.Name, "Mag612") = 1 Then
39
40              ' Get sensor number 1-8
41              Dim sensorNum As Integer
42              sensorNum = CInt(Right(oOcc.Name, Len(oOcc.Name) - InStr(oOcc.Name, ...
                    ":")))
43
44              ' Get origin transformation matrix
45              Dim oMatrix As Matrix
46              Set oMatrix = oOcc.Transformation
47
48              ' Start this row of coordinate data
49              Dim RowStr As String
50              RowStr = sensorNum & ", "
51
52              ' Rotation matrix elements
53              For i = 1 To 3
54                  For j = 1 To 3
55                      RowStr = RowStr & oMatrix.Cell(i, j) & ", "
56                  Next
57              Next
58
59              ' Origin coordinates
60              j = 4
61              For i = 1 To 3
62                  RowStr = RowStr & oMatrix.Cell(i, j) & ", "
63              Next
64
65              ' Trim final comma and space
66              RowStr = Left(RowStr, Len(RowStr) - 2)
67
68              ' Print row for this chip
69              Debug.Print RowStr
70              Print #1, RowStr
71
72
73          End If
74      Next
75
76      Close #1
77
78  End Sub
```

In general, we would like to use our X, Y, Z, and axgrad coils to apply magnetic fields to null out Earth's field at the location of the ions, and apply as pure and constant a $\mathcal{B}'_{\text{axgrad}}$ field

sensor	R_11	R_12	R_13	R_21	R_22	R_23	R_31	R_32	R_33	O_1	O_2	O_3
1	-0.37656	-0.45399	-0.80753	-0.19186	0.891007	-0.41146	0.906308	0	-0.42262	13.52751	6.892613	7.079616
2	-0.19186	0.891007	-0.41146	-0.37656	-0.45399	-0.80753	-0.90631	0	0.422618	6.892613	13.52751	-7.07962
3	0.191865	-0.89101	0.411455	-0.37656	-0.45399	-0.80753	0.906308	0	-0.42262	-6.89261	13.52751	7.079616
4	0.376556	0.45399	0.807526	-0.19186	0.891007	-0.41146	-0.90631	0	0.422618	-13.5275	6.892613	-7.07962
5	0.376556	0.45399	0.807526	0.191865	-0.89101	0.411455	0.906308	0	-0.42262	-13.5275	-6.89261	7.079616
6	0.191865	-0.89101	0.411455	0.376556	0.45399	0.807526	-0.90631	0	0.422618	-6.89261	-13.5275	-7.07962
7	-0.19186	0.891007	-0.41146	0.376556	0.45399	0.807526	0.906308	0	-0.42262	6.892613	-13.5275	7.079616
8	-0.37656	-0.45399	-0.80753	0.191865	-0.89101	0.411455	-0.90631	0	0.422618	13.52751	-6.89261	-7.07962

Table A.3: Example output from the VBA script that saves magnetometer coordinates and orientations. The elements `R_ij` belong to a rotation matrix that transforms the magnetometer magnetic field measurement axes into the laboratory axes. The elements `O_i` are coordinates of the magnetometer's center.

gradient as possible. We would like to simultaneously monitor the magnetic field in the vicinity of the ion trap using our fluxgate magnetometers, and potentially apply real-time feedback. However, a challenge is presented by the fact that our magnetometers are situated very close to our magnetic field coils, and thus cannot be used to accurately parameterize the magnetic field in terms of the "interior" multipoles described in Section A.1. We therefore have to adopt a technique of what we call "coil basis vectors" in order to obtain magnetic field measurements that we can accurately fit with interior multipoles. The general idea is:

(1) At some earlier time (prior to a Ramsey experiment), we collect "coil basis vectors:" values of the magnetic field components $\mathcal{B}_x$, $\mathcal{B}_y$, $\mathcal{B}_z$ experienced by each magnetometer due to a unit current in a particular coil pair. These are shown in Table A.4.

(2) When measuring the magnetic field at later times, subtract the coil basis vectors, scaled by the known current in each coil pair, from each magnetometer's measurement. As long as the magnetometers are operating in a linear regime, this will result in a measurement of the background magnetic field only.

It is important to re-measure the coil unit vectors any time the coils or magnetometers may have moved, or if the current supply for any set of coils is changed. Otherwise, the unit vectors should be fixed by the geometry and the current supply.

Having subtracted the coil unit vectors to obtain the background magnetic fields, we can then perform spherical multipole fitting to obtain estimates of the (L, M) components of the magnetic field about the trap center. Because we only have eight magnetometers with three axes each, we can fit at most up to $L = 4$ (and preferably lower order than this). Typically we extract only the multipole components up to $L = 2$. This fitting is performed by the `process_magnetometers.m` function, which is propagated forward into each day's `matlab` directory on the HfF^+ `jilafile` directory.

As a final step towards predicting the magnetic fields experienced by the ions at the trap center, we must predict the magnetic fields generated by the X, Y, Z, and axgrad coils at that

Sensor	BX_IX	BX_IY	BX_IZ	BX_Iaxgrad	BY_IX	BY_IY	BY_IZ	BY_Iaxgrad	BZ_IX	BZ_IY	BZ_IZ	BZ_Iaxgrad
1	3.338	-1.004	-2.457	3.871	0.234	5.128	-1.115	1.852	0.412	-0.580	5.269	1.859
2	3.881	0.558	1.394	1.932	-0.676	3.710	2.163	3.880	0.138	-0.557	5.103	-1.641
3	3.880	-0.639	1.288	-1.990	0.736	3.633	-1.894	3.783	0.184	0.557	5.658	1.859
4	3.313	1.098	-2.486	-3.798	-0.352	5.162	1.240	2.031	0.499	0.416	4.794	-1.741
5	3.315	-1.177	2.124	-3.910	0.275	4.927	0.927	-1.961	-0.331	0.643	5.629	1.784
6	4.020	0.561	-0.882	-2.123	-0.572	3.745	-2.196	-3.902	-0.324	0.578	5.207	-1.565
7	3.949	-0.405	-0.454	1.945	0.383	3.682	2.490	-3.865	-0.596	-0.654	5.439	1.797
8	3.362	0.984	2.120	3.929	-0.293	4.993	-0.964	-1.981	-0.439	-0.524	5.175	-1.614

Table A.4: Coil unit vectors from May 2019.

location. We do so using a simple parametric model for each pair of coils, with parameters listed in Table A.5, and whose geometric interpretations are shown in Fig. A.6. Initially, I had aimed to tweak these parameters using magnetometer measurements of the fields generated by each coil pair, however it subsequently appeared that the magnetometers are simply too close to the coils to generate sensible results – the model has too many free parameters, and the resulting geometry was clearly inconsistent with the known coil positions. One important lesson from this process was that the number of turns in each coil should remain fixed to the known value, listed in Table A.5. It may be worthwhile to attempt this fitting again in the future, with certain parameters (such as the number of turns, width, thickness, and radius of the coils) held fixed. In this instance, it may be possible to fit the center position of the coil pair `rc` and their azimuthal rotation `phi`, which may be important for systematics studies.

Parameter	X coils	Y coils	Z coils	axgrad coils
rc	[0,0,0]	[0,0,0]	[0,0,0]	[0,0,0]
Rcoil	0.2172	0.1981	0.1713	0.1346
theta	1.57	1.57	0	0
phi	0	1.57	0	0
r_rel	[0,0,0.2159]	[0,0,0.1968]	[0,0,0.1716]	[0,0,0.1922]
theta_rel	0	0	0	0
phi_rel	0	0	0	0
turns	80	85	57	85
w	0.0076	0.0076	0.0089	0.0076
t	0.0102	0.0102	0.0049	0.0102
Nw	8	8	8	8
Nt	8	9	9	9
I_rel	1	1	1	-1

Table A.5: Parameters for magnet coil pairs. The number of turns is the measured value, while the other parameters are taken from our experiment CAD model. The physical meanings of the parameters are shown in Fig. A.6. The parameter `I_rel` indicates the relative sign of the current in the two coils – a negative sign results in a gradient rather than a uniform field. Distances are in meters, angles in radians.

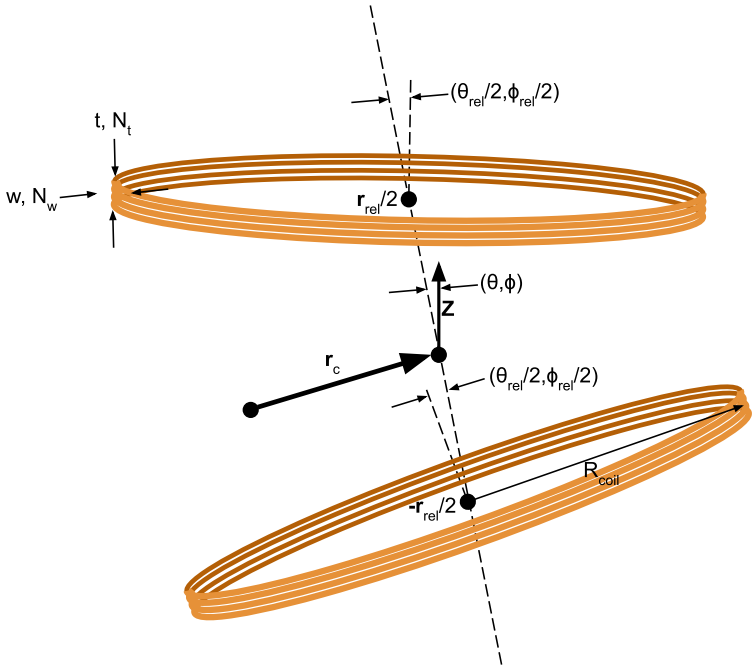

Figure A.6: Parametric description of the orientation of a pair of coils in space. The vector $\boldsymbol{r}_c$ indicates the position of the center of mass of the coil pair. Each coil is located at $\pm\boldsymbol{r}_{\rm rel}$ relative to $\boldsymbol{r}_c$. The coils are rotated by a common set of Euler angles (θ, ϕ, χ) about the laboratory Z axis, and are then rotated by a relative set of Euler angles $\pm(\theta_{\rm rel}, \phi_{\rm rel}, \chi_{\rm rel})/2$ relative to their common z axis. The coils have radius $R_{\rm coil}$, width w, thickness t, and have numbers of turns N_w and N_t along their width and thickness.

Appendix B

Analytic calculations

The goal of this section is to reproduce various analytic calculations done over the years, for the use of future students.

B.1 MCP Transfer Matrices

I assume that the position $x_{d,j}$ of the cloud on the detector along the j^{th} coordinate axis is linearly related to the position of the cloud in the trap:

$$x_{d,j} = m_{11,j} x_{t,j} + m_{12,j} T_d \dot{x}_{t,j} \tag{B.1}$$

where T_d is the time of flight to the detector.

The cloud is given a kick along one of the principal axes of the trap by applying a voltage pulse to two or more of the electrodes. Figure B.1 shows a triangular pulse with a 2 μs rise time and an amplitude of 1 V programmed on the experiment control DAC and measured on one electrode. Integrating the measured potential on one fin for a programmed 1 V, 2 μs pulse (amplified 25$\times$ in the trap driver electronics) gives 50.5(3) V μs. The electric field at the center of the cloud is obtained by COMSOL simulation, with the following results for a 1 V potential applied to one fin

$$\begin{aligned} \frac{\mathcal{E}_y}{V_y} &= \frac{57.21(1)\,\text{mV/cm}}{1\,\text{V}} \\ \frac{\mathcal{E}_z}{V_z} &= \frac{8.75(1)\,\text{mV/cm}}{1\,\text{V}} \end{aligned} \tag{B.2}$$

where the uncertainty is assumed to be simply the magnitude of the smallest digit calculated by COMSOL. To account for trap geometry and amplification, I define the scale factors χ_j which

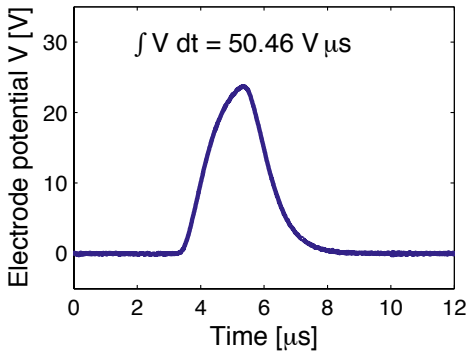

Figure B.1: Potential on one electrode for 1 V on the DAC.

convert the amplitude of a 2 μs pulse to the time-integrated electric field component in direction j at the center of the trap, which I call K_j. This assumes that voltage pulses of various amplitudes applied to different electrodes will have the same overall shape. The χ_j carry units of μs/cm. Numerically, these factors are:

$$\begin{aligned}
\chi_x &= 2\sqrt{3}\left(5.721\times10^{-2}\,\mathrm{cm}^{-1}\right)(50.5\,\mu\mathrm{s}) = \frac{10.00(5)\,\mathrm{V/cm}\ \mu\mathrm{s}}{1\,\mathrm{V}} \\
\chi_y &= 2\left(5.721\times10^{-2}\,\mathrm{cm}^{-1}\right)(50.5\,\mu\mathrm{s}) = \frac{5.774(5)\,\mathrm{V/cm}\ \mu\mathrm{s}}{1\,\mathrm{V}} \\
\chi_z &= 2\left(0.875\times10^{-2}\,\mathrm{cm}^{-1}\right)(50.5\,\mu\mathrm{s}) = \frac{0.8831(5)\,\mathrm{V/cm}\,\mu\mathrm{s}}{1\,\mathrm{V}}
\end{aligned} \tag{B.3}$$

Assuming that the cloud is stationary before receiving a pulse along direction j, the in-trap position and velocity after the pulse are

$$x_{t,j}(t) = \frac{eK_j}{m\omega_j}\sin(\omega_j t) \tag{B.4}$$

$$\dot{x}_{t,j}(t) = \frac{eK_j}{m}\cos(\omega_j t) \tag{B.5}$$

where

$$K_j \equiv \int_{-\infty}^{\infty} E_j(t)dt. \tag{B.6}$$

The measured position on a detector measuring ion motion along direction j is

$$x_{t,j}(t) = A_{d,j}\sin(\omega_j t + \varphi_j) \tag{B.7}$$

$$= A_{d,j}\cos(\varphi_j)\sin(\omega_j t) + A_{d,j}\sin(\varphi_j)\cos(\omega_j t) \tag{B.8}$$

$$= m_{11,j}\frac{eK_j}{m\omega_j}\sin(\omega_j t) + m_{12,j}T_d\frac{eK_j}{m}\cos(\omega_j t). \tag{B.9}$$

Comparing coefficients, I find

$$m_{11,j} = \frac{A_{d,j}\cos(\varphi_j)m\omega_j}{eK_j} \tag{B.10}$$

$$m_{12,j} = \frac{A_{d,j}\sin(\varphi_j)m}{eK_jT_d} \tag{B.11}$$

Then incorporating the fact that $K_j = \chi_j V_j$ where V_j is the amplitude of the voltage pulse applied to opposing fins,

$$m_{11,j} = \frac{A_{d,j}\cos(\varphi_j)m\omega_j}{e\chi_j V_j} \tag{B.12}$$

$$m_{12,j} = \frac{A_{d,j}\sin(\varphi_j)m}{e\chi_j V_j T_d} \tag{B.13}$$

For the "fast" multi-channel plate (MCP), which can resolve only cloud motion in the x direction, the transfer matrix elements have dimensions of μs/mm.

B.2 Relativistic & inertial effects

At one point during the challenging times of systematics investigations, I became curious if there might be additional effects of the rotating, accelerating frame of our measurement, beyond the usual term $H_{\text{rot}} = -\boldsymbol{\omega}\cdot\boldsymbol{F}$. Not surprisingly, this was not a particularly fruitful avenue of investigation, but I reproduce my notes here in case some offshoot becomes useful in the future.

The goal of these notes is to determine in a moderately rigorous way any corrections to the electronic spectrum of an accelerating, rotating atom or molecule in its rest frame, in the presence of external electric and magnetic fields. The approach is to obtain an approximate non-relativistic Hamiltonian for a single electron in (nuclear, other-electronic, or externally applied) electric and magnetic fields by taking the non-relativistic limit of the generally covariant Dirac equation. This

problem is addressed in the case of no external fields by Hehl & Ni in Ref. [59], while the case of rotation but no linear acceleration was addressed in Ref. [111]. The style of Ref. [111] is fairly old-fashioned, confusing, and probably less approximate than we need to be, so we refer only to Ref. [59] here.

Following Hehl & Ni, the Dirac equation for a spin-1/2 particle of charge q viewed from a frame with acceleration $\mathbf{a}$ and rotation $\boldsymbol{\omega}$ is

$$(i\hbar\gamma^{\hat{\mu}}D_{\hat{\mu}} - mc)\psi = 0 \tag{B.14}$$

where the covariant derivatives $D_{\hat{\mu}}$ are

$$\begin{aligned} D_{\hat{0}} &= \frac{1}{1+\frac{\mathbf{a}\cdot\mathbf{x}}{c^2}}\left(\frac{1}{c}\frac{\partial}{\partial t} + \frac{iq\phi}{\hbar c} + \frac{\mathbf{a}\cdot\boldsymbol{\alpha}}{2c^2} - \frac{i}{2\hbar c}\boldsymbol{\omega}\cdot\mathbf{J}\right), \\ D_{\hat{i}} &= \frac{\partial}{\partial x^i} - \frac{iq\mathbf{A}}{\hbar}, \end{aligned} \tag{B.15}$$

and $\mathbf{J} = \mathbf{L} + \mathbf{S}$ is the particle's total angular momentum. Here we have simply used the expression from Hehl & Ni and added the electromagnetic four-potential, assuming it transforms into the non-inertial frame in the same way as the partial derivative ∂_μ.

The Dirac equation is then

$$\frac{i\hbar\gamma^0}{1+\frac{\mathbf{a}\cdot\mathbf{x}}{c^2}}\left(\frac{1}{c}\frac{\partial}{\partial t} + \frac{iq\phi}{\hbar c} + \frac{\mathbf{a}\cdot\boldsymbol{\alpha}}{2c^2} - \frac{i}{2\hbar c}\boldsymbol{\omega}\cdot\mathbf{J}\right)\psi = \left[mc + \boldsymbol{\gamma}\cdot(\mathbf{p} - q\mathbf{A})\right]\psi. \tag{B.16}$$

We obtain the effective Dirac Hamiltonian by isolating $i\hbar\frac{\partial\psi}{\partial t}$, finding

$$H_{\text{Dirac}} = \beta mc^2\left(1 + \frac{\mathbf{a}\cdot\mathbf{x}}{c^2}\right) + q\phi - \boldsymbol{\omega}\cdot\mathbf{J} - \frac{i\hbar}{2c}\boldsymbol{\alpha}\cdot\mathbf{a} + c\left(1+\frac{\mathbf{a}\cdot\mathbf{x}}{c^2}\right)\boldsymbol{\alpha}\cdot\boldsymbol{\pi}, \tag{B.17}$$

where $\boldsymbol{\pi} \equiv \mathbf{p} - q\mathbf{A}$, $\beta \equiv \gamma^0$, and $\boldsymbol{\alpha} \equiv \gamma^0\boldsymbol{\gamma}$. We would then like to take the low-energy limit of the Dirac Hamiltonian, using the Foldy-Wouthuysen transformation [15, 47]. First, we write the Hamiltonian as

$$H_{\text{Dirac}} = \beta mc^2 + \mathbb{E} + \mathbb{O} \tag{B.18}$$

where $\mathbb{E}$ and $\mathbb{O}$ are the even and odd parts of the Hamiltonian with respect to exchanging particles and antiparticles (odd terms contain $\boldsymbol{\alpha}$):

$$\begin{aligned} \mathbb{E} &= e\phi + m(\mathbf{a}\cdot\mathbf{x}) - \boldsymbol{\omega}\cdot\mathbf{J}, \\ \mathbb{O} &= c\boldsymbol{\alpha}\cdot\boldsymbol{\pi} + \frac{1}{2c}\left[(\boldsymbol{\alpha}\cdot\boldsymbol{\pi})(\mathbf{a}\cdot\mathbf{x}) + (\mathbf{a}\cdot\mathbf{x})(\boldsymbol{\alpha}\cdot\boldsymbol{\pi})\right]. \end{aligned} \tag{B.19}$$

The Foldy-Wouthuysen transformation results in the approximate Hamiltonian

$$H_{\mathrm{FW}} = mc^2 + \mathbb{E} + \frac{\mathbb{O}^2}{2mc^2} - \frac{\mathbb{O}^4}{8m^3c^2} - \frac{1}{8m^2c^4}\left[\mathbb{O}, [\mathbb{O}, \mathbb{E}] + i\hbar\dot{\mathbb{O}}\right], \tag{B.20}$$

consisting of even operators only. We will evaluate H_{FW} still more approximately since we are considering non-inertial effects to be small. To be precise, we will drop all terms proportional to $\mathbf{a}\cdot\mathbf{x}/c^2$ where the other factor is of lower order than the kinetic energy $p^2/(2m)$. That is, we would keep $p^2(\mathbf{a}\cdot\mathbf{x})/(2mc^2)$, but drop $-2\mu_B(\mathbf{S}\cdot\mathbf{B})(\mathbf{a}\cdot\mathbf{x})/c^2$. In addition, we will keep terms only up to first order in $\boldsymbol{\omega}$ (this turns out to be all $\boldsymbol{\omega}$-containing terms to this order of the F-W transformation).

B.2.1 Mostly kinetic term

By "mostly kinetic," I'm referring to the term $\frac{\mathbb{O}^2}{2mc^2}$. As a reminder,

$$\begin{aligned}\mathbb{O} &= c\boldsymbol{\alpha}\cdot\boldsymbol{\pi} + \frac{1}{2c^2}\left[(c\boldsymbol{\alpha}\cdot\boldsymbol{\pi})(\mathbf{a}\cdot\mathbf{x}) + (\mathbf{a}\cdot\mathbf{x})(c\boldsymbol{\alpha}\cdot\boldsymbol{\pi})\right] \\ &\equiv c\boldsymbol{\alpha}\cdot\boldsymbol{\Pi}\end{aligned} \tag{B.21}$$

So that using the commutation properties of $\boldsymbol{\alpha}$, $\mathbb{O}^2$ can be written [15]

$$\mathbb{O}^2/c^2 = \boldsymbol{\Pi}^2 + i\boldsymbol{\sigma}\cdot(\boldsymbol{\Pi}\times\boldsymbol{\Pi}) \tag{B.22}$$

Keeping terms only up to first order in $\mathbf{a}$, we get

$$\begin{aligned}\boldsymbol{\Pi}^2 &\approx \boldsymbol{\pi}^2 + \frac{1}{2c^2}\cdot\left[\boldsymbol{\pi}^2(\mathbf{a}\cdot\mathbf{x}) + \boldsymbol{\pi}\cdot(\mathbf{a}\cdot\mathbf{x})\boldsymbol{\pi}\right] + \frac{1}{2c^2}\left[\boldsymbol{\pi}(\mathbf{a}\cdot\mathbf{x})\cdot\boldsymbol{\pi} + (\mathbf{a}\cdot\mathbf{x})\boldsymbol{\pi}^2\right] \\ &= \boldsymbol{\pi}^2 + 2\boldsymbol{\pi}\cdot\left(\frac{\mathbf{a}\cdot\mathbf{x}}{c^2}\right)\boldsymbol{\pi}\end{aligned} \tag{B.23}$$

and

$$\begin{aligned}\boldsymbol{\Pi}\times\boldsymbol{\Pi} &\approx \boldsymbol{\pi}\times\boldsymbol{\pi} + \frac{\boldsymbol{\pi}\times[\boldsymbol{\pi}(\mathbf{a}\cdot\mathbf{x}) + (\mathbf{a}\cdot\mathbf{x})\boldsymbol{\pi}]}{2c^2} + \frac{[\boldsymbol{\pi}(\mathbf{a}\cdot\mathbf{x}) + (\mathbf{a}\cdot\mathbf{x})\boldsymbol{\pi}]\times\boldsymbol{\pi}}{2c^2} \\ &= i\hbar q\mathbf{B} + \frac{2i\hbar q(\mathbf{a}\cdot\mathbf{x})}{c^2}\mathbf{B} - \frac{i\hbar}{c^2}(\mathbf{a}\times\boldsymbol{\pi})\end{aligned} \tag{B.24}$$

So then

$$i\boldsymbol{\sigma}\cdot(\boldsymbol{\Pi}\times\boldsymbol{\Pi}) \approx -\hbar q\boldsymbol{\sigma}\cdot\mathbf{B} - \frac{2\hbar q(\mathbf{a}\cdot\mathbf{x})}{c^2}\boldsymbol{\sigma}\cdot\mathbf{B} + \frac{\hbar}{c^2}\boldsymbol{\sigma}\cdot(\mathbf{a}\times\boldsymbol{\pi}), \tag{B.25}$$

and finally

$$\frac{\mathbb{O}^2}{2mc^2} \approx \frac{\boldsymbol{\pi}^2}{2m} + \frac{\boldsymbol{\pi}(\mathbf{a}\cdot\mathbf{x})\cdot\boldsymbol{\pi}}{mc^2} - \frac{\hbar q}{2m}\boldsymbol{\sigma}\cdot\mathbf{B} + \frac{\hbar}{2mc^2}\boldsymbol{\sigma}\cdot(\mathbf{a}\times\boldsymbol{\pi}) \tag{B.26}$$

where we have neglected the Zeeman effect reduced by $\mathbf{a}\cdot\mathbf{x}/c^2$.

B.2.2 Relativistic correction to kinetic term

Here we will keep only the usual relativistic correction to the kinetic term, since everything proportional to $\mathbf{a}\cdot\mathbf{x}/c^2$ will be on the order of 10^{-20} times smaller than that.

$$-\frac{\mathbb{O}^4}{2m^3c^2}\approx-\frac{\boldsymbol{\pi}^4}{8m^3c^2} \tag{B.27}$$

B.2.3 Interaction term

Let's now think about the interaction term, $-\frac{1}{8m^2c^4}[\mathbb{O},[\mathbb{O},\mathbb{E}]+i\hbar\dot{\mathbb{O}}]$. We will neglect completely the terms of $\mathbb{O}$ proportional to $\mathbf{a}\cdot\mathbf{x}/c^2$. Start with the commutator $[\mathbb{O},\mathbb{E}]$:

$$[\mathbb{O},\mathbb{E}]\approx[c\boldsymbol{\alpha}\cdot\boldsymbol{\pi},q\phi+m\mathbf{a}\cdot\mathbf{x}-\boldsymbol{\omega}\cdot\mathbf{J}] \tag{B.28}$$

For each of these terms, we find

$$[c\boldsymbol{\alpha}\cdot\boldsymbol{\pi},q\phi]=i\hbar qc\boldsymbol{\alpha}\cdot(-\boldsymbol{\nabla}\phi), \tag{B.29}$$

$$[c\boldsymbol{\alpha}\cdot\boldsymbol{\pi},m\mathbf{a}\cdot\mathbf{x}]=-i\hbar mc\boldsymbol{\alpha}\cdot\mathbf{a}, \tag{B.30}$$

$$[c\boldsymbol{\alpha}\cdot\boldsymbol{\pi},-\boldsymbol{\omega}\cdot\mathbf{J}]=i\hbar c\boldsymbol{\alpha}\cdot(\boldsymbol{\pi}\times\boldsymbol{\omega}). \tag{B.31}$$

Combined with

$$i\hbar\dot{\mathbb{O}}\approx-i\hbar qc\boldsymbol{\alpha}\cdot\frac{\partial\mathbf{A}}{\partial t} \tag{B.32}$$

we get

$$[c\boldsymbol{\alpha}\cdot\boldsymbol{\pi},q\phi+i\hbar\dot{\mathbb{O}}]\approx i\hbar qc\boldsymbol{\alpha}\cdot\boldsymbol{\mathcal{E}}. \tag{B.33}$$

The outer commutators are

$$[c\boldsymbol{\alpha}\cdot\boldsymbol{\pi},i\hbar qc\boldsymbol{\alpha}\cdot\boldsymbol{\mathcal{E}}]=\hbar^2c^2q\boldsymbol{\nabla}\cdot\boldsymbol{\mathcal{E}}-\hbar c^2q\boldsymbol{\sigma}\cdot(\boldsymbol{\pi}\times\boldsymbol{\mathcal{E}}-\boldsymbol{\mathcal{E}}\times\boldsymbol{\pi}), \tag{B.34}$$

$$[c\boldsymbol{\alpha}\cdot\boldsymbol{\pi},-i\hbar cm\boldsymbol{\alpha}\cdot\mathbf{a}]=-2\hbar mc^2\boldsymbol{\sigma}\cdot(\mathbf{a}\times\boldsymbol{\pi}), \tag{B.35}$$

$$[c\boldsymbol{\alpha}\cdot\boldsymbol{\pi},i\hbar c\boldsymbol{\alpha}\cdot(\boldsymbol{\pi}\times\boldsymbol{\omega})]=2\hbar c^2[\boldsymbol{\pi}^2(\boldsymbol{\sigma}\cdot\boldsymbol{\omega})-(\boldsymbol{\omega}\cdot\boldsymbol{\pi})(\boldsymbol{\sigma}\cdot\boldsymbol{\omega})]. \tag{B.36}$$

So this contribution to the Hamiltonian is

$$\begin{aligned}-\frac{1}{8m^2c^4}\left[\mathbb{O},[\mathbb{O},\mathbb{E}]+i\hbar\dot{\mathbb{O}}\right]\approx&-\frac{q\hbar^2}{8m^2c^2}\boldsymbol{\nabla}\cdot\boldsymbol{\mathcal{E}}-\frac{q\hbar}{4m^2c^2}\boldsymbol{\sigma}\cdot(\boldsymbol{\mathcal{E}}\times\boldsymbol{\pi})\\&+\frac{\hbar}{4mc^2}\boldsymbol{\sigma}\cdot(\mathbf{a}\times\boldsymbol{\pi})-\frac{\hbar}{4m^2c^2}[\boldsymbol{\pi}^2(\boldsymbol{\sigma}\cdot\boldsymbol{\omega})-(\boldsymbol{\omega}\cdot\boldsymbol{\pi})(\boldsymbol{\sigma}\cdot\boldsymbol{\pi})]\end{aligned} \tag{B.37}$$

B.2.4 Total FW Hamiltonian

Adding together the terms from the previous sections, the single particle Hamiltonian to lowest(-ish) order in $\mathbf{a}$ and $\boldsymbol{\omega}$ is

$$\begin{aligned} H_{\mathrm{FW}} \approx mc^2 + \frac{\boldsymbol{\pi}^2}{2m} - \frac{\boldsymbol{\pi}^4}{8m^3c^2} + q\phi - \frac{q\hbar}{2m}\boldsymbol{\sigma}\cdot\mathbf{B} - \frac{q\hbar^2}{8m^2c^2}\boldsymbol{\nabla}\cdot\boldsymbol{\mathcal{E}} - \frac{q\hbar}{4m^2c^2}\boldsymbol{\sigma}\cdot(\boldsymbol{\mathcal{E}}\times\boldsymbol{\pi}) \\ + m\mathbf{a}\cdot\mathbf{x} - \boldsymbol{\omega}\cdot\mathbf{J} + \frac{\boldsymbol{\pi}(\mathbf{a}\cdot\mathbf{x})\cdot\boldsymbol{\pi}}{mc^2} + \frac{3\hbar}{4mc^2}\boldsymbol{\sigma}\cdot(\mathbf{a}\times\boldsymbol{\pi}) - \frac{\hbar}{4m^2c^2}[\boldsymbol{\pi}^2(\boldsymbol{\sigma}\cdot\boldsymbol{\omega}) - (\boldsymbol{\omega}\cdot\boldsymbol{\pi})(\boldsymbol{\sigma}\cdot\boldsymbol{\pi})]. \end{aligned} \tag{B.38}$$

Here the top line contains "usual" terms, while the bottom line contains inertial terms. In the third and fourth inertial terms, this expression differs from Ref. [59] by factors of order 1. On the other hand, the potential, kinetic, Darwin, spin-orbit, and anomalous Zeeman terms appear with the correct sign and numerical factors.

B.3 Rotation matrix elements

First, apply the Wigner-Eckart theorem:

$$\left\langle I'J'\Omega'F'M_F'\right| \mathcal{D}^{(k)}_{pq}(\omega)^* \left|IJ\Omega FM_F\right\rangle = (-1)^{F'-M_F'} \begin{pmatrix} F' & k & F \\ -M_F' & p & M_F \end{pmatrix} \left\langle I'J'\Omega'F'\middle\| \mathcal{D}^{(k)}_{\cdot q}(\omega)^* \middle\| IJ\Omega F\right\rangle \tag{B.39}$$

Now, apply Eq. 5.174 of Ref. [15] for decoupling J and I. We only want the Wigner D matrix to act on the J part of the wavefunction:

$$\begin{aligned} &\left\langle I'J'\Omega'F'\middle\| \mathcal{D}^{(k)}_{\cdot q}(\omega)^* \middle\| IJ\Omega F\right\rangle = \\ &\qquad \delta_{I,I'}\,(-1)^{F+J'+k+I'}\sqrt{(2F'+1)(2F+1)} \begin{Bmatrix} J & F & I' \\ F' & J' & k \end{Bmatrix} \left\langle J'\Omega'\middle\| \mathcal{D}^{(k)}_{\cdot q}(\omega)^* \middle\| J\Omega\right\rangle. \end{aligned} \tag{B.40}$$

Finally, apply Eq. 5.186 of Ref. [15]:

$$\left\langle J'\Omega'\middle\| \mathcal{D}^{(k)}_{\cdot q}(\omega)^* \middle\| J\Omega\right\rangle = (-1)^{J'-\Omega'} \begin{pmatrix} J' & k & J \\ -\Omega' & q & \Omega \end{pmatrix} \sqrt{(2J'+1)(2J+1)}. \tag{B.41}$$

Multiplying everything together gives Eq. (2.15).

Appendix C

Designs

C.1 Lab layout

As is evident from the lengthy experiment sequence, the experiment uses a large number of lasers, as shown schematically in Fig. C.1. Several of our lasers are water-cooled pulsed YAGs and several more are dye lasers; each of these varieties is quite prone to catastrophic failure, which consumes substantial time and resources. The following is a complete list of lasers used in the HfF^+ experiment:

(1) **Continuum Minilite** ("Abby")

A Q-switched Nd:YAG [1] . Used for laser ablation of Hafnium metal in our supersonic beam source. The Minilite has a variable repetition rate from 0 Hz to 30 Hz, allowing us to trigger it irregularly for ablation and conserve the lifetime of its flashlamps. The price to be paid for the triggerable Q-switch is that the lamps do not "simmer" [2] indefinitely, and the laser shuts off if it is not triggered every few minutes. Huanqian Loh wired an external switch into the simmer restart button, and made the external switch accessible from the main experiment control PC. Around 2015, I wired up a relay to a cheap DAC controlled by the main experiment control Labview program, allowing Abby to be "primed"

[1] Nd:YAG, or usually just abbreviated YAG, meaning a Neodymium-doped Yttrium Aluminium Garnet crystal, $Y_3Al_5O_{12}$

[2] "Simmering" is a technique used to improve repeatability and preserve the lifetime of flashlamps by continuously running a small discharge through the lamp. The small discharge "seeds" the much larger flash that occurs when the lamp is fired, causing the large flash to develop in the center of the lamp and preventing damage to the surrounding area.

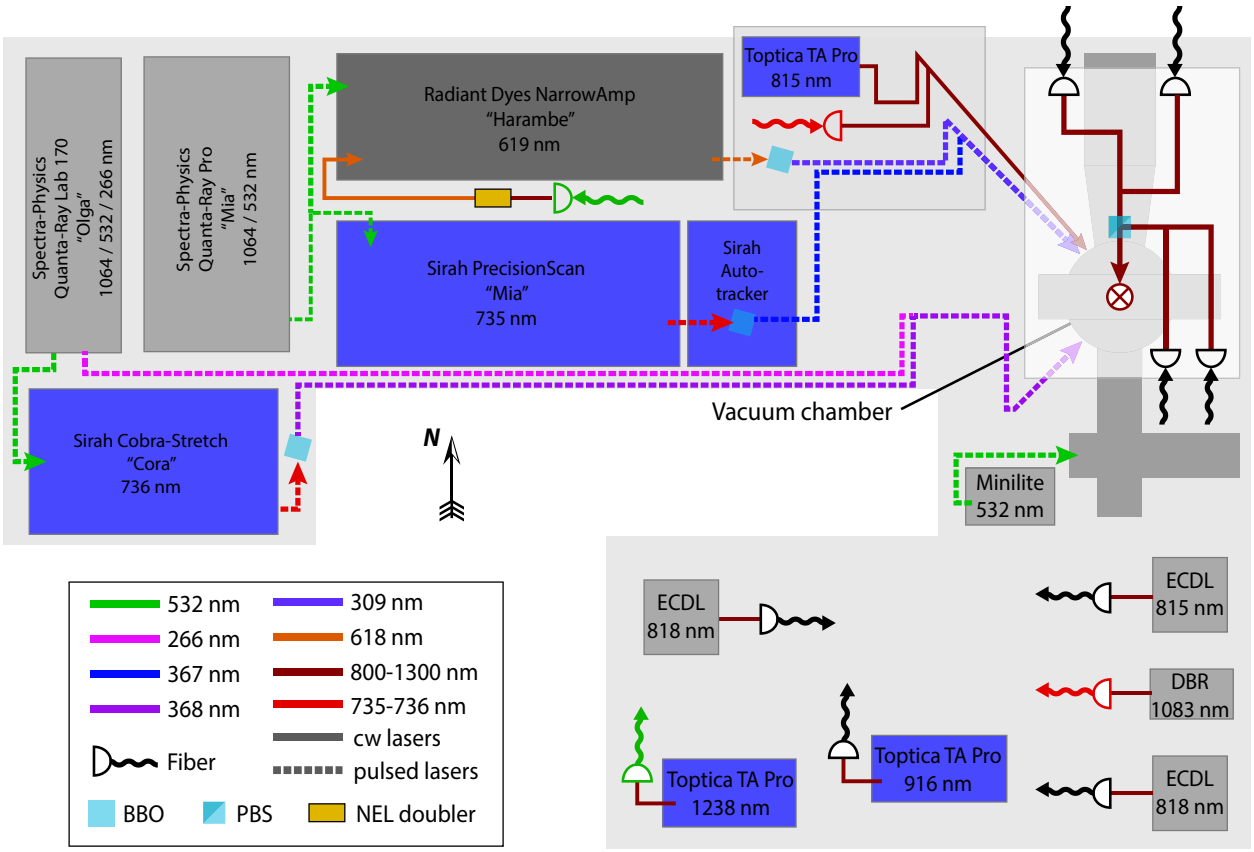

Figure C.1: Geographical layout of the HfF^+ eEDM lab as of June 2019. The colors of optical fiber launchers are simply to correlate the input and output of fibers and are not related to the wavelength. The 818 nm, 961 nm, and 815 nm lasers are combined and sent vertically down through the vacuum chamber from an optical breadboard mounted above (translucent white).

programmatically.

(2) **Spectra-Physics Quanta-Ray Pro** ("Mia")

The Quanta-Ray Pro is a 10 ns Q-switched YAG operating at 1064 nm with a 10 Hz repetition rate. The Pro is equipped with a second harmonic generator module, producing about 1 Joule of light at 532 nm. The 532 nm light is used to pump the PrecisionScan and the NarrowAmp.

(3) **Spectra-Physics Quanta-Ray Lab 170** ("Olga")

The Quanta-Ray Lab is another 10 ns Q-switched YAG with its fundamental at 1064 nm, and with a repetition rate of 30 Hz. It is equipped with 2nd harmonic and 4th harmonic generating crystals. The 532 nm light pumps the Cobra-Stretch, while the 266 nm fourth harmonic is used as the second photon of photodissociation.

(4) **Radiant Dyes NarrowAmp** ("Harambe")

This pulsed dye amplifier replaced a homebuilt setup in Summer 2016, and has made an enormous difference to the stability of the HfF^+ eEDM experiment as a whole. It doesn't achieve this by doing anything particularly clever; it simply has a solid aluminium baseplate with three dye cells and various optics mounted in a simple configuration. We pump Harambe with approximately 50 mJ of 532 nm light from Mia, which amplifies a 619 nm seed produced by doubling 1238 nm light from Tuna. On a good day, we get about 2 mJ of 618 nm pulsed light from Harambe, which we then double using a BBO to get about 200 μJ of 309 nm UV light. This UV light drives the first transition in our two-photon photoionization of HfF.

(5) **Sirah PrecisionScan** ("Bertha")

The PrecisionScan is a YAG-pumped, grating stabilized pulsed dye laser from Sirah Lasertechnik, equipped with a 2nd harmonic generation module and "autotracker," which compensates for changes in beam pointing when the frequency is changed. The PrecisionScan is

equipped with three dye cells, the third of which is a "capillary amplifier," a special tubular dye cell meant to improve the output beam shape, which it does to a limited extent. We typically operate this laser at 735.4650(5) nm or 13596.84(1) cm^{-1}, and use the 2nd harmonic generated by a nonlinear crystal housed in the autotracker (either BBO or KDP, dpeending on the wavelength range) for the second photon of photoionization of HfF.

(6) **Sirah Cobra-Stretch** ("Cora")

The Sirah Cobra-Stretch is another YAG-pumped, grating-stabilized pulsed dye laser. This laser has only two dye cells, but the beam is double-passed through the first cell to form an oscillator plus an amplifier stage. With this laser, we produce the first photon of our two-photon resonance-enhanced photodissociation detection. In the course of this thesis, we have used this laser to its full tunable potential, scanning it from about 570 nm to 760 nm to find suitable intermediate states for photodissociation (Chapter 6).

(7) **Toptica TA Pro (961 nm)** ("Toptica")

"Toptica" was our first laser purchased from Toptica Photonics, and it has been the most reliable laser in the lab. Until Fall 2018, we operated this laser on the $^3\Pi_{0^+} \leftarrow {}^1\Sigma^+ (1,0)$ R(0) transition for stimulated Raman transfer, as described in Refs. [28, 82]. In Fall 2018, we used this laser's impressive tunability to move over to 961 nm and start driving the $^3\Pi_{0^+} \leftarrow {}^1\Sigma^+ (0,0)$ P(1) line for incoherent transfer (Chapter 5).

(8) **Toptica TA Pro (1238 nm)** ("Tuna")

We purchased this TA Pro in Fall 2016 to replace a homebuilt ECDL that featured a high-power 1238 nm gain chip from Innolume. While the details are proprietary, we believe that this new laser uses a very similar gain chip, but also includes a tapered amplifier (TA). This laser produces several hundred mW at 1238 nm, which we double to 619 nm using a ridge waveguide doubler from NEL Photonics. The 619 nm light acts as a seed for the Radiant Dyes NarrowAmp pulsed dye amplifier, Harambe.

(9) **Toptica TA Pro (815 nm)**

The 815 nm TA Pro is our most recent purchase from Toptica, and replaced a cw Ti:sapphire laser that was adopted by Yan and Kia Boon on the ThF^+ eEDM experiment, due to their need for a widely tunable NIR cw laser. The 815 nm laser has been slightly more challenging than our earlier TA Pros, as it has a much worse beam profile, suffers from significant thermal lensing in the TA chip, and has had issues with drifting alignment into the TA. Still, when optimized, the laser produces several Watts of light at 815 nm, which is important for driving the weak ${}^3\Sigma^-_{0^+} \leftarrow {}^3\Delta_1\,(0,0)$ transition for strobed depletion (Chapter 5).

(10) **Photodigm TO-8 DBR (1083 nm)**

It is always nice when there is not much to say about a laser. This DBR laser from Photodigm does what a DBR laser should do: It is always single-mode, it only mode-hops when you expect it to, and it doesn't complain. This laser is used for optical pumping of M_F levels on the ${}^3\Pi_{0^-} \leftarrow {}^3\Delta_1\,(0,0)$ P(1) transition.

(11) **JILA ECDL (818 nm)** ("Stella")

(12) **JILA ECDL (818 nm)**

(13) **JILA ECDL (815 nm)**

These grating-stabilized ECDLs are of the JILA design originated by Scott Papp some years ago. We have swapped out their diodes and gratings a number of times, and their reliability seems to be limited by the quality of diode installed in them, and the degree of care taken in optimizing the optical feedback to achieve lasing on a single external cavity mode. At this point, only Stella has an anti-reflection (AR) coated diode installed, and so it is the most tunable and reliable. For improved future performance, we could purchase AR-coated diodes for these ECDLs. These lasers are all used as cleanups, as described in Chapter 5.

(14) **New-Focus Vortex**

This laser is stabilized to the ^{87}Rb $5S_{1/2}$ $F = 2 \rightarrow 5P_{3/2}$ $F' = 3$ crossover peak at 780.246291 nm. We use this reference to calibrate our HighFinesse WS7 wavemeter, to which we lock all of our other cw lasers. The high temperature of our HfF^+ ions of about 5 Kelvin leads to Doppler widths on the order of 40 MHz, so that the 5 MHz relative precision of the WS7 is sufficient to lock on resonance.

C.2 Generation 2 Ion Trap

Table C.1 contains multipole fit coefficients up to $l = 11$ for the Generation 2 ion trap electrodes, numbered 1-8, T (top), and B (bottom).

The following page shows the mechanical drawings for the Generation 2 custom vacuum chamber, provided by Kimball Physics. These may be useful for future mechanical designs involving this chamber, in particular for mounting electronics or optics to the machined mounting surfaces.

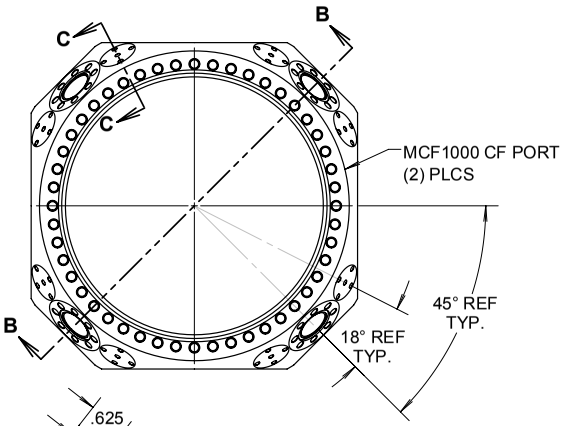

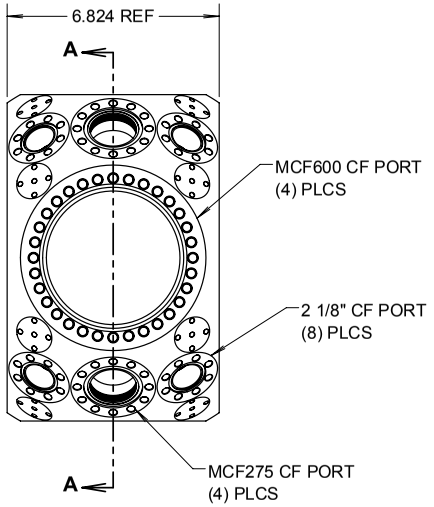

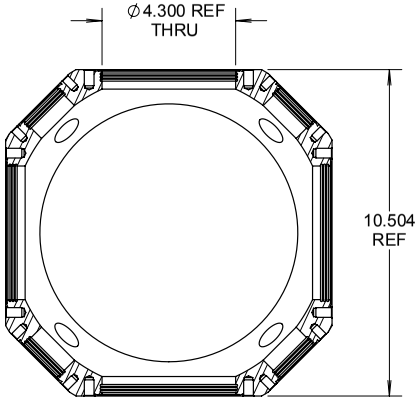

SECTION A-A

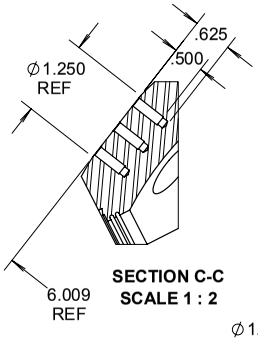

SECTION C-C
SCALE 1 : 2

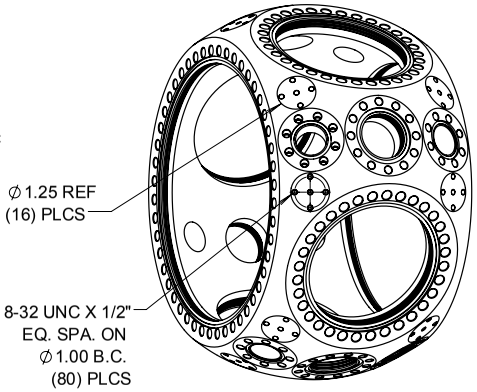

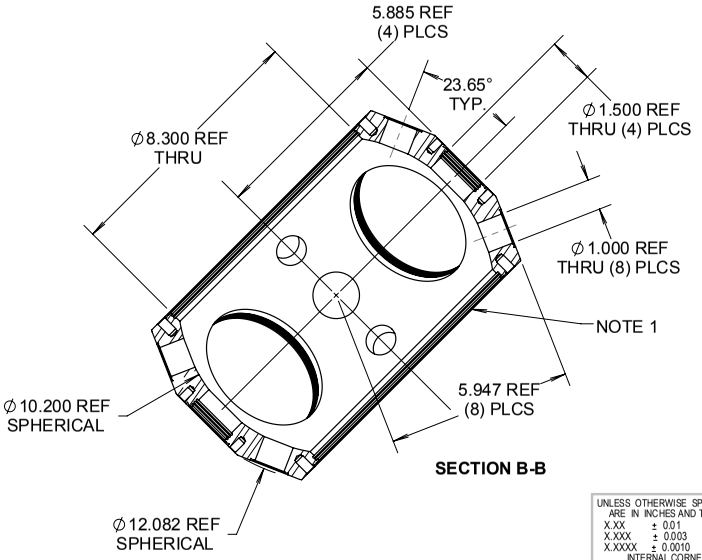

SECTION B-B

PRELIMINARY
FOR CUSTOMER
APPROVAL

SIGNED_____ DATE:_____

NOTES:
1. MAKE FROM 53-183112
2. ESTIMATED FINISHED WEIGHT: 37 lbs./16.8 kg.

REV	REVISION DESCRIPTION	DATE	BY	CHK	ECO	USED ON
B	2 1/8" CF WAS 1.33 CF. 1.25 FLAT WAS 1.33. (80) 8-32 WAS (64)	07/13/16	IMK	IMK		
A	INITIAL RELEASE	07/12/16	IMK	IMK		

UNLESS OTHERWISE SPECIFIED DIMENSIONS ARE IN INCHES AND TOLERANCES ARE:
X.XX ± 0.01 ANGULAR:
X.XXX ± 0.003 X° ± 0.5°
X.XXXX ± 0.0010 .X.X° ± 0.1°
INTERNAL CORNERS R.015 MAX
COAXIAL Ø's CONCENTRIC WITHIN .003 TIR

KIMBALL PHYSICS KPI
KIMBALL HILL RD., WILTON, NH 03086-9742 U.S.A. (603) 878-1616

CHMBR, MCF1000-Cust-H2F4C4B8

MATERIAL	SCALE	DWG. No.	REV.
NOTE 1	1:4	QQ-000369-P3	B
FINISH 16 / BREAK EDGES 0.005/0.010	B SIZE	SHEET 1 OF 1	MODEL No. QQ-000369-P3

'B' SIZE PART TEMPLATE; REV. 6

C.3 Trap amplifier

The following pages contain a reproduction of Terry Brown's circuit designs for the Generation 2 ion trap amplifiers. These are also retained in the electronics shop's record-keeping system.

V3.1

Output range of U1 is scaled to +/- 2.5V maximum to reduce 2nd harmonic distrotion in U1.

Output Monitor offset null. Adjust HV Output Offset Adjustment first. Terminate Input with 50 ohms. While measuring Output Monitor, adjust R77 until Out Monitor is ~0V (10's of microvolts).

HV Output offset null. Terminate Sig Input with 50 ohms. While measuring HV Out, adjust R72 until HV Out is ~0V. Typically HV Out zero is within ~1mV.

Slew Rate limitor circuit to lesson large signal saturation issues. Adjust C26/C27 such that slew rate is ~18 V/us. This rate yields the ~maximum PA94 slew rate.

It is important to use thin-film resistor (not thick-film) for the noise critcal paths due to thin-film superior noise properties.

DNI part values = Do Not Install.

JILA CU-Boulder & NIST ELECTRONICS	High Voltage Composite Amplifier	
	COMPOSITE_AMPLIFIER	
DESIGN BY: T. Brown		BUILT FOR: Cornell / Ye
UPDATE: 7/31/2017	VERSION: V3.1	DRAWN BY: T. Brown
DN: CE085A3.1	DATE: 06/06/2017	SHEET 1 OF 2

V3.1

AC Control Current Input GAIN:
U8 Restores U6's DC offset due to asymmetry in PA94 HV Amp's positive and negative slew rate response. At high square-wave frequencies this aysmmetry can put U6 on the rails.

DNI: R66, and R59 fix issue

R51 Adjustment: While in Open Loop Mode (JP1 Shorted, JP2 open, page 1). With 1Vpp signal input at 100 kHz, adjust HV Out to be 100 Vpp. Comfirm HV Out is 100 Vpp at 100 Hz.

Under normal operation, Pin 4 of PA94, sits 5.4V below the plus power supply (Pin 12). The maximum voltage swings on Pin 4 is +2.0V, -1.5V, or Pin 4 voltage is between 3.4V and 6.9V below the positive supply voltage. Q3 forms a low capacitance clamp to protect pin 4. Q3_Vbe zeners at around -9V, then forward bias at +0.7V. This clamps pin 4 of the PA94 to (+V2 + 0.7), to (+V2 - 9V). Pin 6 tracks the output voltage, pin 7.

Differentiator V to I converter.
Iout = (jw*R50*C17/Rs)*Vc, (Rs = R54+R51)
Gc = Vout/Vc = -Iout/(jw*C14) = (R55/Rs)*(C21/C14).
with R50 = 1k, Rs = 143R, C17, C21 = 33pF, and C14 = 4.7pF
Gc = ~-50. Gc should match PA94 gain from DC control input.

R43/C28 are used to reduce the bandwidth of PA94 to around 24 kHz.
This shuts off the input stage of the PA94, so the PA94 feedback circuit does not cancel the higer frequency bandwidth of the compensation input (pin 4). The Feedback network effectively forms a low pass (DC input to R42) / high pass network via Pin 4 w/crossover frequency ~ 24 kHz. The bandwidth through pin 4 is ~ 4 MHz.

JILA CU-Boulder & NIST ELECTRONICS	High Voltage Composite Amplifier	
	HIGH_VOLTAGE_AMPLIFIER	
DESIGN BY: T. Brown		BUILT FOR: Cornell / Ye
UPDATE: 7/31/2017	VERSION: V3.1	DRAWN BY: T. Brown
DN: CE085A3.1	DATE: 06/06/2017	SHEET 2 OF 2

C.4 Trap synthesizer

The following pages contain a reproduction of Felix Vietmayer's circuit designs for the Generation 2 ion trap synthesizer. These are also retained in the electronics shop's record-keeping system.

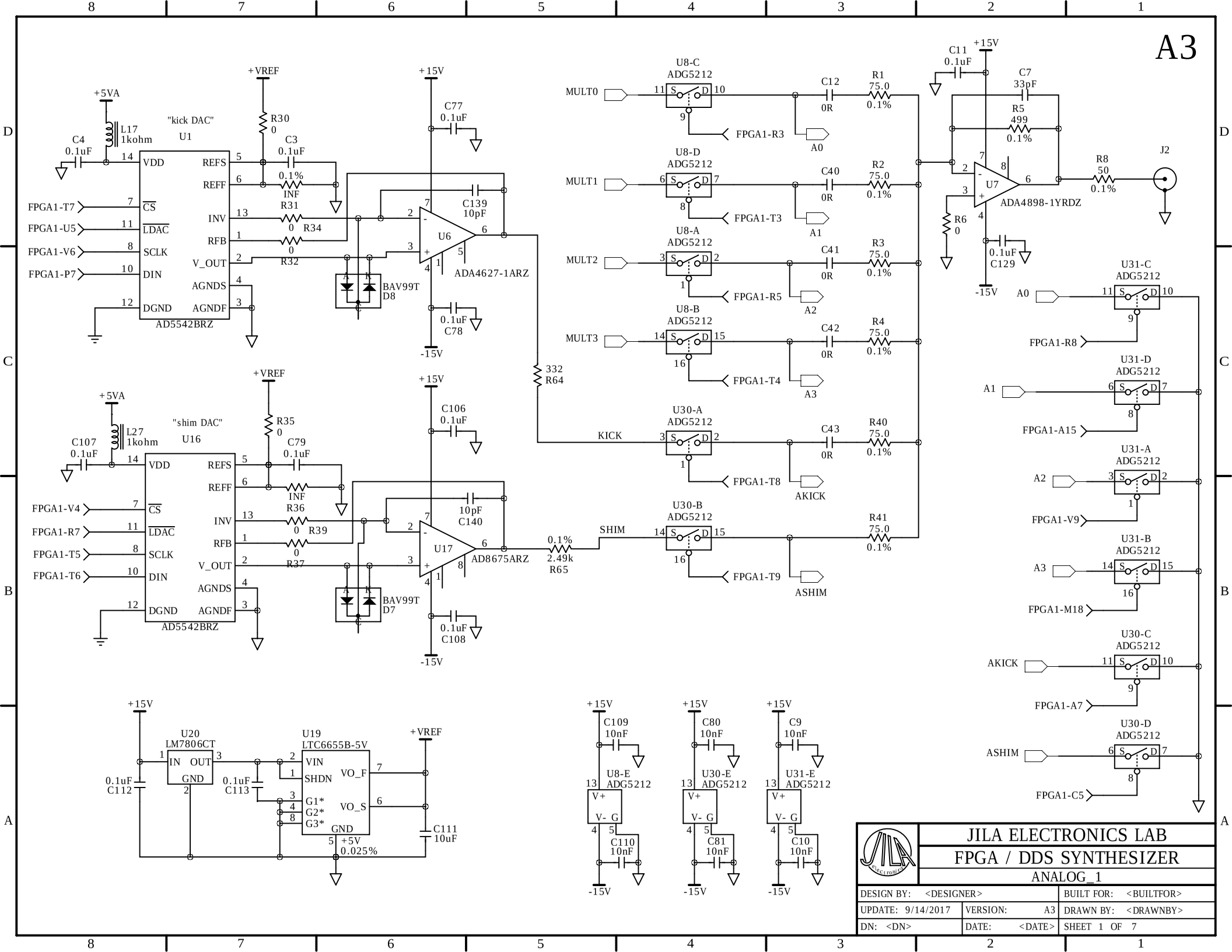
A3
"kick DAC"
U1
AD5542BRZ
"shim DAC"
U16
AD5542BRZ
U6
ADA4627-1ARZ
U17
AD8675ARZ
U7
ADA4898-1YRDZ
U8-A
U8-B
U8-C
U8-D
U8-E
U30-A
U30-B
U30-C
U30-D
U30-E
U31-A
U31-B
U31-C
U31-D
U31-E
ADG5212
U20
LM7806CT
U19
LTC6655B-5V
+5VA
+VREF
+15V
-15V
MULT0
MULT1
MULT2
MULT3
KICK
SHIM
AKICK
ASHIM
FPGA1-T7
FPGA1-U5
FPGA1-V6
FPGA1-P7
FPGA1-V4
FPGA1-R7
FPGA1-T5
FPGA1-T6
FPGA1-R3
FPGA1-T3
FPGA1-R5
FPGA1-T4
FPGA1-T8
FPGA1-T9
FPGA1-R8
FPGA1-A15
FPGA1-V9
FPGA1-M18
FPGA1-A7
FPGA1-C5
A0
A1
A2
A3
BAV99T
D8
D7
J2
JILA ELECTRONICS LAB
FPGA / DDS SYNTHESIZER
ANALOG_1
DESIGN BY: <DESIGNER>
BUILT FOR: <BUILTFOR>
UPDATE: 9/14/2017
VERSION: A3
DRAWN BY: <DRAWNBY>
DN: <DN>
DATE: <DATE>
SHEET 1 OF 7

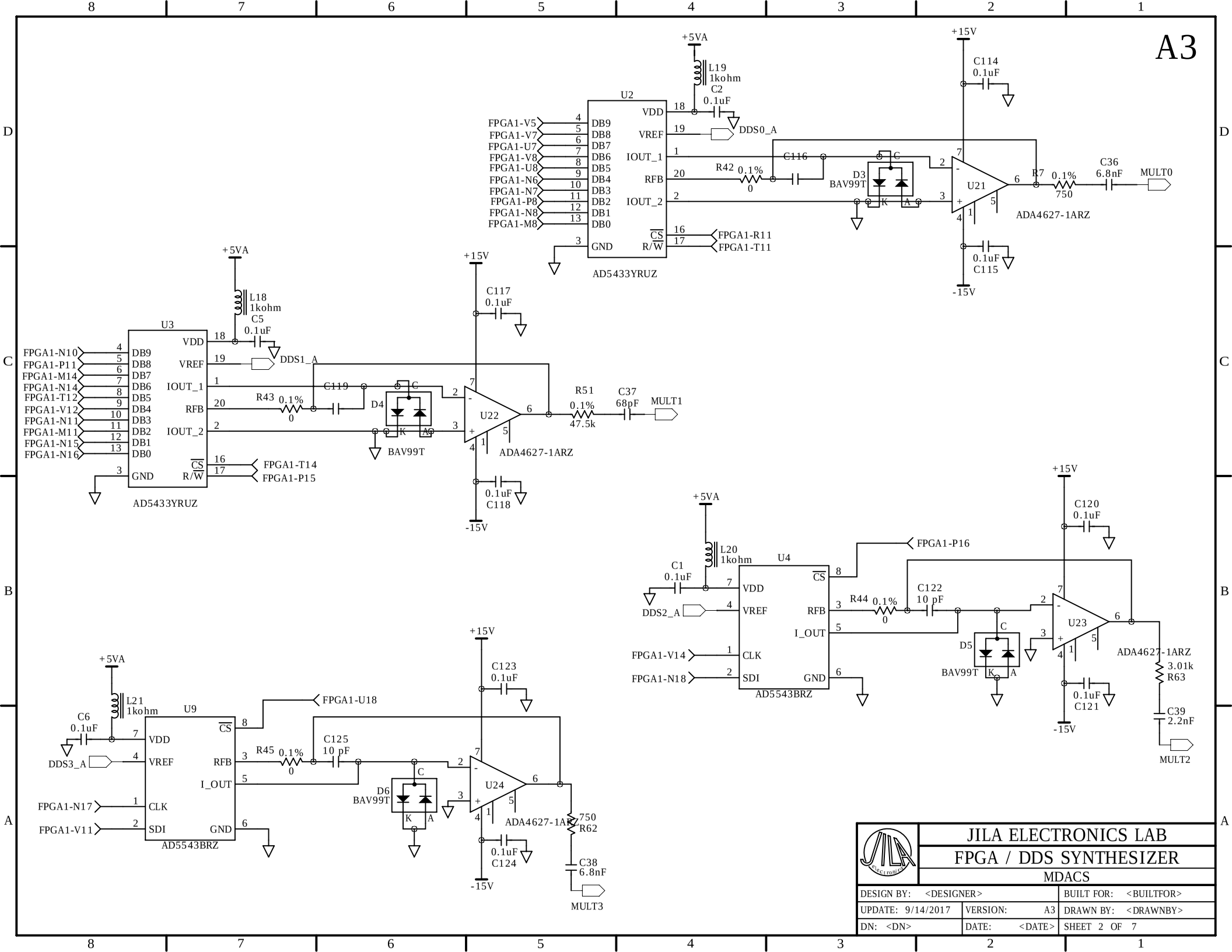
A3
U2
AD5433YRUZ
DDS0_A
FPGA1-V5
FPGA1-V7
FPGA1-U7
FPGA1-V8
FPGA1-U8
FPGA1-N6
FPGA1-N7
FPGA1-P8
FPGA1-N8
FPGA1-M8
FPGA1-R11
FPGA1-T11
L19
1kohm
C2
0.1uF
C114
0.1uF
C116
R42
0.1%
0
D3
BAV99T
U21
ADA4627-1ARZ
R7
0.1%
750
C36
6.8nF
MULT0
C115
0.1uF
U3
AD5433YRUZ
DDS1_A
FPGA1-N10
FPGA1-P11
FPGA1-M14
FPGA1-N14
FPGA1-T12
FPGA1-V12
FPGA1-N11
FPGA1-M11
FPGA1-N15
FPGA1-N16
FPGA1-T14
FPGA1-P15
L18
1kohm
C5
0.1uF
C117
0.1uF
C119
R43
0.1%
0
D4
BAV99T
U22
ADA4627-1ARZ
R51
0.1%
47.5k
C37
68pF
MULT1
C118
0.1uF
U4
AD5543BRZ
DDS2_A
FPGA1-V14
FPGA1-N18
FPGA1-P16
L20
1kohm
C1
0.1uF
C120
0.1uF
C122
10 pF
R44
0.1%
0
D5
BAV99T
U23
ADA4627-1ARZ
3.01k
R63
C39
2.2nF
MULT2
C121
0.1uF
U9
AD5543BRZ
DDS3_A
FPGA1-N17
FPGA1-V11
FPGA1-U18
L21
1kohm
C6
0.1uF
C123
0.1uF
C125
10 pF
R45
0.1%
0
D6
BAV99T
U24
ADA4627-1ARZ
750
R62
C38
6.8nF
MULT3
C124
0.1uF
+5VA
+15V
-15V
JILA ELECTRONICS LAB
FPGA / DDS SYNTHESIZER
MDACS
DESIGN BY: <DESIGNER>
BUILT FOR: <BUILTFOR>
UPDATE: 9/14/2017
VERSION: A3
DRAWN BY: <DRAWNBY>
DN: <DN>
DATE: <DATE>
SHEET 2 OF 7

A3

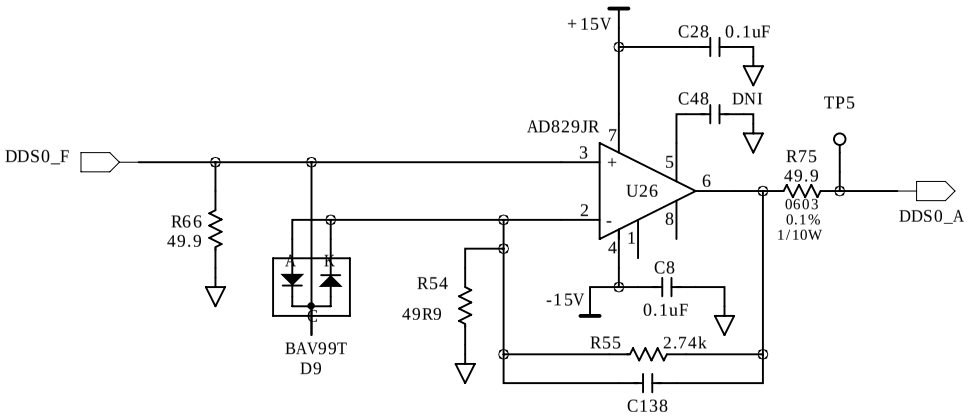

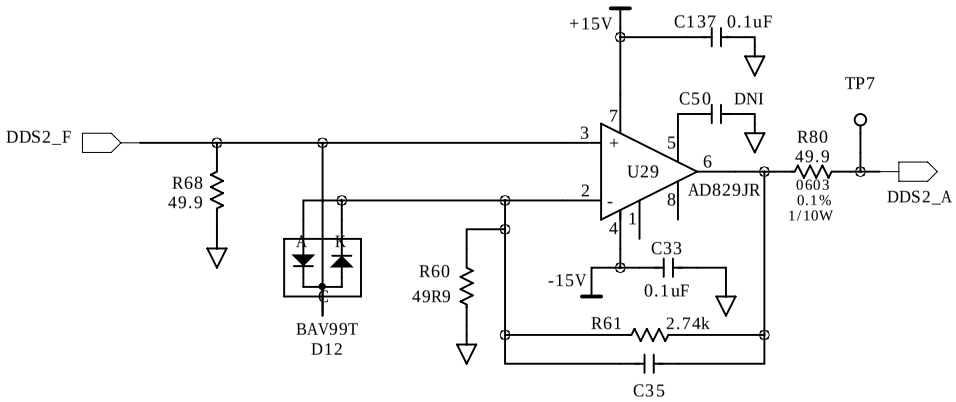

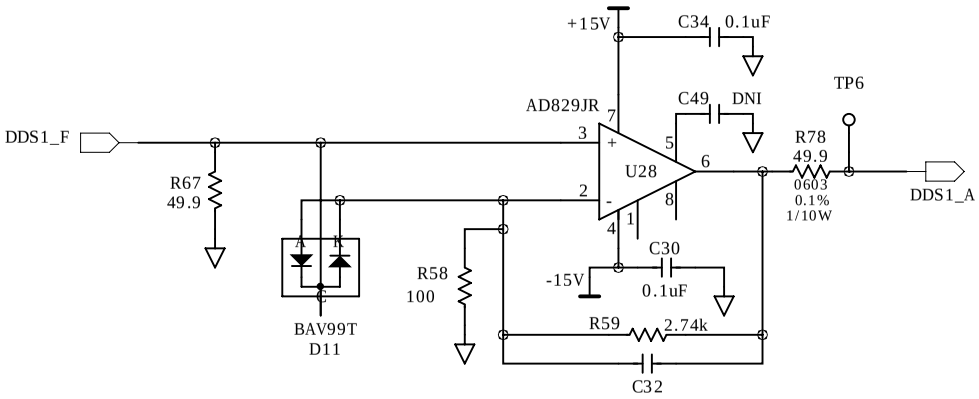

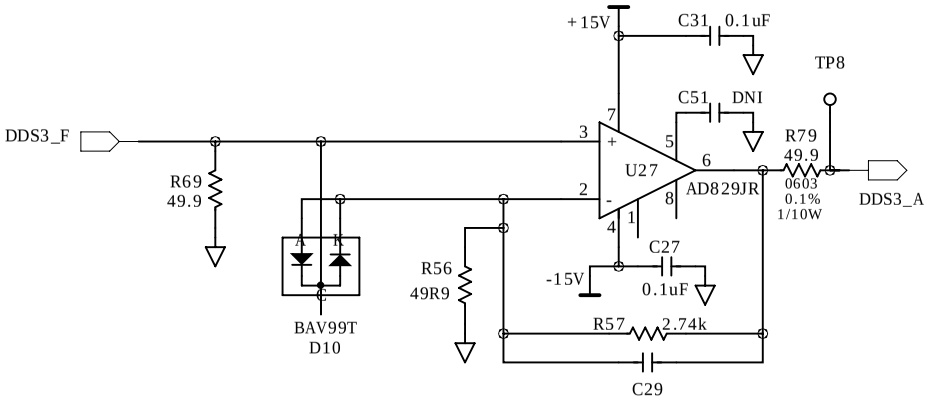

JILA ELECTRONICS LAB		
FPGA / DDS SYNTHESIZER		
PREAMP		
DESIGN BY: <DESIGNER>		BUILT FOR: <BUILTFOR>
UPDATE: 9/14/2017	VERSION: A3	DRAWN BY: <DRAWNBY>
DN: <DN>	DATE: <DATE>	SHEET 3 OF 7

A3

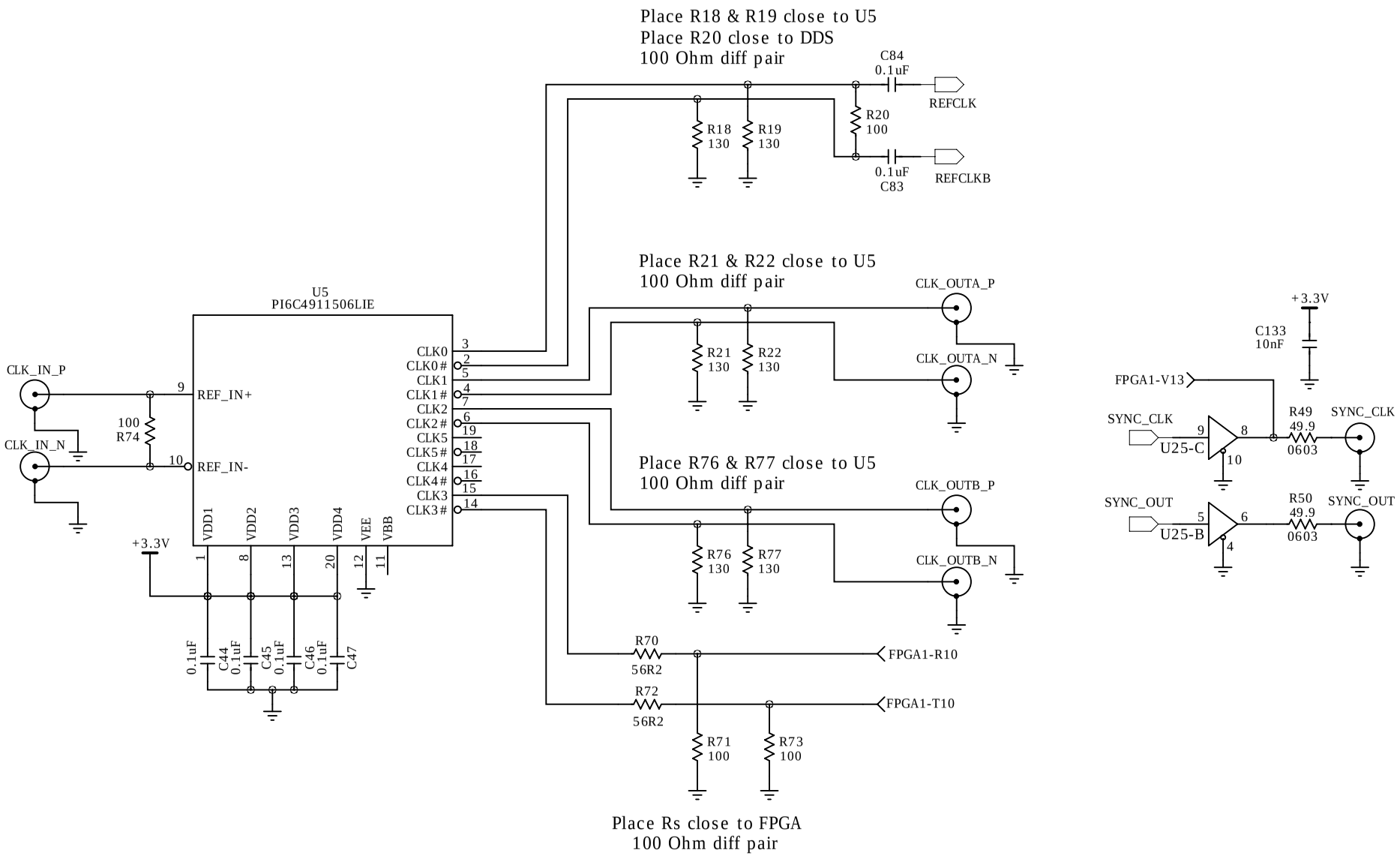

JILA ELECTRONICS LAB		
FPGA / DDS SYNTHESIZER		
CLOCKING		
DESIGN BY: <DESIGNER>		BUILT FOR: <BUILTFOR>
UPDATE: 9/14/2017	VERSION: A3	DRAWN BY: <DRAWNBY>
DN: <DN>	DATE: <DATE>	SHEET 4 OF 7

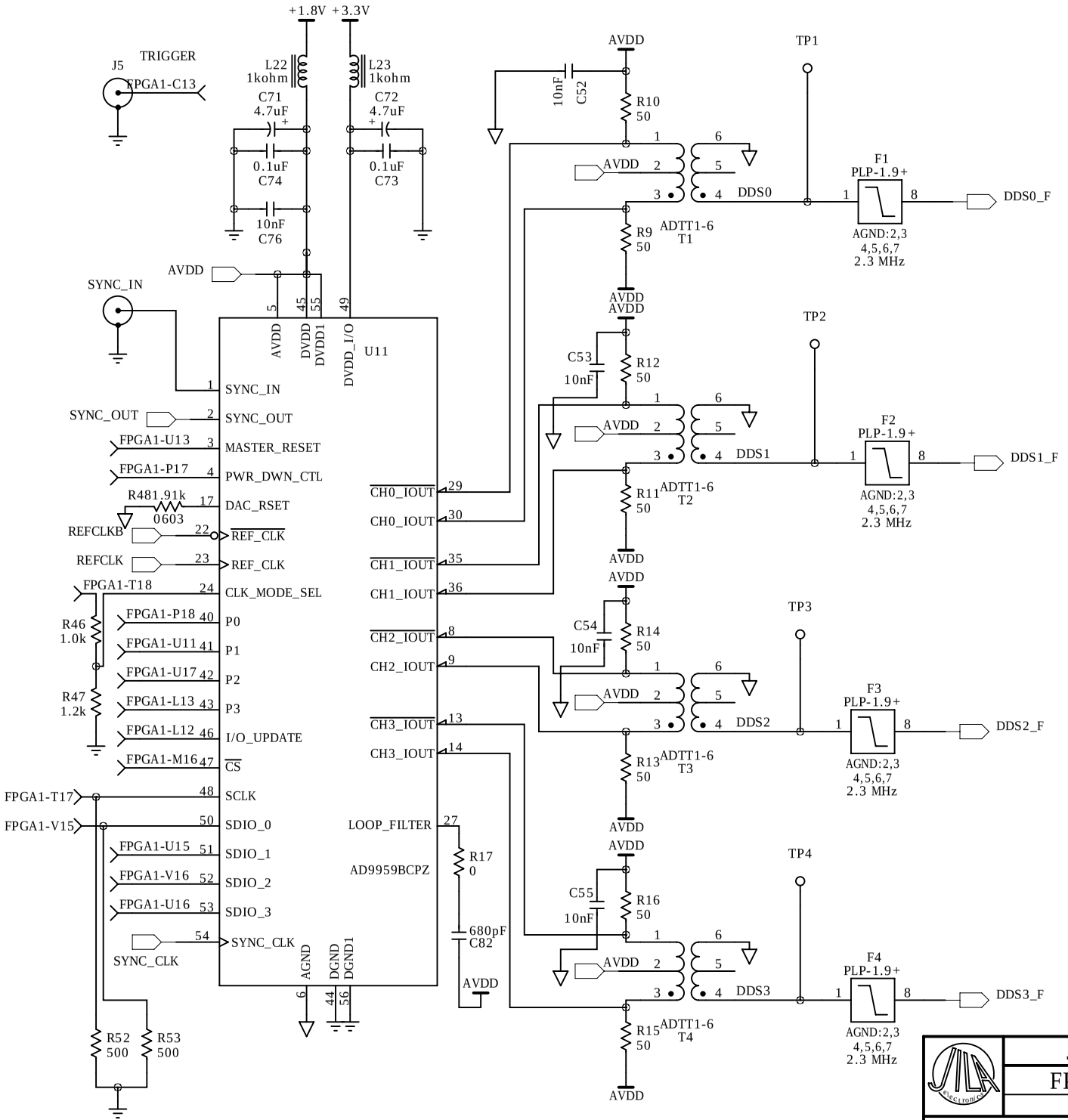

A3

JILA ELECTRONICS LAB		
FPGA / DDS SYNTHESIZER		
DDS		
DESIGN BY: <DESIGNER>		BUILT FOR: <BUILTFOR>
UPDATE: 9/14/2017	VERSION: A3	DRAWN BY: <DRAWNBY>
DN: <DN>	DATE: <DATE>	SHEET 5 OF 7

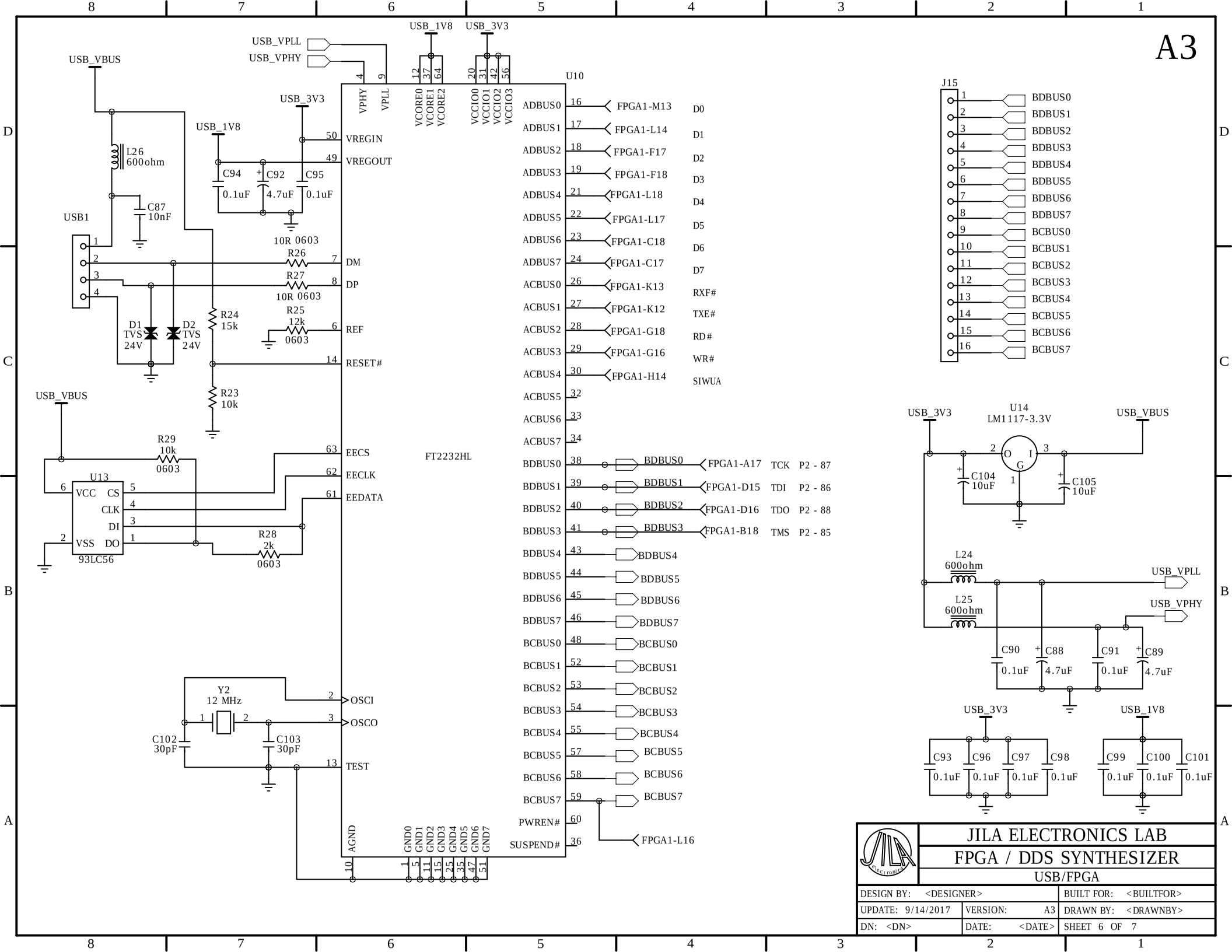
A3
USB_VBUS
USB_VPLL
USB_VPHY
USB_1V8
USB_3V3
L26
600ohm
C87
10nF
C94
0.1uF
C92
4.7uF
C95
0.1uF
USB1
10R 0603
R26
R27
DM
DP
D1
TVS
24V
D2
TVS
24V
R24
15k
R25
12k
0603
REF
RESET#
R23
10k
R29
10k
0603
U13
VCC
CS
CLK
DI
VSS
DO
93LC56
R28
2k
0603
EECS
EECLK
EEDATA
Y2
12 MHz
C102
30pF
C103
30pF
OSCI
OSCO
TEST
AGND
U10
FT2232HL
VPHY
VPLL
VCORE0
VCORE1
VCORE2
VCCIO0
VCCIO1
VCCIO2
VCCIO3
VREGIN
VREGOUT
ADBUS0
ADBUS1
ADBUS2
ADBUS3
ADBUS4
ADBUS5
ADBUS6
ADBUS7
ACBUS0
ACBUS1
ACBUS2
ACBUS3
ACBUS4
ACBUS5
ACBUS6
ACBUS7
BDBUS0
BDBUS1
BDBUS2
BDBUS3
BDBUS4
BDBUS5
BDBUS6
BDBUS7
BCBUS0
BCBUS1
BCBUS2
BCBUS3
BCBUS4
BCBUS5
BCBUS6
BCBUS7
PWREN#
SUSPEND#
GND0
GND1
GND2
GND3
GND4
GND5
GND6
GND7
FPGA1-M13
FPGA1-L14
FPGA1-F17
FPGA1-F18
FPGA1-L18
FPGA1-L17
FPGA1-C18
FPGA1-C17
FPGA1-K13
FPGA1-K12
FPGA1-G18
FPGA1-G16
FPGA1-H14
D0
D1
D2
D3
D4
D5
D6
D7
RXF#
TXE#
RD#
WR#
SIWUA
BDBUS0
BDBUS1
BDBUS2
BDBUS3
FPGA1-A17
FPGA1-D15
FPGA1-D16
FPGA1-B18
TCK P2 - 87
TDI P2 - 86
TDO P2 - 88
TMS P2 - 85
FPGA1-L16
J15
BDBUS0
BDBUS1
BDBUS2
BDBUS3
BDBUS4
BDBUS5
BDBUS6
BDBUS7
BCBUS0
BCBUS1
BCBUS2
BCBUS3
BCBUS4
BCBUS5
BCBUS6
BCBUS7
U14
LM1117-3.3V
C104
10uF
C105
10uF
L24
600ohm
L25
600ohm
C90
0.1uF
C88
4.7uF
C91
0.1uF
C89
4.7uF
C93
C96
C97
C98
C99
C100
C101
0.1uF
JILA ELECTRONICS LAB
FPGA / DDS SYNTHESIZER
USB/FPGA
DESIGN BY: <DESIGNER>
BUILT FOR: <BUILTFOR>
UPDATE: 9/14/2017
VERSION: A3
DRAWN BY: <DRAWNBY>
DN: <DN>
DATE: <DATE>
SHEET 6 OF 7

A3

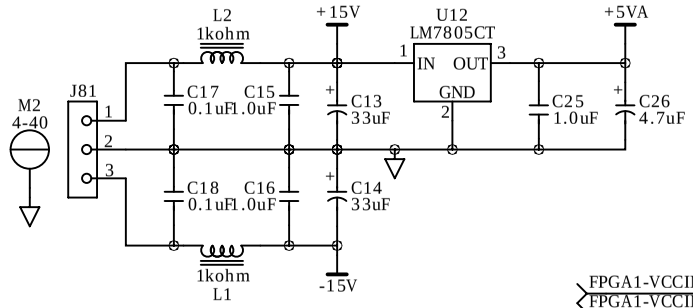

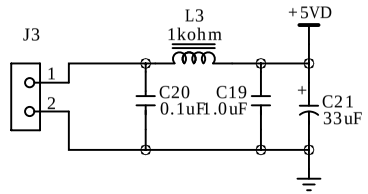

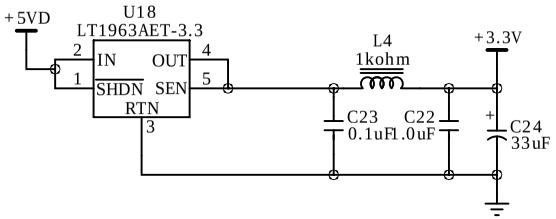

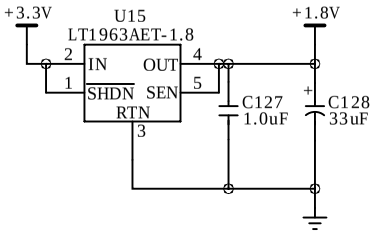

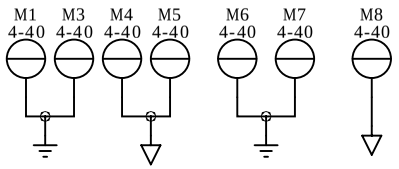

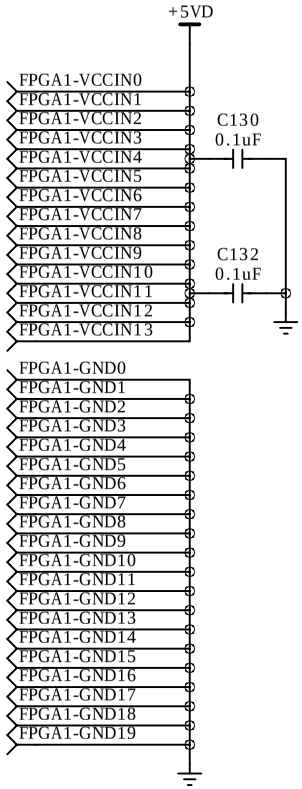

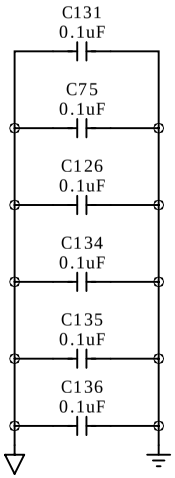

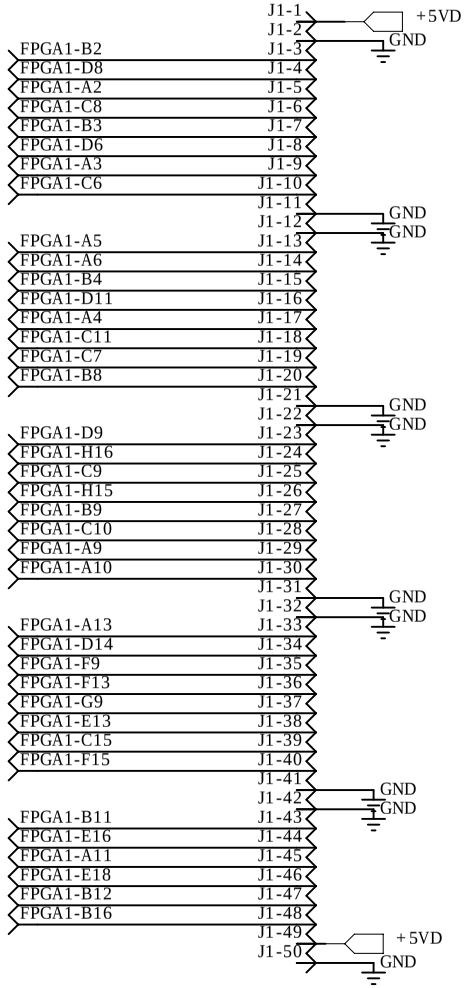

JILA ELECTRONICS LAB		
FPGA / DDS SYNTHESIZER		
POWER		
DESIGN BY: <DESIGNER>		BUILT FOR: <BUILTFOR>
UPDATE: 9/14/2017	VERSION: A3	DRAWN BY: <DRAWNBY>
DN: <DN>	DATE: <DATE>	SHEET 7 OF 7

		electrode									
l	m	1	2	3	4	5	6	7	8	T	B
1	−1	−1.67	−4.04	−4.04	−1.67	1.67	4.04	4.04	1.67		
	0									−0.73	0.73
	1	−4.04	−1.67	1.67	4.04	4.04	1.67	−1.67	−4.04		
2	−2	−2.96	−2.96	2.96	2.96	−2.96	−2.96	2.96	2.96		
	0	0.33	0.33	0.33	0.33	0.33	0.33	0.33	0.33	−0.82	−0.82
	2	−2.96	2.96	2.96	−2.96	−2.96	2.96	2.96	−2.96		
3	−3	−3.30	1.36	1.36	−3.30	3.30	−1.36	−1.36	3.30		
	0									−0.65	0.65
	3	−1.36	3.30	−3.30	1.36	1.36	−3.30	3.30	−1.36		
4	−4	−2.82	2.82	−2.82	2.82	−2.82	2.82	−2.82	2.82		
	−2	−0.03	−0.03	0.03	0.03	−0.03	−0.03	0.03	0.03		
	0	0.11	0.11	0.11	0.11	0.10	0.11	0.11	0.11	−0.42	−0.42
	2	−0.06	0.05	0.06	−0.06	−0.06	0.06	0.06	−0.06		
5	−5	−1.86	0.76	0.75	−1.86	1.86	−0.76	−0.75	1.86		
	−3	−0.04	0.03	0.03	−0.04	0.04	−0.03	−0.03	0.04		
	0									−0.25	0.25
	3	−0.03	0.04	−0.04	0.03	0.03	−0.04	0.04	−0.03		
	5	0.75	−1.86	1.86	−0.75	−0.75	1.86	−1.86	0.75		
6	−6	−0.91	−0.92	0.91	0.92	−0.92	−0.91	0.91	0.91		
	−4	−0.06	0.06	−0.06	0.06	−0.06	0.06	−0.06	0.06		
	−2	−0.03	−0.03	0.03	0.03	−0.03	−0.03	0.03	0.03		
	0	0.02	0.02	0.02	0.02	0.02	0.02	0.02	0.02	−0.15	−0.15
	6	0.91	−0.91	−0.91	0.91	0.91	−0.91	−0.91	0.91		
7	−7	−0.26	−0.59	−0.59	−0.26	0.26	0.59	0.59	0.25		
	−5	−0.04	0.02	0.02	−0.04	0.04	−0.02	−0.02	0.04		
	−3	−0.03			−0.03	0.03			0.03		
	0									−0.08	0.08
	3		0.03	−0.03			−0.03	0.03			
	5	0.02	−0.04	0.04	−0.02	−0.02	0.04	−0.04	0.02		
	7	0.59	0.26	−0.25	−0.59	−0.59	−0.25	0.26	0.58		
8	−8	−0.36	0.36	−0.36	0.36	−0.36	0.36	−0.36	0.36		
	0									−0.04	−0.04
	2	−0.03	0.03	0.03	−0.03	−0.03	0.03	0.03	−0.03		
	8	0.10	0.10	0.10	0.10	0.10	0.10	0.10	0.10	−0.05	−0.05
9	−9	−0.21	0.38	0.37	−0.21	0.21	−0.38	−0.38	0.21		
	0									−0.02	0.02
	8									−0.02	0.02
	9	0.37	−0.21	0.21	−0.38	−0.38	0.21	−0.21	0.38		
10	−10	0.12	0.12	−0.12	−0.12	0.12	0.12	−0.12	−0.12		
	8	0.02	0.02	0.02	0.02	0.02	0.02	0.02	0.02	−0.01	−0.01
	10	0.55	−0.55	−0.55	0.55	0.55	−0.55	−0.55	0.55		
11	−11	0.44	−0.38	−0.38	0.44	−0.44	0.38	0.38	−0.44		
	11	0.38	−0.44	0.44	−0.38	−0.38	0.44	−0.44	0.38		

Table C.1: Multipole fit coefficients up to $l = 11$ for electrodes of Generation 2 ion trap (Fig. 4.1), with units of V/m^l. Rows where all columns have a magnitude less than 0.02 are neglected. Note the absence of all rows $(l, m = \pm 1)$ for odd values of l, which behave as $\mathcal{E}_{\text{rot}} \propto Z^{l-1}$ along the line $(0, 0, Z)$.

Appendix D

Molecular Data

In Tables D.1 and D.2, Maddie Pettine and I have tabulated the observed transitions in our REMPD survey spectrum collected in Fall 2018. For transitions where we performed fine scans to identify Ω of the intermediate state, those are listed. Transition center frequencies ν and strengths are very approximate – they are only eyeballed, and are not from any fit.

Dye	ν (cm^{-1})	Chop	Ω''	Ω'	Strength
Styryl 8	26096	754	$^3\Delta_1$	2	0.17
	26177	754	$^3\Delta_1$	1	0.20
	26202	754	$^3\Delta_1$	1	0.18
	26369	754	$X^1\Sigma^+$, $v = 1$	1	0.24
	26381	754	$^3\Delta_1$, $v = 1$	2	0.14
	26393	754	$X^1\Sigma^+$, $v = 1$	1	0.15
	26518	754	$^3\Delta_1$	2	0.28
	26546	I	$X^1\Sigma^+$, $v = 0$	1	1.07
	26686	I	$^3\Delta_1$	2	0.09
	26707	I	$^3\Delta_1$	1	0.09
Pyridine 2	26759	754	$^3\Delta_1$	1	0.25
	26777	I	$X^1\Sigma^+$, $v = 0$	0	0.09
	26796	961	$^3\Delta_1$	1	0.40
	26864	I	$X^1\Sigma^+$, $v = 1$	2	0.10
	26960	I	$X^1\Sigma^+$, $v = 1$	1	0.17
	26988	754	$X^1\Sigma^+$, $v = 1$	1	0.30
	27137	961	$^3\Delta_1$, $v = 0$	2	0.84
	27154	I	$X^1\Sigma^+$, $v = 0$	1	0.51
	27178	I	$X^1\Sigma^+$, $v = 0$	1	0.05
	27264	I	$X^1\Sigma^+$, $v = 1$	1	0.08
	27345	961	$^3\Delta_1$, $v = 2$	1	0.67
	27394	I	$X^1\Sigma^+$, $v = 0$	0	0.05
	27399	961	$^3\Delta_1$	1	0.64
	27615	I	$X^1\Sigma^+$, $v = 1$	1	0.06
	27659	I	$X^1\Sigma^+$, $v = 0$	2	0.18
	27683	I	$X^1\Sigma^+$, $v = 0$	1	0.11
	27735	I	$X^1\Sigma^+$, $v = 0$	1	0.26
	27752	961	$^3\Delta_1$	2	0.67
	27775	I	$X^1\Sigma^+$, $v = 0$	1	0.25
	27861	754	$X^1\Sigma^+$, $v = 1$	1	0.22
	27942	961	$X^1\Sigma^+$, $v = 1$	2	0.62
	28001*	I	$X^1\Sigma^+$, $v = 0$	0	0.30
	28001*	I	$^3\Delta_1$	1	0.30
	28111	961	$^3\Delta_1$	0	0.69
	28135	754	$X^1\Sigma^+$, $v = 1$	1	0.18
	28194	754	$X^1\Sigma^+$, $v = 1$	1	0.31
	28322	I	$X^1\Sigma^+$, $v = 0$	1	0.28
	28376	I	$X^1\Sigma^+$, $v = 0$	1	0.14

Table D.1: Summary of observed photodissociation transitions, part I.

Dye	ν (cm^{-1})	Chop	Ω''	Ω'	Strength
Pyridine 1	28602	754	$^3\Delta_1$	1	0.20
	28635	754	$^3\Delta_1$	2	0.15
	28650	754	$X^1\Sigma^+$, $v = 0$	1	0.13
	28738	754	$X^1\Sigma^+$, $v = 1$	1	0.29
	28795	754	$X^1\Sigma^+$, $v = 1$	1	0.39
	28920	I	$X^1\Sigma^+$, $v = 0$	1	0.08
	28969	754	$X^1\Sigma^+$, $v = 0$	1	0.12
	29088	I	$X^1\Sigma^+$, $v = 0$	0	0.38
	29146	I	$X^1\Sigma^+$, $v = 0$	0	0.26
	29203	754	$^3\Delta_1$	1	0.16
	29269	754	$^3\Delta_1$	2	0.12
	29328	I	$X^1\Sigma^+$, $v = 0$	1	0.57
	29346	754	$X^1\Sigma^+$, $v = 1$	0	0.16
	29505	I	$X^1\Sigma^+$, $v = 0$	1	0.24
	29524	I	$X^1\Sigma^+$, $v = 0$	1	0.29
	29530	754	$X^1\Sigma^+$, $v = 0$	1	0.25
	29579	I	$X^1\Sigma^+$, $v = 0$	1	0.12
	29671	754	$^3\Delta_1$	1	0.16
	29700	I	$X^1\Sigma^+$, $v = 0$	0	0.45
	29831	I	$X^1\Sigma^+$, $v = 0$	1	0.16
	29879	754	$X^1\Sigma^+$, $v = 1$	1	0.27
Rhodamine 640	30922	754	$^3\Delta_1$	0	0.09
	30946	I	$X^1\Sigma^+$, $v = 0$	0	0.09
	31111	754	$X^1\Sigma^+$, $v = 1$	0	0.25
	31290	I	$X^1\Sigma^+$, $v = 0$	0	1.11
	31511	754	$^3\Delta_1$	0	0.10
	31595	I	$X^1\Sigma^+$, $v = 0$	0	0.09
	31703	754	$X^1\Sigma^+$, $v = 1$	0	0.25
	31761	I	$X^1\Sigma^+$, $v = 0$	0	0.12
	31895	I	$X^1\Sigma^+$, $v = 0$	0	0.96
	32094	754	$^3\Delta_1$	0	0.25
	32255	I	$X^1\Sigma^+$, $v = 0$	0	0.09
	32289	754	$X^1\Sigma^+$, $v = 1$	0	0.37
	32489	I	$X^1\Sigma^+$, $v = 0$	0	1.46

Table D.2: Summary of observed photodissociation transitions, part II.